UC Merced

UC Merced Electronic Theses and Dissertations

Title

ULTRA-HIGH ENERGY DENSITY ROADWAY PIEZOELECTRIC ENERGY HARVESTING SYSTEM

Permalink

https://escholarship.org/uc/item/8pq7b3q7

Author

Chen, Cheng

Publication Date

2021

Copyright Information

This work is made available under the terms of a Creative Commons Attribution-NonCommercial License, availalbe at https://creativecommons.org/licenses/by-nc/4.0/

Peer reviewed|Thesis/dissertation

eScholarship.org Powered by the California Digital Library
University of California

UNIVERSITY OF CALIFORNIA, MERCED

ULTRA-HIGH ENERGY DENSITY ROADWAY PIEZOELECTRIC ENERGY HARVESTING SYSTEM

by

Cheng Chen

A thesis submitted in partial satisfaction of the
requirements for the degree of
Doctor of Philosophy

in

Mechanical Engineering

Committee in charge:
Professor Jian-Qiao Sun, Chair
Professor Arnold Kim
Professor Sachin Goyal
Professor Abel Chuang

©2021 Cheng Chen

©2021 Cheng Chen

All rights are reserved.

The thesis of Cheng Chen is approved:

Jian-Qiao Sun, Chair	Date
Arnold Kim	Date
Sachin Goyal	Date
Abel Chuang	Date

University of California, Merced

©2021 Cheng Chen

To my parents.

Yinyuan Chen 陈银元

Genzhen Liu 刘艮珍

ACKNOWLEDGEMENTS

I would like to express my most sincere appreciation to my advisor, Professor Jian-Qiao Sun for his endless support and nurture throughout my graduate study. He has tirelessly taught me everything I know about research and paved my path to pursue an academic career. Not only was he an integral part of my studies, he was also a life coach. With great patience and tolerance, he often shared valuable life experiences and offered warmhearted advice. I really want to thank Professor Sun for having faith in me and providing tremendous support for my PhD study. I am forever grateful.

I would like to thank my committee members, Professor Arnold Kim and Professor Sachin Goyal and Professor Abel Chuang, for continued support and devotion to this dissertation. I was lucky to participate in Professor Kim's PDE class and Professor Goyal's Multibody Dynamics class, where I have learned not only the knowledge that I am very interested in, but also the importance of optimism and tolerance. It guides me to be a better myself until now and beyond.

I am grateful for all my colleagues and have truly enjoyed working with everyone. Amir Sharafi, thank you for the patient and consistent support for me. The time we spend to search for answers in our design is a wonderful memory in my life. I would like to thank Dr. Huifang Dou for her huge help for the development and test of energy storage circuit. I want to thank Dr. Guangfu Li for his support to the current measurement. I'm so grateful for the undergraduates who worked on

assembling and testing the devices, Jason Flores, Ralph Louie Dela Pena, Priscilla Mendoza, Helen Ayala and Steven Ortiz-Donato. I also want to thank Ghazaale Leylaz Mehrabadi, Shangjie Ma, Anni Zhao, Ala'aldin Alafaghani, my wonderful friends and labmates for their companionship in the lab and the endless gossip sessions.

I would like to offer my deepest gratitude to my parents for their unconditional support and selflessly providing me with the opportunities to pursue my dreams. My father has always been my role model and has given me valuable wisdom and advice in my PhD journey. My mother always has faith in me and encourages me with endless trust during hard times. I also want to thank my sister, Ling, for her undying cheerfulness and good spirits, which always fuels me with energy to continue my studies.

Finally, I would like to thank my wife, Yan. I cannot thank you enough for everything you've done for me, from every delicious meal to conducting drive tests on site, and to our adorable daughter, Emily. Thank you, Emily, for sleeping while I wrote and for the many encouraging smiles. I am deeply thankful for all the blessings.

CURRICULUM VITAE

Education

Ph.D. in Mechanical Engineering, University of California Merced (Merced, USA), 2021.

M.S. in Mechanical Manufacture and Automation, University of Chinese Academy of Sciences (Beijing, China), 2012.

B.S. in Mechanical Engineering and Automation, University of Science and Technology Beijing (Beijing, China), 2009.

Field of study

Piezoelectric energy harvesting and structural dynamics

Publications

Cheng Chen, Tian-Bing Xu, Atousa Yazdani, and Jian-Qiao Sun. "A high density piezoelectric energy harvesting device from highway traffic—System design and road test." Applied Energy 299 (2021): 117331.

Cheng Chen, Amir Sharafi, and Jian-Qiao Sun. "A high density piezoelectric energy harvesting device from highway traffic–Design analysis and laboratory validation." Applied Energy 269 (2020): 115073.

Cheng Chen, Amir Sharafi, Jason Flores, Ralph Louie Dela Pena, Priscilla Mendoza, Helen Ayala, Steven Ortiz-Donato, and Jian-Qiao Sun. "Design and Laboratory Validation of a Force-Amplified Piezoelectric Energy Harvesting Unit." In International Design Engineering Technical Conferences and Computers and Information in Engineering Conference, vol. 83969, p. V007T07A006. American Society of Mechanical Engineers, 2020.

TABLE OF ABBREVIATIONS

PEH	Piezoelectric energy harvesting
PEHU	Piezoelectric energy harvesting unit
PEHT	Piezoelectric energy harvesting tower
PEHB	Piezoelectric energy harvesting box
PEHS	Piezoelectric energy harvesting system
PZT	Lead zirconate titanate
PSO	Particle swarm optimization
FAM	Force amplification mechanism
FEM	Finite element method
MOD	Multi-objective optimal design
MOPSO	Multi-objective particle swarm optimization

TABLE OF CONTENTS

ACKNOWLEDGEMENTS . . . . . **ii**
CURRICULUM VITAE . . . . . **iv**
TABLE OF ABBREVIATIONS . . . . . **vi**
LIST OF FIGURES . . . . . **xi**
LIST OF TABLES . . . . . **xx**
ABSTRACT . . . . . **xxi**

Chapter

1 REVIEW OF PIEZOELECTRIC ENERGY HARVESTING . . . **1**

1.1 Introduction 1
1.2 Piezoelectric Materials in Energy Harvesting 3

1.2.1 Typical Piezoelectric Operating Modes 4
1.2.2 Typical Piezoelectric Materials 6

1.2.2.1 Perovskite Materials 6
1.2.2.2 Wurtzite Materials 13
1.2.2.3 Piezoelectric Polymers 14
1.2.2.4 2D Atomically Thin Sheet Materials 15
1.2.2.5 Summary of Typical Piezoelectric Materials 16

1.3 Mechanical Configurations 17

1.3.1 Piezoelectric Nanogenerators 17
1.3.2 Bending Configurations 22

1.3.2.1 Cantilever 22
1.3.2.2 Circular Diaphragm 28

1.3.2.3 Other Bending Types 31

1.3.3 Compression and Tension Configurations 33
1.3.4 Shear and Torsion Configurations 39

1.4 Applications and Designs 43

1.4.1 Human Body Activity 44
1.4.2 Roadway Traffic 47

1.5 Discussions 53

1.5.1 Challenges 53
1.5.2 Trends 55

1.6 Conclusions 57

2 MATHEMATICAL MODEL OF PEHU 61

2.1 Introduction 61
2.2 Mathematical Model of PEHU 69
2.3 Nonlinear Clamped-Clamped Beam 70
2.4 Finite Element Model of PZT Stack 73

2.4.1 Equations of Motion 73
2.4.2 Dynamic Analysis of PZT Stack 83

2.5 Coupled Analysis of PEHU 87
2.6 Nomenclature 88

3 DYNAMIC ANALYSIS OF PEHU 92

3.1 Equations of Motion 92
3.2 Mode Expansion 94
3.3 Weighted Residual Method 95
3.4 Time Integration Procedure 97
3.5 Dynamic Response to Traffic Load 102

3.5.1 Effect of Damping 104

3.5.2 Effect of Vehicle Speed . . . 108

3.6 Conclusions . . . 111

4 DESIGN AND LABORATORY TEST OF PEHU . . . 112

4.1 Static Analysis of PEHU . . . 112
4.2 Multi-Objective Optimal Design . . . 118

4.2.1 Parameters of PEHS . . . 118
4.2.2 MOD Problem Statement . . . 122
4.2.3 Particle Swarm Optimization . . . 123
4.2.4 Discretized Searching . . . 130

4.3 Prototype and Laboratory Evaluation . . . 139

4.3.1 Comparison of Theoretical and Experimental Results . . . 140
4.3.2 Discussions . . . 142

4.4 Energy Density Estimate . . . 144
4.5 Conclusions . . . 147

5 PIEZOELECTRIC ENERGY HARVESTING TOWER . . . 148

5.1 Piezoelectric Energy Harvesting Unit . . . 148
5.2 Piezoelectric Energy Harvesting Tower . . . 152
5.3 Charging Battery with PEHT . . . 158
5.4 Methods . . . 162
5.5 Conclusions . . . 163

6 PEHS AND ROAD TESTS . . . 164

6.1 Piezoelectric Energy Harvesting System . . . 164
6.2 Construction of PEHS on Road . . . 166
6.3 Road Test Results . . . 167
6.4 Discussions . . . 171

7 SCALED-UP DESIGN FOR HEAVY TRUCKS . . . 173

7.1 Multi-Objective Optimal Design . . . 173
7.2 Energy Density Estimate . . . 186

7.3 Conclusions 191

8 SUMMARY 192
BIBLIOGRAPHY 198

LIST OF FIGURES

1.1 An abbreviated technology roadmap of PEH based on reported studies. 3

1.2 Typical operating modes of piezoelectric energy harvesting. (a) 33-mode; (b) 31-mode; (c) 15-mode; (d) 11-mode. 5

1.3 Typical configurations of PENG. (a) A plane-type PENG based on ZnO NW arrays, reproduced with permission from Wiley-VCH [1]; (b) A fiber-type PENG based on ZnO NW arrays, reproduced with permission from Wiley-VCH [1]; (c) A PENG based on laterally aligned PZT NWs, reprinted with permission from [2], copyright (2017) American Chemical Society; (d) A PENG based on WSe_2 monolayer, reproduced with permission from Wiley-VCH [3]; (e) A KNLN based NCG, reproduced with permission from Wiley-VCH [4]; (f) A PENG based on PZT thin film, reproduced with permission from Wiley-VCH [5]; (g) A NCG composited of BZT-BCT and PVDF with floating Cu electrode, reproduced with permission from Elsevier [6]. 19

1.4 Typical cantilever configurations of PEH devices. (a) A bi-stable harvester, reproduced with permission from Elsevier [7]; (b) A tri-stable harvester, reproduced with permission from Elsevier [7]; (c) A quin-stable harvester with frequency up-conversion, reproduced with permission from Elsevier [8]; (d) A quad-stable harvester with frequency up-conversion, reproduced with permission from Elsevier [9]; (e) A non-linear U-shaped harvester, reproduced with permission from Elsevier [10]; (f) A rotational bi-stable harvester, reproduced with permission from Elsevier [11]; (g) A multi-stable harvester array, reproduced with permission from Elsevier [12];(h) A dual-frequency harvester [13]. 29

1.5 Typical circular diaphragm configurations of PEH devices. (a) A piezoelectric fluid diaphragm harvester, reproduced with permission from Elsevier [14]; (b) A piezoelectric harvester based on diaphragm array, reproduced with permission from American Institute of Physics [15]; (c) A annular diaphragm harvester [16]; (d) A annular diaphragm harvester with notched substrate [17]. 32

1.6 Other bending configurations of PEH devices. (a) A pendulum harvester of PZT-attached binder clips, reproduced with permission from Elsevier [18]; (b) A piezoelectric harvester of multilayered levered mechanism, reproduced with permission from American Institute of Physics [19]; (c) A PEH module based on PVDF thin films, reproduced with permission from Elsevier [20]; (d) A cantilever harvester with revolute joint, reproduced with permission from Elsevier [21]. 34

1.7 PEH configurations of force amplification mechanisms. (a) A mechanically amplified piezoelectric stack, reproduced with permission from Elsevier [22]; (b) A two-stage rhombus-type harvester, reproduced with permission from Elsevier [23]; (c) A two-stage bridge-type harvester, reproduced with permission from Elsevier [24]; (d) A bridge harvester, reproduced with permission from Elsevier [25]; (e) A double-bridge harvester, reproduced with permission from Elsevier [25]; (f) A PEH device with flat clamped-clamped beams, reproduced with permission from Elsevier [26]. 36

1.8 PEH configurations in shear and torsion mode. (a) A 15-mode unimorph cantilever; (b) A 36-mode unimorph cantilever; (c) A sandwiched 15-mode cantilever; (d) PEH from torsional thin-walled tube by PZT patches; (e) A 15-mode bridge-type harvester [27]; (f) A 15-mode halved bridge-type harvester, reproduced with permission from Elsevier [28]. 40

1.9 Examples of PEH from human body activities. (a) A ZnO/PVDF fiber-type PENG harvest energy from elbow bending, reproduced with permission from Wiley-VCH [1]; (b) A flexible ZnO NW array PENG harvest energy from eye blinking, reproduced with permission from Wiley-VCH [29]; (c) A flexible PENG based on p-NC NF composited of BaTiO3 NPs and P(VDF-TrFE) embedded in shoe, reproduced with permission from Elsevier [30]; (d) A PENG made of p-NC of P(VDF-TrFE)/BNNTs harvests energy from stepping, reproduced with permission from Elsevier [31]; (e) A flexible all-in-one NCG harvests energy from running, reproduced with permission from Elsevier [32]; (f) A PENG attached shoe harvests energy from walking, reproduced with permission from Elsevier [33]; (g) A PEH device consisting of 8 bimorph cantilevers harvests energy from walking to power a WSN [34]; (h) A cantilever harvester mounted on leg harvests energy from walking, reproduced with permission from Elsevier [35]. 45

1.10 Examples of PEH from roadway traffic. (a) A PEH module consists of 64 layered Bridges, reproduced with permission from Elsevier [36]; (b) A force-amplified PEH device of high energy density, reproduced with permission from Elsevier [26]; (c) A PZT disk array harvester, reproduced with permission from Elsevier [37]; (d) A PZT disks integrated pavement sample, reproduced with permission from Elsevier [38]; (e) A PEH device of vertical PVDF films, reproduced with permission from Elsevier [39]; (f) A PEH device of horizontal PVDF films, reproduced with permission from Elsevier [20]; (g) A PEH device consisting of 18 clamped-clamped beam harvesters, reproduced with permission from Elsevier [40]; (h) A PEH device consisting of 80 clamped-clamped beam harvesters, reproduced with permission from Elsevier [41]. 49

2.1 Schematic of the piezoelectric energy harvesting device design. . . . 70

2.2 A multi-layer PZT stack made by CeramTec in Germany. 73

2.3 The finite element model of the multi-layer PZT stack. 74

3.1 The open circuit voltage of the piezoelectric energy harvesting device due to a vehicle passing at speed $104.61km/h$ ($65mph$). 105

3.2 The sinking displacement of the piezoelectric energy harvesting device due to a vehicle passes over at speed $104.61km/h$ $(65mph)$. 106

3.3 Dynamic force amplification factor of the piezoelectric energy harvesting device due to a vehicle passes over at speed $104.61km/h$ $(65mph)$. 106

3.4 The compressive force on the PZT stacks in the piezoelectric energy harvesting device due to a vehicle passing at speed $104.61km/h$ $(65mph)$. 107

3.5 The sinking displacement of the piezoelectric energy harvesting device as a function of vehicle speed. 109

3.6 The maximum voltage output of the piezoelectric energy harvesting device as a function of vehicle speed. 109

3.7 The electric potential energy harvested by the piezoelectric energy harvesting device as a function of vehicle speed. 110

3.8 The energy conversion efficiency of the piezoelectric energy harvesting device as a function of vehicle speed. 110

4.1 The force amplification mechanism with PZT rod for PEHU. 113

4.2 A conceptual implementation of the PEHS under the pavement. . 119

4.3 The main algorithm of Multi-objective particle swarm optimization method for PEHU design. 124

4.4 The Pareto set and front of PEHU by multi-objective particle swarm optimization when $h_b = 0.4064mm$. 127

4.5 The Pareto set and front of PEHU by multi-objective particle swarm optimization when $h_b = 0.8128mm$. 128

4.6 The Pareto set and front of PEHU by multi-objective particle swarm optimization when $h_b = 1.6002mm$. 129

4.7 The Pareto set and front of PEHU by multi-objective particle swarm optimization when $h_b = 3.175mm$. 131

4.8 The electric energy E_U of feasible candidates in design space when $h_b = 0.4064mm$. 131

4.9 The sinking displacement d_{sk} of feasible candidates in design space when $h_b = 0.4064mm$. 132

4.10 The feasible candidates in design space and their performance in search space when $h_b = 0.4064mm$. 132

4.11 The electric energy E_U of feasible candidates in design space when $h_b = 0.8128mm$. 133

4.12 The sinking displacement d_{sk} of feasible candidates in design space when $h_b = 0.8128mm$. 133

4.13 The feasible candidates in design space and their performance in search space when $h_b = 0.8128mm$. 134

4.14 The electric energy E_U of feasible candidates in design space when $h_b = 1.6002mm$. 135

4.15 The sinking displacement d_{sk} of feasible candidates in design space when $h_b = 1.6002mm$. 135

4.16 The feasible candidates in design space and their performance in search space when $h_b = 1.6002mm$. 136

4.17 The electric energy E_U of feasible candidates in design space when $h_b = 3.175mm$. 136

4.18 The sinking displacement d_{sk} of feasible candidates in design space when $h_b = 3.175mm$. 137

4.19 The feasible candidates in design space and their performance in search space when $h_b = 3.175mm$. 137

4.20 The electric energy E_U of sampled feasible candidates in design space. 138

4.21 The sinking displacement d_{sk} of sampled feasible candidates in design space. 138

4.22 Experimental setup of the quasi-static compression test on Instron machine. 141

4.23 Input compressive force vs. sinking displacement of the piezoelectric energy harvesting device. 141

4.24 Input compressive force vs. open-circuit voltage of the piezoelectric energy harvesting device. 142

4.25 The vertical preload to the piezoelectric energy harvesting device in Test 3. 144

5.1 Piezoelectric energy harvesting unit. **a**, Conceptual model of proposed force amplification mechanism for energy harvesting. **b**, Realization of piezoelectric energy harvesting unit with optimized parameters. 149

5.2 3D model of the piezoelectric energy harvesting tower. 153

5.3 The sinking displacement d_{sk} of a PEHT prototype under quasi-static compression of 1333N with vertical preload up to about 200N. . . . 154

5.4 The open circuit voltage V_T of a PEHT prototype under quasi-static compression of 1333N with vertical preload up to about 200N. . . . 154

5.5 The sinking displacement (d_{sk}) of a piezoelectric energy harvesting tower during the first 50 quasi-static tests of 1333 N without vertical preload. 156

5.6 The sinking displacement (d_{sk}) of 48 piezoelectric energy harvesting towers under compression force P_{in} of 1333 N without vertical preload during the first 50 tests. 156

5.7 The sinking displacement (d_{sk}) of the 48 piezoelectric energy harvesting towers under compression force P_{in} of 1333 N without vertical preload during the first 50 tests. 157

5.8 Laboratory tests of charging a 12 V DC battery by a PEHT. **a**, Experimental setup. **b**, Schematic circuit diagram. 158

5.9 Voltage of PEHT and battery in the test of charging a 12 V DC battery in 5 quasi-static load cycles with amplitude of 1333 N. . . . 159

5.10 Current of PEHT and battery in the test of charging a 12 V DC battery in 5 quasi-static load cycles with amplitude of 1333 N. . . . 160

5.11 Output power of PEHT and charging power of 12 V DC battery in 5 quasi-static load cycles with amplitude of 1333 N. 160

5.12 Output Energy of PEHT and stored energy in 12 V DC battery in 5 quasi-static load cycles with amplitude of 1333 N. 161

6.1 Schematic of circuit for charging a DC battery on road. **a**, Piezoelectric energy harvesting system. **b**, Piezoelectric energy harvesting box. **c**, A row of PEHTs with a full bridge rectifier. . . . 165

6.2 3D model of a piezoelectric energy harvesting box for implementation in pavement. 166

6.3 Construction progress of the piezoelectric energy harvesting system. **a**, Traffic concrete boxes installation after excavation. **b**, Fixed concrete boxes. **c**, Installation of piezoelectric energy harvesting towers. **d**, Completed piezoelectric energy harvesting system. 167

6.4 Drive test results of piezoelectric energy harvesting system. **a**, Open circuit voltage of PEHS during Altima passage at speed of 40 km/h. Each PEHB was activated twice by the front and rear wheel. Therefore, 16 voltage peaks in each path generated as marked in circles. **b**, Harvested electric energy in tests at different speeds statistically indicates a positive effect of vehicle speed on energy harvesting. **c**, The maximum open circuit voltage in left and right paths at different speeds. **d**, Harvested electric energy in left and right paths at different speeds. 169

6.5 Estimated speeds in drive tests based on open circuit voltage measurements. 170

7.1 The feasible candidates in design space and their performance in search space for heavy trucks when $n_r = 5$, $n_p = 19$, $h_b = 0.4064mm$.175

7.2 The feasible candidates in design space and their performance in search space for heavy trucks when $n_r = 5$, $n_p = 19$, $h_b = 0.8128mm$.176

7.3 The feasible candidates in design space and their performance in search space for heavy trucks when $n_r = 5$, $n_p = 19$, $h_b = 1.6002mm$.176

7.4 The feasible candidates in design space and their performance in search space for heavy trucks when $n_r = 5$, $n_p = 19$, $h_b = 3.175mm$. 177

7.5 The force amplification factor α_f of feasible candidates in design space of n_r and n_p for heavy trucks when $l_b = 200mm$, $b_b = 200mm$, $h_b = 1.6002mm$. 177

7.6 The electric energy E_U of feasible candidates in design space of n_r and n_p for heavy trucks when $l_b = 200mm$, $b_b = 200mm$, $h_b = 1.6002mm$.178

7.7 The sinking displacement d_{sk} of feasible candidates in design space of n_r and n_p for heavy trucks when $l_b = 200mm$, $b_b = 200mm$, $h_b = 1.6002mm$. 178

7.8 The feasible candidates in design space and their performance in search space of n_r and n_p for heavy trucks when $l_b = 200mm$, $b_b = 200mm$, $h_b = 1.6002mm$. 179

7.9 The feasible candidates in design space and their performance in search space of l_b and b_b for heavy trucks when $n_r = 2$, $n_p = 36$, $h_b = 1.6002mm$. 180

7.10 The Pareto set and front of PEHU for heavy trucks by multi-objective particle swarm optimization when $n_r = 2$, $n_p = 36$, $h_b = 1.6002mm$. 181

7.11 The electric energy E_U of sampled feasible candidates in design space when $n_r = 2$, $n_p = 36$. 181

7.12 The feasible candidates in design space and their performance in search space of l_b and b_b for heavy trucks when $n_r = 3$, $n_p = 27$, $h_b = 1.6002mm$. 182

7.13 The Pareto set and front of PEHU for heavy trucks by multi-objective particle swarm optimization when $n_r = 3$, $n_p = 27$, $h_b = 1.6002mm$. 182

7.14 The electric energy E_U of sampled feasible candidates in design space when $n_r = 3$, $n_p = 27$. 183

7.15 The feasible candidates in design space and their performance in search space of l_b and b_b for heavy trucks when $n_r = 4$, $n_p = 22$, $h_b = 1.6002mm$. 184

7.16 The Pareto set and front of PEHU for heavy trucks by multi-objective particle swarm optimization when $n_r = 4$, $n_p = 22$, $h_b = 1.6002mm$. 184

7.17 The electric energy E_U of sampled feasible candidates in design space when $n_r = 4$, $n_p = 22$. 185

7.18 The Pareto set and front of PEHU for heavy trucks by multi-objective particle swarm optimization when $n_r = 5$, $n_p = 19$, $h_b = 1.6002mm$. 185

7.19 The electric energy E_U of sampled feasible candidates in design space when $n_r = 5$, $n_p = 19$. 187

7.20 The energy density ρ_E of feasible candidates in design space of n_r and n_p for heavy trucks when $l_b = 200mm$, $b_b = 200mm$, $h_b = 1.6002mm$.187

7.21 The energy density ρ_E and sinking displacement d_{sk} of feasible candidates in design space of n_r and n_p for heavy trucks when $l_b = 200mm$, $b_b = 200mm$, $h_b = 1.6002mm$. 189

7.22 The harvested energy E and sinking displacement d_{sk} of feasible candidates in design space of n_r and n_p for heavy trucks when $l_b = 200mm$, $b_b = 200mm$, $h_b = 1.6002mm$. 189

LIST OF TABLES

1.1 Summary of typical piezoelectric materials and their performance in applications. The size column refers to the 3D dimension of piezoelectric material if available. 58

1.2 Summary of typical piezoelectric energy harvesting from human body activities. The size column refers to the 3D dimension of piezoelectric material if available. 59

1.3 Summary of typical piezoelectric energy harvesting from roadway traffic. The size column refers to the 3D dimension of piezoelectric material. 60

3.1 The first five natural frequencies of the PEHU. 104

3.2 Modal damping ratios of the four cases. 105

3.3 Peak values of dynamic responses of the piezoelectric energy harvesting device due to a vehicle passing at speed $104.61km/h$ ($65mph$). Case 0 has no damping. 108

4.1 Some known parameters for the PEHU design. 123

4.2 Parameters in MOPSO algorithm. 128

4.3 Selected PEHU design and its static properties. 139

5.1 Electric properties of energy storage. 162

7.1 Selected optimal designs for heavy trucks and their static properties. 190

ABSTRACT

Massive dissipated kinetic energy of roadway traffic is a sustainable energy source that can be harvested via piezoelectric effect. This approach provides a robust and reliable solution of roadway power generation. However, to achieve high energy density remains challenging. This thesis focuses on the development of a high density piezoelectric energy harvesting system from roadway traffic, which reaches an energy density as high as 15.37 J/(m.pass.lane) in drive tests. The high energy density is achieved by incorporating a compression-to-compression force amplification mechanism which amplifies the harvested energy by a factor of 100, as well as an optimized system configuration to take full advantage of dynamic load from vehicles. To the best of our knowledge, the scalable prototype system has achieved the highest energy density, which holds the great potential to enable self-powered smart road on a large scale. Based on the drive test results, implementation of this technology in one lane of 1609.34 m can generate at least electric energy of 7.22×10^4 kWh in one year.

In this dissertation, the details of proposed piezoelectric energy harvesting technology are presented, including mathematical modeling and analysis, optimization of design parameters, mechanical design at all levels, lab test method and results, road implementation and drive test results. The chapters are organized as follows.

Chapter 1 reviews recent developments of piezoelectric energy harvesting, including materials, configurations, and performances, followed by the discussion on the challenges and trends. Chapter 2 introduces the mathematical modeling of proposed design idea, derives the equations of motion for theoretical exploration. Chapter 3 demonstrates the procedure of dynamic analysis for this modeling, and presents simulation results of a selected design. Chapter 4 explains how we conducted parameters optimization for high energy density based on the mathematical modeling, afterwards, illustrates the mechanical design for the realization of an aggressive selected design and its laboratory validation. Chapter 5 introduces the vertical packaging of PEHUs, piezoelectric energy harvesting tower, including mechanical design, quasi-static compression test results, battery charging test results. Chapter 6 shows the system design for the implementation on road from both the electrical and mechanical perspectives. The drive test results based on a prototype system on the campus of UC Merced are presented. Chapter 7 discusses the optimal designs for the traffic of heavy truck for future exploration. Chapter 8 summarizes the thesis and discusses future directions.

Chapter 1

REVIEW OF PIEZOELECTRIC ENERGY HARVESTING

As an emerging renewable energy technology, piezoelectric energy harvesting holds great potential to achieve self-powered sensor networks and portable electronics while substantially reducing the impact of carbon emissions on the environment, and thus attracted increasing attentions from both academia and industry. Many new piezoelectric materials and innovative designs were proposed in the past decade to advance PEH technology. As a result, the output power of piezoelectric energy harvesters from human body activities and roadway traffic have been improved to mW-level and W-level, respectively. In this chapter, we review recent developments of piezoelectric energy harvesting, including materials, configurations, and performances, followed by the discussion on the challenges and trends.

1.1 Introduction

Renewable energy technologies based on multiple energy conversion principles [42] have been developed to generate electricity from sources of solar, vibration, fluid, human motion and so on. Implementation of renewable energy technology worldwide would reduce carbon emissions and toxic waste into the environment, and slow down global warming as well as create millions of new long-term jobs [43]. Piezoelectric energy harvesting (PEH) from mechanical energy is one of the most promising renewable energy technologies [44–46].

Electronics with batteries have the problem of limited service life. Replacement of batteries can be costly and even impossible. PEH from working environment is a possible solution. For example, implantable biomedical electronics, such as cardiac pacemakers and deep brain stimulation, need battery replacement every few years [47]. In addition, surgery brings great economic burden and health risks to patient. PEH from biomechanical energy is a potential solution to extend the lifespan or even make it battery free [48]. Many Lead-free piezoelectric materials have been utilized to fabricate piezoelectric nanogenerator (PENG) for wearable and implantable electronics.

In the era of internet of things (IoT) and artificial intelligence (AI), widely distributed sensor networks in various forms are of importance. They usually need low power supply rather than power grid. PEH technologies are promising to enable self-powered wireless sensor network (WSN). Harvesters in various mechanical configurations have been invented [45, 49, 50]. Recently reported PEH devices based on PZT and PDVF are able to generated W-level power from roadway traffic [26, 51]. This is a significant step towards the realization of self-powered equipment for smart road.

Endeavoring to provide an overview of the state-of-art PEH technologies, we summarized an abbreviated technology roadmap of PEH based on reported studies from the perspective of materials, operation modes, mechanical configurations, scales, and applications, as shown in Figure 1.1. Each combination represents a PEH strategy that has been explored. This Chapter is organized accordingly to provide detailed information in order to help readers better construct a comprehensive technology roadmap. Representative research achievements are introduced briefly to demonstrate the development of each aspect.

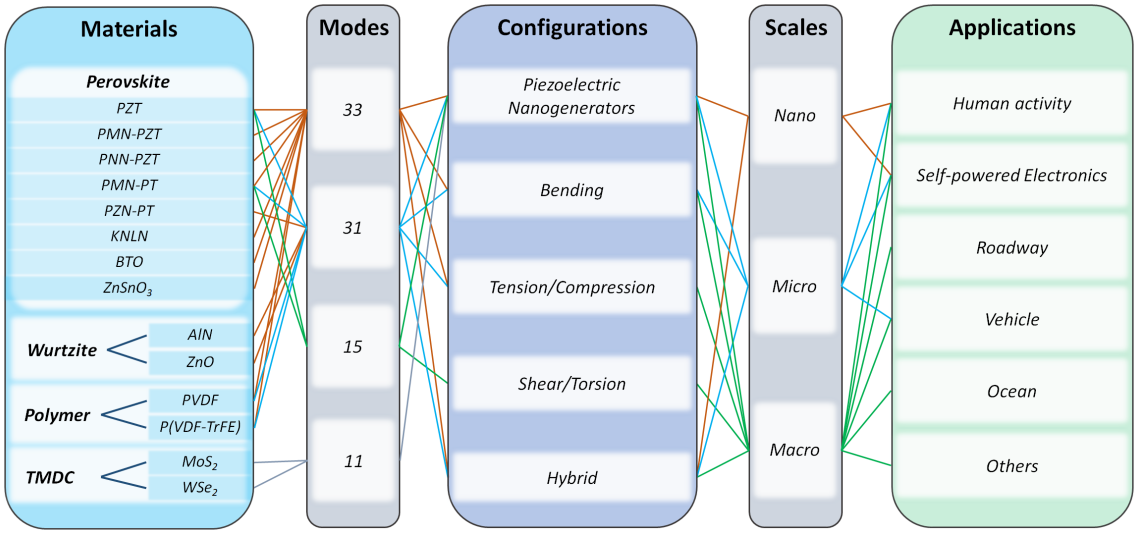

Figure 1.1: An abbreviated technology roadmap of PEH based on reported studies.

The rest of this chapter is outlined as follows. In Section 1.2, we presents various piezoelectric materials that have been used in energy harvesting technologies. Structure-based classification and typical performance reported in literature are employed to introduce piezoelectric materials. In Section 1.3, we systematically summarize various mechanical configurations of PEH devices based on operating modes. Section 1.4 reviews the development of PEH applications in human activities and roadway traffic in the past decade. In Section 1.5, challenges as well as trends of PEH technology are discussed. Finally, this chapter concludes in Section 1.6.

1.2 Piezoelectric Materials in Energy Harvesting

Since quartz was discovered to be piezoelectric in 1880, many piezoelectric materials were found in the nature and created artificially to achieve special properties for various applications. In this section, we will review the common operating

modes and piezoelectric materials for PEH in the past decade, including perovskites, wurtzites, polymers, and transition metal dichalcogenides (TMDCs).

1.2.1 Typical Piezoelectric Operating Modes

Piezoelectricity is a coupling property of materials that are capable to transform mechanical energy into electric energy, and vice versa, including direct and converse piezoelectric effect. For energy harvesting, direct piezoelectric effect is used to collect energy. The constitutive equations that describe the linear piezoelectric effect of a material omitting mechanical and electrical dissipation are defined as

$$\begin{bmatrix} D \\ \varepsilon \end{bmatrix} = \begin{bmatrix} e^{\sigma} & d^{T} \\ d & s^{E} \end{bmatrix} \begin{bmatrix} E \\ \sigma \end{bmatrix} \tag{1.1}$$

Where$D$, E, ε, σ are the electric displacement vector, electric field vector, strain vector, and stress vector, respectively. s^{E}, e^{σ}, and d are the compliance matrix under a constant electrical field, the dielectric permittivity matrix under a constant stress, and the piezoelectric charge constant matrix, which are assumed to be independent of the magnitude and frequency of applied mechanical and electric forces. The superscript T stands for the transpose. In general, piezoelectric charge constants are consistent in direct and converse piezoelectric effect. The piezoelectric charge constants d_{jk} relate the normal stress in k direction (k = 1, 2, 3) or the shear stress in k plane ($k = 4, 5, 6$) to the electric displacement in j direction (j = 1, 2, 3), where 3 is the poling direction or the polar axis, 4, 5, 6 are 2-3 plane, 1-3 plane, and 1-2 plane, respectively. By integration, d_{jk} can be used to estimate generated charges from applied mechanical force.

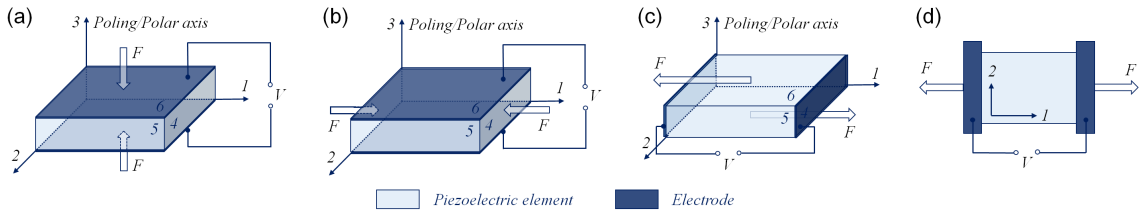

Figure 1.2: Typical operating modes of piezoelectric energy harvesting. (a) 33-mode; (b) 31-mode; (c) 15-mode; (d) 11-mode.

Typical operating modes for PEH include 33-mode, 31-mode, 15-mode, and 11-mode, as shown in Figure 1.2, which are correspondingly named after the subscripts of piezoelectric constants. Harvesters in 33-mode and 31-mode take advantages of normal stress, such as piezoelectric ceramic in bulk form under compression or tension. The polarization is parallel to the applied stress in 33-mode while they are perpendicular to each other in 31-mode. These two modes are the most commonly used in PEH. 15-mode and 36-mode utilize shear stress to generate electric potential, also named as thickness shear mode and surface shear mode, respectively. Due to the small value of d_{36} for most piezoelectric materials, it is not often used in energy harvesting. The in-plane 11-mode describes the stretching of $2D$ atomically thin materials. For harvesters subjected to bending, such as cantilever beams attached with piezoceramic film, it can be designed to work in any of the three modes (33, 31, 15) because of the coexistence of normal and shear stress. The actual working mode depends on the poling direction in piezoelectric material and the setting of electrode.

The dominant piezoelectric constant serves for a good estimate of electric output for a harvester in single operating mode. However, multiple piezoelectric constants need to be considered to obtain a good prediction for the designs in coupled

modes. For example, the evaluation of generated potential of ZnO nanowire in bending operating mode involves d_{33}, d_{31}, and d_{15} [52]. For thin PZT ribbons, the dominance of membrane strain in total strain allows the estimate of potential while ignoring the bending strain. An effective piezoelectric constant integrating 33-mode and 31-mode was adopted for plane-strain deformation ($\varepsilon_{22} = 0$) [53]. In addition, the prediction of the power generation of the Cymbal harvester is based on an effective constant defined as the sum of d_{33} and multiplication of d_{31} and the amplification factor [54].

1.2.2 Typical Piezoelectric Materials

1.2.2.1 Perovskite Materials

Named after the natural perovskite $CaTiO_3$, the perovskite family including lead zirconate titanate (PZT) are the most common and widely studied materials for PEH. For ferroelectric material, a poling process by a large external electric field to align all the domains along the poling direction is needed in order to exhibit optimized piezoelectric effect below Curie temperature. Perovskites are fabricated into multiple forms including bulk ceramics, polycrystalline thick films, single crystal thin films, multilayer stack, MFC, and SFC for energy harvesting.

Perovskite Polycrystalline

PZT polycrystalline exhibits typical characteristics of ceramics, such as a high elastic modulus, brittleness, and low tensile strength. PZT ceramics can be divided into soft and hard PZT ceramics in general. Soft PZT ceramics whose domain walls have less mobility usually exhibit stronger piezoelectric properties than that of hard PZT. Take CeramTec's products as an example, the piezoelectric charge constants d_{33}, d_{31}, and d_{15} of soft PZT ceramics is in the ranges $(375, 870)$, $(-370, -157)$,

and $(490, 770)pC/N$, respectively, while those for hard PZT ceramics are $(240, 315)$, $(-135, -90)$, and $(300, 550)pC/N$, respectively. Furthermore, soft PZT ceramics have larger elastic compliance and higher charge sensitivity. Therefore, soft PZT are widely adopted in energy harvesting studies. Regarding the hard PZT ceramics, its less permittivity and dielectric dissipation factor that contributes to less mechanical and electrical losses, make it more preferable in power applications [55]. PZT ceramics are commercially available in all kinds of shapes, such as tubes, bars, plates, hemispheres, discs, and rings with varying size.

PZT can be fabricated into polycrystalline thick films with a thicknesses in the micrometer range using sol-gel method. PZT thick film for bender energy harvester can be designed in either 31-mode or 33-mode, where the poling direction of 31-mode PZT film is typically along the thickness. Consequently, the electrodes are usually on its upper and lower surfaces. It is worth mentioning that d_{33} is approximately 2.5 times greater than d_{31} for most PZT ceramics, therefore, 33-mode is attractive for higher output. However, PZT film in 33-mode usually requires the poling direction along the length and interdigitated electrodes (IDEs) to induce an in-plane electric field, which increase the cost of manufacturing.

A flexible harvester made of a polycrystalline PZT film (thickness of $7\mu m$, $d_{33} = 406pC/N$) by aerosol deposition (AD) process can convert a maximum output voltage of $200V$ and a current signal of $35\mu A$ from biomechanical bending motions [56]. Hwang *et al.* claim that the AD PZT film has advantages in realization of the mass production due to lower production cost and less process time compared to piezoelectric single crystals. Gao *et al.* recently reported a PNN-PZT ceramic with d_{33} of $1753pm/V$ that is comparable to commercial PMN-PT single crystals. A cymbal harvester utilizing a PNN-PZT strip with the dimension of $26.6mm \times$

$4mm \times 0.5mm$ generated an output power of $14\mu W$ at the acceleration of 3.5 g [57]. Recently, Li *et al.* [58] designed a polycrystalline ceramic Sm-doped PMN–PT through high-temperature solid-state processing. The 2.5Sm-PMN–29PT ceramic has a large d_{33} of $1510pC/N$ and Curie temperature of 89 °C which enables its application in room-temperature energy harvesting.

Perovskite Single Crystals

To further improve the efficiency of PEH, single crystals have become more and more attracting. Piezoelectric single crystals require a more complicated fabrication, but have stronger piezoelectricity in contrast to the polycrystalline. PZT has been fabricated into single crystal (SC) thin films [59] for MEMS harvester and SC nanowires for PENG. Isarakorn *et al.* fabricated a MEMS energy harvester consisting of a $0.5\mu m$ thick single crystal PZT thin film and a cantilever beam of $1mm \times 2.5mm \times 0.015mm$ with a Si proof mass. Compared to other MEMS harvester based on poly-PZT and AlN thin films, the reported single crystal PZT harvester showed the highest power density back then due to its high piezoelectric coefficient and low dielectric constant [60]. Zhao *et al.* fabricated a flexible semitransparent PENG based on laterally aligned PZT single-crystal nanowires (NWs) [2]. The d_{33} of PZT NW is $67pm/V$, which is much larger than ZnO NW. The open circuit voltage reaches $10V$ under $70kPa$ pressure at $90Hz$. The high pressure sensitivity of $0.14V/kPa$ shows a great potential in sensing and self-powered systems. However, the time-consuming fabrication process and unavailability of bulk SC limits the application of SC PZT.

In addition to PZT, $Pb(Mg,Nb)O_3$-$PbTiO_3$(PMN-PT) and $Pb(Zn,Nb)O_3$-$PbTiO_3$(PZN-PT) can be grown as single crystals in bulk or thin films with stronger

piezoelectricity than PZT ceramics. Due to stronger electromechanical coupling and piezoelectricity, PMN-PT based ultrasonic transducers have demonstrated superior performance than PZT type [61]. Ren *et al.* reported a PMN-PT based rectangular cymbal harvester of typical size which produced a better power density that was three times higher than a PZT based cymbal harvester [62]. Amin Karami *et al.* demonstrated that single crystal PMN-PT outperformed polycrystalline PZT-5A and PZT-5H monolithic ceramics in power generation in the same unimorph cantilever beam configuration [63]. Xu and Yao *et al.* explored PMN-PT NWs based flexible PENG for self-powered sensing application [64, 65], where a linear relationship between generated voltage and applied strain was observed. Yang *et al.* conducted an experiment to compare the performance of PMN-PT, PZN-PT single crystals, and PZT in cantilever energy harvesting [66]. Dynamic test results based on prototypes with the same size showed that PZN-PT and PMN-PT surpass PZT a lot in generated power over an optimal resistor in both on-resonance and off-resonance conditions. Additionally, the efficiency of PZN-PT and PMN-PT harvester are five times and three time, respectively, more than that of PZT-based harvester at resonance. Chen *et al.* [67] fabricated a PENG based on SC PMN-PT nanobelt (NB) arrays of superior piezoelectric coefficient $d33 = 677pm/V$. The maximum open-circuit voltage and short-circuit current reaches $6.0V$ and $102\mu A$.

However, several limitations of PMN-PT and PZN-PT exist. First, PMN-PT and PZN-PT has a low phase transition temperature and coercive electric field, which are not desirable for high-power transducers [68]. Amin Karami *et al* reported that the single crystal PMN-PT specimens were prone to break due to brittleness. In addition, low Curie temperature of 160 °C makes connection of electrodes by soldering difficult [63]. Yang *et al.* discovered the inhomogeneous property in

PMN-PT and PZN-PT samples, which implied the challenges in producing large-size uniform-composited single crystals. Finally, the high cost due to the complicated manufacturing process, temperature instability, and fatigue issue limit PZN-PT and PMN-PT single crystals' applications in energy harvesting [66].

To further improve phase transition temperature, PMN-PZT was developed. Although bulk-type PMN-PZT is rigid and brittle, the possibility of PMN-PZT based flexible energy harvester was first explored by Hwang and Lee *et al.* [69], where the nanogenerator based on single crystal PMN-PZT thin film can generate an open-circuit voltage of $100V$ and short-circuit current of $20\mu A$ from human finger flicking. The maximum current density was calculated as $6.1\mu A/cm^2$. This flexible PENG was able to directly lighted up 104 blue LEDs by harvesting energy from finger motions. Later on, Kim *et al.* from the same group further explored biocompatibility and performance of PENG based on PMN-PZT-Mn from rhythmical porcine heartbeats [70], where a high output of 17.8-V voltage and 1.74-μA current were obtained in *in vivo* experiments. This energy was utilized to transmit data wirelessly to a receiver in the distance of $5m$. Little inflammatory reaction showed a good biocompatibility for implantable device.

Lead-free Perovskite

Pb-containing piezoceramics are harmful to both environment and human health. To address this issue, various piezoelectric lead-free perovskite materials, such as $Ba(Zr,Ti)O_3$ (BZT), $(Ba,Ca)(Zr,Ti)O_3$ (BCZT), $(Bi_{1/2}Na_{1/2})TiO_3$ (BNT), $(Sr,Ca)_2NaNb_5O_{15}$ (SCNN), $(Bi,Nd)Ti_3O_{12}$, $SrBi_2Ta_2O_9$, $(K,Na)NbO_3$ (KNN), and KNN-based alkaline niobite, have been studied for an alternative, showing an outstanding piezoelectricity and biocompatibility. Additionally, commercial lead-free

piezoceramic products are available [71], such as BNT-based PIC700 from PI Ceramic (Germany) and $BaTiO_3$-based SONOX P1 LF from CeramTec (Germany).

Park *et al.* reported the first $BaTiO_3$ thin film nanogenerator that can generate an output voltage of up to $1.0V$ from bending. However, only a small increase in d_{33} (from 40 to $105pm/V$) was obtained using the poling process executed at 140 °C under a strong electric field of $100kV/cm$ for about $15h$ [72]. To enhance the power generation, a flexible nanocomposite generator (NCG) made of $BaTiO_3$ nanoparticles and graphitic carbons was proposed, which can be fabricated in a large size and has the capability to harvest energy from human motion to light a commercial red LED [73]. Koka *et al.* developed a PENG based on $BaTiO_3$ NW arrays ($\sim 1\mu m$ long) and demonstrate a high power density that is around 16 times of ZnO NWs based PENG under the same excitation [74]. Extensive research on Ba(Zr, Ti)O_3-(Ba, Ca)TiO_3 (BZT-BCT or BCZT) doped materials [75] reveals that BZT-BCT can be designed to obtain a d_{33} up to $673pC/N$ which is comparable to PZT. However, BZT-BCT only can provide a low Curie temperature (at most $125°C$), resulting in a limited application. Yuan and Cheng *et al.* demonstrated the great potential of BZT-BCT in powering implantable medical devices (IMDs) due to its good biocompatibility [76]. In the following year, they reported a power-free biodetection nanosystem in which a BZT-BCT based NG was utilized to directly power a low-power transmitter for signal transmission [77]. More detailed discussion about $BaTiO_3$-based piezoelectrics can be found in the reference [75].

One of the main concerns of piezoceramics is brittleness, resulting in lower durability of energy harvester. To address this issue, Lead-free piezoelectric nanocomposite (p-NC) consisting of ceramics and polymers have been proposed in order to find a better balance between the piezoelectricity and durability. Siddiqui *et*

al. investigated the piezoelectricity and durability of a lead-free PENG based on nanofibers electrospun from nanocomposite of $BaTiO_3$ nanoparticles (NPs) dispersed P(VDF-TrFE), which is able to generate an open-circuit voltage of $25V$ during human (weighted $600N$) walking and perform stably in 1000 walking steps [30]. Using KNLN Particles and Cu Nanorod Filler, Jeong *et al.* fabricated a flexible lead-free NCG ($30cm \times 30cm$) that generated sub-mW level power from biomechanical energy. The open circuit output could reach up to 140-V voltage and 8-μA current by hand clapping and the instantaneous power over a resistance of $40M\Omega$ was $0.5mW$ [4]. Sun *et al.* explored the piezoelectric potential of (Ba, Ca)(Ti, Sn)O3/BaTiO3 composite (BCTS/BT) using crystallographic texture strategies [78]. The optimal composite sample of d_{33} (as high as $546pC/N$) which is comparable to PZT, was able to generate an output of 21.3-V voltage and 47.3-mA current under $1g$ excitation at $90Hz$ with classic cantilever configuration. The corresponding power density is $4.5\mu W/mm^3$. Shin *et al.* studied nanocomposite with PVDF matrix instead of the universal PDMS matrix that doesn't have piezoelectricity [6]. Five types of nanoparticles were utilized to fabricate composite films for comparison, which are BT, BZT, Cu-BZT, BZT-BCT, and Cu-BZT-BCT. The corresponding piezoelectric charge constants d_{33} are 2.0, 3.0, 4.3, 6.1, and $10pC/N$. The Cu-BZT-BCT/PVDF composite film showed the best performance with an output of 20.61-V voltage and 2.0-μA current under $500N$ force. The energy density was calculated to be $2.79mJ/cm^3$ based on the generated energy of $47.49\mu J$. Additionally, the fabrication process of this flexible lead-free composite is simple and low-cost. Liu *et al.* fabricated a PENG based on nanofiber made of BZT-BCT and P(VDF-TrFE) [79], which is able to generate a output of 13.01-V voltage and 1.44-μW power under mechanical vibration of 6 N at 10 Hz. The BZT-BCT nanoparticles with high d_{33}

contributes to the enhanced piezoelectricity compared to P(VDF-TrFE) nanofiber based PENG. The stable voltage output in 5000 cycles was obtained, demonstrating its good reliability. Bairagi and Ali investigated the influence of percentage of KNN NRs on the performance of PVDF/KNN composite. The best output obtained came from PVDF/3%KNN based PENG, which is 17.5-V voltage and 9.135-μW power from finger tapping [80]. To improve the distribution of KNN NRs inside the PVDF matrix, they recommended to use Amine-based silane (APS) for surface modification of KNN NRs [81]. A PVDF/3%SM-KNN composite based PENG demonstrated enhanced power generation in contrast to the previous designs. The maximum output was increased to 21-V voltage and 22-μA current, which corresponds to a current and power density of $5.5 mA/cm^2$ and $115.5 mW/cm^2$, respectively [82].

1.2.2.2 Wurtzite Materials

Aluminum nitride (AlN) and zinc oxide (ZnO) are well-known nonferroelectric piezoelectric materials with wurtzite structure. PENG based on ZnO nanowires (NWs) array was studied by Prof. Wang's group since 2005 for producing electricity from biomechanical energy [29, 52, 83], where the energy-harvesting pad consisted of nine parallel alligned ZnO NW nanogenerators (each $1cm \times 1cm \times 10\mu m$) is able to generate a high output as high as 58-V voltage and 134-μA current through punching of a human palm [83].

No poling process is needed because the spontaneous polarization cannot be improved by applying an external electric field. AlN films have been applied in MEMS device for energy harvesting due to the high thermal stability, low toxicity, and compatibility with standard complementary metal oxide semiconductor (CMOS) processes [84]. Gablech *et al.* reported a MEMS cantilever with an AlN

thin film ($1500\mu m \times 2000\mu m \times 1\mu m$) that generated a power of $10.33\mu w$ across an optimal resistance of $67.57k\Omega$ with an excitation of 2 g at the first resonance frequency [85]. However, low piezoelectric constant ($e_{31} \approx 1C/m^2$)results in low power generation, which limits the AlN-based energy harvesters in practical applications [4]. Currently, it is still a challenge to obtain high enough power using wurtzite materials for practical applications.

1.2.2.3 Piezoelectric Polymers

PVDF is the most commonly used piezoelectric polymer due to its significant strong piezoelectricity in contrast to other bulk polymers, including Parylene-C and PI(β-CN)APB/ODPA [86]. As a semi-crystalline polymer with polymorphs, PVDF exhibits the strongest piezoelectricity in β phase. To obtain β phase, mechanical stretching and electrical poling are often used to align the polymer chains in a specific direction.

To enhance the piezoelectricity of PVDF, increasing the crystalline proportion in PVDF by adding trifluoroethylene (TrFE) was one of the solutions. The generated polymer named P(VDF-TrFE) has several advantages, such as higher piezoelectric coefficient, better crystallinity, and higher remnant polarization. It is noted that the electricmechanical properties of P(VDF-TrFE) are highly dependent to its fabrication process. The improvement of electricmechanical coupling is at the cost of increased brittleness [87].

Unlike stiff perovskite and wurtzite solids, piezoelectric polymer PVDF and its copolymer P(VDF-TrFE) are very flexible and durable by nature, which makes them suitable for applications of large deformation. In consideration of good biocompatibility, extensive studies have been done to explore their application in wearable

and implantable energy harvesting devices. Jung *et al.* reported a PVDF based PENG for wearable energy harvesting [88]. The proposed flexible curved harvester with a size of $7 \times 4cm^2$ and thickness of $0.6mm$ is able to generate an output of up to 155-V voltage and 700-μA current from finger tapping. The corresponding power was high enough to light up 476 LEDs. Additionally, a highly flexible P(VDF-TrFE) film-based energy harvesting device was reported, which has the capability to power a set of 27 LEDs from vibrational energy source [89]. Both PVDF and P(VDF-TrFE) films were utilized to harvest energy from acoustic vibrations. Applying proper tensile stress could further improve the performance and sensitivity of PEH. In addition, the reported study found that metallic electrode is better than graphene electrode in terms of output power and a thinner piezo film can exhibit better energy conversion efficiency [90]. However, typically the piezoelectric constants of PVDF and P(VDF-TrFE) are significantly smaller than those of PZT ceramics.

1.2.2.4 2D Atomically Thin Sheet Materials

In the past few years, intrinsic piezoelectricity in $2D$ materials have been explored for energy harvesting. $2D$ atomically thin materials, such as $2D$ hexagonal boron nitride (h-BN) nanoflakes and some of the transition metal dichalcogenides (TMDCs) in monolayer form have been demonstrated to be piezoelectric unlike their bulk counterparts. Additionally, $2D$ materials with high crystallinity and the ability to withstand enormous strain were found to have excellent flexibility in contrast to the traditional $1D$ piezoelectric nanostructures [91, 92].

Based on density functional theory calculations, Duerloo *et al.* predicts that some TMDCs in monolayer form, including MoS_2, $MoSe_2$, $MoTe_2$, WS_2, WSe_2, and

WTe_2, are piezoelectric [93]. Wu and Wang *et al.* first investigated the piezoelectricity of $2D$ MoS_2 [91], where a single-layer MoS_2 PENG with a conversion efficiency of 5.08% was demonstrated to be strong piezoelectric. The piezoelectricity disappeared in the cases where even-layered or bulk MoS_2 flakes due to the opposite orientations of adjacent atomic layers. Blonsky *et al.* theoretically studied 37 kinds of $2D$ materials, including metal dichalcogenides, metal oxides, and III-V semiconductor materials, using density functional perturbation theory [94]. Further experimental research on CdO, ZnO, and $CrTe_2$ were recommended in consideration of the large piezoelectric coefficient and low formation energy of those $2D$ materials. To enhance the mechanical durability of monolayer TMDCs and avoid cancellation of polarity in bilayer caused by Bernal stacking, Lee *et al.* proposed a turbostratic stacked WSe_2 bilayer with both reliable piezoelectricity and enhanced durability [3]. Lee *et al.* successfully synthesized $2D$ h-BN nanoflakes through mechanochemical exfoliation process. The piezoelectric voltage coefficient (g_{11}) obtained in the experiment $2.35 \times 10^{-3} Vm/N$. Additionally, with a poling process, a flexible h-BN-based PENG with a surface area of $3 \times 3 cm^2$ generated an output of around 9-V voltage and 200-nA current from bending [92].

1.2.2.5 Summary of Typical Piezoelectric Materials

To help readers better understand the previous discussion and difference between materials, typical piezoelectric materials and their performance in applications are summarized in Table 1.1, where the material structure and piezoelectric constant are listed in addition to design information. According to Table 1.1, several conclusions can be obtained. First, the perovskite materials have the strongest piezoelectricity. d_{33} of PZT and PMN-PT are much higher than those of PVDF and

P(VDF-TrFE) polymers. Second, Perovskite single crystals such as PMN-PT and PMN-PZT have greater d_{33} than PZTs. Furthermore, Lead-free perovskite ceramics can have high d_{33} comparable to PZT, such as BZT-BCT and KNLN. Finally, lead-free material based p-NC exhibited promising performance in wearable devices.

1.3 Mechanical Configurations

In this section, we will review representative mechanical configurations of piezoelectric energy harvesters that have been reported so far. According to the types of piezoelectric material deformation, the configurations are divided into bending type, compression and tension types, and shear and torsion types. The category of bending doesn't include the configurations in shear mode. To be more specific, it only involves bending configurations in 31 mode and 33 mode that make use of normal stress. PENGs are introduced separately as they are more relevant to material sciences and could be subjected to complex loadings, while other classifications usually focus on dynamics analysis and engineering design.

1.3.1 Piezoelectric Nanogenerators

PENG was first named by Wang in 2006 [96] to describe a PEH device of ZnO nanowire (NW) arrays. The original intention of developing PENGs is to achieve self-powered nanosystem by harvesting mechanical energy from working environment. Now, the definition of PENGs is extended to the applications of Maxwell's displacement current in general caused by time-varying electric field or the polarization of materials rather than flow of free charges [97]. Here, we limit the category of PENGs to the techniques involving nanomaterials synthesis in order to distinguish with energy harvesters at larger scales related to structural dynamics.

In the past decade, many materials have been studied to develop PENGs, such as ZnO [29, 83], $BaTiO_3$ [72–74], PZT [5, 98, 99], PVDF [100–102], P(VDF-TrFE) [103], PMN-PT [64,67,104], KNLN [4], BZT-BCT [76,77], and $ZnSnO_3$ [95]. The output power has been increased from pA and mV to mA and hundreds of volt. In this section, we will introduce some typical PENGs.

PENGs has laminated structure consisting of substrates, electrodes, piezoelectric layer, and insulating layer typically. To obtain flexibility, substrates of PENGs are usually plastic thin films, such as polyethylene terephthalate (PET), polyimide (PI), polydimethylsiloxane (PDMS), and Kapton due to their good flexibility and strength [105]. The key component of PENGs is the piezoelectric layer that determines its performance of power generation. Various materials with 1D and 2D nanostructures have been applied to fabricate PENGs, such as nanowire (NW) [83], nanorod (NR), nanoribbon (NB) [99], nanotube (NT), nanofiber (NF), and nanosheet (NS). In addition to nanostructures, thin films of single material or p-NC are also very widely studied.

One of the typical configurations of PENG is vertically aligned NW arrays. Lee *et al.* reported a PENG based on ZnO NWs and PVDF [1], where two shapes of plane type and fiber type were designed, as shown in Figure 1.3 (a) and (b), respectively. ZnO NW arrays were grown on the Au/Cr/Kapton substrate via a hydrothermal process. Dissolved PVDF polymer was spin-cast to fully cover ZnO NW arrays and then dried off to generate the piezoelectric layer with a thickness of $100\mu m$, which is more stable than PVDF film. To obtain an uniform outermost surface, dip-coating process was applied by adding PVDF in fiber shape. Lee *et al.* [29] produced a ZnO NW arrays based PENG with thin Al layer as substrate and electrode. The thickness of insulating layer should be carefully selected to obtain a

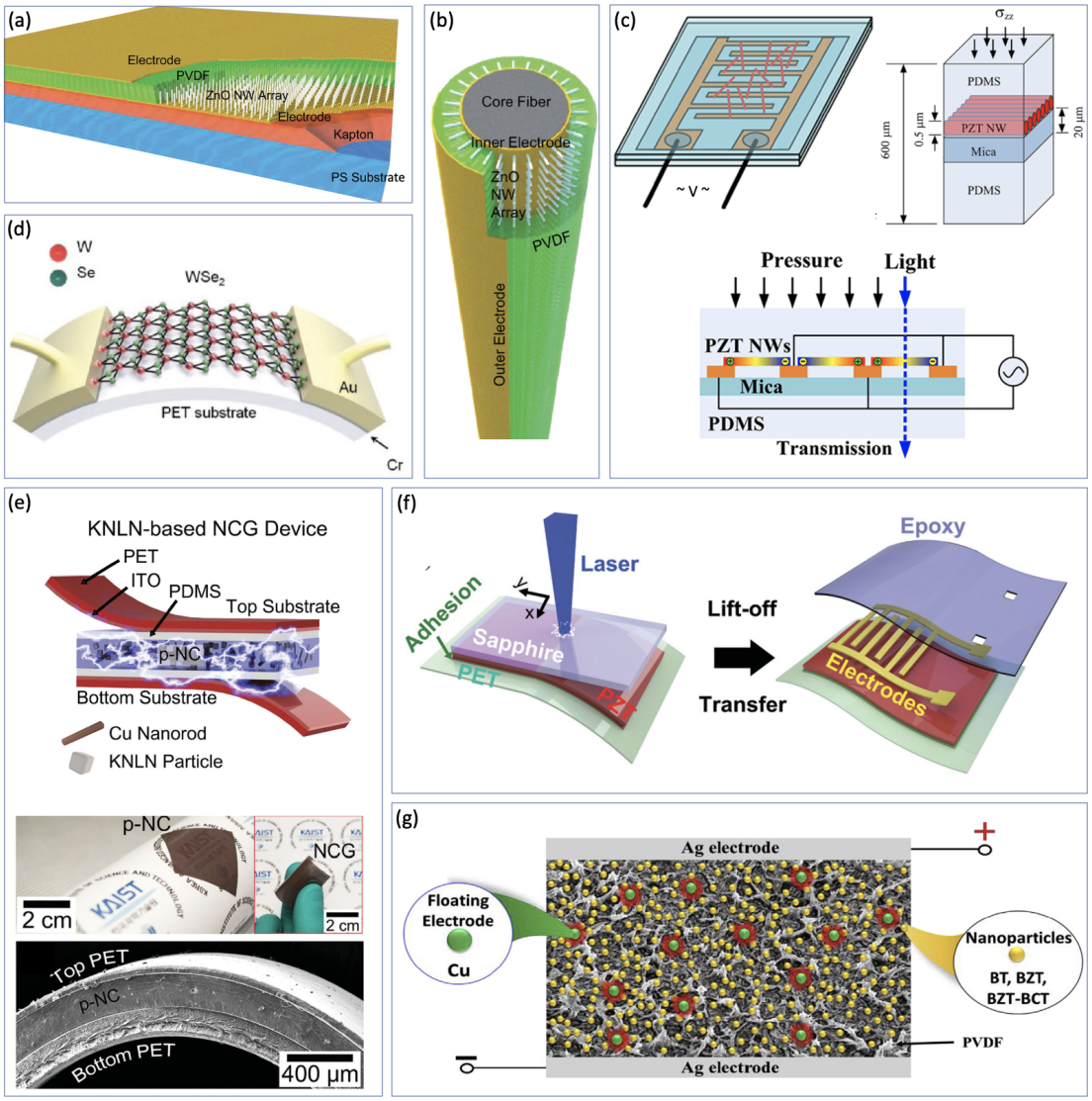

Figure 1.3: Typical configurations of PENG. (a) A plane-type PENG based on ZnO NW arrays, reproduced with permission from Wiley-VCH [1]; (b) A fiber-type PENG based on ZnO NW arrays, reproduced with permission from Wiley-VCH [1]; (c) A PENG based on laterally aligned PZT NWs, reprinted with permission from [2], copyright (2017) American Chemical Society; (d) A PENG based on WSe_2 monolayer, reproduced with permission from Wiley-VCH [3]; (e) A KNLN based NCG, reproduced with permission from Wiley-VCH [4]; (f) A PENG based on PZT thin film, reproduced with permission from Wiley-VCH [5]; (g) A NCG composited of BZT-BCT and PVDF with floating Cu electrode, reproduced with permission from Elsevier [6].

better balance between minimizing short circuits of ZnO NWs and achieving super flexibility. A PENG based on PMN-PT NWs was produced by Xu and Yao *et al.* [65], which is able to generate open circuit voltage up to $7.8V$ from mechanical tapping due to its strong piezoelectricity. Koka *et al.* compared the performance of $BaTiQ_3$ and ZnO in the same configuration of vertically aligned NW arrays [74]. It was reported that $BaTiQ_3$ based PENG produced a power density of $6.27\mu W/cm^3$ which is 16 times higher than that of the ZnO counterpart.

Laterally aligned nanostructures with in-plane electrodes, such as IDEs, also attract attentions in fabrication of PENG. Zhao *et al.* [2] fabricated a semitransparent PENG based on laterally aligned SC PZT NWs, as illustrated in Figure 1.3(c). The PZT NW film was fabricated onto the mica layer, and with IDEs on its top using spin-coating method. Chen *et al.* fabricated a PZT nanofiber PENG with platinum IDEs and silicon substrate packaged by PDMS polymer. In contrast to PZT in form of bulk and thin film, PZT nanofiber by electrospinning exhibits high bending flexibility and mechanical strength [98]. Chang *et al.* reported that PDVF nanofiber PENG has higher energy conversion efficiency than PVDF thin films [100]. Qi *et al.* proposed a prestretch strategy to generate buckled PZT ribbons on silicone substrate [99].

The configuration consisting of piezoelectric thin film is another research focus. Park *et al.* [5] fabricated a transparent PZT thin film PENG with Au IDEs packaged by epoxy, as shown in Figure 1.3(f). The thin PZT film ($35mm \times 35mm \times 2\mu m$) was made using sol-gel method and transferred onto PET substrate from a sapphire substrate via laser lift-off (LLO). Being bended by a human finger, the resulting PENG was able to light up a array of 105 blue LEDs directly that require a turn-on voltage of $250V$. Park *et al.* applied lead-free $BaTiO_3$ thin film NG for the first

time [72]. A porous PVDF based PENG was implanted to a rat's leg to harvest energy from leg motion [102]. IDEs was applied to make PDVF in 33-mode. Observation of six weeks after the implantation confirmed the biocompatibility of this PDMS-encapsulated PVDF PENG. Figure 1.3(d) is a PENG based on monolayer WSe_2 with Cr/Au electrode on PET substrate [3], which represents a typical PENG based on 2D atomically thin materials without packaging.

p-NC has attracted more and more attention in recent years. Scalability and low-cost fabrication are important for potential large-scale industrial production. p-NC usually consists of piezoelectric inorganic nanomaterials and flexible matrix, such as polymers and silicone rubber. Figure 1.3(e) illustrates a typical laminated structure of p-NC based PENGs, designed by Jeong and Lee et al [4]. A 250-μm flexible p-NC layer, that is fabricated by dispersing KNLN NPs and Cu NRs in PDMS matrix, is sandwiched between two indium tin oxide (ITO)-deposited polyethylene terephthalate (PET) flexible substrates. The bottom substrate is thicker than the top one. A large-area prototype ($30cm \times 30cm$) obtained through the bar-coating method can generate an output of 140-V voltage and 8-μA current from hand clapping. The mW-level power was able to light up an array of 14 blue LEDs in series. Park *et al.* [73] fabricated a flexible p-NC with a thickness of $250\mu m$, which is finished by dispersing $BaTiO_3$ NPs and carbon NTs in PDMS matrix. One of the advantage of proposed composite is that it can be done with a large area and low cost. Siddiqui *et al* reported a durable p-NC fabricated by embedding the nanofibers composited of $BaTiO_3$ NPs and P(VDF-TrFE) into PDMS [30].

One of challenges for improving the power generation of NCG is to disperse piezoelectric filler in polymer matrix homogeneously in order to achieve maximized power density [32]. Chou *et al.* presented a stretchable p-NC that was fabricated

by compositing PZT particles and Ag-coated glass microspheres fillers in silicone matrixes [32]. Comparing to polymer matrix with no piezoelectricity, PVDF matrix has the potential to enhance the piezoelectricity of p-NC. Shin *et al.* [6] investigated the performance of p-NC that was obtained by compositing BZT-BCT particles and PVDF matrix with floating Cu electrode ,as illustrated in Figure 1.3(g). It was concluded that the floating electrodes can benefit the collection of charges. Recently, there is an increasing research interest in dopant with the aim of enhancing the performance of p-NC. Jin *et al.* studied the effect of metal dopant, including Co, Na, Ag, and Li ions, on the energy harvesting performance of ZnO-PVDF p-NC [106]. It was found that the Li-doped ZnO-PDVF p-NC generated a significant improved output voltage in contrast to pure ZnO counterpart.

1.3.2 Bending Configurations

1.3.2.1 Cantilever

Cantilever-like configuration can be found in MEMS harvesters and in a wide range of macroscale applications, such as energy harvesting from vibration, human walking, and traffic. Unimorph and bimorph cantilever beams are two common configurations in which a cantilever beam is attached by one piezoelectric element or two, respectively. Classic cantilever is the most popular one that has been well studied for decades due to ease of realization and the mature theory. Pillatsch *et al.* developed a model to calculate the output voltage and power [107] based on the distributed parameter model from Erturk and Inman [108, 109]. Khazaee *et al.* proposed a finite element formulation for non-uniform cantilever havesters based on third-shear-deformation theory. The derived FE model is applicable to

the configurations in which piezoelectric elements has non-uniformity shape or non-constant thickness, or the contact layer thickness can not be ignored [110].

The realization of 33-mode and 31-mode in cantilever configuration requires different design of electrodes and poling direction. With proper pattern of interdigital electrodes (IDEs) on the top of piezoelectric layer in 33-mode, the generated voltage can be higher than that of 31-mode in the same configuration because the piezoelectric coefficient d_{33} is greater than d_{31} for most piezoelectric materials, such as PZT and PMN-PZT [63, 111]. A 33-mode single crystal PMN-PT based MEMS vibration energy harvester with a power density as high as $17,181.8 W/cm^3$ was reported, which is much higher than some reported 31-mode PZT and AlN based MEMS harvesters [112].

Most designs utilizing cantilever idea aim to harvest ambient mechanical energy in form of continuous multi-frequency vibration. To optimize power generation, PEH in cantilever configuration is supposed to work at resonance. The mismatch of frequencies between harvester and excitation result in a decrease in performance due to the narrow bandwidth of harvester. To enhance power generation, various materials and configurations have been investigated. Many piezoelectric materials have been applied to fabricate cantilever harvesters including thin/thick piezoceramic patches, polymers, macro-fiber composites (MFC) [13], and single crystal macro-fiber composites (SFC) [113]. New cantilever-based configurations have been proposed to tune frequencies and broaden bandwidth by employing movable proof mass as well as the optimization of geometry, multi-DOF, and nonlinearity [114]. Detailed information can be found in the reference [115–117].

The maximum strain in classic cantilever harvester is located at the fixed end under external base excitation, while the minimum strain is zero at the free

end. In such a configuration, the piezoelectric material near the free end barely contribute to power generation. To address this issue, two strategies were proposed. First one is to use piezoelectric patches that only cover the segment that is close to the fixed end. The other one is utilizing optimized shape for beams to obtain a uniform strain distribution in piezoelectric materials. Truncated triangular beam with varying cross section area, named $1.5D$ cantilever, can surpass rectangular cantilever in terms of maximum tolerable excitation and power generation [118,119]. Sharpes *et al.* compared the performance of the classic cantilever and a $2D$ zigzag beam with the same surface area that is based on the same PZT patches in 31-mode [120]. The $2D$ zigzag beam exhibited a significantly improved output power and power density as well as a lower natural frequency without proof mass. To further enhance the power generation, they proposed a new configuration named Elephant with improved power density by optimizing $2D$ beam's shape based on the same surface area and materials. In addition, the authors also pointed out that PZT patch concentrated in a small area was beneficial to obtaining a low resonance frequency [121]. Another solution is incorporating additional DOF into harvesters by geometric nonlinearity, resulting in multi-frequency harvesters (also named multi-modal harvesters). It essentially integrates several cantilever harvesters in series or parallel to achieve multiple vibration modes in a discrete manner to handle multi-frequency excitations. The multi-frequency harvester will have several resonance frequencies located in the interested range. However, some deep valleys between distinct adjacent resonance peaks exists in frequency response spectrum. The unactivated modals can cause low efficiency and power density. To address this issue, the multi frequencies can be designed to be close to each other to enable simultaneous activation of multiple modals in order to enhance harvester's output.

Nevertheless, this will cause an decrease in overall bandwidth. Upadrashta and Yang designed a trident-shaped multimodal piezoelectric energy harvester whose first three resonant frequencies are in the range of $15 - 20Hz$ [122]. Multi-frequency configuration also was applied to harvest energy from low speed rotational motion via centrifugal force and gravity [123].

To achieve high efficiency, haverster's resonance frequency is needed to be lowered to match low-frequency external excitation by using long beam and large proof mass by geometric means, which results in an increase in volume. In some cases, this is not allowed due to the restrictions on space and weight. Moreover, ambient mechanical energy is multi-frequency and even random in nature, which indicates the importance of a wide bandwidth for obtaining high efficiency. A promising method to broaden the bandwidth of harvesters is to use frequency up-conversion mechanism that includes both high-frequency and low-frequency oscillators. Kinetic energy absorbed by low-frequency oscillator from ambient vibration can be transferred to high-frequency oscillators via mechanical impact or magnetic force. Both single [124] and multiple [125] impact-driven frequency up-conversion mechanism were demonstrated to be effective in improving the harvesting performance. However, the bandwidth of traditional frequency up-conversion mechanism needs to be further improved for practical application. Rigid stopper that limits the displacement of proof mass introduces nonlinear effect during the vibration of cantilever. Strong stiffness hardening is able to extend the resonance over a wider range towards higher frequency [126]. To reduce to energy loss during impact and further broaden the bandwidth, flexible cantilevers were utilized as stoppers to replace rigid constraints [127]. In such a configuration, piezoelectric elements are attached to flexible stoppers for power generation with high frequency.

To obtain the wideband harvesters for ambient vibrations with low amplitude and low frequency ($< 3m/s^2$, $< 20Hz$), one possible solution is introducing stiffness nonlinearity to linear cantilever using magnetic interaction. The corresponding configurations can have various stability characteristics, which can be mono-stable [128], bi-stable [129, 130], tri-stable [7], quadstable [9], and quin-stable [8]. Mono-stable nonlinear haverster exhibits an increase in bandwidth in contrast to its linear counterpart [128]. Bandwidth can be significantly broadened when the harvester oscillates at a large amplitude. The realization of desired motion is dependent to initial conditions [131]. Bi-stable harvesters, as shown in Figure 1.4(a), have high efficiency in the case of large-amplitude interwell motion between two stable equilibrium positions. To operate in this high-energy orbit, the excitation need to be stronger than a threshold which mono-stable harvesters doesn't have, so that the system have enough kinetic energy to pass through potential wells [7, 12]. This is challenging when the ambient vibration is very weak, and leads to poor performance in low-energy oscillation. To address this issue, multi-stable configuration of more potential wells were introduced to lower the barriers between wells. Zhou *et al.* presented a tri-stable harvester, as shown in Figure 1.4(b). Numerical analysis showed that it required a smaller threshold than bistable energy harvester over a wider range of low frequencies [7].

Each method mentioned before has its own unique features, so the combination of different methods can supplement each other, which have drawn increasing interest. Wang *et al.* [8] proposed a broadband quin-stable energy harvester with frequency up conversion mechanism, as shown in Figure 1.4(c). Two advantages were claimed, which are enhanced output power due to enlarged deflection and extended bandwidth towards lower frequencies. However, this configuration may not

function well if the excitation and initial conditions were too weak to activate the high-energy interwell motion. Wang *et al.* proposed a harvester combining quad-stablity induced by magnetic interaction and frequency up-conversion mechanism with rigid stopper, as shown in Figure 1.4(d). Instead of point contact with tip mass, this rigid stopper has a curved profile along length direction, which can lower energy loss and enhance impact resistance. Both a higher power that 4.2 times of its linear counterpart and broadened bandwidth towards low frequency range were obtained [9]. Sun *et al.* designed a U-shaped harvester with both magnetic nonlinearity and geometric nonlinearity, where two cantilever beams are connected in series with proof mass, as shown in Figure 1.4(e). The first two nature frequencies are as close as $17.366Hz$ and $25.124Hz$ respectively. Due to the small band gap between the first two resonant modes, the harvester outperformed the linear counterpart in power generation [10]. A bi-stable harvester illustrated in Figure 1.4(f) was proposed by Fu *et al.* for low speed rotational motion, demonstrating a wide bandwidth from 1 to 11 Hz [11]. Lai *et al.* presented a multi-stable harvester array configuration consisted of tri-stable and mono-stable cantilevers alternately [12]. Adjacent harvesters share the same fixed magnet to obtain compactness, as shown in Figure 1.4(g). Benefit from both types of nonlinearity, the system can produce high output over a wide bandwidth.

Besides all these passive tuning techniques, configurations with active tuning methods attract research attentions as well recently. Hoffmann *et al.* incorporated a magnetic tuning mechanism into a bistable harvester so that it can adapt eigenfrequency to maintain high output [130]. Experiment results demonstrated an increase in both the operational frequency range and output power by active tuning. However, the system became complicated, and may suffer from increased cost

and volume. To harvest energy from multi-frequency vibrations on a broad range, an actively self-tuning scheme of moving the proof mass was proposed by Shi *et al.* [132]. A circuit that can measure the phase difference between V_{oc} and I_{sc} was employed to detect the difference between the resonant frequency and the ambient excitation frequency without the use of acceleration sensor or laser displacement sensor. Bouhedma *et al.* applied active magnetic frequency tuning scheme in a dual-frequency harvester, as shown in Figure 1.4(h), so that it can adjust itself autonomously according to the ambient frequency based on a control algorithm that can track the maximum voltage [13, 133].

1.3.2.2 Circular Diaphragm

Another common bending configuration is circular diaphragm which is preferable for capturing electric energy from fluctuating pressure and ambient vibration. Mo *et al.* proposed a parametric model for unimorph diaphragm harvesters partially covered by piezoceramics with simply-supported boundary conditions. It is noted that the ignored bonding layer and difficulty in realization of simply support boundary condition may cause decreased accuracy in prediction using this model [134]. They tested PZT based prototypes under clamped boundary conditions. It was found that the bonding layer had a significant effect on output and should be considered in model for accurate prediction [135]. Deterre *et al.* reported a novel flexible MEMS packaged device with a diameter of $6mm$ to harvest energy from blood pressure variations. To obtain large displacement, the device used the spiral-shaped patterns of PZT and electrodes [136]. Huet *et al.* designed a harvester called piezoelectric hybrid fluid diaphragm, as shown in Figure 1.5(a), where incompressible fluid was filled between two thin P(VDF-TrFE) membranes. The

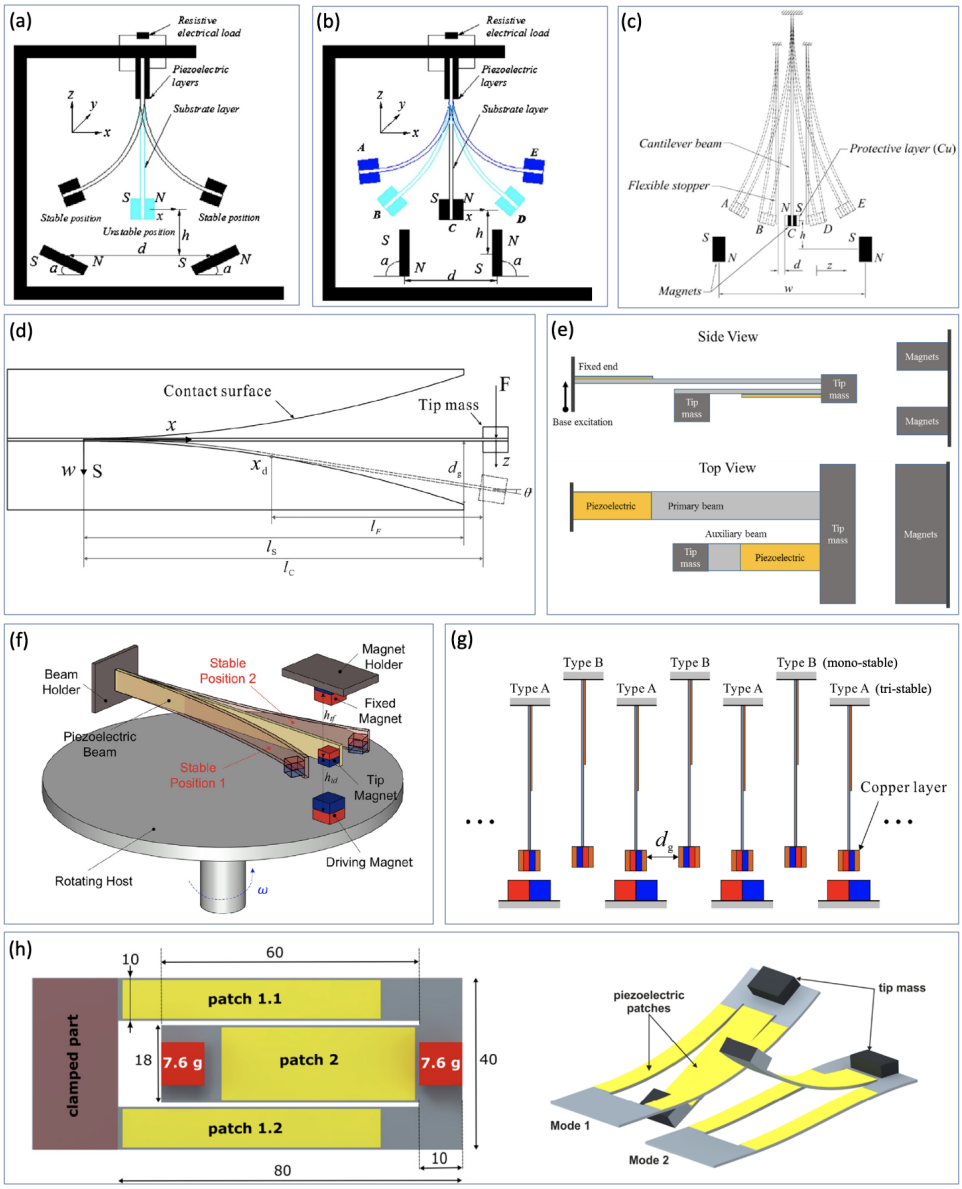

Figure 1.4: Typical cantilever configurations of PEH devices. (a) A bi-stable harvester, reproduced with permission from Elsevier [7]; (b) A tri-stable harvester, reproduced with permission from Elsevier [7]; (c) A quin-stable harvester with frequency up-conversion, reproduced with permission from Elsevier [8]; (d) A quad-stable harvester with frequency up-conversion, reproduced with permission from Elsevier [9]; (e) A non-linear U-shaped harvester, reproduced with permission from Elsevier [10]; (f) A rotational bi-stable harvester, reproduced with permission from Elsevier [11]; (g) A multi-stable harvester array, reproduced with permission from Elsevier [12];(h) A dual-frequency harvester [13].

fluid-structure interaction reduced harvester's resonant frequency and broaden its bandwidth by introducing nonlinearity [14]. Bakhtiari-Shahri *et al.* theoretically conducted an optimization of geometric parameters to maximize the power density of circular diaphragm under stochastic pressure [137].

Circular diaphragm PEH can be used to harvest vibrational energy with proof mass. Chen *et al.* designed a circular diaphragm PEH ($\Phi 30 \times 0.4mm^2$) with a proof mass in the center to lower the resonance frequency. Under a base excitation with an amplitude of $9.8m/s^2$ and a frequency of $113Hz$, a maximum power of $12mW$ was generated across a resister of $33k\Omega$ [138]. Xiao *et al.* integrated four piezoelectric circular diaphragm with different tip masses into a single harvester, as shown in Figure 1.5(b). With appropriate selection of tip masses, a significantly broadened bandwidth can be achieved in this multi-model harvester [15]. Yang *et al.* investigated the optimal geometric parameters in single circular diaphragm model to obtain high power and low eigenfrequency using finite element method. An optimized prototype with a first resonance frequency $219Hz$ produced a power of $16.3mW$ [139]. Thereafter, they proposed a new configuration with annular proof mass instead of center proof mass. With the same key geometric parameters, the output power of a prototype in this new configuration was increased to $19.0mW$ [140]. Yuan *et al.* captured nonlinear dynamic behaviors of a single circular diaphragm with center proof mass and clamped boundary conditions. In a wide observed frequency range from 40 to $140Hz$, softening nonlinearity occurred under the excitations of $0.2g$, $1g$, and $2g$, while hardening nonlinearity only occurred under strong excitation. This nonlinearity was caused by the cubic term in restoring force and claimed to be beneficial to broadening the bandwidth [141]. Shu *et al.* designed a new circular diaphragm harvester by changing the shape of proof mass from concentrated block

to an annular hollow cover, as shown in Figure 1.5(c). The volume of harvester was reduced by around 57% through the modification in shape. The new design with prestress showed an increased output power up to $20.3mW$ [16]. Based on the uneven charge distribution caused by the inhomogeneous strain distribution in piezoelectric disk, Han *et al.* proposed to utilize notched substrate, as shown in Figure 1.5(d), to create additional stress concentration for improving energy conversion efficiency [17].

1.3.2.3 Other Bending Types

Recently, several novel designs in bending configuration are proposed for PEH. Wu *et al.* present a pendulum harvester consisted of PZT-attached common binder clips in series with a heavy proof mass, as shown in Figure 1.6(a). This device could harvest energy from multi-directional motion at low frequency. An maximum output power of $13.29mW$ was obtained from human motion at a low frequency of $\sim 2.03Hz$. However, optimization of design parameters is necessary to reduce the proof mass ($2.03kg$) for further applications in wearable devices [18]. Ansari *et al.* theoretically studied PEH from controlled buckling of beams [142]. Ahn *et al.* proposed a leveraged displacement-amplifying harvester for roadway traffic, where a maximum output power of $3.93mW$ was obtained under an input displacement of $2.5mm$ in laboratory [143]. Jung *et al.* assembled 60 PVDF thin films mechanically in parallel to strengthen the bending stiffness to get rid of substrates. The generated instantaneous output power reached up to $200mW$ across a $40k\Omega$ resistor under a weight of $250kgf$ at speed of $8km/h$ in laboratory [39]. Hua *et al.* proposed a multilayered levered mechanism for energy harvesting from footsteps, as shown in Figure 1.6(b). Lever mechanism was utilized to enlarge user's weight for optimal

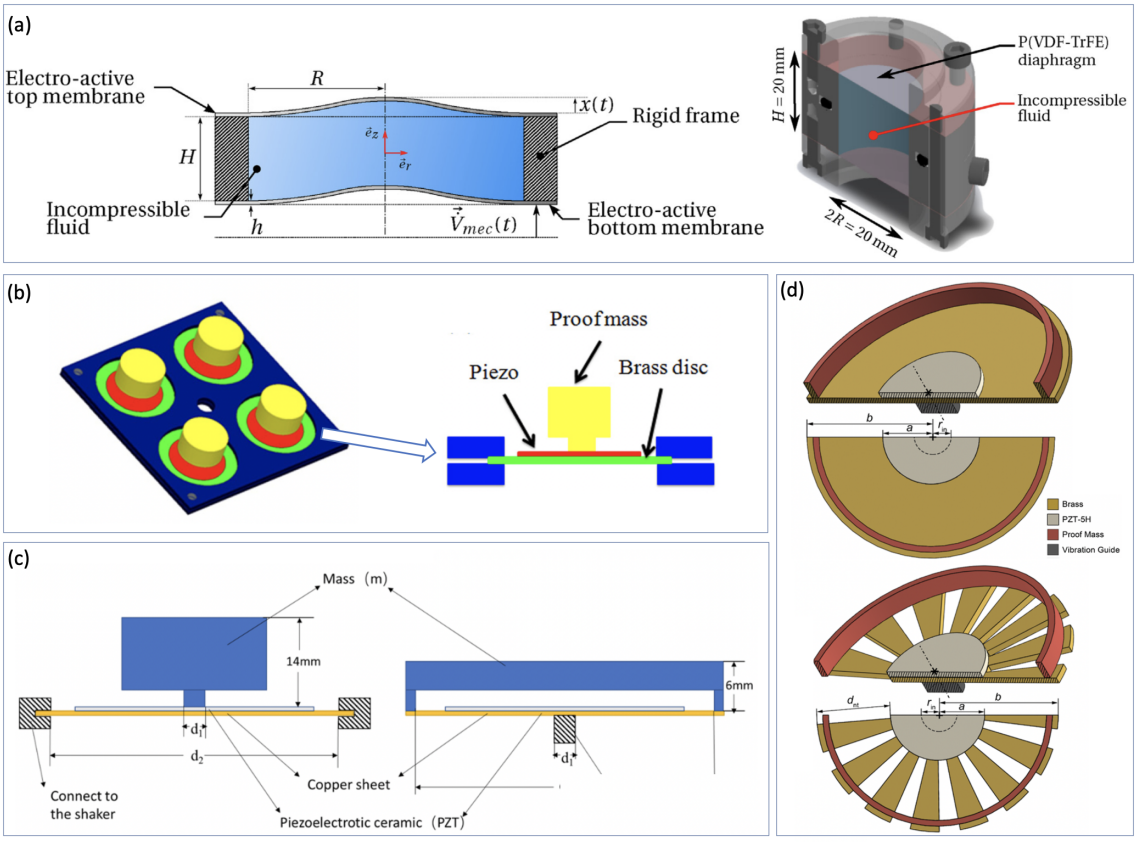

Figure 1.5: Typical circular diaphragm configurations of PEH devices. (a) A piezoelectric fluid diaphragm harvester, reproduced with permission from Elsevier [14]; (b) A piezoelectric harvester based on diaphragm array, reproduced with permission from American Institute of Physics [15]; (c) A annular diaphragm harvester [16]; (d) A annular diaphragm harvester with notched substrate [17].

strain in piezoelectric patches. Under a harmonic excitation of $241N$ at $2.3Hz$, the output reaches up to $172V$ and $13.60mW$ [19]. Shin *et al.* presented a harvester using multiple PVDF thin films in horizontal layout, as shown in Figure 1.6(c), which allows greater strain in PVDF for better performance and reduce the vertical displacement [20]. Li *et al.* [21] increased the flexibility of cantilever harvesters to tune nature frequencies downwards by introducing revolute joints into clamped end or beam plane, as shown in Figure 1.6(d). The bending stiffness of beam was weakened by adding revolute joint. This leads to an improvement of output due to the enlarged strain at resonance compared to the original cantilever. To systematically study the optimal design of revolute joints, a parametric mathematic model is necessary to describe the configuration.

1.3.3 Compression and Tension Configurations

Most piezoelectric elements in compression and tension configurations are piezoceramics subjected to normal stress only. This feature naturally leads to the adoption of 33-mode with no need of interdigitated electrode (IDE) which is necessary in 33-mode bending configuration. Furthermore, harvesters in compression and tension configurations can be designed to withstand heavy load due to high compressive strength of piezoceramics. Therefore, this type of configurations is very popular in heavy load applications, such as traffic [144] and human walking [145]. Additionally, the value of piezoelectric charge constant d_{33} is greater than that of d_{31} for most piezoceramics. All these factors contribute to higher conversion efficiency and power generation of PEHs in compression and tension configurations than those in bending configurations.

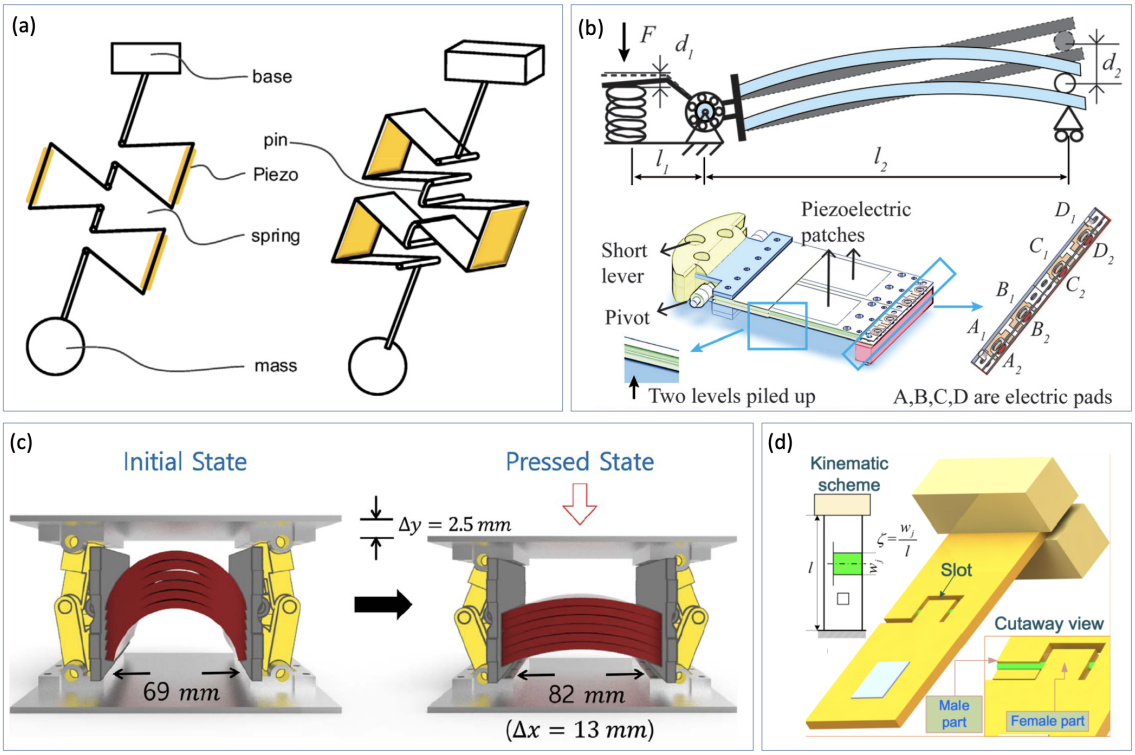

Figure 1.6: Other bending configurations of PEH devices. (a) A pendulum harvester of PZT-attached binder clips, reproduced with permission from Elsevier [18]; (b) A piezoelectric harvester of multilayered levered mechanism, reproduced with permission from American Institute of Physics [19]; (c) A PEH module based on PVDF thin films, reproduced with permission from Elsevier [20]; (d) A cantilever harvester with revolute joint, reproduced with permission from Elsevier [21].

The basic compression configuration is directly applying a force on a piezoelectric element. One method to increase the power output is to extend this single DOF (SDOF) configuration into multiple DOF (MDOF) ones by integrating multiple elements in series vertically [146] or in parallel in plane [37, 147, 148]. Xiao *et al.* proposed a generalized MDOF model for vibrational harvesters in series in one direction. It was found that both harvested energy increases as DOF [149]. To enhance the power density, multiple thick PZT films are stacked up with electrode layers inserted alternately. High capacitance of multilayer PZT stack can hold more charges to increase the in-circuit current [150]. To a reasonable extent, these multilayer PZT stacks mechanically behaviors like a SDOF rod, while electrically like an expanded thin film with large surface area. This is beneficial to accumulating more charges as well as generating high voltage.

Exploring force amplification mechanisms (FAMs) is necessary to further improve power generation, especially in compression configuration. FAMs can increase the magnitude of actual load on piezoelectric materials. Therefore, output voltage and energy can be increased by one order and two order of magnitude, respectively. Representative FAMs that have been applied to PEH are summarized here.

Inspired by classic configurations including Moonie and Cymbal [151–153] as well as Rainbow and Thunder, many new designs with FAM are proposed in the last decade. Feenstra *et al.* developed a mechanically amplified piezoelectric stack that can be used in backpack strap to harvest energy from walking, as shown in Figure 1.7(a). This device converted tension force acting at the aluminum compliant frame to compression force acting at multilayer piezoelectric stack. The change in direction of force transmission is exactly the opposite of Cymbal's. The configuration shared the similar idea of FAM with Cymbal. Feenstra adopted an intact

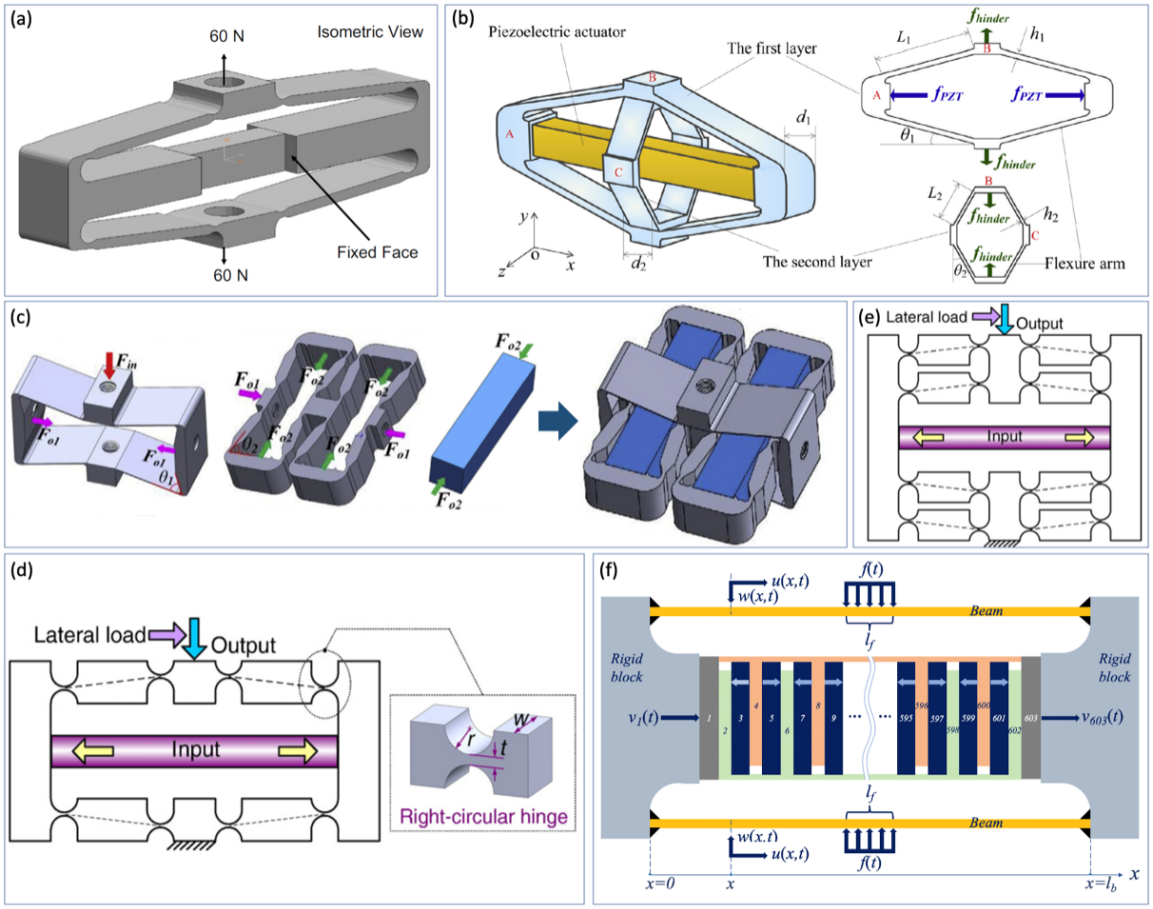

Figure 1.7: PEH configurations of force amplification mechanisms. (a) A mechanically amplified piezoelectric stack, reproduced with permission from Elsevier [22]; (b) A two-stage rhombus-type harvester, reproduced with permission from Elsevier [23]; (c) A two-stage bridge-type harvester, reproduced with permission from Elsevier [24]; (d) A bridge harvester, reproduced with permission from Elsevier [25]; (e) A double-bridge harvester, reproduced with permission from Elsevier [25]; (f) A PEH device with flat clamped-clamped beams, reproduced with permission from Elsevier [26].

aluminum frame with preload to avoid epoxy bonding connection. The mean power was predicted to be approximately $0.4mW$ [22]. Ueda *et al.* proposed a multi-stage strain amplification mechanism called nested rhombus. By coupling multiple stage of amplification mechanisms, it has potential to achieve a high amplification factor [154]. Each rhombus is a configuration similar to Feenstra's design [22]. Ling *et al.* [23] theoretically investigated attenuated displacement amplification in a typical two-stage rhombus-type configuration, as shown in Figure 1.7(b). They defined impedance factor to explain how the stiffness and geometric parameters affect the attenuation. Zhou er al. designed a harvester in the rhombus-type configuration that can achieve a force amplification factor of 5.5 [155]. With the FAM, the harvested mechanical energy was 48.6 times higher than stand-alone PZT stack under the same load. Later on, Liu *et al.* proposed a novel bistable piezoelectric energy harvester based on rhombus-type configuration. A maximum power of $16mW$ was obtained from a $0.3g$ chirp excitation [156].

To avoid the potential buckling failure of convex frame under heavy compressional load, Wang *et al.* proposed a concave rhombus-type configuration to construct a two-stage amplification configuration in the manner of nested rhombus [157]. This two-stage design has a total force amplification factor of 20.8 and a lower basic frequency compared to one-stage design and PZT stacks without FAMs. Chen *et al.* performed an optimization of the concave rhombus-type amplification frame based on a nonlinear parametric model. Two improved designs showed high amplification factors of 8.4 and 8.0 which is much higher than original factor of 3.5. The prototype with amplification factor of 8.4 could generated $4.1mJ$ per simulated walking step. It was pointed out that the power generation was significantly improved by FAM, however, the energy conversion efficiency was reduced due to the

large deformation of frame [158]. Wang *et al.* derived a finite element model for the concave rhombus-type harvester based on Hamilton's principle and piezoelectric constitutive equations [159]. Experimental results illustrated that this FEM had a stronger ability of prediction than SDOF model. In addition, two prototypes with different beam thickness were compared. The thinner one significantly outperformed its counterpart. The produced output voltage and power are 8 times and 112 times higher than the stand-alone PZT stack, respectively.

Several mathematic models were proposed to study the Bridge configuration which is shown in Figure 1.7(d). Ye *et al.* established a mathematic model for bridge-type configuration based on elastic beam theory and kinematic principle [160]. Xu *et al.* proposed a double bridge-type configuration as a displacement amplifier, as shown in Figure 1.7(e). A linear relationship between input and output displacements was observed in experiment [25]. Ling *et al.* developed a mathematical model of bridge-type configuration to investigate the stress concentration effect of the flexure hinges [161]. Liu *et al.* found that the applied load can decrease the displacement amplification ratio significantly through simulation [162]. Choi *et al.* developed a fully compliant mathematical model without assumption of rigid body for the classic bridge-type configuration [163]. Analysis based on their model revealed that the width of the flexure hinge is the most sensitive variable and narrower flexure hinge is desirable.

Wang *et al.* [164] developed a Cymbal-like configuration containing 4 multilayer PZT stacks. A prototype generated a potential electric energy up to $25.45\mu J$ under a loading of $600N$. Wen *et al.* [165] proposed a two-stage harvester in convex rhombus-type configuration, where compound beams were utilized in the frame design to increase the stiffness for large load. The number of beams was studied in

range of 1 to 4. Double beams was selected for a good balance between amplification and safety. Additionally, a quasi-linear relationship between applied load and output power was reported. This observation matches the linearity nature of Euler-Bernoulli beam bending theory. Qian *et al.* designed a energy harvesting device consisted of 4 two-stage harvesters in parallel. Each two-stage harvester, as shown in Figure 1.7(c), has two bridge-type amplifiers as the first stage [24]. The average output power reached $23.9mW$ at $2Hz$ in experiments. The total force amplification factor decreased from 12.8 to 4.5 approximately as the input force increased from $0N$ to $500N$. Cheng *et al.* [26] proposed a novel flat clamped-clamped beam configuration, as shown in Figure 1.7(f). Mathematical model was derived based on nonlinear beam theory, finite element method, and coupling of force and displacement at boundary. The separation of classic intact amplification frame enable the use of different materials in different parts, which is crucial for exploring the ambitious performance under heavy load. A prototype of multi-objective optimal design generated a high output of 128-V voltage and 120-mJ electric energy in a quasi-static load cycle of $1333N$. Geometric nonlinearity of the proposed configuration contributes to a broad bandwidth and fast dynamic response.

1.3.4 Shear and Torsion Configurations

For soft PZT ceramics, the value of d_{15} is usually larger than d_{33}, and even larger than d_{31}. Take popular PZT5A and PZT5H as examples, their piezoelectric charge constants d_{15}, d_{33}, d_{31} are 584, 374, $-171pC/N$ and 741, 593, $-275pC/N$, respectively. Regarding PMN-PT, d_{15} and d_{33} can be as high as 5980 and 2500 pC/N, respectively [166]. These numbers may explain researchers' interest in 15-mode. Unlike 31-mode and 33-mode cantilever configurations, cantilevers in shear

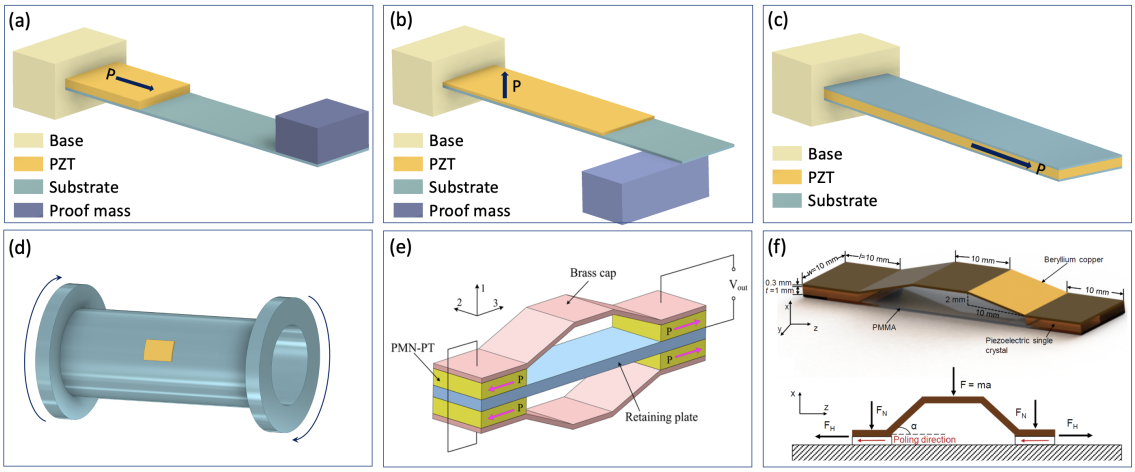

Figure 1.8: PEH configurations in shear and torsion mode. (a) A 15-mode unimorph cantilever; (b) A 36-mode unimorph cantilever; (c) A sandwiched 15-mode cantilever; (d) PEH from torsional thin-walled tube by PZT patches; (e) A 15-mode bridge-type harvester [27]; (f) A 15-mode halved bridge-type harvester, reproduced with permission from Elsevier [28].

mode make use of shear stress including 15-mode and 36-mode. Figure 1.8(a) illustrates a typical 15-mode unimorph cantilever harvester with proof mass. The poling direction inside the piezoceramic is along the length, and the electrodes are on its upper and lower surfaces. To obtain optimal energy density, the piezoelectric wafer is often set to be close to the fixed end. Figure 1.8(b) illustrates a unimorph cantilever in 36 mode. An eccentric proof mass is attached to cantilever to generate torsion from base excitation. d_{36} is much smaller than d_{15} for soft PZT, such as PZT5H ($d_{36} = 18.5pC/N$), leading to a weaker output in 36-mode in contrast to that in 15-mode [167].

Ren *et al.* fabricated a 15-mode cantilever harvester using a PMN-PT single crystal plate with a size of $13mm \times 6mm \times 1mm$ [166]. A high peak voltage of $91.23V$

was captured under a dynamic load of $0.05N$ at $60Hz$. The maximum power across optimal resistance of $1M\Omega$ was $4.16mW$. Wang and Liu tried to harvest energy from water flow by diaphragm harvester containing a 15-mode PZT5H film [168]. Zhao *et al.* demonstrated that the output voltage of 15-mode cantilever harvester can be increased by dividing one PZT wafer into two pieces connected in series electrically in the same configuration [169]. The harvester consisted of two PZT51 elements ($d_{15} = 700pC/N$, $13mm \times 6mm \times 1mm$) generated an open voltage of $25.4V$ and output a power of $8.7\mu W$ at resonance. Zhou *et al.* reported that 15-mode outperforms 31-mode in output voltage for PMN-PT based cantilever configuration through finite element simulation [170]. Zeng *et al.* [171] developed a configuration combining pure shearing sandwich structures and cantilever with proof mass. A maximum voltage was $60.8V$ at resonance. Yuan *et al.* [172] proposed a shear mode MFC polarized along thickness. d_{15} was calculated to be $400pm/V$ based on measurements from a cantilever prototype.

Malakooti and Sodano [173] developed a dynamic model based on Timoshenko beam theory for shear cantilever configuration in which the PZT layer is sandwiched by two substrate layers, as shown in Figure 1.8(c). Theoretical analysis revealed that this 15-mode shear sandwich configuration can generate higher power than typical 31-mode bimorph of similar geometric parameters up to 50% in the studied cases. Banerjee and Roy [174] also concluded that 15-mode is superior to 31-mode in output power theoretically. Zheng *et al.* developed a dynamic model for 15-mode bimorph cantilever configuration based on Timoshenko beam model [175]. Qin *et al.* [176] studied the effects of the geometric parameters on the electromechanical coupling coefficient k_{15} of 15-mode PZT5A ceramic. It was found that the ratio of width to thickness has significant effect on k_{15}, which was recommended to

be 1.2. The coupling between 15-mode and other unwanted modes can decrease k_{15}.

In addition, 15 mode can be employed to harvest energy from torsional stress in the configuration shown in Figure 1.8(d). Kulkarni *et al.* applied 15-mode PZT patches in torsional thin-walled tube for vibrational energy harvesting [177]. The RMS of output power was $0.57mW$ from the base excitation of $1g$ at resonance, which is higher than cantilever counterpart. It is pointed out that this torsional harvester had a less charge cancellation compared to cantilevers because of more uniform strain distribution. Qian *et al.* [178] investigated the effect of axial position and orientation on the output power in energy harvesting from torsional shaft. They found that the pure shear 15-mode when orientation angle was $0\,^\circ$ or $90\,^\circ$ outperformed the coupling of 31 -mode and 33-mode when orientation angle was $45\,^\circ$. The optimal performance was obtained by coupling all the three modes when transducer was placed at the end of shaft with angle of $15\,^\circ$.

He *et al.* [27] developed a 15-mode bridge configuration by inserting PMN-PT plates in the rectangular contact area, as shown in Figure 1.8(e). The proposed design demonstrated a flat response over $20 - 38Hz$ under $0.5g$ acceleration. The output of around $19.93mV$ and $12.12mW$ was claimed to be much better than 31-mode counterpart. Gao *et al.* [28] studied the halved bridge configuration in shear mode, as shown in Figure 1.8(f). The strong piezoelectricity of single crystal PIN-PMN-PT plates ($d_{15} = 3480pC/N$) in shear mode resulted in an output of $21.6V$ and $0.6mA$ under vibration of $3g$ at $1020Hz$, which was high enough to light up 200 LEDs. Li *et al.* [179] proposed a L-shaped configuration combining 31-mode and 36-mode to harvest ambient vibration from multi-direction over a wide frequency range. The MFC that they used has a high d_{36} of $129.51pC/N$. Both the normal and shear strain in bending deformation can be utilized to enhance the power generation.

To date, potential in shear configuration is not fully explored yet. Compared to bending and compression types, there are relatively few studies on shear configuration. The main reason is the challenge on poling of piezoceramics along the length direction at large size [174]. Another reason is the difficulty in evaluation of output of shear mode harvesters [173]. Piezoelectric elements subjected to bending or torsion could involve coupling of shear mode and normal modes. The effect of this interaction between multiple modes on the power generation and energy conversion efficiency is not well studied yet. This coupling also involves the design of electrodes to minimize charge cancellation for high efficiency. It is worth mentioning that the challenges in polarization and electroding also exist in 33-mode cantilever harvesters, which contributes to the popularity of 31-mode in bending configurations.

1.4 Applications and Designs

Mechanical energy sources in various applications have different characteristics, such as continuous and discontinuous external excitations, high and low frequencies, and large and small amplitudes. Additionally, different design requirements need to be met for different working environments, including temperature, waterproof, lifetime, weight, volume, and biocompatibility. To translate the discussed designs to practical applications, comprehensive engineering design and testing are essential. PEH technologies have been explored in a wide range of applications, including human body activities, roadway traffic, ocean water, wind, rain, and vibrations. Here, we only review PEH studies on human body activities and roadway traffic over the past decade because these two applications are explored the most. Typical designs will be discussed and summarized to give an overview of the development.

1.4.1 Human Body Activity

Flexible PENG has great potential to be applied in wearable and implantable devices as power supply due to its ability of harvesting energy from human body activities. For example, biomechanical energy in heartbeat, lung motion, and blood circulation can be harvested to power implantable medical electronics (IMEs) including cardiac pacemakers, deep brain stimulators, and cochlear implants [180].

Lee *et al.* [1] utilized a flexible PENG based on the p-NC fiber consisting of ZnO NWs and PVDF to harvest energy from elbow bending, as shown in Figure 1.9(a). A single fiber harvester generated a voltage of $\sim 0.1V$. Lee *et al.* [29] produced a ZnO NW arrays based PENG ($5mm \times 13mm$) with super flexibility and attached it to the skin next to a human eye. It generated an output of $0.2V$ and $2nA$ from blinking, as shown in Figure 1.9(b). Nanofibers composited of BaTiO3 NPs and P(VDF-TrFE) were embedded into PDMS to produce a durable p-NC by Siddiqui *et al.* [30]. A PENG ($30mm \times 30mm$) based on this p-NC with top and bottom ITO-coated PET substrates, as shown in Figure 1.9(c), was integrated into a shoe to harvest energy from walking. The open circuit voltage reached up to $25V$ from walking of a human (weight: $\sim 60Kg$). Chou *et al.* proposed a flexible and stretchable PENG in an all-in-one structure [32]. PZT particles and Ag-coated glass microspheres were uniformly dispersed into silicone matrix. This PENG, as shown in Figure 1.9(e), can generate a voltage up to $\sim 22V$ from finger bending and $\sim 33V$ from arm motion during running.

Recently, Ye *et al.* fabricated a PENG based on micropillar arrays that are composited of P(VDF-TrFE) and boron nitride nanotubes (BNNTs) [31]. This p-NC outperformed pristine P(VDF-TrFE) film in power generation and pressure sensitivity. It was demonstrated to be able to harvest energy from various human

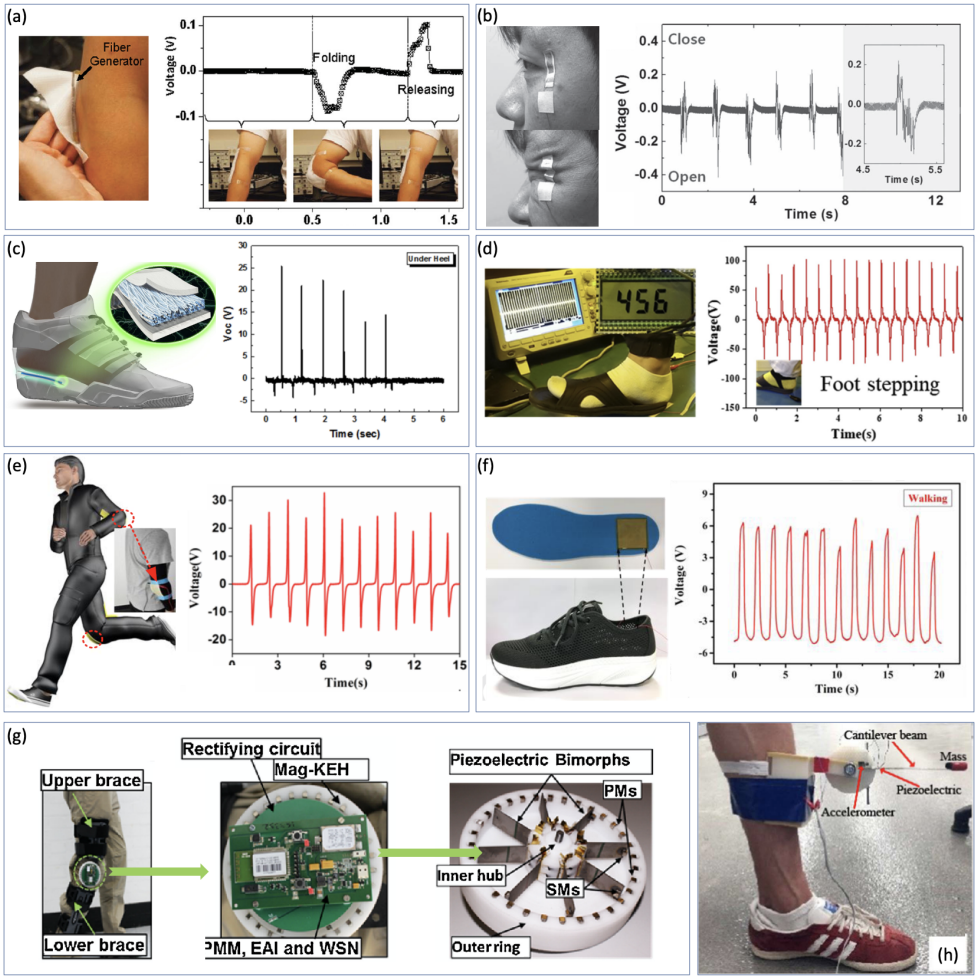

Figure 1.9: Examples of PEH from human body activities. (a) A ZnO/PVDF fiber-type PENG harvest energy from elbow bending, reproduced with permission from Wiley-VCH [1]; (b) A flexible ZnO NW array PENG harvest energy from eye blinking, reproduced with permission from Wiley-VCH [29]; (c) A flexible PENG based on p-NC NF composited of BaTiO3 NPs and P(VDF-TrFE) embedded in shoe, reproduced with permission from Elsevier [30]; (d) A PENG made of p-NC of P(VDF-TrFE)/BNNTs harvests energy from stepping, reproduced with permission from Elsevier [31]; (e) A flexible all-in-one NCG harvests energy from running, reproduced with permission from Elsevier [32]; (f) A PENG attached shoe harvests energy from walking, reproduced with permission from Elsevier [33]; (g) A PEH device consisting of 8 bimorph cantilevers harvests energy from walking to power a WSN [34]; (h) A cantilever harvester mounted on leg harvests energy from walking, reproduced with permission from Elsevier [35].

motions, including finger tapping, elbow bending, knee bending, and foot stepping. Among them, foot stepping generated the highest voltage of $\sim 100V$, as shown in Figure 1.9(d), which was strong enough to light up a LCD directly. Guan *et al.* [33] fabricated a flexible harvester based on p-NC of $BaTiO_3$ and P(VDF-TrFE) to harvest energy from human activities. A voltage up to $7.2V$ was generated from a human running with PENG embedded shoe, as shown in Figure 1.9(f).

Besides wearable device, PENG is also investigated to be applied in plantable devices that can harvest energy from organs. Hwang *et al.* explored the feasibility of using SC PMN-PT based PENG as self-powered cardiac pacemaker [104]. The corresponding prototype with an area of $17mm \times 17mm$ containing a PMN-PT thin film with thickness of $8.4\mu m$ was powerful enough to light up 50 green LEDs under mechanical bending. Furthermore, this power was able to stimuli a living heart of rat as a self-powered artificial heart pacemaker. A BZT-BCT NWs based PENG was proved to be biocompatible by Yuan *et al.* [76]. Cheng *et al.* built an implantable self-powered blood pressure monitoring system based on a PVDF PENG to harvest energy from aorta [181].

Other configurations were also explored to harvest energy from human body activities. Kuang *et al.* [182] designed a harvester consisting of 8 bimorph cantilevers in a ring array to harvest energy from knee motion, as shown in Figure 1.9(g). In one gait cycle, this harvester generated an output energy of $6.4mJ$ with an average power of $5.8mW$. Then, this device was applied to power wireless sensors in order to collect accelerometer, temperature, and humidity data during walking. This self-powered electronics was able to sample 482 readings in each active cycle of $2s$ and transmit it to a nearby station [34]. Fan *et al.* [183] developed a nonlinear harvester that can be mounted in shoes to harvest energy from human walking. The device consists of

a single crystal PZT based cantilever with frequency up-conversion mechanism by magnetic plucking. The prototype was able to capture motions in all directions and generated a power up to $0.35mW$. Izadgoshasb *et al.* [35] investigated the effect of cantilever's orientation on energy harvesting from walking. The cantilever harvester was mounted on a human leg, as shown in Figure 1.9(h). It was found that the maximum output power of $2.779mW$ was produced at the orientation of 70°. They also reported that excitations generated by shaker is too simple to simulate the actual walking, and the damping was higher in walking than in shaker tests due to the existence of muscles and skin.

To show the development of PEH from human activities in the past decade, we summarized some typical design in Table 1.2. Information of material, configuration, and excitation as well as output are listed in chronological order. Many piezoelectric materials have been applied in fabricating PENG for wearable electronics. PZT, PMN-PT, and PIN-PMN-PT thin films based PENGs had demonstrated mW-level output power. Lead-free nanostructures based p-NC with enhanced power density have been proposed. PVDF and P(VDF-TrFE) are popular matrix material for p-NC due to its piezoelectricity and flexibility. The output voltage and power of PENGs have been improved from $1V$-level and μW-level to over $100V$ and mW-level, respectively. Harvesters in bending configurations can generate output voltage and power up to $172V$ and $13.6mW$, respectively.

1.4.2 Roadway Traffic

With rapid advances in piezoelectric material, piezoelectric energy harvesting (PEH) from working environment has attracted substantial interest from both academia and industry, especially in the past two decades [44, 46, 48, 50, 188]. As

society has entered the era of the Internet of Things (IoT) and artificial intelligence (AI), widely distributed sensor networks in various forms further facilitate the development of smart roads [189–192], which can be powered by harvested energy from normally wasted massive kinetic energy of traffic via piezoelectric effect [193]. Additionally, speed and weight of moving vehicles can be sensed by PEH devices as well as traffic volume [194–196]. More importantly, PEH holds advantages in no need of extra land, independence on weather, and utilizing dynamic load from traffic in contrast to solar energy harvesting, which make PEH promising to the realization of self-powered smart road. Currently, most PEH devices for roadway involve the bending and compression configurations only.

The Cymbal harvester has attracted a lot of attentions in roadway application since it was invented in 1990s [151, 152, 197]. Moure *et al.* studied the effects of geometric parameters on the performance of Cymbal through laboratory tests on prototypes [198]. Then the selected Cymbals were integrated into asphalt for the first time. An output of $12V$ and $16\mu W$ was generated by a single Cymbal under $0.9MPa$ from one passage of a heavy vehicle. Zhao *et al.* found bridge harvester is more efficient than the Cymbal by FEM [153]. Bridge can light up LEDs under dynamic load. However, the failure of PZT plate inside Bridge was reported, which indicated that the external load should be below $0.8MPa$. To further improve the performance, a modified Bridge utilizing layered PZT strip was proposed [199]. To increase the energy density of PEH device, Jasim *et al.* [36, 200, 201] designed an energy harvester which consists of 64 layered Bridges in a 3D configuration of $4 \times 4 \times 4$ to better use the space below road surface, as shown in Figure 1.10(a). It can generate an output power up to $2.1mW$ under a dynamic loading of $2.224kN$ at $5Hz$. To maximize the PEH potential of roadway, Chen *et al.* [26] proposed a novel

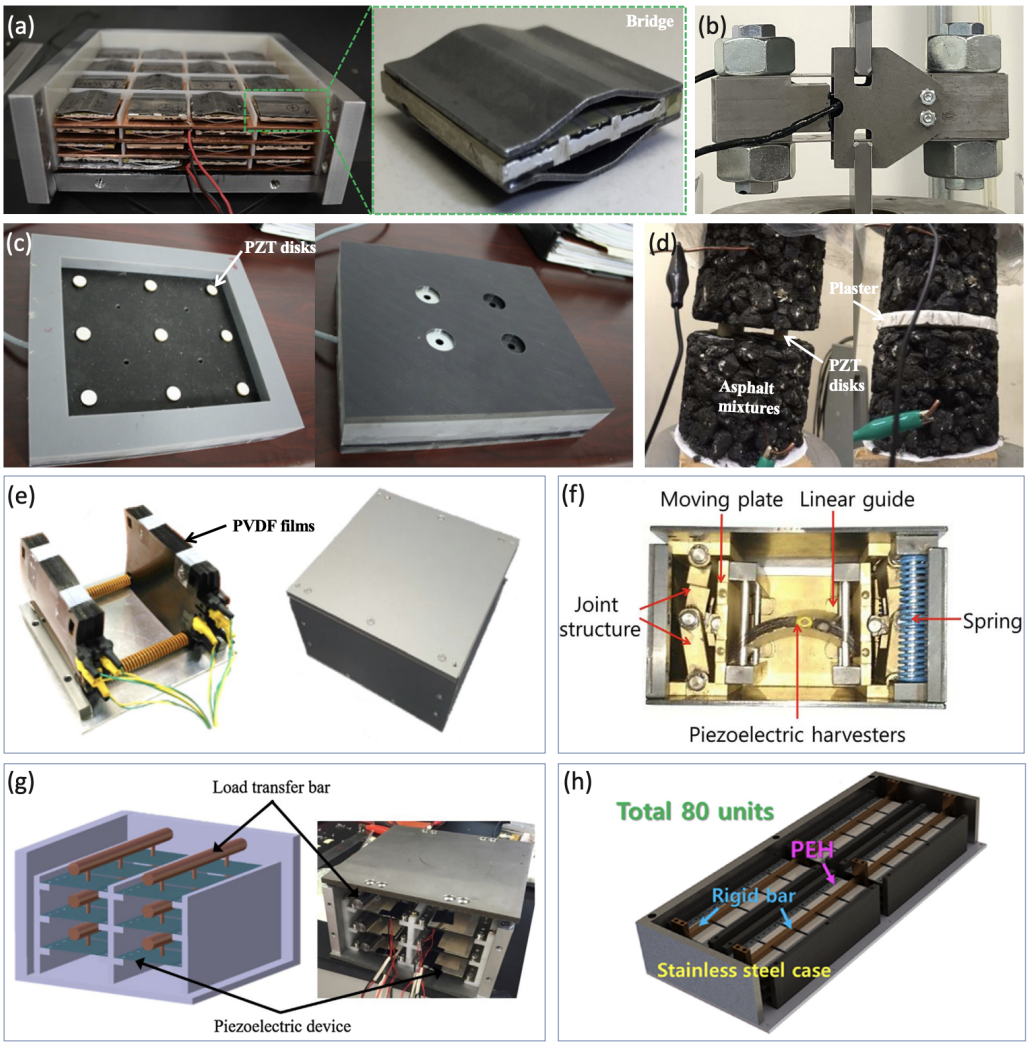

Figure 1.10: Examples of PEH from roadway traffic. (a) A PEH module consists of 64 layered Bridges, reproduced with permission from Elsevier [36]; (b) A force-amplified PEH device of high energy density, reproduced with permission from Elsevier [26]; (c) A PZT disk array harvester, reproduced with permission from Elsevier [37]; (d) A PZT disks integrated pavement sample, reproduced with permission from Elsevier [38]; (e) A PEH device of vertical PVDF films, reproduced with permission from Elsevier [39]; (f) A PEH device of horizontal PVDF films, reproduced with permission from Elsevier [20]; (g) A PEH device consisting of 18 clamped-clamped beam harvesters, reproduced with permission from Elsevier [40]; (h) A PEH device consisting of 80 clamped-clamped beam harvesters, reproduced with permission from Elsevier [41].

force-amplified device with high power generation, as shown in Figure 1.10(b). The proposed PEH unit has an high amplification factor (> 10) and can withstand heavy load. In a quasi-static load cycle of $1333N$, it generated an open circuit potential electric energy of $120mJ$. A PEH system based on the proposed unit was developed, which has the capability to obtain a energy density as high as $15.37J/(m{\cdot}pass{\cdot}lane)$ in real road test [202].

Designs in PZT stack and disk array configuration are popular due to high efficiency of 33-mode and ease of implementation. Additionally, they have the ability to withstand heavy load and have shown great potential in applications on large scale. Jiang *et al.* fabricated a harvester containing three piezoelectric multilayer stacks of size $\phi 20 \times 34mm^3$ in parallel, where each stack consists of 36 PZT8 wafers of thickness $0.85mm$ [203]. Under a dynamic load of $1360N$ at $6Hz$ in laboratory, this harvester output a power of $85mW$. Yang *et al.* investigated the fatigue properties of a stacked-array PEH device containing 9 piezoelectric stacks in 3×3 array [204]. The test results confirmed sufficient strength of this device for real road implementation. A harvester consisting of 12 PZT stacks (each $\phi 20 \times 23.2mm$) in a 3×4 array was fabricated for drive tests on highway. On-site tests showed that a Highlander SUV can light up a LED board requiring $150V$ and $10mA$ [144]. Papagiannakis *et al.* compared performance of prototypes with different stacked-array configurations [146]. Based on experimental results, it was predicted that a maximum power of $1.8W$ was achievable for heavy trucks. Khalili *et al.* proposed a stacked-array harvester to enable an axle load sensing system self-powered. [205]. A high output of $1190V$ and $1400mW$ was generated from dynamic load of $11kN$ at $66Hz$. Wang *et al.* designed two packaged PEH devices for light and heavy traffic [206, 207]. To optimize the performance, they investigated the effects of materials selection, electric

connections and dynamic loadings. Under dynamic load of $0.7MPa$ at $15Hz$, the two prototype output a power of $11.67mW$ and $50.41mW$, respectively.

Xiong and Wang designed a disk-array harvester, as shown in Figure 1.10(c). In drive tests in a weight station, this packaged device generated a power up to $116mW$ from moving heavy truck at speed of $40km/h$ [37]. To simplify design and improve cost-effectiveness, Guo and Lu [38] studied the feasibility of energy harvesting pavement by integrating PZT disks into the conductive asphalt pavement directly, as illustrated in Figure 1.10(d). Roshani *et al.* explored the effects of layout of PZT disks on the overall performance under the same loading [148]. A nonlinear relationship between stress in PZT and the output was reported. In addition, the increase in the number of PZT disks in a prototype resulted in the decreased output power. This finding indicates that it is not feasible to increase the power generation just by simply adding more piezoelectric materials in design, if the load is assumed to be the same. Zhang *et al.* concluded that the embedded depth of PZT disks should be reduced to enhance the output power. MC nylon is employed as the package material due to its similar elastic modulus to asphalt mixtures [147].

The bending-type PEH devices usually consist of PVDF films or PZT attached beam array. Jung *et al.* fabricated a PEH module containing 60 PVDF films in parallel, as shown in Figure 1.10(e). This harvester generated a power up to $200mW$ under a compression force of $250kg$ at the speed of $8km/h$ [39]. However, this high power density is achieved at the cost of large vertical displacement of $10mm$ due to the flexibility of PDVF. This shortcoming will affect the driving safety and comfort in practical application. Shin *et al.* designed an horizontally-placed PVDF films based PEH module with a bridge-type displacement amplification mechanism,

as shown in Figure 1.10(f). Compared to vertically placed PVDF films, this configuration has the advantage of reduced vertical displacement [20]. Drive tests showed that this PEH module with an area of $150 \times 300mm^2$ can generate $5.2mJ$ electric energy from one passage of a mid-sized vehicle. Song *et al.* [208] integrated 12 cantilevers into a harvesting device with a size of $150 \times 150 \times 100mm^3$ that generated a maximum power of $0.184mW$ under excitation of $1mm$ at $10Hz$ in laboratory. Kim *et al.* employed fixed-fixed beams to achieve a high power generation with small vertical deformation [40]. A prototype of 18 beams, as shown in Figure 1.10(g), was fabricated and tested. Ahn *et al.* proposed a leverage-type displacement-amplifying PEH device [143]. Sung *et al.* [41] proposed a PEH device consisting of 80 clamped-clamped beams connected in parallel electrically, as shown in Figure 1.10(h). This device was able to capture $115.7mJ$ electric energy from a minivan of $2137kg$ driving over at speed of $90km/h$ in road test. A power generation at this level enables low-power electronics off-grid and battery-free. Later on, this prototype was applied in smart road relevant exploration, including vehicle counting, illuminating LEDs [209], charging mobile phones [210], temperature and humidity monitoring [211].

Table 1.3 summarized the typical designs in PEH from roadway traffic over the past decade in chronological order. Important details including material, operating mode, configuration, and performance are presented, from which, we can clearly see that the generated electric energy of PEH devices have been increased from mJ-level to $100mJ$-level. The corresponding peak power have been increased from mW-level to W-level. Drive tests demonstrated the great potential of PEH technologies in self-powered WSN for smart road.

1.5 Discussions

1.5.1 Challenges

PEH has been explored in a variety of fields in the past decade. Many innovative materials and designs have been proposed to advance its capability of power generation, which represent a significant step forward for the translation of academic research to practical application. However, to achieve self-powered systems using PEH technologies remains challenging, and thus a few of improvements need to be implemented.

The primary challenge is enhancing power generation. From Tables 1.2 and 1.3, it can be found that the output power in reported studies could reach up to mW-level and W-level in wearable and roadway PEH, respectively, which is only able to drive low-power electronics. The two main limiting factors are the energy conversion efficiency of PEH and the input of mechanical work. For example, the mechanical energy from Human body motions such as walking, elbow bending, finger bending usually is in the level of sub-W. With energy conversion efficiency of a few percentages, PEH can only generate mW-level power from human body motions. To improve the output power, we can improve the efficiency of PEH and/or increase the input mechanical work. One of the solutions to improve the efficiency is to apply the materials with high piezoelectricity, such as PMN-PT single crystals, since the energy conversion efficiency of PEH device is highly related to the utilized piezoelectric material and structure design. Additionally, input of mechanical work can be increased through integration of multiple PEH elements, such as the increase in area of PENG or number of harvesters. However, this method is subjected to design requirements on space, weight, and cost. Another promising solution to increase the input work under the same load is FAMs, which has been demonstrated

to be able to improve the input work by a factor of 100 under same load. With enlarged force acting on piezoelectric materials, the output power can be significantly enhanced. Nevertheless, it may cause an increase in complexity of system structure.

More studies on storage of the harvested energy in an usable form are required. To evaluate the performance of PEH device, researchers often use optimal resistor to calculate potential power, or light up LEDs directly to demonstrate its capability. However, they are not in the manner how a reliable power source works. Power regulation circuit are necessary in practical applications because the harvested electric energy can be alternating and discontinuous. One of the common solutions to self-powered sensor node [213] is using full bridge rectifier to turn the vibrational output from AC to DC and then store electric energy in a capacitor, which allows low-power sensor node to work periodically. In the near future, with advance to higher power generation, PEH is promising to enable low-power electronics work continuously. Meanwhile, advanced power management techniques, such as dynamic voltage scaling and dynamic frequency scaling, can be incorporated in PEH devices in order to provide both high-quality and stable power supply for electronics with advanced features. Furthermore, the impact of irregular charging on lifetime of battery and capacitor using different power management units needs to be studied in order to find an optimal way to store the energy.

Translation of theoretical model to engineering prototype can be challenging. Assumptions of boundary conditions in theoretical analysis may be difficult to realize. For example, the epoxy failure is hard to predict accurately by theoretical analysis. Additionally, the clamped beam subjected to enormous stretching stress may be difficult to implement. Another typical example is that to realize a PEH device with relative motion waterproof without supporting drainage system

is challenging. To further improve reliability, more studies on fatigue, waterproof, anti-corrosion, and high temperature resistance, may need to be done before massive production of laboratory prototype.

1.5.2 Trends

To fully take advantage of mechanical energy, the target source of PEH should include not only the wasted mechanical energy (such as ambient vibrations, wind, and ocean wave energy), but also active energy (including human biomechanical energy, kinetic energy of moving objects) as long as the presence of PEH devices doesn't disrupt normal operation of working environment.

With the rapid advancement in material, new lead-free materials with strong piezoelectricity will emerge on the market to address consumers' increased health [71]. In the past decades, lead-free ferroelectric materials attracted increasing attentions and have been significantly improved, even though its overall performance is still not comparable to benchmark PZT. Currently, Lead-free ceramics and films are commercially available and have demonstrated promising performance. Additionally, lead-free p-NC based on inorganic nanomaterial and polymers matrix have shown the great potential for large-scale applications due to advantages of mechanical robustness and cost-effective manufacturing [214]. Techniques to improve the dispersion and interaction for enhanced power generation of p-NC are necessary. With continuous improvement in flexibility [215] and energy density of PENGs, self-powered wearable electronics in health monitoring are expected to be realized in the next ten years.

Hybridization of multiple energy conversion effects is also a possible solution

to increase harvester's power generation. Piezoelectricity-based hybrid energy harvester can be used to harvest energy from single source of mechanical energy or multiple sources. A self-powered triboelectric-piezoelectric-electromagnetic hybrid nanogenerator with a dimension of $\phi 48 \times 7mm$ and a light weight of $80g$ has been reported, which is able to output a power over $100mW$ and transmit temperature and vibration signal to computer using harvested vibrational energy [216]. Hybrid nanogenerators combining piezoelectric and triboelectric effect have demonstrated strengthened power generation [214]. Perovskite materials and PVDF polymers demonstrate both piezoelectric and pyroelectric effects after poling, which can be used to harvest mechanical and thermal energy simultaneously [42, 217].

Novel mechanical configuration for different applications will be studied. FAM could be a research focus to achieve high energy density by fully exploring the conversion potential from external excitations, since the energy gain is proportional to the force amplification factor's square [26]. Modeling and optimization are of great importance to fully understand the potential of a design idea. The multi-stage FAM needs to be further investigated as it has the advantages of compactness and high force amplification factor.

Enabling electronic devices in smart road systems battery-free and off the grid by PEH technologies will be a future focus. First of all, in consideration of the huge kinetic energy of moving traffics, the generated power potentially can reach high level with a typical energy conversion efficiency. W-level designs have been reported in literature. Secondly, plenty of space under the road surface enables the scalability of PEH system in 3D space, contributing to the desired high power generation. Furthermore, PEH can save the cost of laying cables to provide power for traffic electronics, such as sensors, cameras, data transmission electronics, especially

for those in rural and remote locations in a widely distributed manner. In addition, with the sensor nature, PEH device has ability to measure traffic information, such as vehicle speed, vehicle weight, and traffic volume, without extra sensors.

To harvest energy from other sources, such as wind [218], ocean [219], bridge [212], building [220], self-powered sensor [213], and tire [221, 222], cantilever configuration is commonly used. Harvesters of novel configruations, such as PENG and FAM, can also be applied to above applications to further enhance output. New fields such as, toy, self-powered keyboard, and fitness equipment, are also of great interests to be explored. With the increased power generation of PEH, different kinds of self-powered sensors and electronics are expected to be invented in the age of IoT.

1.6 Conclusions

In summary, the state-of-the-art PEH technologies over the past 10 years are reviewed in this Chapter. A technical roadmap of PEH, including materials, operating modes, mechanical configurations, and performance in applications, was provided to help readers better understand the current state of PEH research, with the hope of inspiring more novel PEH designs and applications research ideas. PEH opens new avenues for ambient energy harvesting and becomes an attractive alternative energy source. With the continuous advancement of PEH technology, we believe that it has great potential to enable completely self-powered devices in the future.

Table 1.1: Summary of typical piezoelectric materials and their performance in applications. The size column refers to the 3D dimension of piezoelectric material if available.

Materials	Category	Structure	Piezoelectric constant	Application	Size	Peroformance	Reference
PZT	Perovskite	Ceramic disk	$e_{33} = 15.5C/m^2$	Roadway	$\phi 11.4 \times 10.6mm^3$	$7.6V$, $1.2mW$ under excitation of $133N$ at $1Hz$	[38]
PZT	Perovskite	Poly film	$d_{33} = 406pC/N$	Self-powered	$40mm \times 30mm \times 7\mu m$	$200V$, $5\mu A$ from human finger motion	[56]
PZT	Perovskite	Multilayer stack	$e_{33} = 16.9C/m^2$	Roadway	$32.4 \times 7 \times 7mm^3$	$128V$, $120mJ$ under quasi-static load $1333N$	[26]
PZT	Perovskite	SC NW array	$d_{33} = 67pm/V$	Self-powered	$10mm \times 10mm \times 0.5\mu m$	$10V$, $70kPa$ pressure at $90Hz$	[2]
PMN-PT	Perovskite	SC NB array	$d_{33} = 677pm/V$	MEMS	$100\mu m \times 5\mu m \times 0.5\mu m$(NB)	$6.0V$, $102\mu A$ under a 0.2% strain agitation	[67]
PMN-PT	Perovskite	Composite	$d_{33} = 371pm/V$	Self-powered	$10mm \times 5mm \times 150\mu m$	$7.8V$, $2.29\mu A$ under mechanical tappings	[65]
PMN-PT	Perovskite	SC film	$d_{31} = -920pC/N$	Vibration	$10mm \times 7.2mm \times 0.4mm$	$20.21V$, $0.257mW$ at resonance ($1g$, $38Hz$)	[66]
PZN-PT	Perovskite	SC film	$d_{32} = -1346pC/N$	Vibration	$10mm \times 7.2mm \times 0.4mm$	$47.01V$, $0.43mW$ at resonance ($1g$, $37.5Hz$)	[66]
PMN-PZT	Perovskite	SC film	$d_{33} = 2000pC/N$	Vibration	$22.5mm \times 5mm \times 0.28mm$	$25.13V/g$, $1.16mA/g$ and $0.148mW/g^2$	[63]
PMN-PZT-Mn	Perovskite	SC film	$d_{33} = 1140pC/N$	Implantable	$30mm \times 20mm \times 20\mu m$	$17.8V$, $1.74\mu A$ from porcine heartbeats	[70]
PNN-PZT	Perovskite	Ceramic plate	$d_{33} = 1753pm/V$	Vibration	$26.6mm \times 4mm \times 0.5mm$	$32.1V$, $2.5mA$, and $14mW$ ($3.5g$, $780Hz$)	[57]
$BaTiO_3$	Lead-free	Thin film	$d_{33} = 105pm/V$	Self-powered	$82mm^2 \times 300nm$	$\sim 1V$, $26nA$, power density of $\sim 7mW/cm^3$	[72]
BZT-BCT	Lead-free	NW film	$d_{33} = 620pC/N$	Implantable	$\phi(210 \pm 50)nm \times (0.2 \sim 5)\mu m$(NW)	$0.3V$, $15nA$, biocompatibility in vitro and vivo	[76]
$ZnSnO_3$	Lead-free	Composite	$d_{33} = 49pC/N$	Human motion	$10mm \times 10mm \times 0.3mm$	$20V$ and $0.6\mu A$ under bending	[95]
BCTS/BT	Lead-free	Composite	$d_{33} = 546pC/N$	Vibration	$7.5mm \times 7.5mm \times 0.5mm$	$21.3V$, $47.3mA$ under $1g$ excitation at $90Hz$	[78]
KNLN	Lead-free	Composite	$d_{33} = 310pC/N$	Wearable	$300mm \times 300mm \times 0.25mm$	$140V$, $8\mu A$, $0.5mW$ by hand clapping	[4]
BZT-BCT	Lead-free	Composite	$d_{33} = 10pC/N$	Vibration	$10mm \times 10mm$	$20.61V$, $2.0\mu A$, $47.49\mu J$ under $500N$ force	[6]
BZT-BCT	Lead-free	Composite	—	Vibration	$10mm \times 10mm \times 40\mu m$	$13.01V$, $1.44\mu W$ under excitation of $6N$ at $10Hz$	[79]
KNN/PVDF	Lead-free	Composite	—	Wearable	$2200mm^2$	$21V$, $22\mu A$, power density of $115.5mW/cm^2$	[82]
ZnO	Wurtzite	NW array	$d_{33} = 15pm/V$	Implantable	$10mm \times 10mm \times 10\mu m$	$58V$, $134\mu A$ from punching of a human palm	[83]
AlN	Wurtzite	Thin film	$d_{33} = 7.33pC/N$	MEMS	$1500\mu m \times 2000\mu m \times 1\mu m$	$10.33\mu w$, under excitation of 2 g at resonance	[85]
PVDF	Polymer	Thin film	$d_{33} = \sim -25pC/N$	Wearable	$70mm \times 40mm \times 0.1mm$	$155V$, $700\mu A$, power density of $3.9mW/cm^2$	[88]
P(VDF-TrFE)	Polymer	Thin film	$d_{33} = \sim 20pC/N$	Wearable	$20mm \times 20mm \times 7\mu m$	$5.8V$, $3.2\mu A$ under excitation of $1.75g$ at $30Hz$	[89]
MoS2	TMDC	2D nanosheet	$d_{11} = 3.73pm/V$	Wearable	$10\mu m \times 5\mu m$	$15mV$, $20pA$ at 0.53% strain, power density $2mW/m^2$	[91]
WSe2	TMDC	2D nanosheet	$d_{11} = 3.26pm/V$	self-powered	$100\mu m \times 50\mu m$	$85mV$ at 0.95% strain, $4.05pW$ at 0.89% strain	[3]

Table 1.2: Summary of typical piezoelectric energy harvesting from human body activities. The size column refers to the 3D dimension of piezoelectric material if available.

No.	Year	Configuration	PiezoMaterial	Size	Motion	Output	Reference
1	2020	PENG	KNN+PVDF	$22cm^2$ (PENG area)	Finger tapping	$21V$, $22\mu A$, $115.5\mu W/cm^2$	[82]
2	2020	PENG	BZT-BCT+P(VDF-TrFE)	$10mm \times 10mm \times 200\mu m$	Finger joint	$\sim 1V$, $1.44\mu W$	[79]
3	2020	PENG	ZnO+PVDF	$40mm \times 30mm \times 90\mu m$	Finger tapping	$53.4\mu W$, $494mW/cm^3$	[106]
4	2020	PENG	BT+P(VDF-TrFE)	$25mm \times 25mm \times \sim 50\mu m$	Walking/running	$6.7V/7.2V$	[33]
5	2019	PENG	BN+P(VDF-TrFE)	$10mm \times 10mm \times 120\mu m$	Foot stepping	$\sim 100V$	[31]
6	2019	PENG	PZT thin film	$40mm \times 40mm \times 2\mu m$	Mechanical bend	$165V$, $1.5\mu A$	[184]
7	2018	Bending	PZT5H(PPA-4011)	$46mm \times 20.8mm \times 600\mu m \times 4$	Walking(shoe)	$172V$, $13.6mW$	[19]
8	2018	Cantilever	MFC	$37mm \times 18mm \times 300\mu m$	Walking(leg)	$58V$, $2.779mW$	[35]
9	2018	PENG	PZT	$\sim 40mm \times 40mm \times 800\mu m$	Arm motion	$\sim 33V$, $\sim 1.7\mu A$	[32]
10	2017	PENG	$ZnSnO_3$ NPs	$10mm \times 10mm \times 300\mu m$	Finger bending	$20V$, $0.6\mu A$	[95]
11	2017	Cantilever	PZT5H patch	$19.1mm \times 7.1mm \times 245\mu m$	Human walking	$3.55V$, $0.35mW$	[183]
12	2017	PENG	PMN-PT NBs	$100\mu m \times 5\mu m \times 0.5\mu m$(NB)	Mechanical bend	$6V$, $102\mu A$	[67]
13	2016	PENG	PVDF	$20mm \times 10mm \times 30\mu m$	Rat's leg	$0.26V$, $0.17\mu A$	[102]
14	2016	Bending	PZT5H bimorph	$38.1mm \times 12.7mm \times 380\mu m \times 8$	Walking(knee)	$\sim 42V$, $5.8mW$, $6.4mJ$	[182]
15	2016	PENG	BT+P(VDF-TrFE)	$30mm \times 30mm \times 90\mu m$	Human walking	$25V$	[30]
16	2016	PENG	PVDF	$\phi 17mm$, thickness $200\mu m$	Blood pressure	$2.3\mu W$, $173mV/mmHg$	[181]
17	2015	PENG	PIN-PMN-PT	$17mm \times 17mm \times 10\mu m$	Finger bending	$11V$, $0.57mA$, $0.7mW$	[185]
18	2014	PENG	PZT thin film	$35mm \times 35mm \times 2\mu m$	Finger bending	$250V$, $8.7\mu A$, $150\mu A/cm^2$	[5]
19	2014	PENG	SC PMN-PT	$17mm \times 17mm \times 8.4\mu m$	Mechanical bend	$8.2V$, $223\mu A$, $2.7\mu J$/bend	[104]
20	2014	PENG	PVDF yarn	$150mm \times 53mm \times 3.5mm$	Impact($0.1MPa$)	$14V$, $29.8\mu A$, $0.4mW$	[101]
21	2014	PENG	KNLN NPs	$300mm \times 300mm \times 250\mu m$	Hand clapping	$140V$, $8\mu A$, $0.5mW$	[4]
22	2014	Bending	PVDF	$80mm \times 50mm \times 30\mu m$	Walking(shoe)	$136V$, $1mW$	[186]
23	2013	PENG	PMN-PT NWs	$10mm \times 5mm \times 150\mu m$	Handle tapping	$7.8V$, $2.29\mu A$, $4.58\mu A/cm^2$	[65]
24	2013	PENG	ZnO NWs	$13mm \times 5mm \times 18\mu m$	Eye blinking	$0.2V$, $2nA$	[29]
25	2012	PENG	$BaTiO_3$	$40mm \times 15mm \times 250\mu m$	Finger bending	$0.2V$, $7nA$	[73]
26	2012	PENG	ZnO+PVDF	$\phi 0.2mm \times 20mm$	Elbow bending	$0.1V$, $10nA$, $16\mu W/cm^3$	[1]
27	2012	PENG	ZnO NWs	$10mm \times 10mm \times 10\mu m \times 9$	Palm punching	$58V$, $134\mu A$, $0.78W/cm^3$	[83]
28	2011	PENG	PVDF	$20mm \times 2mm \times 17\mu m$	Respiration	$0.5V$, $20mJ/12minutes$	[187]
29	2010	PENG	$BaTiO_3$	$82mm^2 \times 300nm$	Finger bending	$1.0V$, $26nA$, $7mW/cm^3$	[72]
30	2010	PENG	PZT NFs	$\phi 60nm \times 500\mu m$(NF)	Finger tapping	$1.63V$, $0.03\mu W$	[98]

Table 1.3: Summary of typical piezoelectric energy harvesting from roadway traffic. The size column refers to the 3D dimension of piezoelectric material.

No.	Year	Configuration	PiezoMaterial	Mode	3D layout	Size	Load	Output	Drive test	Reference
1	2020	Compression	PZT	33	N/A	$142 \times 84 \times 42mm^3$	Quasi-static $1333N$	$120mJ/pulse$, $128V$	Yes	[26]
2	2019	Stack array	PZT840	33	2×2	$1270 \times 203 \times 40.8mm^3$	$11kN$ at $66Hz$	$1400mW$, $\sim 1190V$	No	[205]
3	2019	Bending	PZT	31	$2 \times 4 \times 10$	Area:$500 \times 200mm^2$	$2137Kg$ at $90km/h$	$4.3W$, $115.7mJ/passage$	Yes	[41]
4	2018	Bending	PVDF	31	N/A	$150 \times 300 \times 100mm^3$	$1540Kg$ at $80km/h$	$620.2mW$, $5.2mJ/passage$	Yes	[20]
5	2018	Stack array	PZT	33	3×3 in plane	$150 \times 150 \times 30mm^3$	$0.7MPa$ at $15Hz$	$50.41mW$	No	[207]
6	2018	Disk array	PZT	33	4 in plane	$\phi 8 \times 8mm^3 \times 4$	$3000N$ at $20Hz$	$15mW$	No	[148]
7	2018	Stack array	PZT	33	4 in plane	$100 \times 100mm^2$	$0.7MPa$ at $15Hz$	$11.67mW$, $\sim 19V$	No	[206]
8	2018	Disk array	PZT5H	33	3×4 in plane	$300 \times 300 \times 80mm^3$	$1800Kg$, $20 - 80km/h$	$250 - 400V$	Yes	[144]
9	2018	Bridge array	PZT5X	$33 + 31$	$4 \times 4 \times 4$	$178 \times 178 \times 76mm^3$	$2224N$ at $5Hz$	$2.1mW$; $(95V, 0.42mJ)/pulse$	No	[36]
10	2017	Disk array	PZT	33	3 in plane	$\phi 11.4 \times 10.6mm^3 \times 3$	$133N$ at $1Hz$	$1.2mW$, $7.6V$	No	[38]
11	2017	Bending	PVDF	31	N/A	$150 \times 150 \times 90mm^3$	$250Kg$ at $8km/h$	$200mW$, $\sim 140V$	No	[39]
12	2017	Cymbal-like	PZT	33	N/A	$400 \times 36mm^3 \times 4$	$600N$ at $1Hz$	$25.45\mu J$, $16.5V$	No	[164]
13	2017	Stack array	PZT5H	33	3×3 in plane	$300 \times 300 \times 68mm^3$	$1800Kg$ at $17.6km/h$	Front$84V$, Rear$280V$	Yes	[204]
14	2017	Stack array	PZT	33	3 in plane	$20 \times 20 \times 42mm^3 \times 3$	$2500N$ at $10Hz$	$\sim 23mW$	No	[146]
15	2016	Cantilever array	PZT-PZNM	31	$2 \times 2 \times 3$	$150 \times 150 \times 100mm^3$	$1mm$ at $10Hz$	$184\mu W$, $3.59V$	No	[208]
16	2016	Disk array	PZT850	33	3×3 in plane	$\phi 40 \times 20mm^3 \times 9$	$359.9kN$ at $40km/h$	Up to $116mW$	Yes	[37]
17	2016	Cymbal	PZT	$33 + 31$	N/A	$\phi 29 \times 3.6mm^3$	$0.9MPa$	$16\mu W$, $\sim 12V$	Yes	[198]
18	2014	Stack array	PZT8	33	3 in plane	$\phi 20 \times 34mm^3 \times 3$	$1360N$ at $6Hz$	$85mW$, $\sim 160V$	No	[203]
19	2013	Cantilever	QuickPack	31	N/A	$220 \times 40 \times 0.8mm^3$	$0.2m/s^2$ at $14.4Hz$	$0.19mW$, $3.6V$	Yes	[212]
20	2012	Bridge	PZT5H	$33 + 31$	N/A	$30 \times 20 \times 6mm^3$	$0.7MPa$	$1.13mJ$, $\sim 170V$	No	[153]

Chapter 2

MATHEMATICAL MODEL OF PEHU

In this chapter, some PEH designs in the literature developed for roadway will be introduced as the background of our innovation. The mathematical model of proposed design idea has been setup for theoretical exploration. The derivation for the equations of motion is the focus of this chapter.

2.1 Introduction

Harvesting energy from ambient sources has been an active research topic for many years, motivated by the desires to power sensor networks and portable electronics without batteries as well as to address the issue of climate change and global warming. In many circumstances, replacing batteries of equipment and systems is troublesome and costly, which leads to the demand of harvesting energy from ambient resources so as to achieve self-powered or extended battery life. Since the energy demand of the world has been continuously increasing and mainly relying on fossil fuels, the global climate change due to CO_2 emission in the atmosphere is intensifying. Development of sustainable, renewable, and secure energy technologies has seen increasing interests in recent years. This paper reports the recent advances in the development of an ultra-high density piezoelectric energy harvesting system from highway traffic.

Multiple technologies [193,223] have been developed for energy harvesting devices such as photovoltaic, thermoelectric, piezoelectric, thermal gradient, dynamic loadings and vibrations [224]. Energy sources include human movement [225, 226], pedestrian walking [145, 220], moving vehicles [227, 228], ocean wave [229], wind [230], and even raindrops [231]. Each technology has its advantages and limitations [51], and utilizes a unique set of materials and system design different from others. Highway as an important component of infrastructure all over the world is seen as a huge potential source for energy harvesting in the future. For the energy harvesting from roadway, piezoelectric materials are commonly used and are promising.

To date, the photovoltaic system is the most commercially successful technology. However, when it comes to applications on highway, the photovoltaic system is not the best choice. The heavy traffic proposes severe strength and durability requirements for the light transmissive glass as pavement, reduces the energy conversion efficiency and increases the cost significantly compared to the off-road application. It was reported recently that the world's first solar road ($1km$) in 2016 at a cost of $5.2 million funded by the French government had been announced to be a failure (https://bigthink.com/technology-innovation/france-solar-road).

The piezoelectric materials have been well developed in the past century. The lead zirconate titanate, a polycrystalline monolithic piezoelectric ceramic known as PZT, is the most common piezoelectric material, which can be doped with niobium or lanthanum to form soft or hard ceramic. PZTs are relatively affordable and are widely used in sensors and actuators due to their direct and good piezoelectric coupling [44]. Another common piezoelectric material is a polymer, polyvinylidene fluoride (PVDF), which is lightweight and flexible, but has lower coupling than the

PZT ceramic.

Heavy traffic on highway generates a significant amount of mechanical energy in the road that can be captured with piezoelectric devices. In the future, the road way will be smart so that it can detect the weight and speed of passing vehicles, estimate the traffic volume, and provide information for optimizing traffic lights. These are the additional functions, which the piezoelectric energy harvesting system can readily provide. Various types of piezoelectric energy harvesting devices have been developed in the past years. The devices can be classified into tension-type, compression-type, and bending-type according to the ways the piezoelectric materials are deformed. In order to develop the piezoelectric energy harvesting system, we must consider the physical configuration of piezoelectric energy harvesting devices, the electric connection methods, materials selection, external circuits and integration with the pavement [232, 233].

The invention of cymbal developed by the researchers at the Pennsylvania State University in 1990s has received much attention from others in their design of energy harvesters [197]. Kim *et al.* investigated the energy harvesting performance of cymbal transducer for several different PZT materials [151]. The study also found that the product of the piezoelectric charge constant and piezoelectric voltage constant was the most important parameter for the material selection in the energy harvesting application. A prototype of the cymbal transducer with a cylinder PZT ($\phi 9 \times 1mm^3$) generated $39mW$ under a force of $7.8N$ at frequency $100Hz$ measured across a $400k\Omega$ resistor. Kim *et al.* further reported that the cymbal transducer generated $100mW$ power under a force of $70N$ at frequency $200Hz$ measured across a $200k\Omega$ resistor [152]. Piezoelectric cymbals with $29mm$ diameter were manufactured and integrated into asphalt for the first time by Moure *et al.* [198]. The output

voltage of a single cymbal was $12V$ and the power was up to $16\mu W$ for one pass of a heavy vehicle that generated a stress of $0.9MPa$ at frequency $4Hz$. A modified version of the cymbal, called the bridge, was shown to have higher efficiency than the cymbal by a finite element analysis [153].

Jasim *et al.* performed a comparison of the finite element simulation and laboratory tests of an energy harvester which consists of 64 layered bridge piezoelectric transducers with PZT strips of dimension of $32 \times 32 \times 2mm^3$ in the configuration of $4 \times 4 \times 4$ [36, 200, 201]. A maximum output power of $2.1mW$ was obtained at a resistance of $400k\Omega$ under a dynamic loading of magnitude $2.224kN$ at frequency $5Hz$. This is better than the output of the traditional bridge and cymbal transducer [199]. The tensile and shear failure of the bridge PZT harvester during cyclic loading was also reported. Inspired by the cymbal, Wang *et al.* developed a novel flex-compressive piezoelectric energy harvesting cell (F-C PEHC), in which two multilayer PZT stacks (cross-sectional area $400mm^2$, length $36mm$) were compressed [164]. Experimental results agreed with the theoretical results that double piezoelectric energy harvesting cell (DPEHC) consisting of two F-C PEHCs in parallel sharing one end is more efficient than two F-C PEHCs working independently. The electric energy of $25.45\mu J$ was generated by DPEHC under a loading of $600N$. Jiang *et al.* fabricated a piezoelectric energy harvesting unit consisting of three piezoelectric multilayer stacks (each $\phi 20 \times 34mm^3$) [203].

A maximum average DC power of $85mW$ was captured across an external resistor of $350k\Omega$ when the unit was excited by a dynamic force with amplitude of $1360N$ at frequency $6Hz$ in laboratory. Yang *et al.* explored the fatigue properties of a stacked-array of piezoelectric energy harvesting devices ($300 \times 300 \times 68mm^3$) consisting of 9 piezoelectric stacks in the configuration of 3×3 array [204]. The

piezoelectric energy harvesting package remained good after $100,000$ cyclic loadings and was able to bear load up to $150kN$. It was concluded that the proposed design can sustain the traffic loading. For in-site roadway testing, Yang *et al.* fabricated a stacked array of the piezoelectric energy harvesting devices ($300 \times 300 \times 80mm^3$) consisting of 12 PZT stacks (each $\phi 20 \times 23.2mm$) in a 3×4 array. A LED board of 181 lamp beads requiring working voltage of $150V$ and working current of $10mA$ was lightened while a Highlander SUV passed over the energy harvesting package installed on highway [144]. Papagiannakis *et al.* conducted an experimental comparison between five different piezoelectric energy harvesting prototypes of stacked-array configurations [146]. The best testing results came from the Prototype X-Ax3 containing 3 PZT stacks each of that consists of 21 rectangular PZT elements $20 \times 20mm^2$ in the cross section and $2mm$ in thickness and electrically connected in parallel. The experimental data was used to develop a regression relation between the stress and RMS power. A $1.8W$ power was predicted under a truck load of $44.5kN$. Khalili *et al.* proposed a piezoelectric energy harvester for a self-powered axle load sensing system [205]. This device consists of 4 PZT stacks. Each stack was made of 6 disks ($\phi 25.1 \times 6.8mm$) mechanically in parallel. Under sinusoidal loads with peaks of $11kN$ at $66Hz$, a maximum voltage of $1190V$ and RMS power of $1400mW$ were captured.

Wang *et al.* explored the maximum power of a piezoelectric energy harvesting unit covering an area of $100 \times 100mm^2$ on the road by specifying different configurations of PZT stacks, electric connections and dynamic loadings [206]. The maximum power was obtained to be $11.67mW$ across an optimum load $10k\Omega$ under a $0.7MPa$ load and at $15Hz$. Furthermore, Wang *et al.* optimized a pavement energy

harvesting device based upon the traffic information by considering various selections of materials, dimensions and electric connections [207]. A maximum power $50.41mW$ across an optimal resistor $4k\Omega$ was generated in laboratory by a prototype ($150 \times 150 \times 30mm^3$) with 9 PZT stacks inside under the loading of $0.7MPa$ at frequency $15Hz$.

PZT disks are also often used for piezoelectric energy harvesting. Xiong and Wang fabricated a piezoelectric energy harvesting unit consisting of 9 piezo ceramic disks (850 series PZT) with a diameter of $40mm$ and a thickness of $20mm$ electrically connected in parallel [37]. The device was installed on a section of road in a weight station. The harvester was loaded by trailer trucks of weight up to $359.9kN$ at a speed around $40km/h$ to generate a maximum instant power of $0.116W$ and maximum average power of $3.106mW$. In addition, the authors claimed that for high-level load from moving vehicles, the piezoelectric material in 33-mode is more efficient than in 31-mode. Guo and Lu proposed a theoretical model to investigate the feasibility of energy harvesting pavement by directly integrating PZT disks into the asphalt pavement containing conductive asphalt layers [38]. With the lab test results, Guo and Lu predicted that the maximum electric power from a system consisting of 58 PZT disks with a diameter $11.4mm$ and a thickness $10.6mm$ can reach the level of $300mW$ excited at a high frequency of $30Hz$. Roshani *et al.* compared different layout of PZT disks of $8mm$ in diameter and $8mm$ in thickness individually in a harvester under the same loading [148]. A half sine loading with peak values of $3kN$ and frequency of $20Hz$ enabled the system to generate a power output around $15mW$. Experimental results showed that increasing the number of PZT disks from 4 to 16 did not change the power generation much due to the nonlinear effect of stress on the output. Another prototype made of a stack of 11

PZT disks with a diameter of $50mm$ and a thickness of $3mm$ electrically connected in parallel was tested under the same loading and a power output approximately $0.55mW$ was observed. Zhang *et al.* claimed that the embedded depth of PZT disks and external resistance have a great influence on the output power of a piezoelectric energy harvesting package made of MC nylon in experimental tests [147].

The bending-type piezoelectric energy harvesting devices usually consist of elastic beams with thin PZT patches attached to the surfaces of the beam. Peigney *et al.* captured an average power of $0.03mW$ from a cantilever piezoelectric harvester attached to a traffic-induced bridge. The cantilever is made of a $40\times220\times0.8mm^3$ steel plate with 2 PZT patches bonded on the upper and lower surfaces [212]. Ansari *et al.* theoretically studied roadway energy harvesting from controlled buckling of piezoelectric beams [142]. Simulation results showed that an average power of $42.3mW$ was generated across a $10k\Omega$ resistor by a $254mm$ long and $38.1mm$ wide piezoelectric bimorph with $0.762mm$ thick steel substrate and $1.016mm$ PZT-5A patches under a loading force of $2450N$. Song *et al.* fabricated a piezoelectric energy harvesting device ($300 \times 300 \times 100mm^3$) with 48 piezoelectric cantilever beams [208]. A maximum power of $736\mu W$ was generated while the beam was excited by a base motion with displacement amplitude of $1mm$ at frequency of $10Hz$ in laboratory. Kim *et al.* carried out a robust design optimization of piezoelectric energy harvesting unit with respect to manufacturing uncertainties. The unit is fixed-fixed stainless steel beam ($60\times40\times0.2mm^3$) with PZT ceramic plates ($38\times38\times0.2mm^3$) attached to the beam surfaces [40]. An optimally designed prototype was tested in laboratory to produce a peak-to-peak output voltage $112.937V$, which was an increased output from $92.312V$. Ahn *et al.* proposed a bending-type piezoelectric energy harvesting device ($120 \times 60 \times 70mm^3$) with a displacement-amplifying mechanism containing

a thin piezoelectric ceramic panel ($38 \times 38 \times 0.2mm^3$) [143]. A maximum output power of $3.93mW$ was obtained across an optimal matching resistor of $130k\Omega$ under an input displacement of $2.5mm$ corresponding to an input force of $21.9kg$ in laboratory. Sung *et al.* proposed a systematic design of energy harvester covering an area of $500 \times 200mm^2$ on the road, which has 80 units electrically connected in parallel. Each unit is a clamped-clamped beam with PZT ($38 \times 38mm^2$) attached [41, 209–211]. In the road test, one passage of a minivan weighted $2137kg$ at a speed of $90km/h$ generated $115.7mJ$ electric energy. In addition, they contributed great efforts to explore the practical applications of their impressive invention, such as self-powered temperature monitoring, illuminating LED indicators, powering Internet of Things (IoT) system, and charging mobile phones. Jung *et al.* tested a polymer-based piezoelectric energy harvesting module ($150 \times 150 \times 90mm^3$) made of 60 PVDF films, which generated instantaneous power output of up to $200mW$ across a $40k\Omega$ resistor when the vehicle travels at the speed of $8km/h$ and weighs $250kg$. The power density is about $8.9W/m^2$ [39]. Shin *et al.* designed an energy harvesting module with PVDF that utilizes a bridge-type displacement amplification mechanism to reduce the vertical displacement while it allows greater strain in PVDF for better output [20]. In-site testing results showed that the electric energy generated by a $150 \times 300mm^2$ module from one passage of a mid-sized vehicle weighted $1540kg$ was $5.2mJ$.

The literature studies indicate that the evaluation of the piezoelectric energy harvesting devices was mostly done dynamically at a user-chosen frequency. This is understandable because the response of piezoelectric materials is highly sensitive to the frequency of dynamic loading. We should point out that the highway traffic

delivers a series of impulsive type forces at random time intervals. Another observation from the literature is that almost all the piezoelectric energy harvesting technologies produce the electricity that has very low power level. In this thesis, we report an attempt to create an ultra-high density of piezoelectric energy harvesting system from highway traffic so that the harvested electricity has much higher power level.

To achieve this, we introduce an force amplification mechanism into the design of PEHU. This mechanism is able to amplify the compression from traffic so that the actual force loaded on PZT will be significantly enlarged for higher power generation. In addition, this mechanism enables the device working in off-resonance mode with great performance, which means our design will not be sensitive to the frequency of excitation in the interested range. Furthermore, impulsive compressional load reflects well the actual working condition in road application. The focus of this chapter is the mathematical model of the PEHU and derivation of the equations of motion for dynamic analysis.

2.2 Mathematical Model of PEHU

Figure 2.1 shows the design of the proposed PEHU. The device consists of a frame holding the 33-mode PZT stacks in the middle. The ends of the frame perform the clamped-clamped boundary conditions for the top and bottom elastic beams going through both extension and deflection and provide the compressive force on the PZT stacks.

The extension and deflection of the elastic beams are coupled such that the dynamics of the beams are nonlinear. The details of the mathematical model of the nonlinear elastic beams are presented in 2.3.

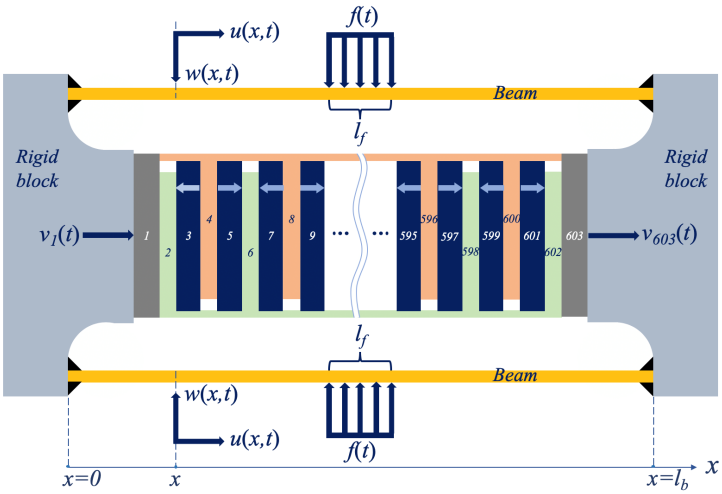

Figure 2.1: Schematic of the piezoelectric energy harvesting device design.

The PZT stack consists of many thin layers of the PZT material as well as thin layers of copper. Such a stacked thin structure naturally leads to the finite element model. The details of the FEM model of the PZT stack are presented in 2.4.1.

The decoupled analyses of the beam and the PZT stack are presented in 2.3 and 2.4.1, while the coupled analysis is presented in 2.5. The internal force balance and displacement continuity of the frame and the PZT stacks are imposed in order to couple the beams and the PZT stacks.

2.3 Nonlinear Clamped-Clamped Beam

Let $f(t)$ be a uniformly distributed force applied at the middle span of width l_f of a clamped-clamped uniform beam. $u(x,t)$ denotes the longitudinal displacement of the middle surface of the beam in x direction and $w(x,t)$ is its transverse displacement in z direction. l, h, b, ρ and E denote the length, thickness, width,

mass density and Young's modulus of the beam. The subscript b refers to the beam. We adopt the nonlinear beam theory for small strain and moderate rotation. The Green's strain of the beam is given by

$$E_{xx} = \varepsilon_{xx} - kz \tag{2.1}$$

where

$$\begin{aligned} \varepsilon_{xx} &= \frac{\partial u(x,t)}{\partial x} + \frac{1}{2}\left(\frac{\partial w(x,t)}{\partial x}\right)^2 \\ k &= \frac{\partial^2 w(x,t)}{\partial x^2} \end{aligned} \tag{2.2}$$

The kinetic energy T_b and potential energy V_b of the beam are given by

$$T_b = \frac{1}{2}\int_0^{l_b} \rho_b A_b \left[\left(\frac{\partial u(x,t)}{\partial t}\right)^2 + \left(\frac{\partial w(x,t)}{\partial t}\right)^2\right] dx \tag{2.3}$$

$$V_b = \frac{1}{2}\int_0^{l_b} \left(E_b A_b \varepsilon_{xx}^2 + E_b I_b k^2\right) dx \tag{2.4}$$

where $I_b = \int_A z^2 dA = b_b h_b^3/12$ is the moment of inertia of the cross section area of the beam with respect to y axis. $A_b = b_b h_b$ is the cross-section area of beam.
The virtual work δW_b done by the applied forces is given by

$$\begin{aligned} \delta W_b = &\int_0^{l_b} f(t)\left[H\left(x - \frac{l_b}{2} + \frac{l_f}{2}\right) - H\left(x - \frac{l_b}{2} - \frac{l_f}{2}\right)\right]\delta w(x,t)dx \\ &- \frac{1}{2}P(t)\,\delta u(0,t) + \frac{1}{2}P(t)\,\delta u(l_b,t) \end{aligned} \tag{2.5}$$

Applying Hamilton's principle $\int_{t_1}^{t_2}(\delta T_b - \delta V_b + \delta W_b)dt = 0$, we derive the equations of motion for the beam as follows,

$$\rho_b A_b \frac{\partial^2 u(x,t)}{\partial t^2} - E_b A_b \left(\frac{\partial^2 u(x,t)}{\partial x^2} + \frac{\partial w(x,t)}{\partial x} \frac{\partial^2 w\,(x,t)}{\partial x^2} \right) = 0 \tag{2.6}$$

$$\begin{aligned} &\rho_b A_b \frac{\partial^2 w(x,t)}{\partial t^2} + E_b I_b \frac{\partial^4 w(x,t)}{\partial x^4} \\ &- E_b A_b \left[\frac{\partial^2 u(x,t)}{\partial x^2} \frac{\partial w(x,t)}{\partial x} + \frac{\partial u\,(x,t)}{\partial x} \frac{\partial^2 w(x,t)}{\partial x^2} + \frac{3}{2} \left(\frac{\partial w(x,t)}{\partial x} \right)^2 \frac{\partial^2 w(x,t)}{\partial x^2} \right] \\ &= f\,(t) \left[H\left(x - \frac{l_b}{2} + \frac{l_f}{2} \right) - H\left(x - \frac{l_b}{2} - \frac{l_f}{2} \right) \right] \end{aligned} \tag{2.7}$$

and the boundary conditions,

$$E_b A_b \left[\frac{\partial u\,(0,t)}{\partial x} + \frac{1}{2} \left(\frac{\partial w\,(0,t)}{\partial x} \right)^2 \right] = \frac{1}{2} P\,(t) \tag{2.8}$$

$$E_b A_b \left[\frac{\partial u\,(l_b,t)}{\partial x} + \frac{1}{2} \left(\frac{\partial w\,(l_b,t)}{\partial x} \right)^2 \right] = \frac{1}{2} P\,(t) \tag{2.9}$$

$$u\,(0,t) = 0,\ u\,(l_b,t) = 0 \tag{2.10}$$

Note that the axial force $P(t)$ at the end of the beam is due to the coupling with the PZT stacks. In the coupled model, this force is the internal force of the device PEHU. Eqs. (2.6) and (2.7) are coupled nonlinear partial differential equations. The deformation of beam subjects to the coupled stretching and bending.

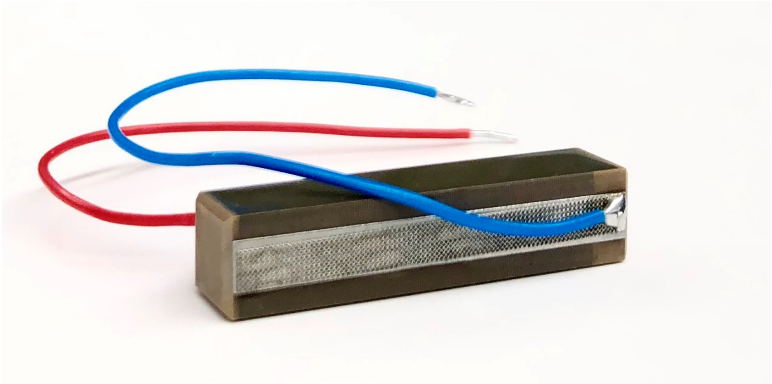

Figure 2.2: A multi-layer PZT stack made by CeramTec in Germany.

2.4 Finite Element Model of PZT Stack

2.4.1 Equations of Motion

The multi-layer PZT stack made by CeramTec in Germany showed in Figure 2.2 is used in this project. Each stack has the nominal external dimensions of $7 \times 7 \times 32.4\ mm^3$ and contains 300 PZT layers. Each layer has a thickness of $0.1\ mm$. The PZT material is Sonox $P505$ of d_{33} mode. The 33 mode has a higher mechanical to electric energy conversion efficiency than other modes. This PZT stack mechanically behaves like a uniform rod within a large stress range, and electrically is equivalent to one expanded thin layer with a large surface area. As a result, it has a high capacitance to carry electric charges.

In the stack, thin PZT layers and electrode layers are alternately bounded together. This configuration naturally calls for the finite element method to model the multi-layer PZT stack. The FE model is showed in Figure 2.3. Assume that the displacement and voltage are uniform in every cross-section and that there is no electrical potential difference in each electrode and two end layers.

301 elements representing electrode layers are labeled as $2, 4, 6, ..., 602$. 300

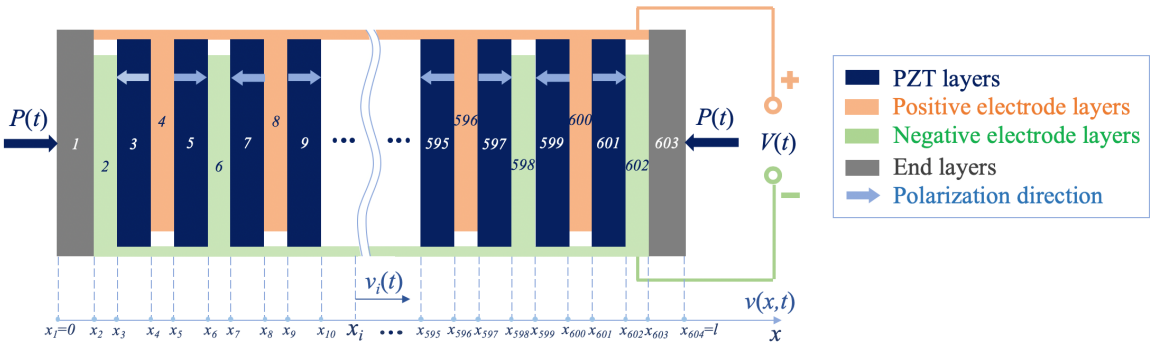

Figure 2.3: The finite element model of the multi-layer PZT stack.

PZT elements are labeled as $3, 5, 7, ..., 601$. The two end elements are marked 1 and 603. A pair of compression forces $P(t)$ act on the ends of the PZT stack in x direction. Let v^i, ϕ^i, A^i, ρ^i, E^i and l^i denote the displacement, voltage, cross-section area, mass density, Young's modulus, and element length of the i^{th} element. Let x_i, v_i and ϕ_i denote the global coordinates, displacement and voltage of the i^{th} node in x direction ($i = 1, 2, 3, ..., 604$).

We ground the electrode at the lower end. The output of the upper electrode denoted as $V(t)$ is given by

$$V(t) = \frac{1}{151} \sum_{i=3,7,11...}^{603} \phi_i \tag{2.11}$$

where

$$\phi_i = 0, \ i = 4, 5, 8, 9, 12, 13..., 600, 601, \text{ and } i = 1, 604 \tag{2.12}$$

$$\phi_i = \phi_{i+1}, \ i = 2, 6, 10, ..., 602 \tag{2.13}$$

Each element has the following properties.

$$\rho^i = \begin{cases} \rho_s, & i = 1, 603 \\ \rho_p, & i = 3, 5, 7, ..., 601 \\ \rho_e, & i = 2, 4, 6, ..., 602 \end{cases}, \; E^i = \begin{cases} E_s, & i = 1, 603 \\ E_p, & i = 3, 5, 7, ..., 601 \\ E_e, & i = 2, 4, 6, ..., 602 \end{cases} \tag{2.14}$$

$$A^i = \begin{cases} A_s, & i = 1, 603 \\ A_p, & i = 3, 5, 7, ..., 601 \\ A_e, & i = 2, 4, 6, ..., 602 \end{cases}, \; l^i = \begin{cases} l_s, & i = 1, 603 \\ l_p, & i = 3, 5, 7, ..., 601 \\ l_e, & i = 2, 4, 6, ..., 602 \end{cases} \tag{2.15}$$

The global coordinates of each node are given by

$$x_i = \begin{cases} 0 & i = 0 \\ l_s + (\lceil \frac{i}{2} \rceil - 1) l_e + (i - 1 - \lceil \frac{i}{2} \rceil) l_p & , \; i = 2, 3, 4, ..., 603 \\ l & i = 604 \end{cases} \tag{2.16}$$

where $\lceil \cdot \rceil$ is the ceiling function. For continuity, we have

$$v^i \left(x_{i+1}, t \right) = v^{i+1} \left(x_{i+1}, t \right) = v_{i+1} \left(t \right), \; i = 1, 2, 3, ..., 602 \tag{2.17}$$

Consider the i^{th} element with the global coordinate $x \in (x_i, x_{i+1})$. Because each layer is very thin, we can consider linear Lagrange interpolating functions ψ_1^i and ψ_2^i as the shape functions of v^i and ϕ^i given by

$$\psi_1^i(x) = \frac{x_{i+1} - x}{x_{i+1} - x_i}, \quad \psi_2^i(x) = \frac{x - x_i}{x_{i+1} - x_i} \tag{2.18}$$

and

$$v^i(x,t) = v_i(t)\psi_1^i(x) + v_{i+1}(t)\psi_2^i(x) \tag{2.19}$$

$$\phi^i(x,t) = \phi_i(t)\psi_1^i(x) + \phi_{i+1}(t)\psi_2^i(x) \tag{2.20}$$

Define a normalized local coordinate variable $\overline{x} \subset (0,1)$. The global coordinate x can be expressed as

$$x = x_i + \overline{x} l_i \tag{2.21}$$

Hence,

$$d\overline{x}/dx = 1/l_i \tag{2.22}$$

The shape functions Ψ_1 and Ψ_2 in terms of the normalized local coordinates are given by

$$\Psi_1(\overline{x}) = 1 - \overline{x}, \quad \Psi_2(\overline{x}) = \overline{x} \tag{2.23}$$

The first order derivatives become constants

$$\frac{d\Psi_1(\overline{x})}{d\overline{x}} = -1, \quad \frac{d\Psi_2(\overline{x})}{d\overline{x}} = 1 \tag{2.24}$$

The transformation from the global coordinate to the normalized local coordinate is given by

$$\frac{d\psi_1^i(x)}{dx} = \frac{d\Psi_1(\overline{x})}{d\overline{x}} \frac{d\overline{x}}{dx} \tag{2.25}$$

$$\frac{d\psi_2^i(x)}{dx} = \frac{d\Psi_2(\overline{x})}{d\overline{x}} \frac{d\overline{x}}{dx} \tag{2.26}$$

The displacement field of the i^{th} element in the local coordinate is given by

$$V^i(\overline{x},t) = v_i(t)\Psi_1(\overline{x}) + v_{i+1}(t)\Psi_2(\overline{x}) \tag{2.27}$$

and its derivatives are

$$\frac{dV^i(\overline{x},t)}{d\overline{x}} = -v_i(t) + v_{i+1}(t) \tag{2.28}$$

$$\frac{dV^i(\overline{x},t)}{dt} = \frac{dv_i(t)}{dt}\Psi_1(\overline{x}) + \frac{dv_{i+1}(t)}{dt}\Psi_2(\overline{x}) \tag{2.29}$$

Apply the boundary conditions Eqs. (2.12) and (2.13), we obtain the voltage and its gradient across the i^{th} element in the normalized local coordinates as

$$\Phi^i(\overline{x},t) = \begin{cases} \phi_i(t)\Psi_1(\overline{x}), & i = 3,7,11,...,599 \\ \phi_{i+2}(t)\Psi_2(\overline{x}), & i = 5,9,13,...,601 \end{cases} \tag{2.30}$$

$$\frac{d\Phi^i(\overline{x},t)}{d\overline{x}} = \begin{cases} -\phi_i(t), & i = 3,7,11,...,599 \\ \phi_{i+2}(t), & i = 5,9,13,...,601 \end{cases} \tag{2.31}$$

Since the polarization directions in two adjacent layers are opposite, the constitutive equations for the two layers can be written as

$$\begin{cases} \sigma_i = E^i\varepsilon_i - e_{33}E_i \\ D_i = \varepsilon^T E_i + e_{33}\varepsilon_i \end{cases}, i = 3,7,11,...,601 \tag{2.32}$$

$$\begin{cases} \sigma_i = E^i\varepsilon_i + e_{33}E_i \\ D_i = -\varepsilon^T E_i + e_{33}\varepsilon_i \end{cases}, i = 5,9,13,...,599 \tag{2.33}$$

where, σ_i, ε_i, D_i, E_i are stress, strain, electric displacement and electric field strength in i^{th} element respectively.

By definition, we have

$$\varepsilon_i = \frac{\partial v^i}{\partial x},\ E_i = -\frac{\partial \phi^i}{\partial x},\ i = 3, 5, 7, ..., 601 \tag{2.34}$$

We are now ready to write down the potential energy like term for the PZT stack including the electrode layers. Note that the differential element of the volume for each layer can be written as $A^i dx$.

$$\begin{aligned} V_p = &\sum_{i=3,7,11...}^{599} \frac{1}{2}\int_{x_i}^{x_{i+1}} \left(\sigma_i \varepsilon_i - E_i D_i\right) A^i dx + \sum_{i=5,9,13...}^{601} \frac{1}{2}\int_{x_i}^{x_{i+1}} \left(\sigma_i \varepsilon_i + E_i D_i\right) A^i dx \\ &+ \sum_{i=2,4,6...}^{602} \frac{1}{2}\int_{x_i}^{x_{i+1}} \sigma_i \varepsilon_i A^i dx + \sum_{i=1,603} \frac{1}{2}\int_{x_i}^{x_{i+1}} \sigma_i \varepsilon_i A^i dx \end{aligned} \tag{2.35}$$

In terms of the displacement v^i and electric potential function ϕ^i, we have

$$\begin{aligned} V_p = &\sum_{i=3,5,7...}^{603} \frac{1}{2}\int_{x_i}^{x_{i+1}} A^i E^i \left(\frac{\partial v^i}{\partial x}\right)^2 dx - \sum_{i=3,5,7...}^{601} \frac{1}{2}\int_{x_i}^{x_{i+1}} A^i \varepsilon^T \left(\frac{\partial \phi^i}{\partial x}\right)^2 dx \\ &+ \sum_{i=3,7,11...}^{599} \int_{x_i}^{x_{i+1}} A^i e_{33} \frac{\partial v^i}{\partial x}\frac{\partial \phi^i}{\partial x} dx - \sum_{i=5,9,13...}^{601} \int_{x_i}^{x_{i+1}} A^i e_{33} \frac{\partial v^i}{\partial x}\frac{\partial \phi^i}{\partial x} dx \\ &+ \sum_{i=2,4,6...}^{602} \frac{1}{2}\int_{x_i}^{x_{i+1}} A^i E^i \left(\frac{\partial v^i}{\partial x}\right)^2 dx + \frac{1}{2}\int_{x_1}^{x_2} A^1 E^1 \left(\frac{\partial v^1}{\partial x}\right)^2 dx \\ &+ \frac{1}{2}\int_{x_{603}}^{x_{604}} A^{603} E^{603} \left(\frac{\partial v^{603}}{\partial x}\right)^2 dx \end{aligned} \tag{2.36}$$

In terms of the local coordinate $\overline{x}$ and nodal quantities, we have

$$
\begin{aligned}
V_p = & \sum_{i=1,2,3\ldots}^{603} \frac{1}{2}\int_0^1 \frac{A^i E^i}{l^i}\left(-v_i + v_{i+1}\right)^2 d\overline{x} - \sum_{i=3,7,11\ldots}^{599} \frac{1}{2}\int_0^1 \frac{A^i \varepsilon^T}{l^i}\left(-\phi_i\right)^2 d\overline{x} \\
& - \sum_{i=5,9,13\ldots}^{601} \frac{1}{2}\int_0^1 \frac{A^i \varepsilon^T}{l^i}\left(\phi_{i+2}\right)^2 d\overline{x} + \sum_{i=3,7,11\ldots}^{599} \int_0^1 \frac{A^i e}{l^i}(-v_i + v_{i+1})(-\phi_i) d\overline{x} \\
& - \sum_{i=5,9,13\ldots}^{601} \int_0^1 \frac{A^i e}{l^i}(-v_i + v_{i+1})\phi_{i+2} d\overline{x} \\
= & \sum_{i=1,2,3\ldots}^{603} \frac{1}{2}\frac{A^i E^i}{l^i}\left(-v_i + v_{i+1}\right)^2 - \sum_{i=3,7,11\ldots}^{599} \frac{1}{2}\frac{A^i \varepsilon^T}{l^i}\left(\phi_i\right)^2 - \sum_{i=5,9,13\ldots}^{601} \frac{1}{2}\frac{A^i \varepsilon^T}{l^i}\left(\phi_{i+2}\right)^2 \\
& - \sum_{i=3,7,11\ldots}^{599} \frac{A^i e_{33}}{l^i}(-v_i + v_{i+1})(\phi_i) - \sum_{i=5,9,13\ldots}^{601} \frac{A^i e_{33}}{l^i}(-v_i + v_{i+1})\phi_{i+2}
\end{aligned} \tag{2.37}
$$

The kinetic energy of the PZT stack in the open circuit can be obtained as

$$
\begin{aligned}
T_p &= \sum_{i=1,2,3\ldots}^{603} \frac{1}{2}\int_{x_i}^{x_{i+1}} A^i \rho^i \left(\frac{\partial v^i}{\partial t}\right)^2 dx \\
&= \sum_{i=1,2,3\ldots}^{603} \frac{1}{2}\int_0^1 A^i \rho^i l^i \left(\frac{\partial V^i}{\partial t}\right)^2 d\overline{x} \\
&= \sum_{i=1,2,3\ldots}^{603} \left\{\frac{1}{6} A^i \rho^i l^i \left[(\dot{v}_i)^2 + \dot{v}_i \dot{v}_{i+1} + (\dot{v}_{i+1})^2\right]\right\}
\end{aligned} \tag{2.38}
$$

The virtual work done by the block forces at the end of the PZT stack is given by

$$
\delta W = P(t)\delta v_1(t) - P(t)\delta v_{604}(t) \tag{2.39}
$$

The nodal quantities v_i $(i = 1, 2, ..., 604)$ and ϕ_i $(i = 3, 7, 11, ..., 603)$ are the generalized coordinates for the PZT stack. Write them in the vector form as

$$\begin{aligned} \mathbf{v} &= \{v_1, v_2, v_3, ..., v_{604}\}^T, \\ \phi &= \{\phi_3, \phi_7, \phi_{11}, ..., \phi_{603}\}^T, \\ \mathbf{q} &= \{\mathbf{v}, \phi\}^T \end{aligned} \tag{2.40}$$

Eq. (2.39) gives us the generalized forces as

$$\mathbf{Q}_{v(604\times1)} = \{P(t), 0, 0, ..., 0, 0, -P(t)\}^T, \tag{2.41}$$

$$\mathbf{Q}_{\phi(151\times1)} = \{0, 0, ..., 0\}^T, \tag{2.42}$$

$$\mathbf{Q}_{(755\times1)} = \{\mathbf{Q}_v, \mathbf{Q}_\phi\}^T$$

Define the Lagrange function as $L_p = T_p - V_p$. Applying the Lagrange equations,

$$\frac{d}{dt}\left(\frac{\partial L_p}{\partial \dot{q}_i}\right) - \frac{\partial L_p}{\partial q_i} = Q_i \tag{2.43}$$

we obtain the equations of motion for the PZT stack as

$$\mathbf{M}\ddot{\mathbf{q}} + \mathbf{K}\mathbf{q}(t) = \mathbf{Q} \tag{2.44}$$

where

$$\mathbf{M} = \begin{bmatrix} \mathbf{M}_{vv(604\times604)} & \mathbf{M}_{v\phi(604\times151)} \\ \mathbf{M}_{\phi v(151\times604)} & \mathbf{M}_{\phi\phi(151\times151)} \end{bmatrix} \tag{2.45}$$

$$\mathbf{K} = \begin{bmatrix} \mathbf{K}_{vv(604\times604)} & \mathbf{K}_{v\phi(604\times151)} \\ \mathbf{K}_{\phi v(151\times604)} & \mathbf{K}_{\phi\phi(151\times151)} \end{bmatrix} \tag{2.46}$$

$$\mathbf{M}_{vv} = \begin{bmatrix} \frac{1}{3}a_1 & \frac{1}{6}a_1 & & & & & & \\ \frac{1}{6}a_1 & \frac{1}{3}(a_1+a_2) & \frac{1}{6}a_2 & & & & & \\ & \frac{1}{6}a_2 & \frac{1}{3}(a_2+a_3) & \frac{1}{6}a_3 & & & & \\ & & \frac{1}{6}a_3 & \ddots & \ddots & & & \\ & & & \ddots & \ddots & \frac{1}{6}a_{602} & & \\ & & & & \frac{1}{6}a_{602} & \frac{1}{3}(a_{602}+a_{603}) & \frac{1}{6}a_{603} & \\ & & & & & \frac{1}{6}a_{603} & \frac{1}{3}a_{603} & \end{bmatrix} \tag{2.47}$$

$$\mathbf{M}_{v\phi} = {\mathbf{M}_{\phi v}}^T = [\mathbf{0}]_{604\times151} \tag{2.48}$$

$$\mathbf{M}_{\phi\phi} = [0]_{151\times151} \tag{2.49}$$

$$\mathbf{K}_{vv} = \begin{bmatrix} b_1 & -b_1 & & & & & & \\ -b_1 & (b_1+b_2) & -b_2 & & & & & \\ & -b_2 & (b_2+b_3) & -b_3 & & & & \\ & & -b_3 & \ddots & \ddots & & & \\ & & & \ddots & \ddots & -b_{602} & & \\ & & & & -b_{602} & (b_{602}+b_{603}) & -b_{603} & \\ & & & & & -b_{603} & b_{603} & \end{bmatrix} \tag{2.50}$$

$$\mathbf{K}_{v\phi} = \mathbf{K}_{\phi v}^T = \begin{bmatrix} \mathbf{K}_{v\phi1} & & & \\ & \mathbf{K}_{v\phi2} & & \\ & & \ddots & \\ & & & \mathbf{K}_{v\phi151} \end{bmatrix} \tag{2.51}$$

where

$$\mathbf{K}_{v\phi i} = \left\{-c_{4i-3}, c_{4i-3}, -c_{4i-1}, c_{4i-1}\right\}^T, i = 1, 2, 3, ..., 151 \tag{2.52}$$

$$\mathbf{K}_{\phi\phi} = \begin{bmatrix} d_3 & & & & & \\ & (d_5 + d_7) & & & & \\ & & (d_9 + d_{11}) & & & \\ & & & \ddots & & \\ & & & & (d_{597} + d_{599}) & \\ & & & & & d_{601} \end{bmatrix} \tag{2.53}$$

$$a_i = A^i \rho^i l^i, \ b_i = \frac{A^i E^i}{l^i}, \quad i = 1, 2, 3, ..., 603 \tag{2.54}$$

$$c_i = \begin{cases} \frac{A^i e_{33}}{l^i}, & i = 3, 5, 7, ..., 601 \\ 0, & i = 2, 4, 6, ..., 602, \text{ and } i = 1, 603 \end{cases} \tag{2.55}$$

$$d_i = \begin{cases} \frac{A^i \varepsilon^T}{l^i}, & i = 3, 5, 7, ..., 601 \\ 0, & i = 2, 4, 6, ..., 602, \text{ and } i = 1, 603 \end{cases} \tag{2.56}$$

Alternatively, Eq. (2.44) can be written in the following form

$$\mathbf{M}_{vv}\ddot{\mathbf{v}} + \mathbf{K}_{vv}\mathbf{v} + \mathbf{K}_{v\phi}\phi = \mathbf{Q}_v \tag{2.57}$$

$$\mathbf{K}_{\phi v}\mathbf{v} + \mathbf{K}_{\phi\phi}\phi = 0 \tag{2.58}$$

Since d_i are all non-zero and $\mathbf{K}_{\phi\phi}$ is invertible, ϕ can be obtained from Eq. (2.58) in terms of $\mathbf{v}$

$$\phi = -\mathbf{K}_{\phi\phi}^{-1}\mathbf{K}_{\phi v}\mathbf{v} \tag{2.59}$$

By substitute Eq. (2.59) into Eq. (2.57), we come to the equations of motion for

the displacement, which is decoupled from $\mathbf{v}$,

$$\mathbf{M}_{vv}\ddot{\mathbf{v}} + \left(\mathbf{K}_{vv} - \mathbf{K}_{v\phi}\mathbf{K}_{\phi\phi}^{-1}\mathbf{K}_{\phi v}\right)\mathbf{v} = \mathbf{Q}_v \tag{2.60}$$

Introduce several stiffness matrices to simplify the programming for numerical solutions as follows,

$$\mathbf{K}_a = \mathbf{K}_{\phi\phi}^{-1}\mathbf{K}_{\phi v}, \quad \mathbf{K}_b = \mathbf{K}_{v\phi}\mathbf{K}_a, \quad \mathbf{K}_p = \mathbf{K}_{vv} - \mathbf{K}_b \tag{2.61}$$

The equations of motion of the PZT stack without damping now reads

$$\mathbf{M}_{vv}\ddot{\mathbf{v}} + \mathbf{K}_p\mathbf{v} = \mathbf{Q}_v \tag{2.62}$$

$$\phi = -\mathbf{K}_a\mathbf{v} \tag{2.63}$$

We should point out that the generalized force $\mathbf{Q}_v$ contains the internal force $P(t)$ of the PEHU. In order to obtain the voltage output of the PZT stack, we must solve the coupled static or dynamic problem of the beams and PZT stack.

2.4.2 Dynamic Analysis of PZT Stack

Base on the finite element model of PZT stack, we can investigate the natural frequencies and dynamic response of a PZT stack. The following demonstrates the procedure of dynamic analysis of a PZT stack with its left end fixed and a compression force acting at the right end.

Applying Constraints

The fixed left end of PZT stack introduces the only geometric constraint which is $u_1(t) = 0$. This constraint can be implemented by modifying the corresponding row and column of both mass matrix and stiffness matrix so as to make sure $\ddot{\mathbf{u}}(t)$ be zero always. Therefore, the initial value $u_1(0) = 0$ will be kept at all time steps. The operations in detail are as follow

$$\mathbf{M}_{uu}(1,:) = 0, \quad \mathbf{M}_{uu}(:,1) = 0, \quad \mathbf{M}_{uu}(1,1) = 1 \tag{2.64}$$

$$\mathbf{K}_p(1,:) = 0, \quad \mathbf{K}_p(:,1) = 0 \tag{2.65}$$

where $(1,:)$ and $(:,1)$ denote the first row and the first column of a matrix, respectively. $(1,1)$ denotes the element in the first row and the first column of matrix.

Natural Frequencies

After applying constraint, we can check the natural frequencies of PZT stack by solving the generalized eigenproblem of

$$\mathbf{M}_{uu}\ddot{\mathbf{u}} + \mathbf{K}_p\mathbf{u} = 0 \tag{2.66}$$

which can be transformed into the modal form

$$\mathbf{K}_p\mathbf{V}_m = \mathbf{M}_{uu}\mathbf{V}_m\mathbf{\Omega}^2 \tag{2.67}$$

$$\mathbf{V}_m = [\mathbf{v}_1, \mathbf{v}_2, ..., \mathbf{v}_{604}] \tag{2.68}$$

where $\mathbf{v}_i$ is called the ith-mode shape vector, $\mathbf{V}_m$ is the mode transformation matrix.

$$\mathbf{\Omega}^2 = \begin{bmatrix} \omega_1^2 & & & \\ & \omega_2^2 & & \\ & & \ddots & \\ & & & \omega_{604}^2 \end{bmatrix} \tag{2.69}$$

where ω_i (rad/s) is the ith natural frequency in ascending order, i.e., $0 \leq \omega_1^2 \leq \omega_2^2 \leq \omega_3^2 \leq ... \leq \omega_{604}^2$, which can be converted into Hz by being divided by 2π.

Rayleigh Damping

Rayleigh damping can be counted in to approximate the overall energy dissipation in dynamics. The damping matrix $\mathbf{C}_p$ is assumed of the form

$$\mathbf{C}_p = \alpha \mathbf{M}_{uu} + \beta \mathbf{K}_p \tag{2.70}$$

where α and β are constants to be determined from two given damping ratios ξ_i and ξ_j that correspond to two unequal frequencies of vibration by solving Eqs. (2.71) and (2.72).

$$\alpha + \beta \omega_i^2 = 2\omega_i \xi_i \tag{2.71}$$

$$\alpha + \beta \omega_j^2 = 2\omega_j \xi_j \tag{2.72}$$

Time Integration Scheme

Because of the unconditionally stablity for linear system, the Newmark method is a good choice to analyze the dynamic response of PZT stack. The constant-average-acceleration assumption (also called trapezoidal rule) is included.

$$\dot{\mathbf{u}}(t+\Delta t) = \dot{\mathbf{u}}(t) + \left[\delta \ddot{\mathbf{u}}(t+\Delta t) + (1-\delta)\,\ddot{\mathbf{u}}(t)\right]\Delta t \tag{2.73}$$

$$\mathbf{u}(t+\Delta t) = \mathbf{u}(t) + \dot{\mathbf{u}}(t)\Delta t + \left[\eta \ddot{\mathbf{u}}(t+\Delta t) + \left(\frac{1}{2} - \eta\right)\ddot{\mathbf{u}}(t)\right]\Delta t^2 \tag{2.74}$$

where $\delta = 0.5$, $\eta = 0.25$.

The implict equilibrium equations at time $t + \Delta t$ are considered

$$\mathbf{M}_{uu}\ddot{\mathbf{u}}(t+\Delta t) + \mathbf{C}_p\dot{\mathbf{u}}(t+\Delta t) + \mathbf{K}_p\mathbf{u}(t+\Delta t) = \mathbf{Q}_u(t+\Delta t) \tag{2.75}$$

From Eqs. (2.73,2.74), two equations for the relationship between $\ddot{\mathbf{u}}(t+\Delta t)$ and $\dot{\mathbf{u}}(t+\Delta t)$ in terms of the unkown displacements $\mathbf{u}(t+\Delta t)$ can be obtained. Then substitute them into Eq. (2.75) to solve for $\mathbf{u}(t+\Delta t)$ based on the information at previous time step. The same precedure will be applied to calculate solutions of the next time step. To simplify calculations, we can set new constants that don't change in each time step. The displacements are be evaluated by

$$\begin{aligned}\mathbf{u}(t+\Delta t) = \mathbf{K}_{pinv}\,\{&\mathbf{Q}_u(t+\Delta t) + \mathbf{M}_{uu}\left(a_0\mathbf{u}(t) + a_2\dot{\mathbf{u}}(t) + a_3\ddot{\mathbf{u}}\,(t)\right) \\ &+ \mathbf{C}_p\left[a_1\mathbf{u}(t) + a_4\dot{\mathbf{u}}(t) + a_5\ddot{\mathbf{u}}(t)\right]\end{aligned} \tag{2.76}$$

where

$$\mathbf{K}_{pinv} = \left(\mathbf{K}_p + a_0\mathbf{M}_{uu} + a_1\mathbf{C}_p\right)^{-1} \tag{2.77}$$

$$\begin{aligned}a_0 = \frac{1}{\eta\Delta t^2}; a_1 = \frac{\delta}{\eta\Delta t}; a_2 = \frac{1}{\eta\Delta t}; a_3 = \frac{1}{2\eta} - 1; \\ a_4 = \frac{\delta}{\eta} - 1; a_5 = \frac{\Delta t}{2}\left(\frac{\delta}{\eta} - 2\right)\end{aligned} \tag{2.78}$$

Furthermore, accelerations and velocities at time $t + \Delta t$ can be estimated by

$$\ddot{\mathbf{u}}(t + \Delta t) = a_0(\mathbf{u}(t + \Delta t) - \mathbf{u}(t)) - a_2\dot{\mathbf{u}}(t) - a_3\ddot{\mathbf{u}}(t) \tag{2.79}$$

$$\dot{\mathbf{u}}(t + \Delta t) = \dot{\mathbf{u}}(t) + a_6\ddot{\mathbf{u}}(t) + a_7\ddot{\mathbf{u}}(t + \Delta t) \tag{2.80}$$

where

$$a_6 = \Delta t\,(1 - \delta)\,; a_7 = \delta\Delta t \tag{2.81}$$

Voltages of elements at time $t + \Delta t$ can be evaluated by

$$^{t+\Delta t}\phi = -\mathbf{K}_a\mathbf{u}(t + \Delta t) \tag{2.82}$$

The open circuit voltage of PZT stack can be evaluated by Eq. (2.11)

$$\phi_p(t + \Delta t) = \frac{1}{151}\sum_{i=3,7,11\ldots}^{603}\phi_i(t + \Delta t) \tag{2.83}$$

Since the PZT stack starts from resting state, the initial conditions are

$$\mathbf{u}(0) = 0; \dot{\mathbf{u}}(0) = 0; \ddot{\mathbf{u}}(0) = 0; \phi(0) = 0; \phi_p(0) = 0 \tag{2.84}$$

2.5 Coupled Analysis of PEHU

The PZT stack is coupled to the beams by the displacement continuity and the internal force balance at two ends. The displacement continuity requires

$$u\,(0, t) = v_1\,(t)\,,\ u\,(l_b, t) = v_{603}\,(t) \tag{2.85}$$

while the internal force balance amounts to substituting the expression for $P(t)$ in Eqs. (2.8) and (2.9) to Eq. (2.41).

2.6 Nomenclature

Variables of Multi-layer PZT Stack

Symbol	Description	Unit
P	Force applied at both end of PZT stack	N
ρ_s, ρ_p, ρ_e	Mass density of end layer, PZT and electrode	kg/m^3
E_s, E_p, E_e	Young's modulus of end layer, PZT and electrode	Pa
A_s, A_p, A_e	Cross-sectional area of end layer, PZT and electrode	m^2
l_s, l_p, l_e	Thickness of end layer, PZT and electrode	m
l	Length of PZT stack	m

Symbol	Description	Unit
e_{33}	Piezoelectric constant of PZT stack	C/m^2
ε^T	Dielectric constant of PZT stack	F/m
ε_0	Vacuum permittivity	F/m
v^i	Displacement field of the i^{th} element	m
ϕ^i	Voltage field of the i^{th} element	V
A^i	Cross-sectional area of the i^{th} element	m^2
ρ^i	Mass density of the i^{th} element	kg/m^3
E^i	Young's modulus of the i^{th} element	Pa
l^i	Length of i^{th} element	m
x_i	Global coordinate of the i^{th} node	m
v_i	Displacement of the i^{th} node	m
ϕ_i	Voltage of the i^{th} node	V
V	Voltage of multi-layer PZT stack	V
σ_i	Stress of the i^{th} element	Pa
ε_i	Strain of the i^{th} element	
D_i	Electric displacement of the i^{th} element	C/m^2
E_i	Electric field strength of the i^{th} element	V/m
V_p	Potential energy of multi-layer PZT Stack	J
T_p	Kinetic energy of multi-layer PZT Stack	J
δW_p	Virtual work of multi-layer PZT Stack	J
L_p	Lagarange function of multi-layer PZT Stack	J
$\mathbf{v}$	Vector of nodal displacements	m
ϕ	Vector of nodal voltages	V

Variables of the PEHU

Symbol	Description	Unit
u, w	Longitudinal and transverse displacement of the beam	m
f	Force density applied at the middle of the beam	N/m
l_f	Span of the applied force	m
l_b, h_b, b_b	Length, thickness and width of the beam	m
ρ_b	Mass density of the beam	kg/m^3
A_b	Cross-sectional area of the beam	m^2
E_b	Young's modulus of the beam	Pa
I_b	The second moment of area of the beam	m^4
w_i	The i^{th} mode function of the beam	
ζ	Damping ratio	
P_{in}	The equivalent concentrated load on the beam	N
C_U	The capacitance of a PEHU	μF
α_f	Force amplification factor of the PEHU	
α_e	Energy gain of the PEHU	
E_U	Electric potential energy of a PEHU	J
E_0	Electric potential energy of the PZT stack	J
d_U	Sinking displacement of a PEHU	m
V_U	Voltage of PEHU	V
σ_r	Stress in the equivalent rod of the PZT stack	Pa
σ_b	Stress in the beam	Pa
n_p	Number of PZT stacks in one PEHU	
W_{in}	Work done by the input force P_{in}	J
η	Mechanical-to-electric energy conversion efficiency	

Variables of the PEHS

Symbol	Description	Unit
G_{car}	Gravity of a typical mid-size vehicle	N
n_r	Number of PEHUs in a row	
V_U	Voltage of a PEHU	V
n_c	Number of PEHUs in a column	
n_l	Number of rows in one-meter-length lane	
d_{sk}	Total sinking displacement of PEHS	m
ρ_E	Energy density of PEHS	$J/(m.pass.lane)$
η_s	Efficiency of energy storage	
E	The harvested energy of PEHS	J
L_{rd}	Length of implemented roadway	m
N_{lane}	Number of implemented lanes	
N_{pas}	Number of passages in a lane during a period	
t_U	Time span of a zigzag force	s
S_p	Speed of vehicle	mph or km/h
w_{tp}	Width of top plate	m

Chapter 3

DYNAMIC ANALYSIS OF PEHU

In this chapter, the dynamic analysis of PEHU based on the mathematical model will be discussed in details. The performance of selected design with respect to impulsive traffic load was evaluated. In addition, the effect of vehicle speed on energy harvesting was investigated.

3.1 Equations of Motion

Due to the lack of information about damping coefficients of Titanium beam and PZT stacks, Rayleigh damping was adopted to evaluate the damping effect. With damping items omitted, the equations of motion for PEHU including boundary conditions states as follows.

$$\rho_b A_b \frac{\partial^2 u(x,t)}{\partial t^2} - E_b A_b \left(\frac{\partial^2 u(x,t)}{\partial x^2} + \frac{\partial w(x,t)}{\partial x} \frac{\partial^2 w(x,t)}{\partial x^2} \right) = 0 \tag{3.1}$$

$$\begin{aligned} &\rho_b A_b \frac{\partial^2 w(x,t)}{\partial t^2} + E_b I_b \frac{\partial^4 w(x,t)}{\partial x^4} \\ &- E_b A_b \left[\frac{\partial^2 u(x,t)}{\partial x^2} \frac{\partial w(x,t)}{\partial x} + \frac{\partial u(x,t)}{\partial x} \frac{\partial^2 w(x,t)}{\partial x^2} + \frac{3}{2} \left(\frac{\partial w(x,t)}{\partial x} \right)^2 \frac{\partial^2 w(x,t)}{\partial x^2} \right] \\ &= f(t) \left[H\left(x - \frac{l_b}{2} + \frac{l_f}{2} \right) - H\left(x - \frac{l_b}{2} - \frac{l_f}{2} \right) \right] \end{aligned} \tag{3.2}$$

$$E_b A_b \left[\frac{\partial u\left(0,t\right)}{\partial x} + \frac{1}{2}\left(\frac{\partial w\left(0,t\right)}{\partial x} \right)^2 \right] = \frac{1}{2} P\left(t\right) \tag{3.3}$$

$$E_b A_b \left[\frac{\partial u\left(l_b,t\right)}{\partial x} + \frac{1}{2}\left(\frac{\partial w\left(l_b,t\right)}{\partial x} \right)^2 \right] = \frac{1}{2} P\left(t\right) \tag{3.4}$$

$$u\left(l_b,t\right) = v_{603}\left(t\right) \tag{3.5}$$

$$u\left(0,t\right) = v_1\left(t\right) \tag{3.6}$$

$$M_{vv}\ \ddot{v} + K_p\, v = Q_v \tag{3.7}$$

$$\phi = -\ K_a\, v \tag{3.8}$$

Since $u(x,t)$ is supposed to be much smaller than $w(x,t)$, we can omit the longitudinal inertia force in Eq. (3.1) and integrate it from 0 to l_b, then combine with Eqs. (3.3)-(3.6), we will have equations for $w\left(x,t\right)$ and $P\left(t\right)$ and $v\left(t\right)$.

$$\begin{aligned} &\rho_b A_b \frac{\partial^2 w\left(x,t\right)}{\partial t^2} + E_b I_b \frac{\partial^4 w\left(x,t\right)}{\partial x^4} \\ &- \frac{P\left(t\right)}{2} \cdot \frac{\partial^2 w\left(x,t\right)}{\partial x^2} \\ &= f\left(t\right)\left[H\left(x - \frac{l_b}{2} + \frac{l_f}{2} \right) - H\left(x - \frac{l_b}{2} - \frac{l_f}{2} \right) \right] \end{aligned} \tag{3.9}$$

$$P\left(t\right) = \frac{2E_b A_b}{l_b}\left[-v_1\left(t\right) + v_{603}\left(t\right) + \right] + \frac{E_b A_b}{l_b} \int_0^{l_b} \left(\frac{\partial w\left(x,t\right)}{\partial x} \right)^2 dx \tag{3.10}$$

To get rid of unknown internal force $P(t)$, substitute Eq. (3.10) into Eq. (3.9), we can have the PDE for longitudinal displacement $w(x,t)$ coupled with PZT

deformation as shown in Eq. (3.11).

$$\begin{aligned}&\rho_b A_b \frac{\partial^2 w\left(x,t\right)}{\partial t^2} + E_b I_b \frac{\partial^4 w\left(x,t\right)}{\partial x^4} \\ &- \frac{E_b A_b}{l_b}\left[-v_1\left(t\right) + v_{603}\left(t\right)\right] \cdot \frac{\partial^2 w\left(x,t\right)}{\partial x^2} - \frac{E_b A_b}{2l_b}\int_0^{l_b}\left(\frac{\partial w\left(x,t\right)}{\partial x}\right)^2 dx \cdot \frac{\partial^2 w\left(x,t\right)}{\partial x^2} \\ &= f\left(t\right)\left[H\left(x - \frac{l_b}{2} + \frac{l_f}{2}\right) - H\left(x - \frac{l_b}{2} - \frac{l_f}{2}\right)\right]\end{aligned} \tag{3.11}$$

3.2 Mode Expansion

Based on expansion theorem, $w(x,t)$ can be approximated by a series of linear combination of mode functions multiplied by unknown temporal coordinates in the form of

$$w(x) = \sum_{i=1}^{n} c_i\left(t\right) w_i\left(x\right) \tag{3.12}$$

where n stands for the number of modes used in the mode expansion to approximate $w(x,t)$ and coefficient $c_i(t)$ is the temporal coordinate corresponding to each mode function $w_i\left(x\right)$.

The mode functions $w_i(x)$ for clamped-clamped beam are defined as Eq. (3.13). To reduce computation in iterations, normalized mode functions $w_{yi}(y)$ were defined additionally as Eq. (3.14). The two parameters λ and σ in the mode functions are defined as Eq. (3.15).

$$w_i\left(x\right) = \cosh\frac{\lambda_i x}{l_b} - \cos\frac{\lambda_i x}{l_b} - \sigma_i\left(\sinh\frac{\lambda_i x}{l_b} - \sin\frac{\lambda_i x}{l_b}\right) \quad 0 \le x \le l_b \tag{3.13}$$

$$w_{yi}\left(y\right) = \cosh\lambda_i y - \cos\lambda_i y - \sigma_i\left(\sinh\lambda_i y - \sin\lambda_i y\right) \quad 0 \le y \le l_b \tag{3.14}$$

$$\lambda_i = \begin{cases} 4.73004074 & i=1 \\ 7.85320462 & i=2 \\ 10.9956079 & i=3 \\ 14.1371655 & i=4 \\ 17.2787597 & i=5 \\ (2i+1)\frac{\pi}{2} & i>5 \end{cases} \quad \sigma_i = \begin{cases} 0.982502215 & i=1 \\ 1.000777312 & i=2 \\ 0.999966450 & i=3 \\ 1.000001450 & i=4 \\ 0.999999937 & i=5 \\ 1.0 & i>5 \end{cases} \tag{3.15}$$

3.3 Weighted Residual Method

Substituting $w(x,t)$ with the mode expansion into Eq. (3.11) leads to a residual function $R_g(x,t)$ defined in Eq. (3.16) which is a measure of error away from balance, as this approximate solution usually can not satisfy the differential equation of $w(x,t)$.

$$\begin{aligned} R_g(x,t) = {} & \rho_b A_b \frac{\partial^2 w(x,t)}{\partial t^2} + C_w \frac{\partial w(x,t)}{\partial t} + E_b I_b \frac{\partial^4 w(x,t)}{\partial x^4} \\ & - \frac{E_b A_b}{l_b} \left[-v_1(t) + v_{603}(t) \right] \cdot \frac{\partial^2 w(x,t)}{\partial x^2} - \frac{E_b A_b}{2 l_b} \int_0^{l_b} \left(\frac{\partial w(x,t)}{\partial x} \right)^2 dx \cdot \frac{\partial^2 w(x,t)}{\partial x^2} \\ & - f(t) \left[H\left(x - \frac{l_b}{2} + \frac{l_f}{2} \right) - H\left(x - \frac{l_b}{2} - \frac{l_f}{2} \right) \right] \end{aligned} \tag{3.16}$$

Use Galerkin's weighted residual method with mode functions as weight functions,

$$\int_0^{l_b} R_g(x,t)\, w_i(x)\, dx = 0, i = 1, 2, ..., n \tag{3.17}$$

ODEs of temporal coordinates $c_i(t)$, $i = 1, 2, ..., n$ for all the employed modes can be obtained. Together with Eq. (3.7) for PZT, the equations of motion for PEHU

with Rayleigh damping can be written in the matrix form as following.

$$M\ddot{q} + C\dot{q} + Kq + F_{nl} = f_{in} \tag{3.18}$$

$$\begin{aligned} v &= \{v_1(t), v_2(t), ..., v_{603}(t)\}^T, \\ c &= \{c_1(t), c_2(t), ..., c_n(t)\}^T, \\ q &= \{v, c\}^T \end{aligned} \tag{3.19}$$

$$M = \begin{bmatrix} M_{vv} & 0 \\ 0 & M_b \end{bmatrix}, K = \begin{bmatrix} K_{pb} & 0 \\ 0 & K_c \end{bmatrix} \tag{3.20}$$

$$C = \alpha M + \beta K \tag{3.21}$$

$$M_b(j,i) = \begin{cases} \rho_b A_b l_b g_j, & j = i \\ 0, & j \neq i \end{cases}, \ j, i = 1, 2, ..., n \tag{3.22}$$

$$K_{pb} = K_p + K_b \tag{3.23}$$

$$K_b(j,i) = \begin{cases} -\frac{2E_b A_b}{l_b}, j = 1, i = 1, 603 \\ \frac{2E_b A_b}{l_b}, j = 603, i = 1, 603 \\ 0, else \end{cases} \tag{3.24}$$

$$K_c(j,i) = \frac{E_b A_b}{l_b^3} S_{ji} \tag{3.25}$$

$$F_{nl} = \begin{Bmatrix} F_p \\ F_b \end{Bmatrix} \tag{3.26}$$

$$F_p = \begin{cases} \frac{2E_b A_b}{l_b^2} c^T D c, j = 1, 603 \\ 0, 1 < j < 603 \end{cases} \tag{3.27}$$

$$F_{bj} = \frac{E_b A_b}{l_b^2} (v_1 - v_{603}) Z_{(j,:)} c - \frac{E_b A_b}{2 l_b^3} Z_{(j,:)} c c^T D c, j = 1...n \tag{3.28}$$

$$f_{in} = \begin{Bmatrix} 0 \\ f_b \end{Bmatrix} \tag{3.29}$$

$$f_b = H_f \cdot f\left(t\right) \tag{3.30}$$

$$g_j = \int_0^1 w_{yj}^2 dy \ , \ j = 1, 2, ..., n \tag{3.31}$$

$$S_{ji} = \int_0^1 \frac{d^4 w_{yi}}{dy^4} w_{yj} dy \ , \ j, i = 1, 2, ..., n \tag{3.32}$$

$$D_{rk} = \int_0^1 \frac{dw_{yr}}{dy} \frac{dw_{yk}}{dy} dy \ , \ r, k = 1, 2, ..., n \tag{3.33}$$

$$Z_{ji} = \int_0^1 \frac{d^2 w_{yi}}{dy^2} w_{yj} dy \ , \ j, i = 1, 2, ..., n \tag{3.34}$$

$$H_{fj} = \int_0^{l_b} \left[H\left(x - \frac{l_b}{2} + \frac{l_f}{2}\right) - H\left(x - \frac{l_b}{2} - \frac{l_f}{2}\right) \right] w_j dx \ , \ j = 1, 2, ..., n \tag{3.35}$$

3.4 Time Integration Procedure

The widely used implicit time integration procedure including trapezoidal rule and Newton-Raphson iteration was used to solve the above nonlinear ODEs.

The basic equations of dynamics to be solved in nonlinear analysis (balanced at time $t + \Delta t$) are

$$^{t+\Delta t}\widetilde{R}\left(q^*\right) - {}^{t+\Delta t}F\left(q^*\right) = o \tag{3.36}$$

Where

$$^{t+\Delta t}\widetilde{R}\left(q^*\right) = {}^{t+\Delta t}R - M\ {}^{t+\Delta t}\ddot{q}^* \tag{3.37}$$

$$^{t+\Delta t}F\left(q^*\right) = C\ {}^{t+\Delta t}\dot{q}^* + K\ {}^{t+\Delta t}q^* + \left.{}^{t+\Delta t}F_{nl}\right|_{q^*} \tag{3.38}$$

Newton-Raphson iteration was found to be very effective for finding the solution q^* of the equations

$$r(q^*) = o \tag{3.39}$$

where

$$r(q^*) = {}^{t+\Delta t}\widetilde{R}\,(q)\Big|_{q^*} - {}^{t+\Delta t}F\,(q)\big|_{q^*} \tag{3.40}$$

Use Taylor expansion of $r(q^*)$ at ${}^{t+\Delta t}q^{(i-1)}$ and neglect orders higher than 1, i denotes the i^{th} iteration result

$$r(q^*) = r(q)|_{{}^{t+\Delta t}q^{(i-1)}} + \left[\left.\frac{\partial \widetilde{R}}{\partial q}\right|_{{}^{t+\Delta t}q^{(i-1)}} - \left.\frac{\partial F}{\partial q}\right|_{{}^{t+\Delta t}q^{(i-1)}}\right]\left(q^* - {}^{t+\Delta t}q^{(i-1)}\right) \tag{3.41}$$

where

$$r(q)|_{{}^{t+\Delta t}q^{(i-1)}} = {}^{t+\Delta t}\widetilde{R}\left(q^{(i-1)}\right) - {}^{t+\Delta t}F\left(q^{(i-1)}\right) \tag{3.42}$$

$${}^{t+\Delta t}\widetilde{R}\left(q^{(i-1)}\right) = {}^{t+\Delta t}f_{in} - M\,{}^{t+\Delta t}\ddot{q}^{(i-1)} \tag{3.43}$$

$${}^{t+\Delta t}F\left(q^{(i-1)}\right) = C\,{}^{t+\Delta t}\dot{q}^{(i-1)} + K\,{}^{t+\Delta t}q^{(i-1)} + {}^{t+\Delta t}F_{nl}^{(i-1)} \tag{3.44}$$

Here, the trapezoidal rule was applied to the implicit time integration method because of its relatively good stability and accuracy characteristics. The basic assumptions of the trapezoidal rule include

$${}^{t+\Delta t}\dot{q}^{(i-1)} = {}^{t}\dot{q} + \frac{\Delta t}{2}\left({}^{t+\Delta t}\ddot{q}^{(i-1)} + {}^{t}\ddot{q}\right) \tag{3.45}$$

$${}^{t+\Delta t}q^{(i-1)} = {}^{t}q + \frac{\Delta t}{2}\left({}^{t+\Delta t}\dot{q}^{(i-1)} + {}^{t}\dot{q}\right) \tag{3.46}$$

Then, we have

$${}^{t+\Delta t}\dot{q}^{(i-1)} = \frac{2}{\Delta t}\left({}^{t+\Delta t}q^{(i-1)} - {}^{t}q\right) - {}^{t}\dot{q} \tag{3.47}$$

$${}^{t+\Delta t}\ddot{q}^{(i-1)} = \frac{4}{\Delta t^2}\left({}^{t+\Delta t}q^{(i-1)} - {}^{t}q\right) - \frac{4}{\Delta t}\,{}^{t}\dot{q} - {}^{t}\ddot{q} \tag{3.48}$$

Use the above two equations to eliminate ${}^{t+\Delta t}\dot{q}^{(i-1)}$ and ${}^{t+\Delta t}\ddot{q}^{(i-1)}$,

$$ {}^{t+\Delta t}\widetilde{R}\left(q^{(i-1)}\right) = {}^{t+\Delta t}f_{in} - M\left[\frac{4}{\Delta t^2}\left({}^{t+\Delta t}\,q^{(i-1)} - {}^{t}q\right) - \frac{4}{\Delta t}\,{}^{t}\,\dot{q} - {}^{t}\,\ddot{q}\right] \tag{3.49} $$

$$ {}^{t+\Delta t}F\left(q^{(i-1)}\right) = C\left[\frac{2}{\Delta t}\left({}^{t+\Delta t}\,q^{(i-1)} - {}^{t}q\right) - {}^{t}\,\dot{q}\right] + K\,{}^{t+\Delta t}q^{(i-1)} + {}^{t+\Delta t}F_{nl}^{(i-1)} \tag{3.50} $$

$$ \left.\frac{\partial \widetilde{R}}{\partial q}\right|_{{}^{t+\Delta t}q^{(i-1)}} = -\frac{4}{\Delta t^2}M \tag{3.51} $$

$$ \left.\frac{\partial F}{\partial q}\right|_{{}^{t+\Delta t}q^{(i-1)}} = \frac{2}{\Delta t}C + {}^{t+\Delta t}\,\widehat{K}^{\,(i-1)} \tag{3.52} $$

where ${}^{t+\Delta t}\,\widehat{K}^{\,(i-1)}$ is the tangent stiffness matrix in iteration $i-1$, which contains a constant linear part K and a nonlinear part K_{nl}.

$$ \widehat{K} = K + {}^{t+\Delta t}K_{nl}^{(i-1)} \tag{3.53} $$

$$ {}^{t+\Delta t}K_{nl}^{(i-1)} = \left.\frac{\partial F_{nl}}{\partial q}\right|_{{}^{t+\Delta t}q^{(i-1)}} \tag{3.54} $$

where

$$ K_{nl(p,j)} = b \cdot c^T \cdot B_{(p,j)} \cdot c \tag{3.55} $$

$$ B_{(p,j)} = 2 \cdot D_{(:,j)} \cdot Z_{(p,:)} + D \cdot Z_{(p,j)} \tag{3.56} $$

where subscript (p, j) denotes the element in p^{th} row and j^{th} column of a matrix, and : denotes a whole row or a whole column of a matrix. B is a four-dimensional array, $B_{(p,j)}$ is a n by n matrix, p, j go from 1 to n.

Define the increment of q of i^{th} iteration at time $t + \Delta t$

$$\Delta q^{(i)} = q^* - {}^{t+\Delta t}q^{(i-1)} \tag{3.57}$$

Substitute above equations into Eq. (3.41), yields

$$\begin{aligned}\left(\frac{2}{\Delta t}C + {}^{t+\Delta t}\widehat{K}^{(i-1)}\right)\Delta q^{(i)} = {}^{t+\Delta t}f_{in} - C\left[\frac{2}{\Delta t}\left({}^{t+\Delta t}q^{(i-1)} - {}^{t}q\right) - {}^{t}\dot{q}\right] \\ - K\,{}^{t+\Delta t}q^{(i-1)} - {}^{t+\Delta t}F_{nl}^{(i-1)} \\ - M\left\{\frac{4}{(\Delta t)^2}\left({}^{t+\Delta t}q^{(i-1)} - {}^{t}q\right) - \frac{4}{\Delta t}\,{}^{t}\dot{q} - {}^{t}\ddot{q}\right\}\end{aligned} \tag{3.58}$$

where

$${}^{t+\Delta t}\widehat{K}^{(i-1)} = \frac{4}{(\Delta t)^2}M + K_l + {}^{t+\Delta t}K_{nl}^{(i-1)} \tag{3.59}$$

The displacement increment can be used to obtain the next displacement approximation.

$${}^{t+\Delta t}q^{(i)} = {}^{t+\Delta t}q^{(i-1)} + \Delta q^{(i)} \tag{3.60}$$

When the termination criteria is satisfied, integration can move onto the next time interval with the initial conditions

$${}^{t+\Delta t}\widehat{K}^{(0)} = {}^{t}\widehat{K}\ ,\ {}^{t+\Delta t}\widehat{F}^{(0)} = {}^{t}F\ ,\ {}^{t+\Delta t}q^{(0)} = {}^{t}q \tag{3.61}$$

Convergence criteria is necessary to terminate iterating at each time step and achieve preset tolerances for a tight convergence. Combination of the out-of-balance forces and the incremental internal energy is an effective convergence criteria because increments in both force and energy tending to zero near the solution can

provide some measure of the accuracy of both displacements and forces. Eq. 3.62 is a force convergence criterion that requires the norm of the out-of-balance load vector be within a preset tolerance ϵ_F of the original load increment. Eq. 3.63 is a force convergence criterion that requires the work done by the out-of-balance load vector on the increments of generalized coordinates be within a preset tolerance ϵ_E of the initial internal energy increment.

$$\left\| {}^{t+\Delta t}\widetilde{R}^{(i)} - {}^{t+\Delta t}F^{(i)} \right\|_2 \leq \epsilon_F \left\| {}^{t+\Delta t}R - {}^{t}F - M\,{}^{t}\ddot{q} \right\|_2 \tag{3.62}$$

$$\Delta q^{(i)} \left({}^{t+\Delta t}R - {}^{t+\Delta t}F^{(i-1)} - M\,{}^{t+\Delta t}\ddot{q}^{(i-1)} \right) \leq \epsilon_E\, \Delta q^{(1)t} \left({}^{t+\Delta t}R - {}^{t}F - M\,{}^{t}\ddot{q} \right) \tag{3.63}$$

To obtain a very tight convergence, ϵ_F and ϵ_E are preferably to be very small. However, this strategy could fail when the out-of-balance forces and the incremental internal energy are already very small initially. In such cases, the above criteria can be very hard to achieve because the out-of-balance force and energy are compared to a given percentage of the values in previous step. To make the convergence criterion more robust, a relative convergence criteria rather than an absolute tolerance have been created. If the difference of out-of-balance forces and the incremental internal energy between two continuous iterations are bounded in a preset small range in terms of percentage, we assume that the convergence has been achieved.

Define the rate of out-of-balance forces as follows:

$$r_F^{(i)} = \frac{e_F^{(i)}}{\left(e_F^{(i)} + e_F^{(i-1)} \right)/2} \tag{3.64}$$

where

$$e_F^{(i)} = \left\| {}^{t+\Delta t}\widetilde{R}^{(i)} - {}^{t+\Delta t}F^{(i)} \right\|_2 \tag{3.65}$$

Define the the rate of the incremental internal energy as follow:

$$r_E^{(i)} = \frac{e_E^{(i)}}{\left(e_E^{(i)} + e_E^{(i-1)}\right)/2} \tag{3.66}$$

where

$$e_E^{(i)} = \Delta q^{(i)} \left({}^{t+\Delta t}\widetilde{R}^{(i)} - {}^{t+\Delta t}F^{(i)} \right) \tag{3.67}$$

Now we can define a neighborhood to confine the rates:

$$P_{F\,\min} < r_F^{(i)} < P_{F\,\max} \tag{3.68}$$

$$P_{E\,\min} < r_E^{(i)} < P_{E\,\max} \tag{3.69}$$

When both of the two requirements are satisfied, we can stop iterating at the current time step and move onto the next step. Note that the relative percentage criteria is the supplement of the force and energy criteria. At the end of each iteration, the force and energy criteria will be checked first, if they are not satisfied, then check the relative percentage criteria. As long as either of these two sets of criteria is fulfilled, the convergence has been obtained.

3.5 Dynamic Response to Traffic Load

We assume that the wheel of a passing vehicle provides a triangular shape impulsive compressional force on the PEHU. The duration of the impulse is equal to the time t_U the vehicle takes to pass the PEHU, and the peak value of the

impulse is determined by the weight of the vehicle as well as the dynamic reaction of the vehicle suspension. The amplitude of the impulsive force on the PEHU is $P_{in} = 1333N$ same as the force considered in the static analysis for the purpose of comparison. We design the road surface such that the tire of the wheel exerts the force on the PEHU over a short span $w_{tp} = 115mm$. Assume that the vehicle speed is $S_p = 104.61km/h$ $(65mph)$. Hence, it takes about $8ms$ for the vehicle to pass the PEHU. The duration of one impulse is thus $8ms$.

In the dynamic analysis, the FE model of PZT stacks is used. For the nonlinear beams, we ignore the dynamics of the axial displacement because the frequency of the axial vibration is much higher than that of the deflections. We apply the Rayleigh-Ritz method and express the deflection of the beam in terms of the first five modes of a clamped-clamped beam. The mode function of the clamped-clamped beam is given by

$$\phi_i(x) = \cosh\frac{\lambda_i x}{l_b} - \cos\frac{\lambda_i x}{l_b} - \sigma_i\left(\sinh\frac{\lambda_i x}{l_b} - \sin\frac{\lambda_i x}{l_b}\right) \quad 0 \le x \le l_b \tag{3.70}$$

where the coefficients λ_i and σ_i are listed in Table 3.1. The first five natural frequencies of the PEHU without preloading in the coupled analysis are computed and listed in the table also. The example of the PEHU considered in the dynamic analysis has the first natural frequency greater than $1kHz$. This is consistent with the assumption in the static design of the PEHU reported in Section 4.2. Because the frequency contact of the traffic load is less than $1kHz$ and the 3^{rd} natural frequency of the PEHU is more than $5kHz$, the Rayleigh-Ritz solution with the first five modes in the expansion is sufficiently accurate. The results of the solutions using the five mode expansion are reported next.

Table 3.1: The first five natural frequencies of the PEHU.

Order i	1	2	3	4	5
λ_i	4.7300	7.8532	10.9956	14.1372	17.2787
σ_i	0.9825	1.0008	0.9999	1.0000	1.0000
Frequency (kHz)	1.03	2.85	5.58	9.23	13.79

Before presenting the simulation results, we should point out that the numerical method for integrating the coupled nonlinear differential equations is validated. In particular, we check the weighted residual errors of the differential equations to be in the order of $10^{-6}N$, which corresponds to the error in the generated energy in the order of $10^{-9}J$.

3.5.1 Effect of Damping

The advantage of having a mathematical model of the PEHU is that the model allows us to simulate various dynamic conditions that are otherwise very hard to realize in experiments. We first study the effect of structural damping on the dynamic response when the vehicle speed is fixed at $104.61km/h$ $(65mph)$. A quarter weight of a Camry is used in the simulation studies. The Rayleigh damping of the beams is assumed. The linear inertial and stiffness matrices of the beams are used to determine the Rayleigh damping. Four cases are considered and compared with the zero damping case. The damping ratios for the five modes of the beams in the four cases are listed in Table 3.2. The damping in the PZT stacks is not considered.

Figures 3.1, 3.2, 3.3 and 3.4 show the temporal responses of the generated open circuit voltage, the sinking displacement of the unit, the dynamic force amplification factor and the dynamic compressive force on the PZT stacks. The oscillations

Table 3.2: Modal damping ratios of the four cases.

Case	Mode 1	Mode 2	Mode 3	Mode 4	Mode 5
1	0.01	0.01	0.0157	0.0246	0.0361
2	0.02	0.02	0.0315	0.0492	0.0721
3	0.03	0.03	0.0472	0.0738	0.1082
4	0.04	0.04	0.063	0.0984	0.1443

in the response are at the 1^{st} natural frequency of the PEHU. In general, as is in the case of structural vibrations, the higher the damping, the smaller peak values of the oscillations.

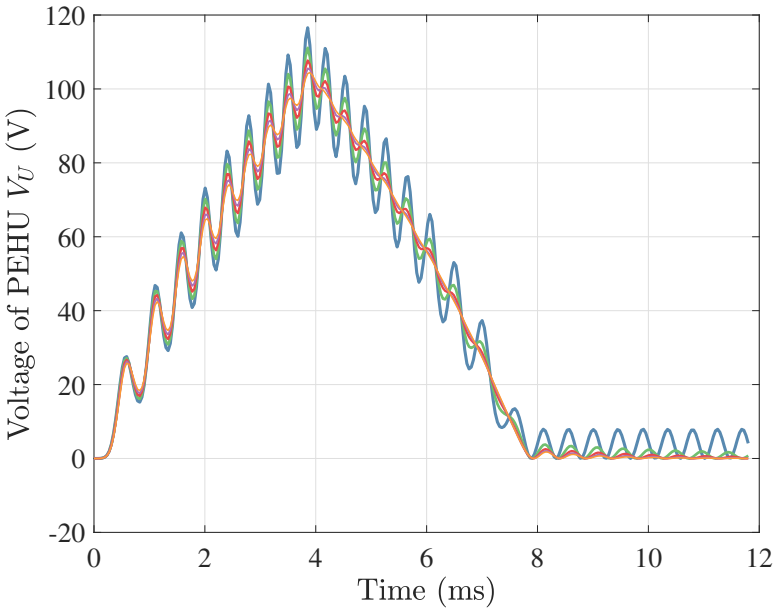

Figure 3.1: The open circuit voltage of the piezoelectric energy harvesting device due to a vehicle passing at speed $104.61km/h$ ($65mph$).

We should point out that in the real PEHU, the damping due to friction can be much higher than those specified in Table 3.2. The oscillations will be smaller

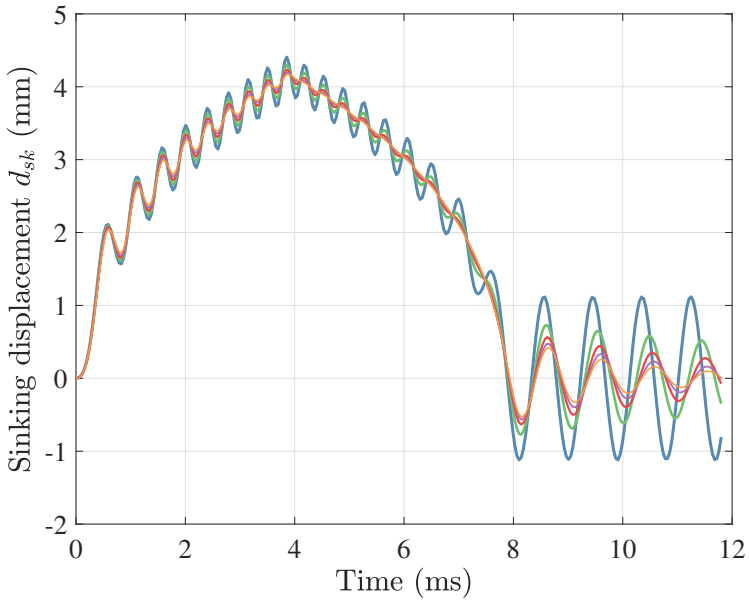

Figure 3.2: The sinking displacement of the piezoelectric energy harvesting device due to a vehicle passes over at speed $104.61 km/h$ ($65 mph$).

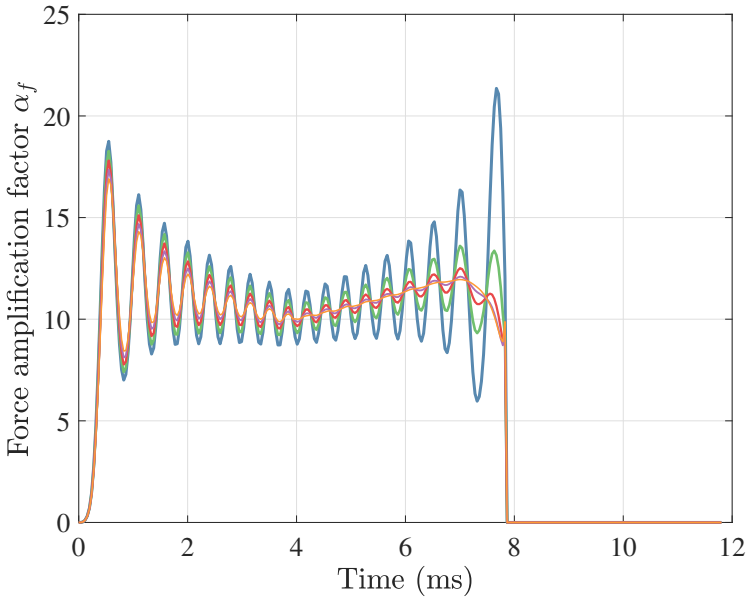

Figure 3.3: Dynamic force amplification factor of the piezoelectric energy harvesting device due to a vehicle passes over at speed $104.61 km/h$ ($65 mph$).

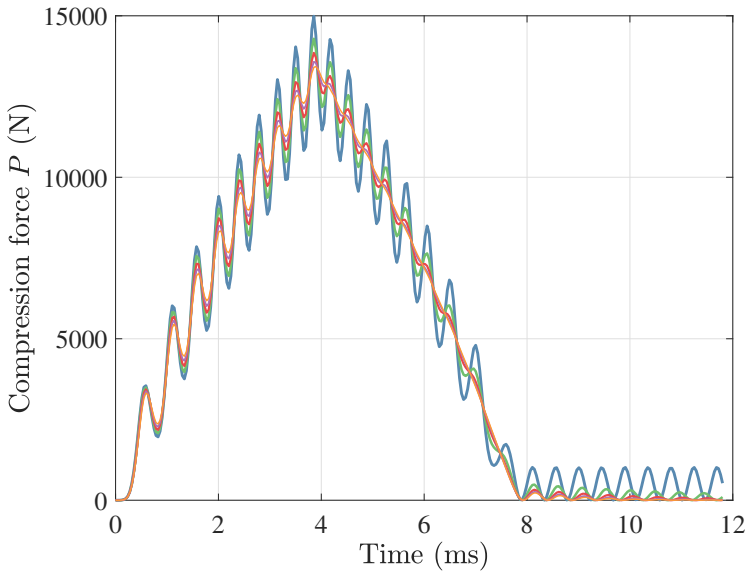

Figure 3.4: The compressive force on the PZT stacks in the piezoelectric energy harvesting device due to a vehicle passing at speed $104.61 km/h$ $(65 mph)$.

than those in the figures. What is interesting to point out is that the dynamic force amplification factor is greater than 10 on average as shown in Figure 3.3. Recall that the amplification factor 10 is the static design. The dynamic loading appears to be beneficial as far as the force amplification is concerned while the damping does not seem to lower the force amplification factor. The peak values of various responses in the figures are listed in Table 3.3.

Some notations used in Table 3.3 are defined herein. $max(d_{sk})$ is the peak sinking displacement (d_{sk}), which is twice the displacement at the middle of beam, $d_{sk} = 2w(l_b/2, t)$. $max(V_U)$ is the peak value of the generated voltage (V_U). $E_p = 2\int_0^{max(V_U)} C_U V_U dV_U$ is the electric potential energy of the PEHU. The electric potential energy in the PZT stacks is collected in the complete loading and unloading cycle with a bridge rectifier. $W_{in} = \int_0^{t_U/2} P_{in} w'(l_b/2, t) dt$ is the mechanical work

by the gravity. $\eta = E_p/W_{in}$ represents the mechanical-to-electric energy conversion efficiency of the PEHU. It is seen from Table 3.3 that the damping does have a tendency to lower the electric energy output of the PEHU.

Table 3.3: Peak values of dynamic responses of the piezoelectric energy harvesting device due to a vehicle passing at speed $104.61km/h$ ($65mph$). Case 0 has no damping.

Case	$max(d_{sk})$ (mm)	$max(V_U)$ (V)	E_p (mJ)	W_{in} (mJ)	η $(\%)$
0	4.46	116.56	121.19	2078.53	5.83
1	4.30	111.12	102.91	1939.53	5.31
2	4.23	107.71	92.64	1851.60	5.00
3	4.19	105.55	86.65	1796.12	4.82
4	4.17	104.43	83.45	1767.50	4.72

3.5.2 Effect of Vehicle Speed

When a vehicle travels at high speed, it generates a dynamic reaction force on the road surface through the suspension. The dynamic reaction force can even have much larger amplitude than the vehicle weight. To obtain the dynamic reaction force, one must have a full dynamic model of the vehicle. In this part of the study, we assume that the dynamic reaction force has the same amplitude as the weight of the vehicle. The impulsive force P_{in} due to different vehicle speeds S_p will have varying duration time t_U. Let us consider the damping case 2 in Table 3.2. We consider the speeds in the range of $8.05 - 128.75km/h$ ($5 - 80mph$).

Figure 3.6 shows that as the vehicle speed increases from $8.05km/h$ ($5mph$) to $128.75km/h$ ($80mph$), the maximum sinking displacement of the PEHU increases slightly from $4.15mm$ to $4.28mm$. The maximum change in d_{sk} is just $0.13mm$ or

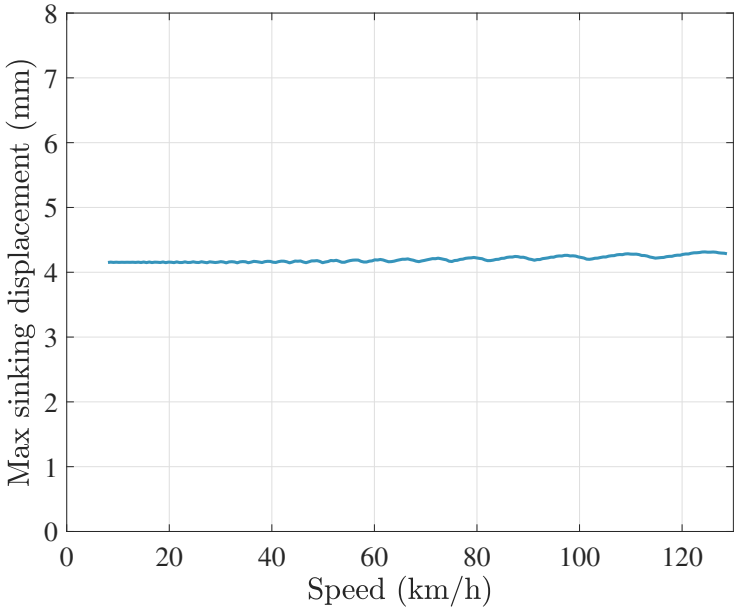

Figure 3.5: The sinking displacement of the piezoelectric energy harvesting device as a function of vehicle speed.

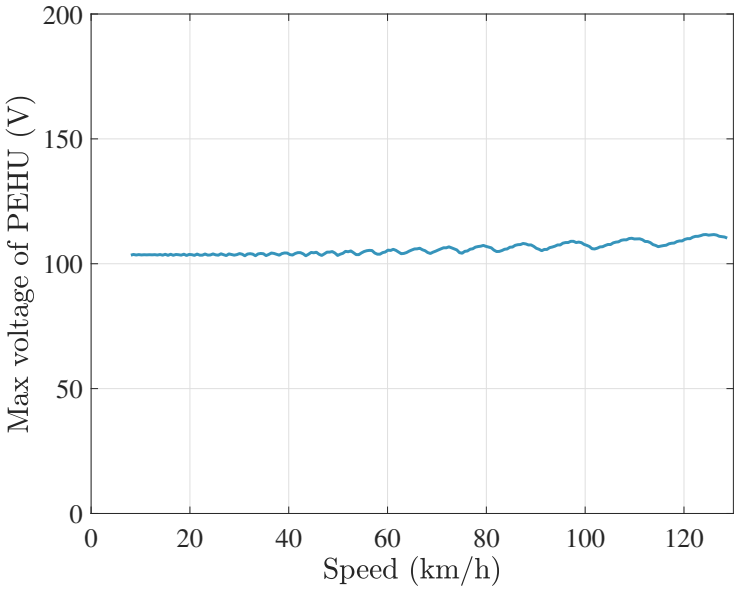

Figure 3.6: The maximum voltage output of the piezoelectric energy harvesting device as a function of vehicle speed.

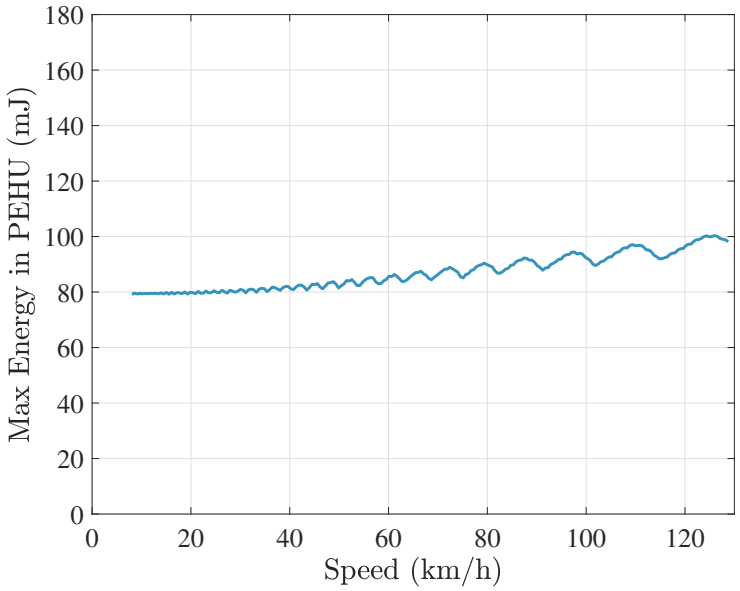

Figure 3.7: The electric potential energy harvested by the piezoelectric energy harvesting device as a function of vehicle speed.

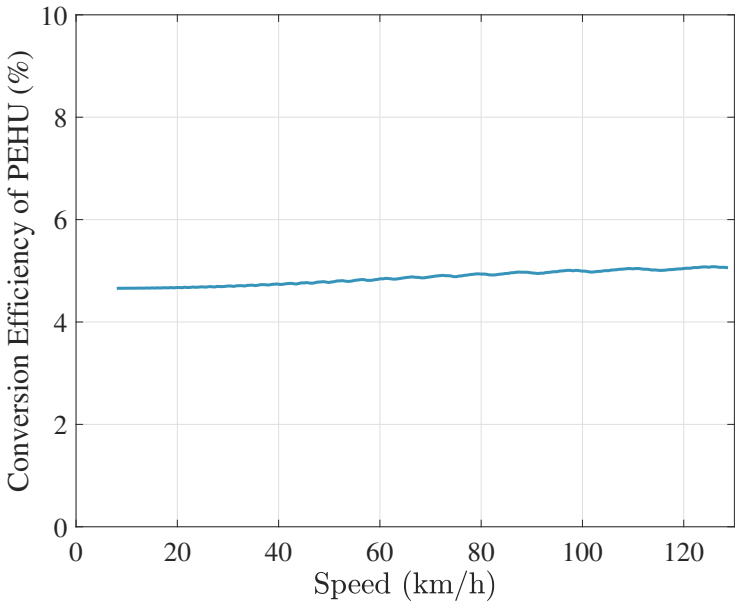

Figure 3.8: The energy conversion efficiency of the piezoelectric energy harvesting device as a function of vehicle speed.

approximately 3%. The maximum generated voltage V_U also grows slightly from $103.44V$ to $110.26V$ as shown in Figure 3.6. The voltage change is $6.82V$ or 6%. Figure 3.7 shows that the range of the electric potential energy is between $89.57mJ$ to $100.32mJ$ with a small increasing trend with the speed. Figure 3.8 shows that the speed effect on the energy conversion efficiency of the PEHU slightly improves with the increasing vehicle speed and exceeds 5% at $128.75km/h$ ($80mph$).

The numerical simulations indicate that there is a positive correlation between the vehicle speed and the responses of the PEHU when the impulse force amplitude is fixed. The speed in the studied range does not introduce significant changes to the amount of the harvested energy. This seems to imply that the proposed PEHU is robust with respect to the speed of traffic.

3.6 Conclusions

In this chapter, the dynamic analysis of PEHU has been demonstrated for theoretical exploration. The procedure of applying numerical methods to simulate dynamic response of PEHU to impulsive loading has been explained in details. Damping effect has been investigated in the range of no damp to 0.04 applied at the first two modes. High vehicle speed was found to be beneficial to power generation in numerical analysis.

Chapter 4

DESIGN AND LABORATORY TEST OF PEHU

In this chapter, the design and realization of PEHU will be introduced. Optimal design parameters of beam were obtained via multi-objective optimization based on the static analysis of PEHU. Mechanical design was conducted to translate the mathematics model into prototypes. Quasi-static compression test results in laboratory will be presented.

4.1 Static Analysis of PEHU

In roadway implementation, each PEHU is supposed to work in a discontinuous manner. Electricity will be generated during the short interactions between wheels and PEHU. The frequency of impulsive load from traffic is significantly lower than the natural frequency of PEHU. These facts enables the preliminary selection of design parameters based on static analysis.

In order to reduce the numerical computational cost, the mathematical model of PEHU was simplified by using a PZT rod instead of multi-layer PZT stack, as shown in Fig. 4.1. It is a normal form of the proposed compression-to-compression force amplification mechanism. This change eliminates trouble in root-finding of high dimensional finite element equations coupled with nonlinear beam, especially, when evolutionary optimization algorithm is involved.

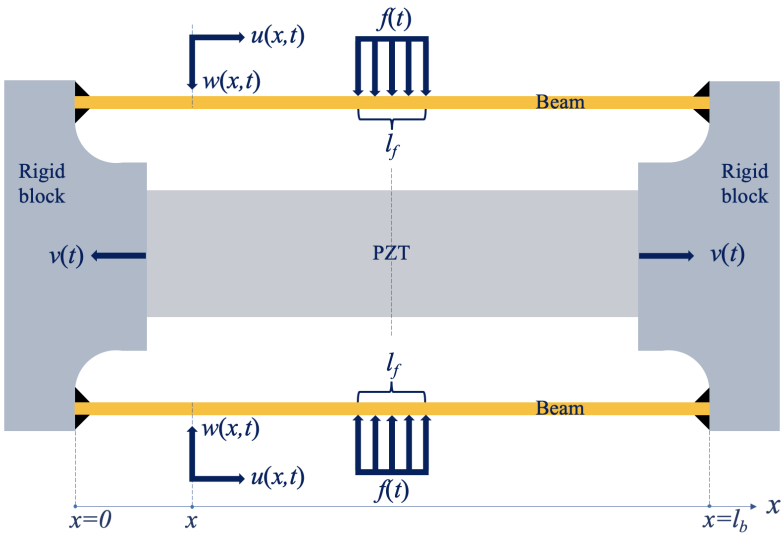

Figure 4.1: The force amplification mechanism with PZT rod for PEHU.

Under the assumption that the vertical center line is fixed for no translation motion, the two ends of PZT rod share the same displacement $v(t)$ but opposite direction. $P(t)$ denotes the resultant force acting at the ends of rod. The equations of motion are simplified as following.

$$\rho_b A_b \frac{\partial^2 u(x,t)}{\partial t^2} - E_b A_b \left(\frac{\partial^2 u(x,t)}{\partial x^2} + \frac{\partial w(x,t)}{\partial x} \frac{\partial^2 w\,(x,t)}{\partial x^2} \right) = 0 \tag{4.1}$$

$$\begin{aligned} &\rho_b A_b \frac{\partial^2 w(x,t)}{\partial t^2} + E_b I_b \frac{\partial^4 w(x,t)}{\partial x^4} \\ &- E_b A_b \left[\frac{\partial^2 u(x,t)}{\partial x^2} \frac{\partial w(x,t)}{\partial x} + \frac{\partial u\,(x,t)}{\partial x} \frac{\partial^2 w(x,t)}{\partial x^2} + \frac{3}{2} \left(\frac{\partial w(x,t)}{\partial x} \right)^2 \frac{\partial^2 w(x,t)}{\partial x^2} \right] \\ &= f(t) \left[H\left(x - \frac{l_b}{2} + \frac{l_f}{2} \right) - H\left(x - \frac{l_b}{2} - \frac{l_f}{2} \right) \right] \end{aligned} \tag{4.2}$$

$$E_b A_b \left[\frac{\partial u\left(0,t\right)}{\partial x} + \frac{1}{2}\left(\frac{\partial w\left(0,t\right)}{\partial x} \right)^2 \right] = \frac{1}{2} P(t) \tag{4.3}$$

$$E_b A_b \left[\frac{\partial u\left(l_b,t\right)}{\partial x} + \frac{1}{2}\left(\frac{\partial w\left(l_b,t\right)}{\partial x} \right)^2 \right] = \frac{1}{2} P(t) \tag{4.4}$$

$$u\left(l_b,t\right) = v(t) \tag{4.5}$$

$$u\left(0,t\right) = -v(t) \tag{4.6}$$

$$E_r A_r \frac{2v(t)}{l_r} = -P(t) \tag{4.7}$$

Since $u(x,t)$ is supposed to be much smaller than $w(x,t)$, we can omit the longitudinal inertia force term in Eq. (4.1) and integrate it from 0 to l_b, then combine with Eqs. (4.5)-(4.7), we will have equations for $w(x,t)$.

$$\begin{aligned} &\rho_b A_b \frac{\partial^2 w(x,t)}{\partial t^2} + E_b I_b \frac{\partial^4 w(x,t)}{\partial x^4} \\ &- \frac{E_b A_b}{l_b}\left[-\frac{E_b A_b}{l_b} \Big/ \left(\frac{2E_b A_b}{l_b} + \frac{E_r A_r}{l_r} \right) + \frac{1}{2} \right] \int_0^{l_b} \left(\frac{\partial w\left(x,t\right)}{\partial x} \right)^2 dx \cdot \frac{\partial^2 w\left(x,t\right)}{\partial x^2} \\ &= f(t)\left[H\left(x - \frac{l_b}{2} + \frac{l_f}{2} \right) - H\left(x - \frac{l_b}{2} - \frac{l_f}{2} \right) \right] \end{aligned} \tag{4.8}$$

$P(t)$ and $v(t)$ can be solved afterward by following equations.

$$P(t) = \frac{2E_b A_b}{l_b}\left[2v(t) + \frac{1}{2}\int_0^{l_b} \left(\frac{\partial w\left(x,t\right)}{\partial x} \right)^2 dx \right] \tag{4.9}$$

$$v(t) = \left[\frac{2E_b A_b}{l_b} \Big/ \left(\frac{4E_b A_b}{l_b} + \frac{2E_r A_r}{l_r} \right) \right] \int_0^{l_b} \left(\frac{\partial w(x,t)}{\partial x} \right)^2 dx \tag{4.10}$$

Once the stress and strain are obtained, the generated voltage and electric energy can be evaluated using linear piezoelectric effect based on PZT working mode and its corresponding piezoelectric constant.

The similar procedure introduced in Chapter 3 is effective to this simplified problem. By using Galerkin's weighted residual method with mode functions as weight functions, Eq. 4.8 can be approximated by ODEs in mode coordinates.

$$M\ddot{c} + F = R \tag{4.11}$$

$$M_{ji} = \begin{cases} \rho_b A_b l_b g_j, & j = i \\ 0, & j \neq i \end{cases} \ , \ j, i = 1, 2, ..., n \tag{4.12}$$

$$F = \underbrace{a \cdot S \cdot c}_{linear} + \underbrace{b \cdot c^T \cdot D \cdot c \cdot Z \cdot c}_{nonlinear} \tag{4.13}$$

$$R = H_f . f(t) \tag{4.14}$$

$$c = \{c_1(t), c_2(t), ..., c_n(t)\}^T \tag{4.15}$$

$$g_j = \int_0^1 w_{yj}^2 dy \ , \ j = 1, 2, ..., n \tag{4.16}$$

$$a = E_b A_b / l_b^3 \tag{4.17}$$

$$b = 2\frac{E_b^2 A_b^2}{l_b^4} \Big/ \left(\frac{4E_b A_b}{l_b} + 2\frac{E_r A_r}{l_r} \right) - \frac{E_b A_b}{2l_b^3} \tag{4.18}$$

$$S_{ji} = \int_0^1 \frac{d^4 w_{yi}}{dy^4} w_{yj} dy \ , \ j, i = 1, 2, ..., n \tag{4.19}$$

$$D_{rk} = \int_0^1 \frac{dw_{yr}}{dy} \frac{dw_{yk}}{dy} dy \ , \ r, k = 1, 2, ..., n \tag{4.20}$$

$$Z_{ji} = \int_0^1 \frac{d^2 w_{yi}}{dy^2} w_{yj} dy \ , \ j, i = 1, 2, ..., n \tag{4.21}$$

$$H_{fj} = \int_0^{l_b} \left[H\left(x - \frac{l_b}{2} + \frac{l_f}{2} \right) - H\left(x - \frac{l_b}{2} - \frac{l_f}{2} \right) \right] w_j dx \ , \ j = 1, 2, ..., n \tag{4.22}$$

Omitting the inertia terms in Eqs. (4.1) and (4.2), the governing equations

in static case are as follows

$$E_b A_b \left(\frac{\partial^2 u(x)}{\partial x^2} + \frac{\partial w(x)}{\partial x} \frac{\partial^2 w\,(x)}{\partial x^2} \right) = 0 \tag{4.23}$$

$$E_b I_b \frac{\partial^4 w(x)}{\partial x^4} - E_b A_b \left[\frac{\partial^2 u(x)}{\partial x^2} \frac{\partial w(x)}{\partial x} + \frac{\partial u\,(x)}{\partial x} \frac{\partial^2 w(x)}{\partial x^2} + \frac{3}{2} \left(\frac{\partial w(x)}{\partial x} \right)^2 \frac{\partial^2 w(x)}{\partial x^2} \right] \tag{4.24}$$

$$= f(t) \left[H\left(x - \frac{l_b}{2} + \frac{l_f}{2} \right) - H\left(x - \frac{l_b}{2} - \frac{l_f}{2} \right) \right]$$

$$E_b A_b \left[\frac{\partial u\,(0)}{\partial x} + \frac{1}{2} \left(\frac{\partial w\,(0)}{\partial x} \right)^2 \right] = \frac{1}{2} P \tag{4.25}$$

$$E_b A_b \left[\frac{\partial u\,(l_b)}{\partial x} + \frac{1}{2} \left(\frac{\partial w\,(l_b)}{\partial x} \right)^2 \right] = \frac{1}{2} P \tag{4.26}$$

$$u\,(l_b) = v \tag{4.27}$$

$$u\,(0) = -v \tag{4.28}$$

$$E_r A_r \frac{2v}{l_r} = -P \tag{4.29}$$

Eq. (4.23) is equivalent to

$$\frac{\partial^2 u(x)}{\partial x^2} = -\frac{\partial w(x)}{\partial x} \frac{\partial^2 w(x)}{\partial x^2} \tag{4.30}$$

Integrate Eq. (4.23) from 0 to x, and substitute Eq. (4.25) and Eq. (4.26) in , we can obtain

$$\frac{\partial u(x)}{\partial x} + \frac{1}{2} \left(\frac{\partial w(x)}{\partial x} \right)^2 = \frac{P}{2 E_b A_b} \tag{4.31}$$

Integrating Eq. (4.31) from 0 to l_b, we have

$$u\left(l_b\right) - u\left(0\right) + \int_0^{l_b} \frac{1}{2} \left(\frac{\partial w(x)}{\partial x}\right)^2 dx = \frac{P l_b}{2 E_b A_b} \tag{4.32}$$

Substitute Eq. (4.27) and Eq. (4.28) into Eq. (4.32) , then replace P using Eq. (4.29), the equation to solve v is obtained as

$$v = -\frac{E_b A_b l_r}{4 E_b A_b l_r + 2 E_r A_r l_b} \int_0^{l_b} \left(\frac{\partial w(x)}{\partial x}\right)^2 dx \tag{4.33}$$

Based on Eq. (4.29), we know P can be solved using

$$P = \frac{E_b A_b E_r A_r}{2 E_b A_b l_r + E_r A_r l_b} \int_0^{l_b} \left(\frac{\partial w(x)}{\partial x}\right)^2 dx \tag{4.34}$$

To eliminate $u(x)$ from Eq. (4.24) without involving P, substitute Eq. (4.30) and Eq. (4.34) into Eq. (4.24), we obtain the nonlinear ODE for $w(x)$

$$\begin{aligned} &E_b I_b \frac{\partial^4 w(x)}{\partial x^4} - \left[\frac{E_b A_b E_r A_r}{4 E_b A_b l_r + 2 E_r A_r l_b} \int_0^{l_b} \left(\frac{\partial w(x)}{\partial x}\right)^2 dx\right] \frac{\partial^2 w(x)}{\partial x^2} \\ &= f(t) \left[H\left(x - \frac{l_b}{2} + \frac{l_f}{2}\right) - H\left(x - \frac{l_b}{2} - \frac{l_f}{2}\right)\right] \end{aligned} \tag{4.35}$$

Now the mode expansion and weighted residual method explained in dynamics analysis can be applied to Eq. (4.35). The coefficient c_i in mode expansion are constants here as we are working on the static case, where the first mode alone could be accurate enough. Therefore, the computation cost is significantly reduced in search for the optimal design parameters.

$$w(x) = c_1 w_1(x) \tag{4.36}$$

$$w(y) = c_1 w_{y1}(y) \tag{4.37}$$

where $w_1(x)$ and $w_{y1}(y)$ are the first mode as defined in Eq. (3.13) and Eq. (3.14) individually.

By using Galerkin's weighted residual method with mode functions as weighting functions,

$$\int_0^{l_b} R(x) w_1(x) dx = 0 \tag{4.38}$$

We obtain the algebraic equation of up to 3^{rd} order of c_1

$$p c_1^3 + q c_1 - f(t) H_{f1} = 0 \tag{4.39}$$

where

$$p = -\frac{E_b A_b E_r A_r}{4 E_b A_b l_r + 2 E_r A_r l_b} \frac{D_{11} Z_{11}}{l_b^2}, q = \frac{E_b I_b S_{11}}{l_b^3} \tag{4.40}$$

The above 3^{rd} order polynomial of c_1 will have a pair of conjugate complex roots and a real root. The latter will be the solution of c_1. It can be used to calculate v and p by Eqs. (4.41) and (4.42) respectively.

$$v = -\frac{E_b A_b l_r}{4 E_b A_b l_r + 2 E_r A_r l_b} \frac{D_{11} c_1^2}{l_b} \tag{4.41}$$

$$P = \frac{E_b A_b E_r A_r}{2 E_b A_b l_r + E_r A_r l_b} \frac{D_{11} c_1^2}{l_b} \tag{4.42}$$

4.2 Multi-Objective Optimal Design

4.2.1 Parameters of PEHS

A typical implementation of the PEHS on the road is shown in Fig. 4.2. The energy source is the mechanical work done by the gravity of the vehicles passing

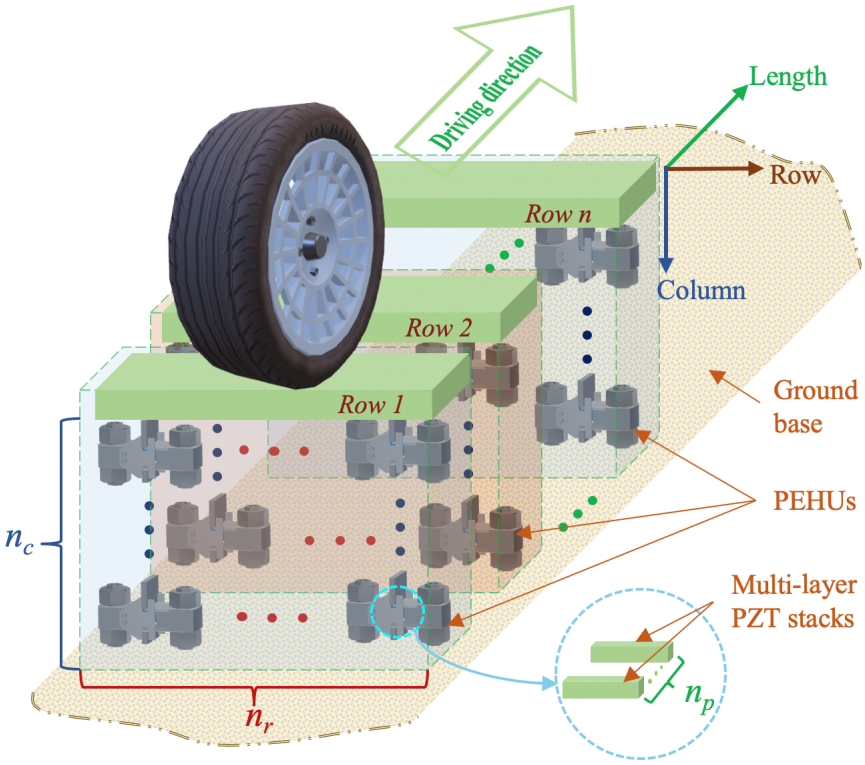

Figure 4.2: A conceptual implementation of the PEHS under the pavement.

over the PEHUs. The PEHS is designed to convert as much the mechanical energy to electricity as possible and have as small an interruption to the traffic as possible. We should point out that the focus of this chapter is on the design analysis and laboratory validation of the proposed PEHU. Figure 4.2 clearly suggests that there must be a need for special design of the road in order to implement the proposed PEHS. How to assemble many PEHUs to form a PEHS and how to implement the PEHS on the road in large scale will be discussed in Chapters 5 and 6.

There are many parameters influencing the electric energy harvested at the system level. In Figure 4.2, the effects of the parameters such as the number n_r of

columns of the PEHUs in one row to share the load of the vehicle, and the number n_c of the PEHUs stacked up in each column and the total sinking displacement of a row d_{sk} will be investigated in a separate paper where the road test results are reported.

Another design variable is the number of the PZT stacks n_p in one PEHU. Because we have to design the PEHU based on the commercially available products, the design freedom is limited. Based on the product we purchased, we have chosen $n_p = 3$. Three PZT stacks are used in each PEHU and are connected in parallel both mechanically and electrically.

In this Chapter, we focus on the frame structural design. The parameters including beam thickness, length, width and material can be used to obtain optimal designs in order to meet different objectives. Within the practical ranges of all these parameters, we have found through extensive numerical simulations that the first order resonant frequency of the integrated mechanical-piezoelectric system is in the order of hundreds Hz, which is much greater than the frequency of the traffic-induced pulse forces which is in the order of Hz. This allows us to conduct the design based on the static analysis. Because the maximum stress in the elastic beams can be higher than the yield strength of typical structural steel, we have used Grade 5 Titanium alloy as the material for the beam.

The solution of the static response of the PEHU is obtained by using a single mode expansion for the nonlinear beams and an equivalent rod for the multi-layer PZT stack generator. The voltage of the PEHU is evaluated by decoupling the piezoelectric effect of the PZT material, because the stress and deformation generated by the internal electric field of the PZT material are much smaller than the mechanical loading. The equivalent cross section area of the PZT stacks is

$A_r = n_p A_p$, and the capacitance is $C_U = n_p C_p = n_p(n-1)\frac{\varepsilon^T A_p}{l_p}$. The stress in the equivalent PZT stack due to the internal mechanical loading P can be evaluated as

$$\sigma_r = \frac{P}{A_r} = \frac{P}{n_p A_p} \tag{4.43}$$

The voltage of the PEHU V_U will be equal to that of each PZT stack.

$$V_U = \frac{e_{33} P l_p}{n_p E_p \varepsilon^T A_p} \tag{4.44}$$

The force amplification factor α_f and the energy gain factor α_e are defined as

$$\alpha_f = \frac{P}{P_{in}},\ \alpha_e = \frac{E_U}{E_0} \tag{4.45}$$

where P_{in} is the equivalent concentrated force acting on the beams, E_U is the electric energy generated by one PEHU, E_0 is the electric energy generated when the same force P_{in} directly acts on the PZT stacks without the force amplification mechanism.

$$E_U = \frac{1}{2} C_U V_U^2 = \frac{1}{2} n_p C_p \left(\frac{e_{33} P l_p}{n_p E_p \varepsilon^T A_p} \right)^2 \tag{4.46}$$

$$E_0 = \frac{1}{2} C_U V_0^2 = \frac{1}{2} n_p C_p \left(\frac{e_{33} P_{in} l_p}{n_p E_p \varepsilon^T A_p} \right)^2 \tag{4.47}$$

It is interesting to point out that the two factors are related by

$$\alpha_e = \alpha_f^2 \tag{4.48}$$

This result indicates the importance of the force amplification mechanism.

4.2.2 MOD Problem Statement

The multi-objective optimal design problem to minimize the sinking displacement d_{sk} and maximize the electric energy E_U of a PEHU can be stated as follows:

$$\min_{\mathbf{k}} (d_{sk}, -E_U) \tag{4.49}$$

where $\mathbf{k} = \{l_b, b_b, h_b, n_p, n_r\} \in Q$ and Q is the union of the following sets of the design parameters.

$$\begin{aligned} &\{32.4 \leq l_b \leq 100\}, \quad \{21 \leq b_b \leq 70\} \\ &\{h_b \subset \{0.4064, 0.8128, 1.6002, 3.175\}\} \\ &\{n_p, n_r = 3\}, \quad \{d_{sk} \leq 4\} \\ &\{\max\{\sigma_r(x)\} \leq 100MPa\}, \quad \{\max\{\sigma_b(x,z)\} \leq \sigma_{yield} FoS\} \end{aligned} \tag{4.50}$$

where $\max(\sigma_b(x,z))$ denotes the maximum stress of the beam, σ_{yield} is the yield strength of the material of the beam, and FoS is the factor of safety. The maximum of the normal stress of the beam consists of a stretching term and a bending term given by

$$\max(\sigma_b(x,z)) = \underbrace{\frac{P}{2A_b}}_{stretching} + \underbrace{\frac{c_1 h_b}{2} max \left| \frac{\partial^2 w_1(x)}{\partial x^2} \right|}_{bending} \tag{4.51}$$

It should be noted that in this paper, we have chosen $n_r = n_p = 3$. To develop the optimal system design, these two parameters can vary. The set Q contains some practical constraints the strength of the Titanium sheets and the resulting range of the feasible strength of the beams, the limit of the stress in the PZT stacks, the tire width and driving comfort. Besides these constraints, other considerations must

be taken into account when choosing the design parameters including the cost and the space underneath the pavement. The values of some known parameters for the PEHU are listed in Table 4.1.

Table 4.1: Some known parameters for the PEHU design.

Parameters	Values	Units
G_{car}	16000	N
l_f	8	mm
A_p	21	mm^2
E_r	106	GPa
E_b	110	GPa
e_{33}	16.9	C/m^2
ε^T	$1880\varepsilon_0$	F/m
ε_0	8.854×10^{-12}	F/m

4.2.3 Particle Swarm Optimization

To determine the key parameters of PEHU in terms of the dimensions of beam, the multi-objective particle swarm optimization method was employed to find the pareto optimal. The static analysis of PEHU explained in previous section was used to evaluate the performance of feasible designs in the search space.

The available thickness of Titanium sheet from market is discontinuous and has only a few options in our interested range. No machining of thickness was preferred because it can minimize the waste of material which is very expensive and save the cost of manufacturing. Therefore, the thickness of beam is designed to be the same as commercial available sizes. The optimal front in each thickness case were explored by multi-objective particle swarm optimization (MOPSO) with length (l_b) and width (b_b) of beam as design variables.

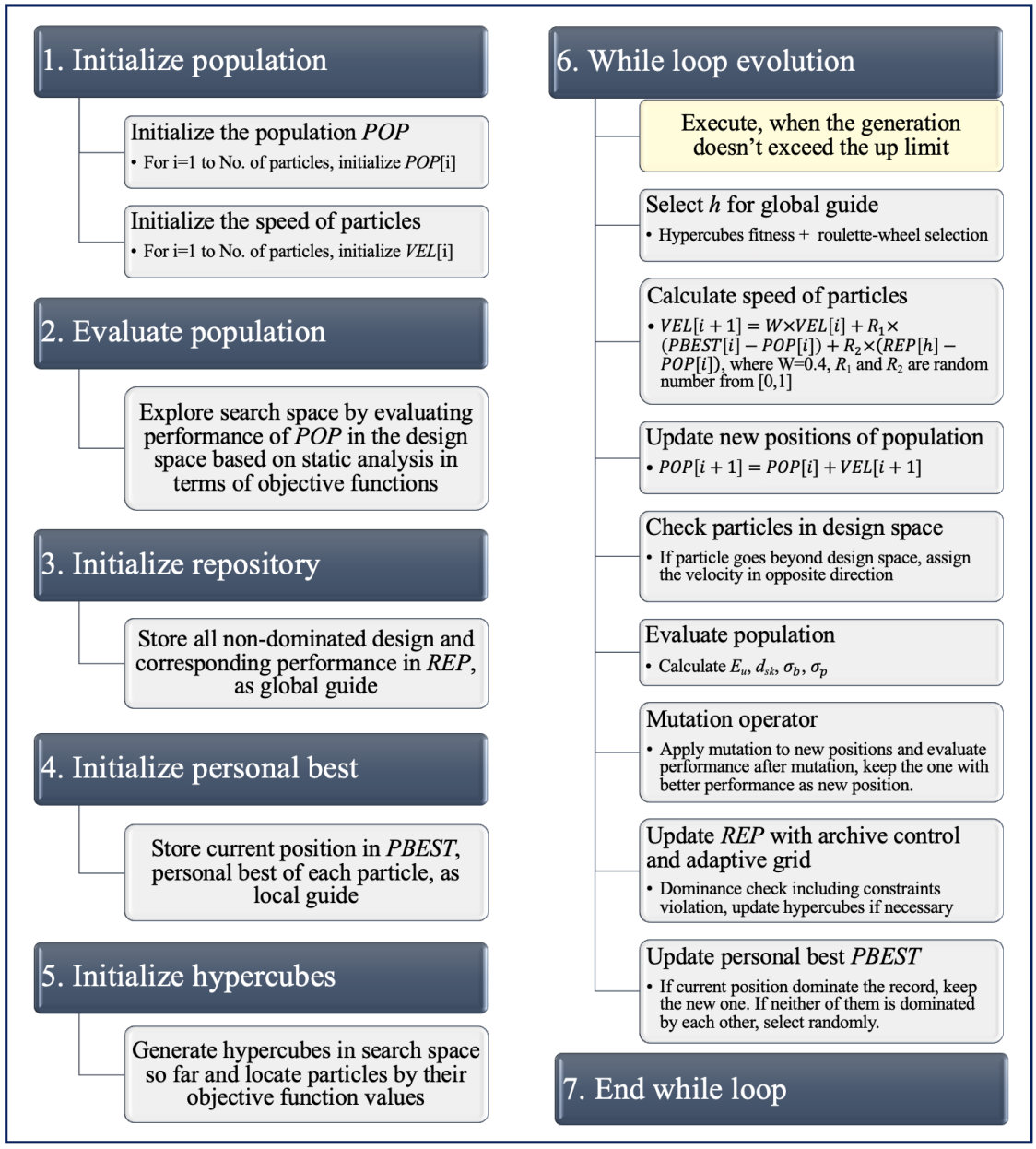

Figure 4.3: The main algorithm of Multi-objective particle swarm optimization method for PEHU design.

The main algorithm of MOPSO method is illustrated in Fig. 4.3. First, population of n_{pop} particles was randomly generated in the 2D design space with zero initial velocity. Second, the static performance of each particle was evaluated using static analysis method explained in previous chapter. The electric energy E_u and sinking displacement d_{sk} are the objective functions. The maximum stress in beam (σ_b) and PZT (σ_p) are necessary for constraint violation check. Then, the initialization of external repository where stores all non-dominated design and corresponding performance will be executed. The handling of constraints was integrated into the dominance check in the following way.

Given two positions in search space $P_1 = \{E_{u1}, d_{sk1}, n_{cv1}\}^T$ and $P_2 = \{E_{u2}, d_{sk2}, n_{cv2}\}^T$, where n_{cv} is the number of constraints that it violates, with a value from 0 up to 3. $n_{cv} = 0$ means it satisfies all the constraints, therefore, is feasible. When check their dominance, n_{cv} always comes first. If one is feasible, the other is infeasible, the feasible dominates. Such as $n_{cv1} = 0$ and $n_{cv2} \neq 0$, then P_1 is the winner no matter what objective function values they have. If both are not feasible ($n_{cv1} \neq 0$ and $n_{cv2} \neq 0$), the one with less constraints violation dominates. If they are both feasible, dominance is determined as definition based on E_u and d_{sk}.

After the evaluation of all particles in the first generation, hypercubes in the search space should be initialized. In our case with two design variables, it generates a 2D grid. Particles are located by their objective function values. The grid will be employed to select global guidance and control the archive. Meanwhile, information of all particles will be stored in *PBEST*, which is used to keep a record of individual best in the whole search history.

The evolution of population consisting of n_{pop} particles is carried out in a while loop, which is controlled by the maximum number of generation Gen_{max}. In

each generation , a parameter h is determined first for the calculation of velocity by applying hypercubes fitness with fitness control parameter x_{fit} and afterwards randomly chosen based on roulette wheel selection. h is essentially used to select a global guidance from the elite archive, meanwhile, the personal best of particles $PBEST$ serves as the local guidance. The velocity can be evaluated by Eq. (4.52).

$$VEL[i+1] = W \cdot VEL[i] + R_1 \cdot (PBEST[i] - POP[i]) + R_2 \cdot (REP[h] - POP[i]) \quad (4.52)$$

where $W = 0.4$, R_1 and R_2 are random numbers uniformly distributed in $[0, 1]$.

Then, candidates of new positions are evaluated based on velocity,

$$POP[i+1] = POP[i] + VEL[i+1] \quad (4.53)$$

Two extra tasks need to be done to determine new positions. First, check particles are still in design space or not. If a particle goes beyond the design space, opposite direction search can be effective by assigning velocity with minus sign. Second, mutation operator with parameter r_{mu} will be applied to increase search diversity. If it generates better performance, mutation will be accepted, otherwise, the position before mutation will be accepted.

For each new position, its performance based on static analysis is the basis for external archive. It will be compared with all the record in archive so as to decide the necessary change to update REP. This process involves archive control and adaptive grid. In addition, the new positions will be used to update $PBEST$ based on dominance check.

Table 4.2 lists the parameters adopted in MOPSO algorithm. Within only 10 generations, convergence was obtained. Pareto set and pareto front in four cases

corresponding to different thickness are showed in Figs. 4.4-4.7, where design parameters accord with their performance in color.

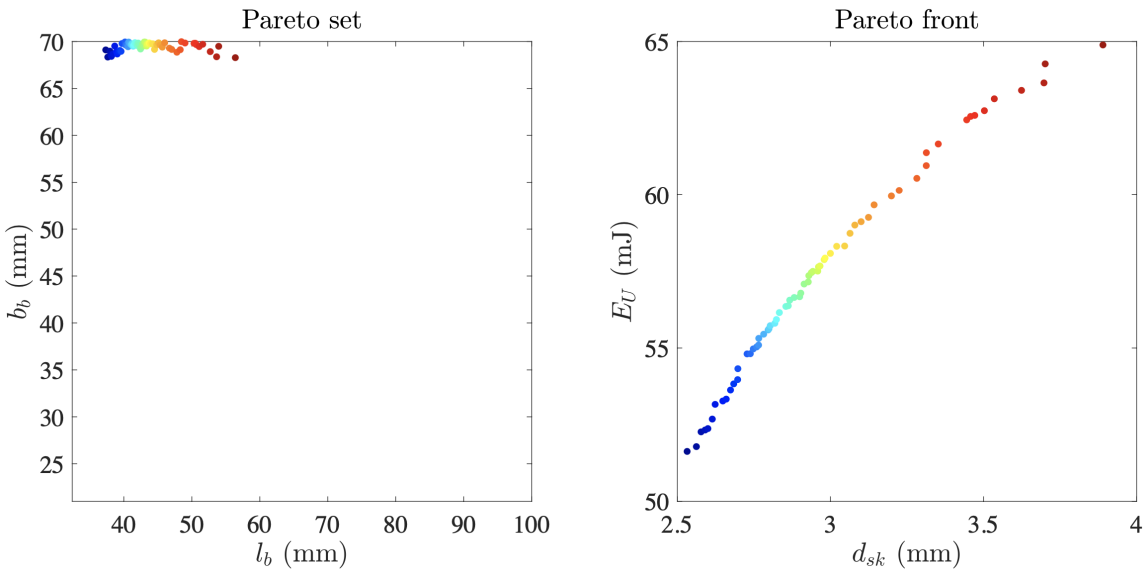

Figure 4.4: The Pareto set and front of PEHU by multi-objective particle swarm optimization when $h_b = 0.4064mm$.

With $h_b = 0.4064mm$, the optimal design sets are concentrated in the region of $\{67mm \leq b_b \leq 70mm, 40mm \leq b_b \leq 60mm\}$, as shown in Fig. 4.4. The result implies only wide beam survived in this case due to constraints. With the width b_b close to $70mm$, longer beam is preferable for high energy density. As the length l_b increases from $36mm$ to $58mm$, electric energy was increased from $52mJ$ to $65mJ$. However, the increased sinking displacement restricts the maximum generated energy.

Similar pattern can be observed in the case of $h_b = 0.8128mm$, as shown in Fig. 4.5. The region of optimal set is expanded to longer beam up to $l_b = 70mm$. With width in the small range of $[65mm, 70mm]$, the positive effect of l_b on power

Table 4.2: Parameters in MOPSO algorithm.

Parameters	Values	Meaning
n_{pop}	100	Number of particles
Gen_{max}	10	Maximum generations
n_{rep}	100	Size of external archive
n_{grid}	40	Number of subdivisions in grid
x_{fit}	10	Fitness control parameter
W	0.4	Initial weight of velocity
r_{mu}	0.5	Mutation rate
SoF	1.03	Safety factor
σ_{yield}	827.37 MPa	Yield stress of Titanium alloy
σ_{PZT}	100 MPa	Allowed stress in PZT

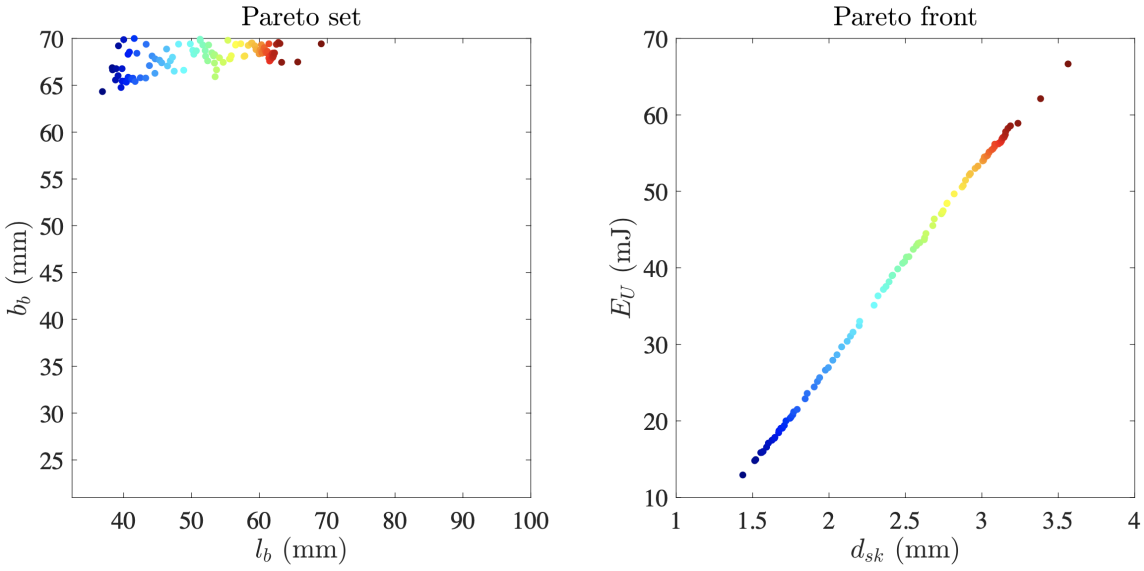

Figure 4.5: The Pareto set and front of PEHU by multi-objective particle swarm optimization when $h_b = 0.8128mm$.

generation was observed as well. As the length l_b increases from $40mm$ to $70mm$, electric energy was increased from $12mJ$ to $68mJ$, while displacement d_{sk} increased from $1.4mm$ to $3.5mm$.

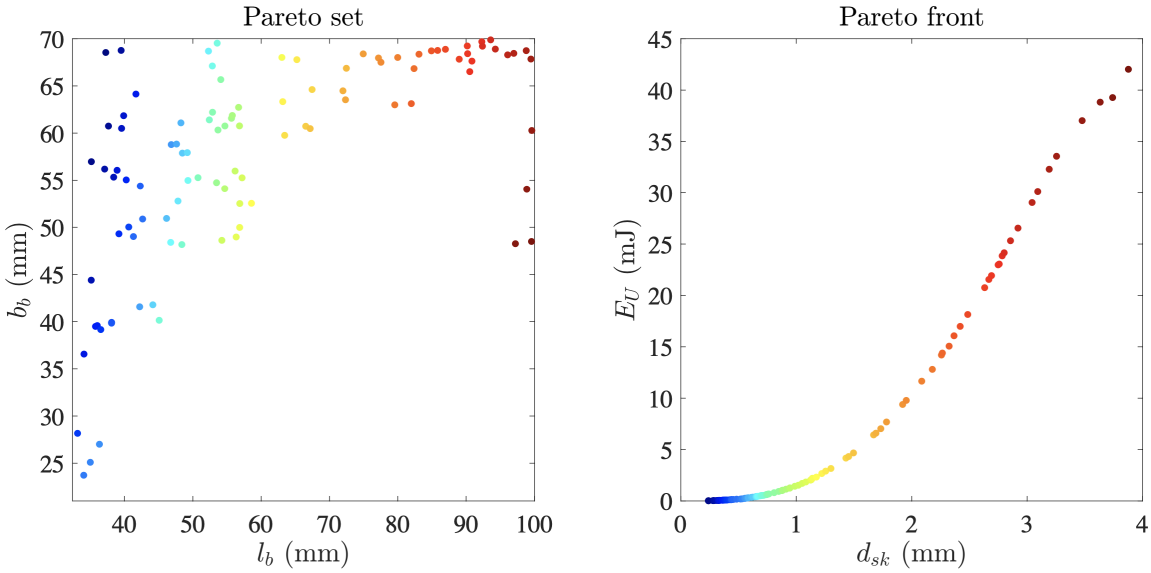

Figure 4.6: The Pareto set and front of PEHU by multi-objective particle swarm optimization when $h_b = 1.6002mm$.

As beam becomes as thick as $1.6002mm$, both bending and axial stiffness are improved significantly. The optimal design sets expend to a larger region, as shown in Fig. 4.6. However, the maximum electric energy was decreased to $43mJ$, and the desired beam length increased to $100mm$. The degraded performance became even worse when beam has a thickness of $3.175mm$, as shown in Fig. 4.7. Although optimal design sets distribute in a big part of the design space, they barely generate electricity. Beam with this thickness has a high bending stiffness with respect to interested loading. The coupling of bending and stretching is too weak to amplify the compression on PZT. The force amplification factor was too small to harvest

energy.

4.2.4 Discretized Searching

To understand the distribution of feasible designs and their performance as well as to validate the pareto front of MOPSO, the discretized searching in the whole design space was conducted. For each thickness, the domains of l_b and b_b were evenly divided into 50 and 30 segments, respectively. For each case with a specific thickness, the distribution of E_U and d_{sk} of the feasible design will be illustrated. Additionally, the feasible design and corresponding performance will be presented to validate the MOPSO results.

For beams with thickness of $0.4064mm$, the feasible sampled design sets are distributed in the region of $\{47mm \leq b_b \leq 70mm, 38mm \leq b_b \leq 58mm\}$, approximately. Fig. 4.8 and 4.9 show the E_U and d_{sk} of feasible designs, from which, we can conclude that wide beam is beneficial to more electric energy and less displacement for a given length. Additionally, long beam is able to generate more energy than short beam for a given width. Based on sampled positions, the feasible candidates in design space and their performance in search space is illustrated in Fig. 4.10, which reflects the feasible region in the design space and search space. The results of MOSPO in Fig. 4.4 matches well with the feasible region. The wide beams dominate the design space, and the pareto front is the upside boundary of the feasible region in search space. These patterns found in the case of $h_b = 0.4064mm$ also exist in other three cases for thicker beams.

As h_b increases from $0.4064mm$ to $3.175mm$, the feasible region in design space extends gradually until the whole space is filled, as shown in Figs. 4.9, 4.12, 4.15, and 4.18. Thin beams with thickness of $0.4064mm$ or $0,8128mm$ exhibit

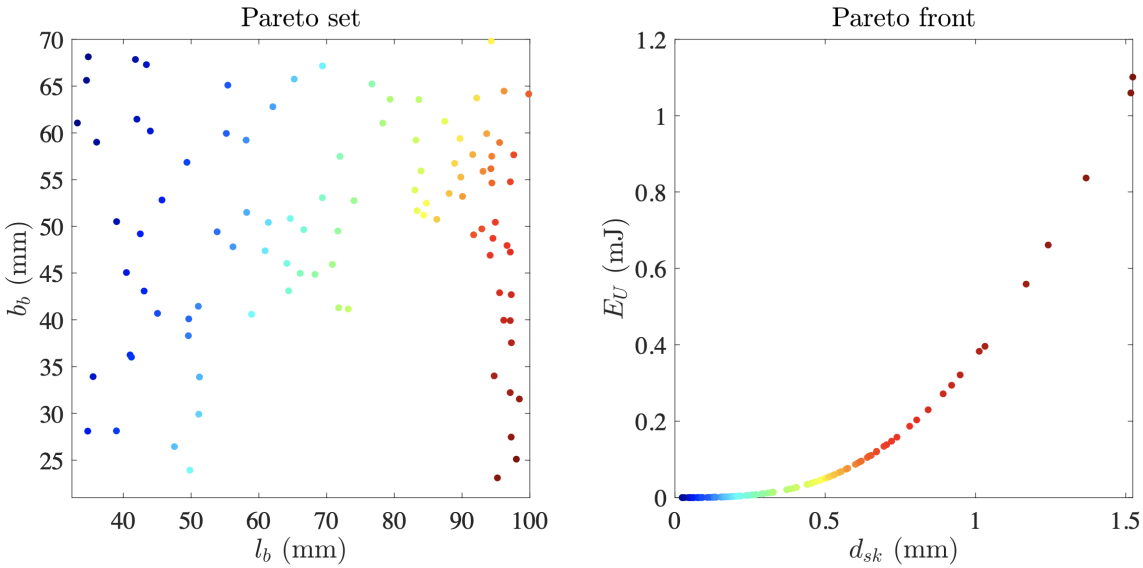

Figure 4.7: The Pareto set and front of PEHU by multi-objective particle swarm optimization when $h_b = 3.175mm$.

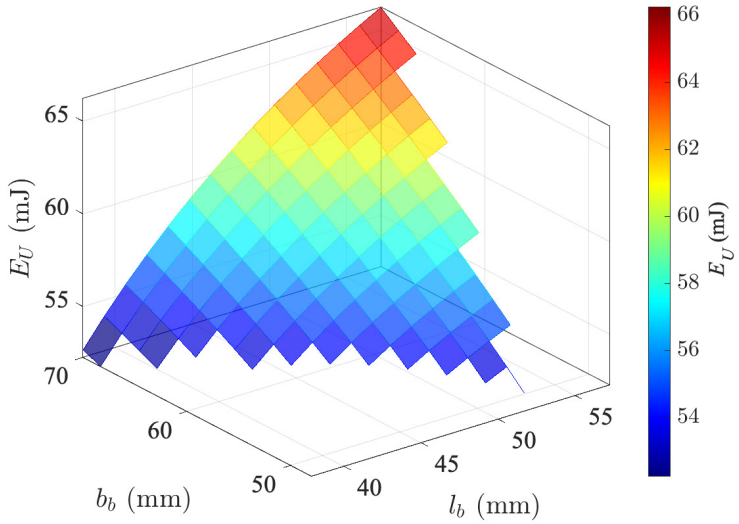

Figure 4.8: The electric energy E_U of feasible candidates in design space when $h_b = 0.4064mm$.

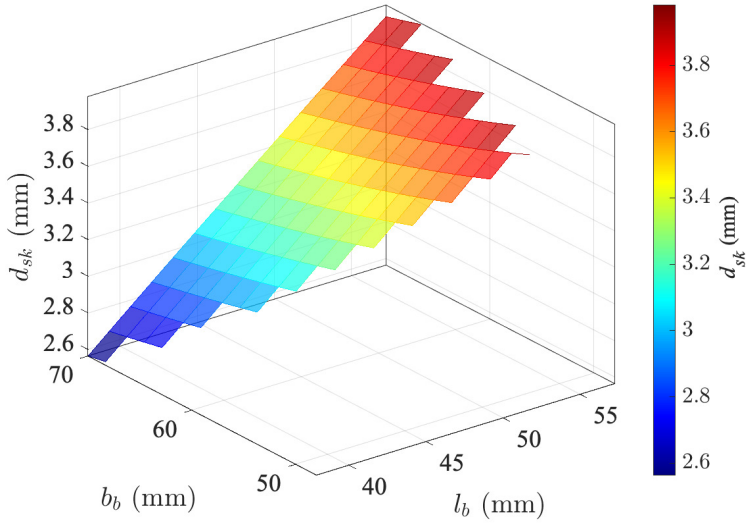

Figure 4.9: The sinking displacement d_{sk} of feasible candidates in design space when $h_b = 0.4064mm$.

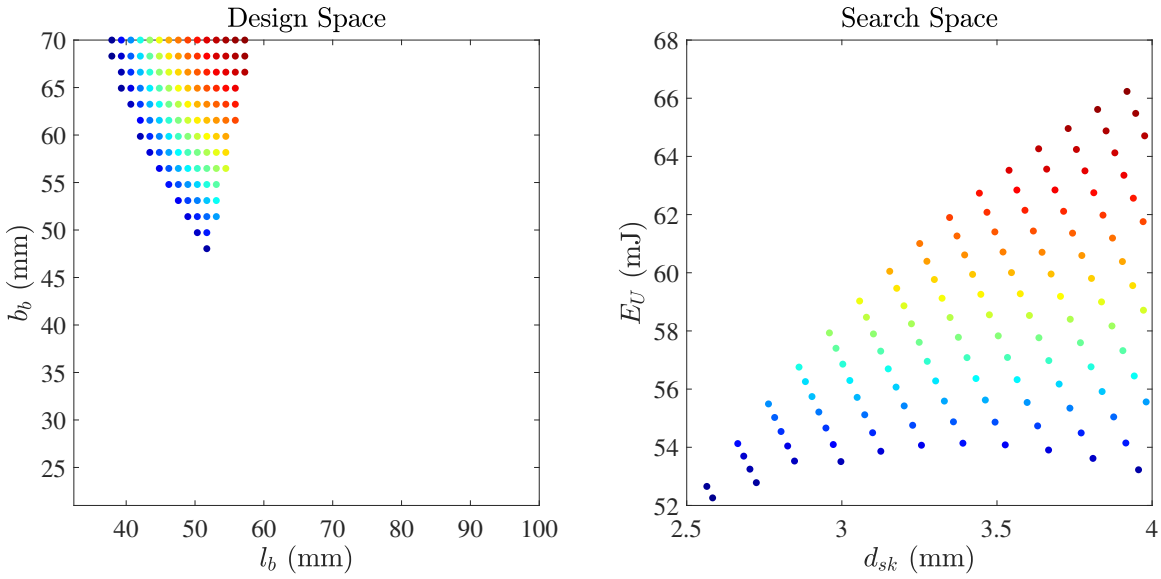

Figure 4.10: The feasible candidates in design space and their performance in search space when $h_b = 0.4064mm$.

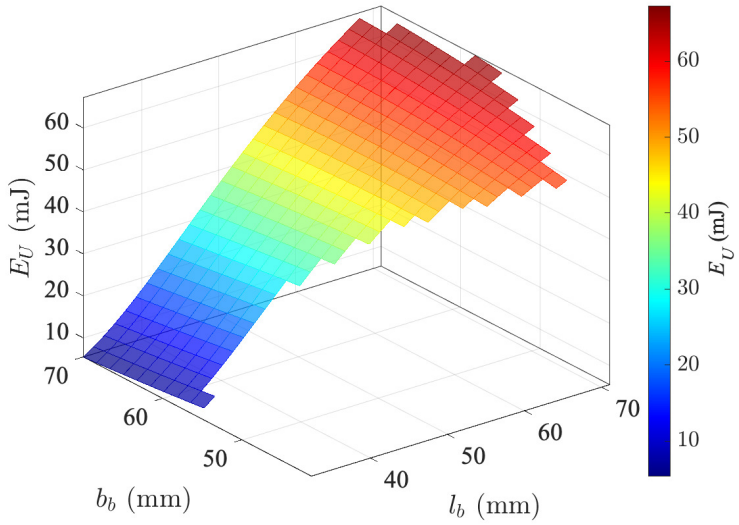

Figure 4.11: The electric energy E_U of feasible candidates in design space when $h_b = 0.8128mm$.

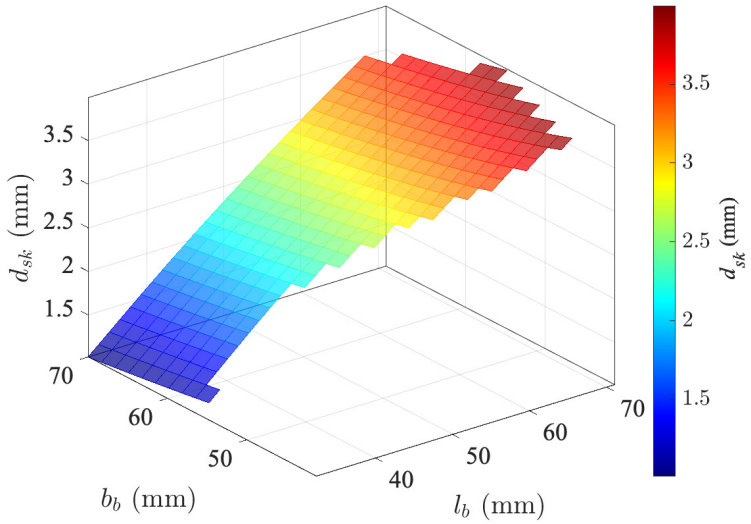

Figure 4.12: The sinking displacement d_{sk} of feasible candidates in design space when $h_b = 0.8128mm$.

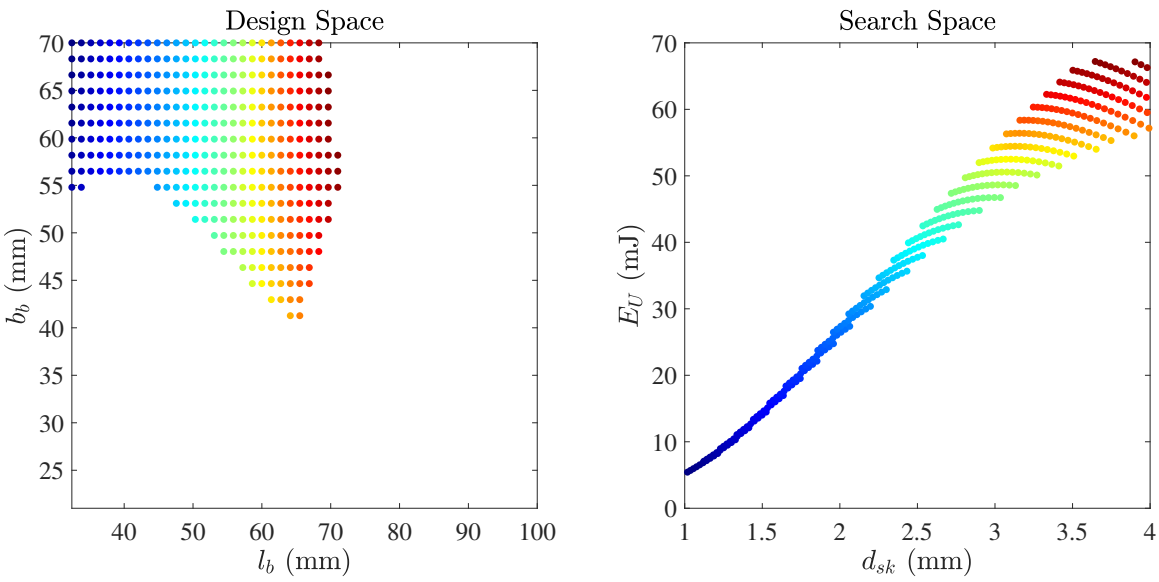

Figure 4.13: The feasible candidates in design space and their performance in search space when $h_b = 0.8128mm$.

potential for higher energy density than thicker beams. The maximum E_U reached $\sim 66mJ$ and $\sim 68mJ$, respectively, as shown in Figs. 4.8 and 4.11. In contrast, it decreases to $\sim 44mJ$ when $h_b = 1.6002mm$, as shown in Fig. 4.14. In the case of $h_b = 3.175mm$, beams can hardly generate electric energy, as shown in Fig. 4.17.

The feasible designs and their performance are illustrated in Figs. 4.10, 4.13, 4.16, and 4.19 for different beam thickness. By comparing them with the results of MOPSO, correspondingly, Figs. 4.4, 4.5, 4.6, and 4.7, we can identify that the pareto fronts are a part of the up boundary of feasible regions. The results of MOPSO are validated by the discretized searching.

Many feasible and optimal designs have been found. Figs. 4.20 and 4.21 illustrate the distribution of harvested energy and sinking displacement of optimal designs in the search space. Further selection was based on consideration of

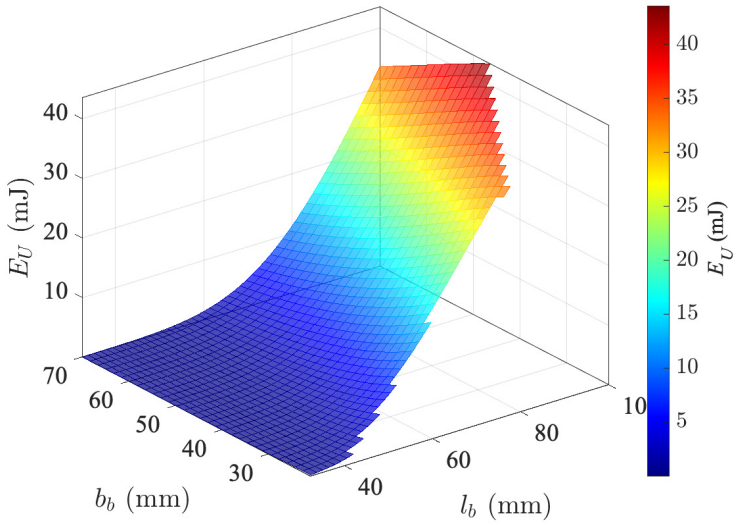

Figure 4.14: The electric energy E_U of feasible candidates in design space when $h_b = 1.6002mm$.

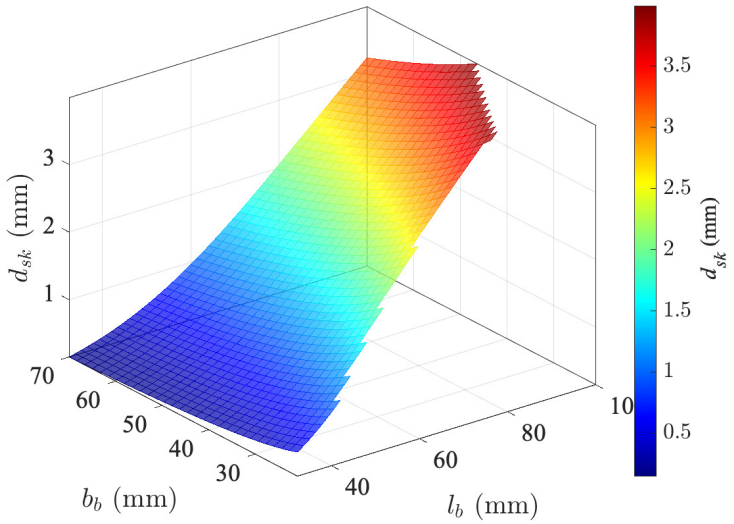

Figure 4.15: The sinking displacement d_{sk} of feasible candidates in design space when $h_b = 1.6002mm$.

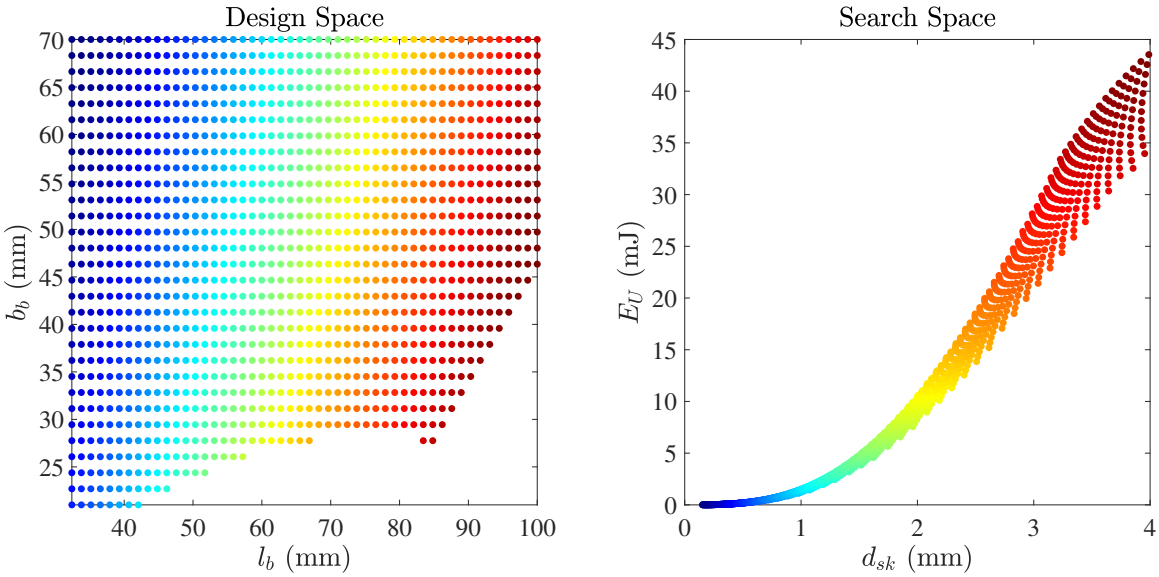

Figure 4.16: The feasible candidates in design space and their performance in search space when $h_b = 1.6002mm$.

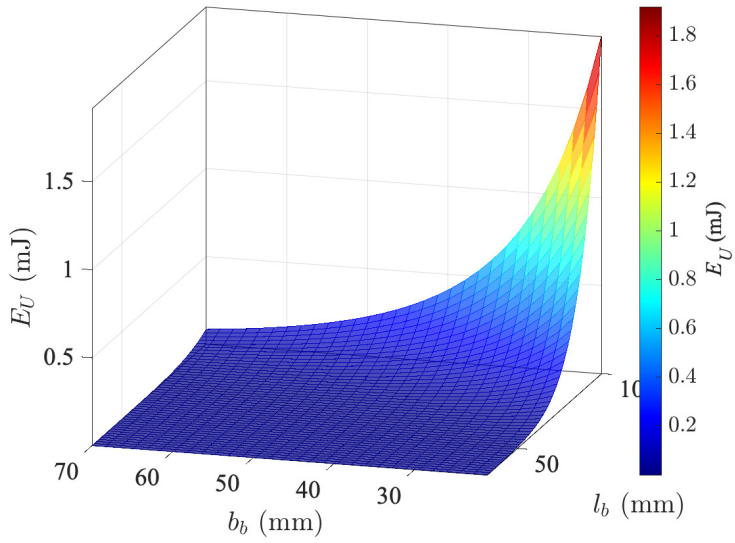

Figure 4.17: The electric energy E_U of feasible candidates in design space when $h_b = 3.175mm$.

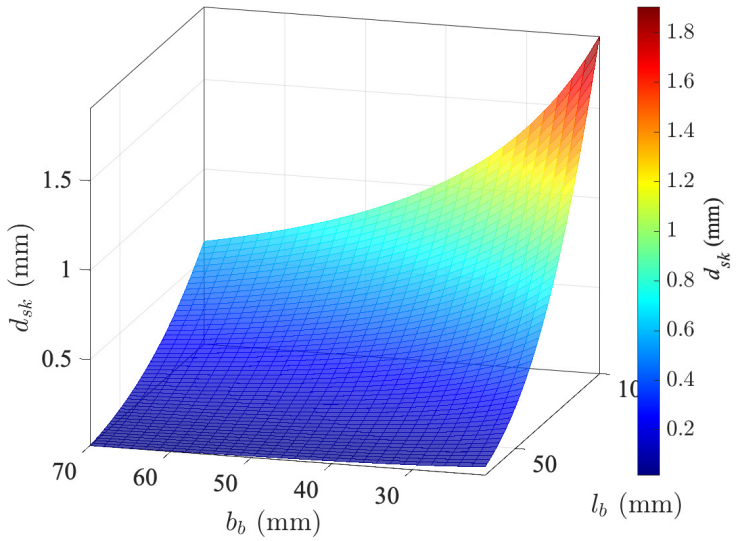

Figure 4.18: The sinking displacement d_{sk} of feasible candidates in design space when $h_b = 3.175mm$.

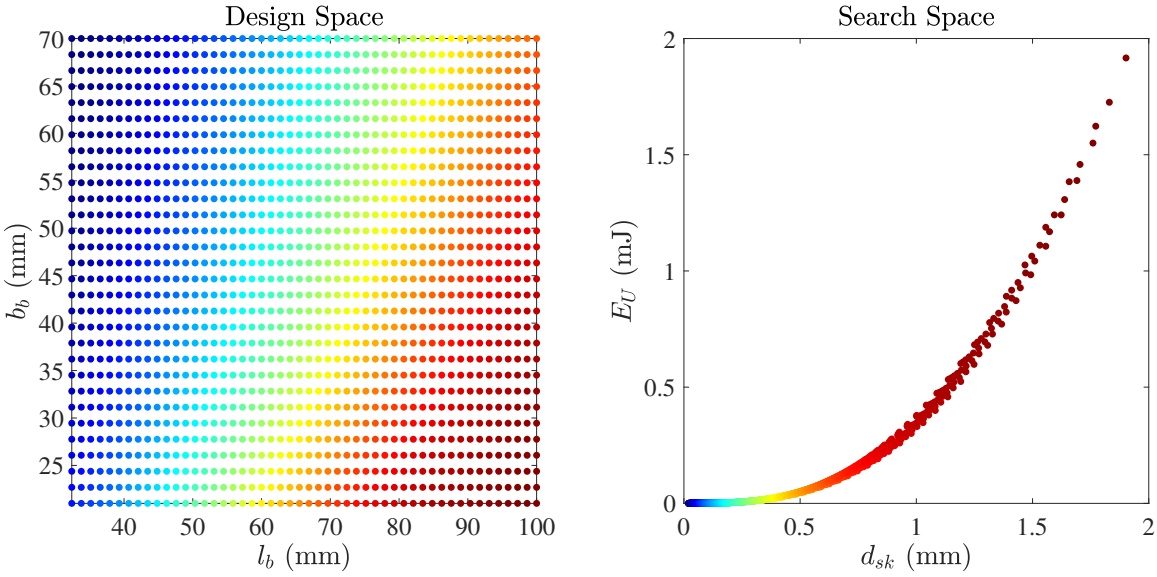

Figure 4.19: The feasible candidates in design space and their performance in search space when $h_b = 3.175mm$.

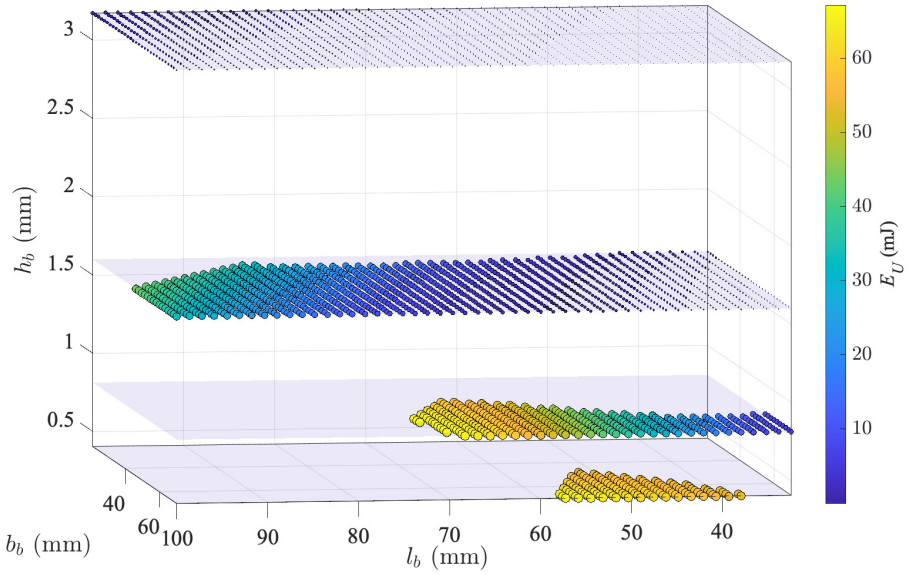

Figure 4.20: The electric energy E_U of sampled feasible candidates in design space.

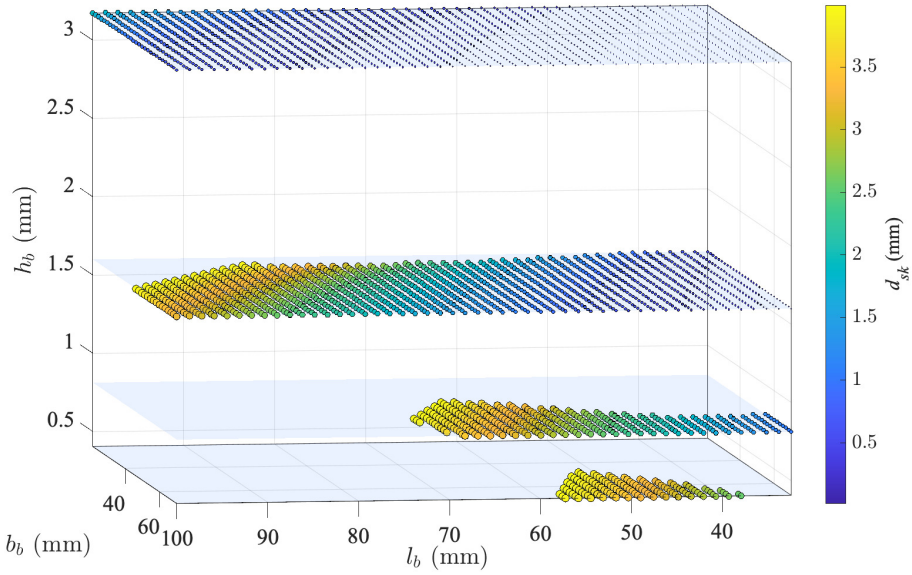

Figure 4.21: The sinking displacement d_{sk} of sampled feasible candidates in design space.

cylinder tube design of second-level assembly and maximum width of a row. In addition to that, narrow beams were preferred due to the difficulty of applying evenly-distributed loading along width direction, which may break the plane stress assumption and cause force concentration at the clamped ends. Some chosen optimal design parameters and the static properties of the optimal PEHU are listed in Table 4.3.

Table 4.3: Selected PEHU design and its static properties.

Parameters	Values	Units
l_b	65	mm
h_b	0.8128	mm
b_b	40	mm
n_p	3	N/A
n_r	3	N/A
P_{in}	1333.33	N
f	166.67	N/mm
C_U	7.32	μF
α_f	10.08	N/A
α_e	101.61	N/A
d_U	4	mm
V_U	87.56	V
E_U	28.06	mJ

4.3 Prototype and Laboratory Evaluation

The challenging part of the mechanical design of the PEHU is how to implement the clamped-clamped boundary conditions. The selected design of the PEHU has an amplification factor greater than 10 with respect to the vertical input force of $1333N$, which means that the compression force on the PZT stacks is nearly $13.3kN$ and the horizontal stretching force at ends of both the beams is over $6.6kN$. We

made prototypes of different designs for testing. We created a mechanism to provide the clamped-clamped boundary condition subject to such a large force. We should indicate that the dimensions of the Titanium beams are $65 \times 40 \times 0.8128mm^3$ and the external dimension of a PEHU is $142 \times 42 \times 84mm^3$.

4.3.1 Comparison of Theoretical and Experimental Results

Although our ultimate goal is to store the harvested electric energy into a battery or to feed to the power grid, in the laboratory test, we only measure the open circuit voltage of the PEHU in order to evaluate its performance. We report quasi-static compression tests on the PEHU prototypes in the setup shown in Figure 4.22. We use an Instron machine to apply compressive force from 0 to $1333N$ by controlling the displacement at a rate of $25mm/min$, and measure the voltage output of the PEHU with an oscilloscope (B&K Precision, 2540b-GEN). Three different thicknesses of shims are used inside the PEHU to adjust the preload on the PZT. The values are $0.4mm$, $0.8mm$ and $1.2mm$. The corresponding laboratory test results are labeled as Test 1, Test 2 and Test 3. It is difficult to directly measure the preload on the PZT stacks once the unit is assembled. Because the $0.4mm$ shim is too thin to introduce the preload on the PZT stacks, Test 1 is therefore considered as the zero preload baseline.

The comparison between numerical and laboratory test results of sinking displacements (d_U), applied load (P_{in}), and generated voltage (V_U) are presented in Figures 4.23 and 4.24. The numerical results are obtained by sweeping different input forces based on the simplified static model of the PEHU. We should point out that the experimental results are quite repeatable.

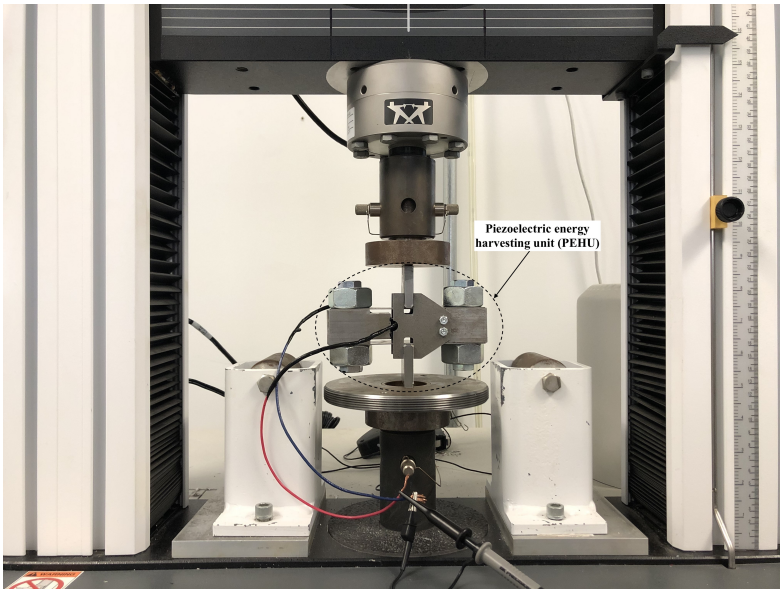

Figure 4.22: Experimental setup of the quasi-static compression test on Instron machine.

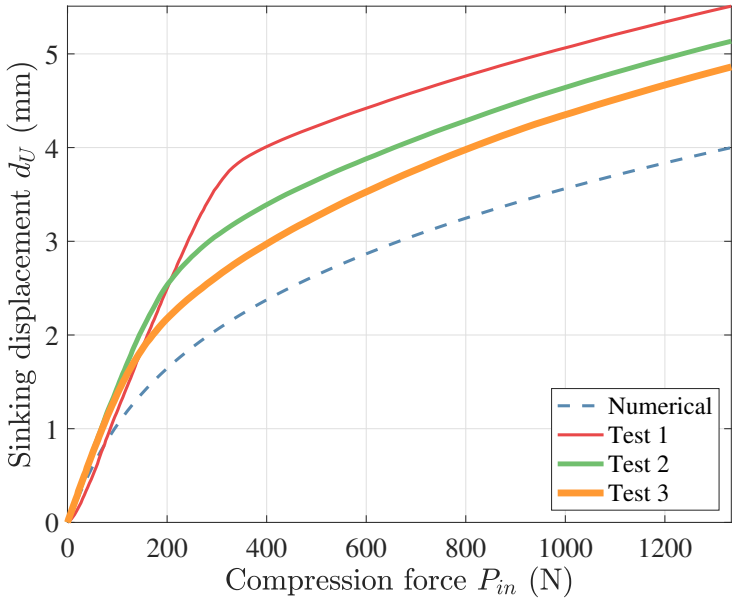

Figure 4.23: Input compressive force vs. sinking displacement of the piezoelectric energy harvesting device.

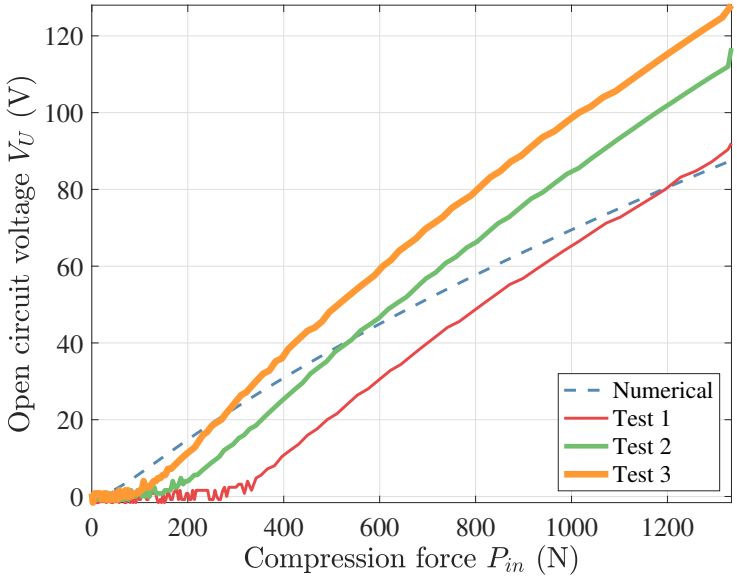

Figure 4.24: Input compressive force vs. open-circuit voltage of the piezoelectric energy harvesting device.

4.3.2 Discussions

The differences of the predicted and measured sinking displacements and open circuit voltages shown in Figures 4.23 and 4.24 are likely attributed to the imperfect dimensions of the mechanical components for the PEHU and inaccurate material constants used in the model. Figure 4.23 clearly shows that the stiffness of the PEHU increases with the input force. The PEHU mechanically behaves like a nonlinear spring. The experimental results match the trend of the theoretical prediction. Once the PEHU is compressed tight enough so that the loose ends in the mechanical components are all tightened up, the stiffness is predicted accurately by the static model as the slope of the prediction curve in the figure shows. With almost no preload in Test 1, it takes nearly $300N$ and $4mm$ to compress the PEHU enough before the unit behaves like a strong nonlinear spring. Note that at the

maximum load $1333N$, the displacements of the PEHUs are $5.51mm$ for Test 1, $5.16mm$ for Test 2, and $4.86mm$ for Test 3. The theoretical prediction is $4.00mm$. The displacement of the PEHUs in tests is greater than the static model prediction because of the gaps in the prototype. To remove the gap in the road test, we calibrate all the PEHUs and determine the needed pre-compression for each of the unit. When the PEHUs are integrated into the system, we apply the calibrated compression to PEHUs to provide necessary preload to the unit.

Figure 4.24 clearly shows the benefits of preload as the higher preload leads to higher voltage output. The flat part of the voltage output as the compressive force increases is due to the gaps in the mechanical components of the PEHU. Higher the preload in the PZT stack, the shorter the flat region. This is another evidence that the preload in the PZT stack is beneficial to the energy conversion. The voltage reading in the flat region is essentially the measurement noise. Beyond the flat region when the compressive force is large enough, the voltage increases linearly with the magnitude of the force. On the other hand, the prediction of the voltage output with the static model has a flatter slope than the experimental curves, which makes the prediction non-conservative when the force magnitude is small and conservative when the force magnitude is large. This may be due to the linear model of the piezoelectric material as well as the inaccurate piezoelectric constants used in the model, in addition to the mechanical model without taking into account of the gaps.

In summary, the laboratory tests qualitatively validated the static prediction based on the theoretical model of the PEHU. Many cyclic compressional tests have also validated the static strength analysis of the PEHU. The dynamic fatigue tests are needed to study the service life of the PEHU. Now that the mathematical model of the PEHU has been qualitatively validated, we are ready to consider the dynamic

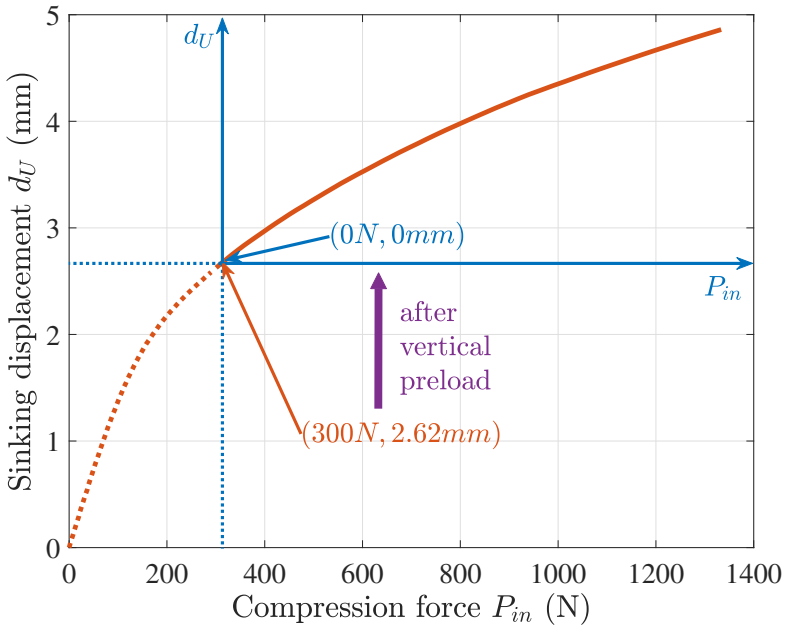

Figure 4.25: The vertical preload to the piezoelectric energy harvesting device in Test 3.

response of the PEHU to the traffic load by making use of the model.

4.4 Energy Density Estimate

The dynamic analysis of the PEHU without the preload on the PZT stacks predicts the output voltage at least $103V$ in the range of speed from $8.05km/h$ ($5mph$) to $128.75km/h$ ($80mph$), which is greater than the static prediction of $87V$. As discussed in Section 4.3, the preload on the PZT stacks inside the PEHU is beneficial for energy harvesting. Therefore, the PEHU with the preload on the PZT stacks can generate more electric energy under dynamic loading.

In the implementation of the PEHU for road test, we take another measure to improve the performance of the PEHU. We stack the PEHUs and apply a vertical preload on P_{in} to reduce the total sinking displacement d_{sk} while providing the

preload on the PZT stacks at the same time. As illustrated in Figure 4.25, which shows the experimental result of Test 3, we apply a vertical preload of $300N$ to skip the soft region. The initial state of the PEHU already has a sinking displacement $2.62mm$. Hence, we reduce the total sinking displacement d_{sk} of the PEHU for Test 3 from $4.86mm$ to $2.54mm$ when the compressive load of $1333N$ is applied.

Furthermore, the vertical preload also improves the energy conversion efficiency η. Since d_{sk} is almost halved, the work done by the gravity is also halved. Because the generated electric energy is about the same as that without the vertical preload when the load reaches $1333N$, the mechanical-to-electric energy conversion efficiency is approximately 10% in the dynamic case at speed $104.61km/h$.

We should also point out that the preload increases the stiffness and therefore the natural frequencies of the PEHU. Hence, the static design in Section 4.2 becomes even more reliable, and the dynamic response at low frequencies will catch even less effects of high frequency resonances.

With the established confidence in the mathematical model of the PEHU, we shall use the model to estimate the maximum energy density of the PEHS when a large number of the PEHUs are installed on a busy highway. Because the electric energy is harvested in a discrete manner, the instant power output varies with weight and speed of vehicles. To better describe the capability of energy harvesting, we define the energy density ρ_E as the harvested electric energy by of the PEHS that can be stored in a battery with one passage of a midsize vehicle with weight 16000N over a 1 meter long lane where the energy harvesting technology is implemented. For the PEHUs, we suppose the efficiency η_s of the battery storage is 50%. The energy density ρ_E per unit length of the instrumented road per lane and per passage of vehicle is defined as

$$\begin{aligned}\rho_E &= 4n_r n_c n_l E_p \eta_s \\ &= 4 \times 3 \times 3 \times 4 \times 0.12 \times 50\% \\ &= 8.64 J/(m.pass.lane)\end{aligned} \tag{4.54}$$

where n_l is the number of rows of the PEHUs in one meter long lane. Each row has three towers ($n_r = 3$). Each tower contains three PEHUs stacked ($n_c = 3$). $E_p = 0.12J$ is an estimate of the generated energy based on the simulated results and measured data. The harvested energy E of the PEHS on a large scale can be estimated by

$$E = \rho_E L_{rd} N_{lane} N_{pas} \ (J/year) \tag{4.55}$$

where L_{rd} is the length of the implemented roadway, N_{lane} is the number of lanes, N_{pas} is the number of passages of traffic in one year.

If we assume that the traffic follows the 3 second safety rule all day long, the energy that can be harvested and stored in batteries from one lane of $1609.34m$ (one-mile) long roadway is estimated as

$$\begin{aligned}E &= 8.64 \times 1609.34 \times 1 \times \frac{365 \times 24 \times 3600}{3} (J/year) \\ &= 1.46 \times 10^{11} \ J/year \\ &= 4.06 \times 10^{4} \ kWh/year\end{aligned} \tag{4.56}$$

4.5 Conclusions

We proposed an innovative piezoelectric device for energy harvesting from highway traffic. The finite element model for the multi-layer piezoelectric ceramic stacks is presented in details. The mathematical model of the device with nonlinear beam elements is developed and validated through static and dynamic analyses. Quasi-static tests in laboratory have validated the innovative compression-to-compression force amplification design and the theoretical model. We have also studied both numerically and experimentally the effect of the preload on the piezoelectric ceramic stacks. The numerical simulations and experimental results support the conclusion that the preloaded piezoelectric energy harvesting device is able to generate at least $120mJ$ by a load with amplitude $1333N$. The results of this work further support the following estimates: The piezoelectric energy harvesting system based on the traffic of mid-size vehicles is potentially able to achieve an energy density of $8.64J/(m.pass.lane)$. The application of the piezoelectric energy harvesting system in one lane of $1609.34m$ (one-mile) long roadway could generate the electric energy $4.06 \times 10^4 kWh$ per year. Finally, we must also point out that the application of the proposed piezoelectric energy harvesting device is not limited to highway traffic. Other potential applications may be found to warehouses, seaport, aircraft runway and railroad.

Chapter 5

PIEZOELECTRIC ENERGY HARVESTING TOWER

In this Chapter, the vertical packaging of PEHUs will be introduced, which leads to the second-level assembly, the piezoelectric energy harvesting tower (PEHT) in proposed system. Quasi-static compression test results validates the mechanical design of PEHT. Furthermore, the performance of PEHT in charging a DC battery was explored based on an energy storage circuit.

5.1 Piezoelectric Energy Harvesting Unit

Mechanical work on piezoelectric materials done by the dynamic interaction between wheel and pavement can be partially converted into electric energy. To enhance the output of PEH from traffic of mid-size vehicles, materials with strong piezoelectricity and high energy conversion efficiency are commonly used. However, this is not enough to significantly improve the outcome due to the limited input mechanical energy. A promising strategy is to introduce force amplification mechanism (FAM) into PEH devices [22,26,145,159,234,235], which can enlarge the actual force acting on PZT so as to further increase the harvested energy.

We developed an innovative compression-to-compression FAM to design the piezoelectric energy harvesting unit (PEHU). Fig. 5.1a shows the conceptual model which can be developed into a parametric mathematical model for design and analysis. Two clamped-clamped nonlinear elastic beams are coupled at both ends with

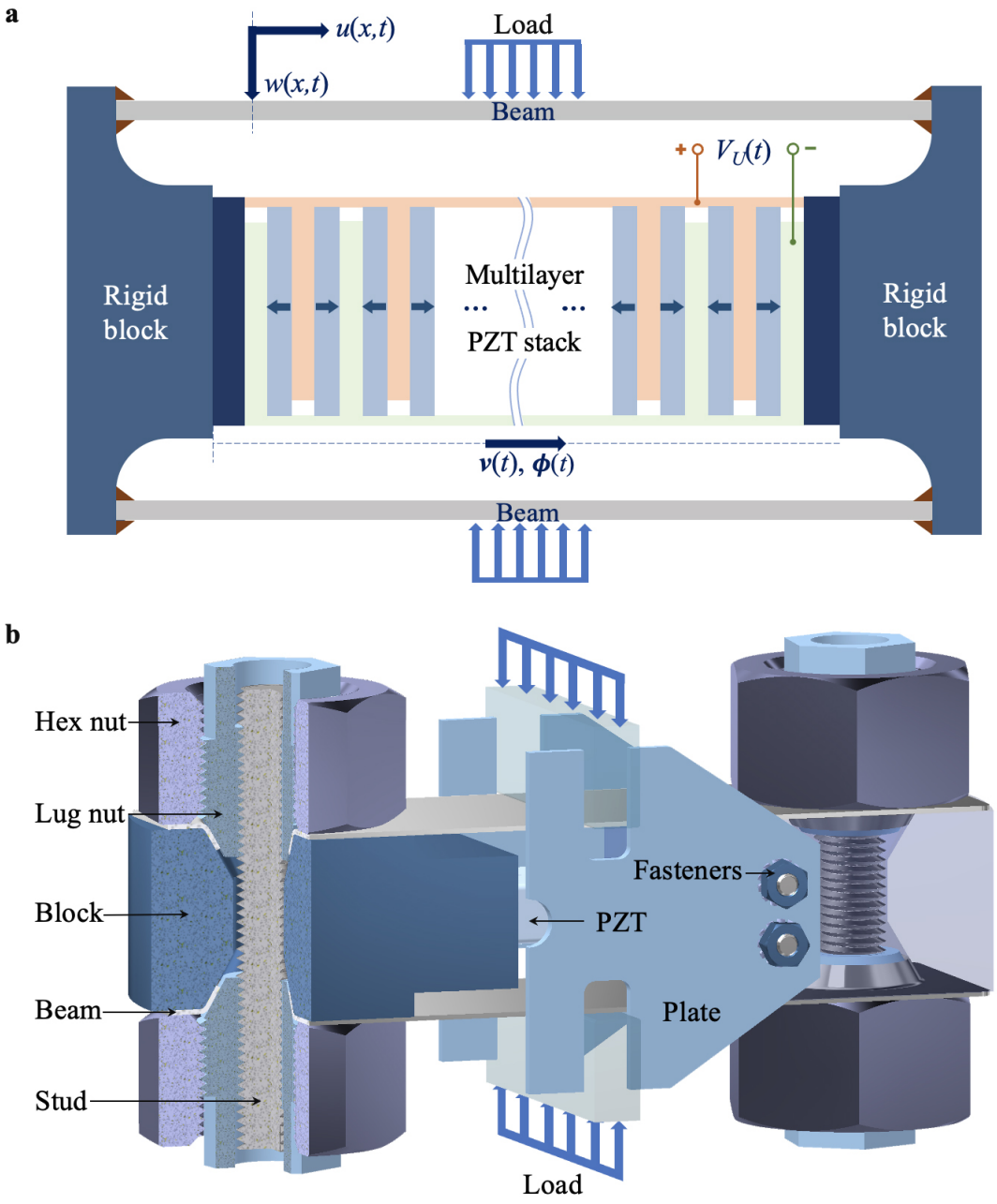

Figure 5.1: Piezoelectric energy harvesting unit. **a**, Conceptual model of proposed force amplification mechanism for energy harvesting. **b**, Realization of piezoelectric energy harvesting unit with optimized parameters.

a multi-layer PZT stack placed in the center. Dynamic load from moving vehicles acts vertically in the middle of beams, which can be transferred into horizontal compression force on PZT stack. The equations of motion of PEHU without damping are derived in the following.

$$\rho_b A_b \frac{\partial^2 u\left(x,t\right)}{\partial t^2} - E_b A_b \left(\frac{\partial^2 u\left(x,t\right)}{\partial x^2} + \frac{\partial w\left(x,t\right)}{\partial x} \frac{\partial^2 w\left(x,t\right)}{\partial x^2} \right) = 0 \tag{5.1}$$

$$\begin{aligned} &\rho_b A_b \frac{\partial^2 w\left(x,t\right)}{\partial t^2} + E_b I_b \frac{\partial^4 w\left(x,t\right)}{\partial x^4} \\ &- E_b A_b \left[\frac{\partial^2 u\left(x,t\right)}{\partial x^2} \frac{\partial w\left(x,t\right)}{\partial x} + \frac{\partial u\left(x,t\right)}{\partial x} \frac{\partial^2 w\left(x,t\right)}{\partial x^2} + \frac{3}{2} \left(\frac{\partial w\left(x,t\right)}{\partial x} \right)^2 \frac{\partial^2 w\left(x,t\right)}{\partial x^2} \right] \\ &= f\left(t\right) \left[H\left(x - \frac{l_b}{2} + \frac{l_f}{2} \right) - H\left(x - \frac{l_b}{2} - \frac{l_f}{2} \right) \right] \end{aligned} \tag{5.2}$$

$$\mathbf{M}_{vv} \ddot{\mathbf{v}}(\mathbf{t}) + \mathbf{K}_p \mathbf{v}(\mathbf{t}) = \mathbf{Q}_v(t) \tag{5.3}$$

$$\phi(\mathbf{t}) = -\mathbf{K}_a \mathbf{v}(t) \tag{5.4}$$

With the coupled boundary conditions,

$$E_b A_b \left[\frac{\partial u\left(0,t\right)}{\partial x} + \frac{1}{2} \left(\frac{\partial w\left(0,t\right)}{\partial x} \right)^2 \right] = \frac{1}{2} P\left(t\right) \tag{5.5}$$

$$E_b A_b \left[\frac{\partial u\left(l_b,t\right)}{\partial x} + \frac{1}{2} \left(\frac{\partial w\left(l_b,t\right)}{\partial x} \right)^2 \right] = \frac{1}{2} P\left(t\right) \tag{5.6}$$

$$u\left(0,t\right) = v_l\left(t\right), \; u\left(l_b,t\right) = v_r\left(t\right) \tag{5.7}$$

Where $u\left(x,t\right)$ and $w\left(x,t\right)$ denotes the longitudinal and transverse displacements of the middle surface of the beams, respectively. A_b, E_b, I_b, ρ_b, l_b denote cross-sectional area, Young's modulus, moment of inertia with respect to y axis, mass density, the

length and of the beam. $f(t)$ and l_f are the force density and span of the applied load. $\mathbf{v}(t)$ and $\phi(t)$ are the vectors of nodal displacement and voltage in multi-layer PZT stack. $\mathbf{M}_{vv}$ is the mass matrix and $\mathbf{K}_p$ and $\mathbf{K}_a$ are the simplified stiffness matrices of PZT stack. The axial force $P(t)$ at the end of PZT stack is the internal force of the PEHU due to the coupling with beams. The generalized force $\mathbf{Q}_v(t)$ contains the internal force $P(t)$ at the leftmost and rightmost nodes. v_l and v_r are the displacements of left and right ends of PZT stack.

Eqs. (5.1) and (5.2) model the dynamics of the nonlinear elastic beams, and Eqs. (2.62) and (2.63) describe the motion of the PZT stack by finite element method. The PZT stack is coupled to the beams by virtue of the displacement continuity and the internal force balance at two ends, which are defined in Eqs. (5.5), (5.6) and (5.7). Based on the mathematical model of PEHU, parameters are determined via multi-objective optimization with space layout consideration and dynamic analysis under impulsive loading to maximize energy density and minimize sinking displacement for good driving experience. More detailed discussion on the theoretical analysis can be found in our previous report [26].

The realization of an optimal design is illustrated in Fig. 5.1b. This PEHU holds a force amplification factor equal to 10, which amplifies the generated electricity by a factor of 100 in contrast to piezoelectric material under direct compressive loading without FAM. While improving power generation capacity, this FAM has brought a great challenge on how to realize the clamped boundary condition. The actual stretching force at ends of the beams is greater than 6.6 kN under a load 1333 N, which is not feasible to be balanced by friction only. Additionally, welding titanium alloy and structural steel is very challenging, especially when the thickness of beam is as thin as 0.8128 mm. Therefore, we proposed a durable and robust

mechanical connection to address this issue, as illustrated in Fig. 5.1b. Titanium beams are stamped into cone shape near ends. The contact between beams and blocks consists of the cone area and the flat circular area, which are enforced by hex nut and lug nuts, respectively. Any sliding between beams and blocks will involve not only friction due to the large tension in threaded connection, but also the deformation of cone shape. This is crucial for the realization of clamped boundary under such a large horizontal stretching force.

5.2 Piezoelectric Energy Harvesting Tower

Multiple PEHUs can be stacked up vertically to improve the energy density. Essentially, they are analogous to multiple nonlinear springs connected in series mechanically. As long as the stress wave generated by a moving vehicle can travel downwards through all the PEHUs during the short interaction, the number of PEHUs in each column (n_c) is reasonable for power generation. However, two important factors must be considered to determine the value of n_c. The first one is driving comfort and safety. The cost of improving system's energy density by increasing n_c includes not only the higher economic expenditure, but also the increase of total sinking displacement ($d_{sk} = n_c d_U$). This displacement should be limited in the deflection range of suspension system to ensure driving comfort and safety. Another concern is mechanical stability. The accumulated manufacturing error causes the PEHUs stack not ideally centered vertically. This shape error generates moments acting on PEHUs under compression. When n_c is too large, the PEHUs stack will be unstable. Furthermore, the enhanced friction due to the interaction between PEHUs results in more mechanical losses. Based on the above considerations, we have found that n_c=3 is a well-balanced choice.

The piezoelectric energy harvesting tower (PEHT) as shown in Fig. 5.2 consists of three PEHUs connected in parallel electrically. The middle PEHU forms a 90 degree angle to the upper and lower PEHUs for enhanced mechanical stability. Rubber cover is adopted to prevent dust and gravel from falling to the gap between shaft and bearing. To achieve waterproof, silicone sealant is used to seal the inner corner at the bottom and the seam under rubber cover below stainless clamp. Mechanical protection to avoid damage from heavy load is achieved by setting a proper distance between upper top surfaces of shaft and tube wall.

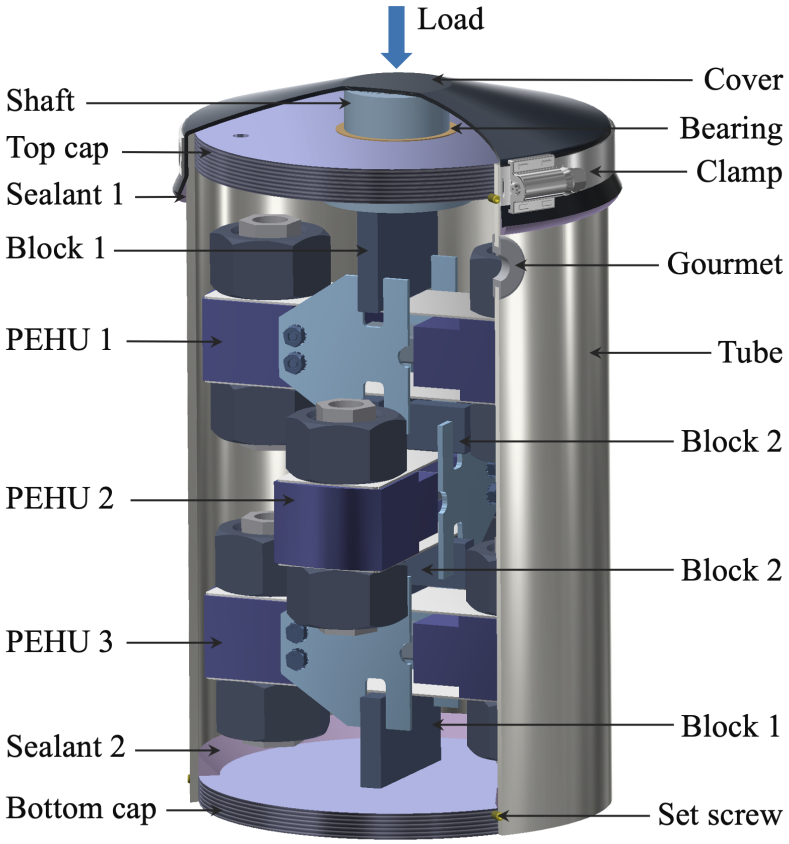

Figure 5.2: 3D model of the piezoelectric energy harvesting tower.

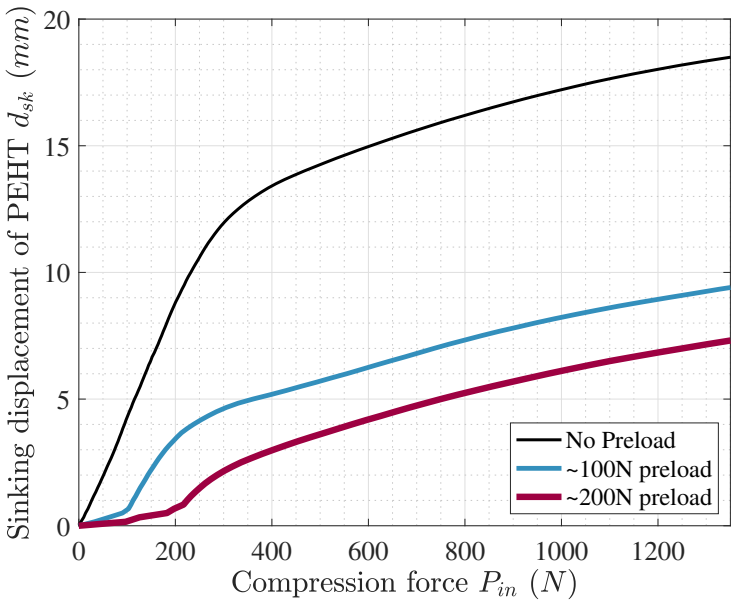

Figure 5.3: The sinking displacement d_{sk} of a PEHT prototype under quasi-static compression of 1333N with vertical preload up to about 200N.

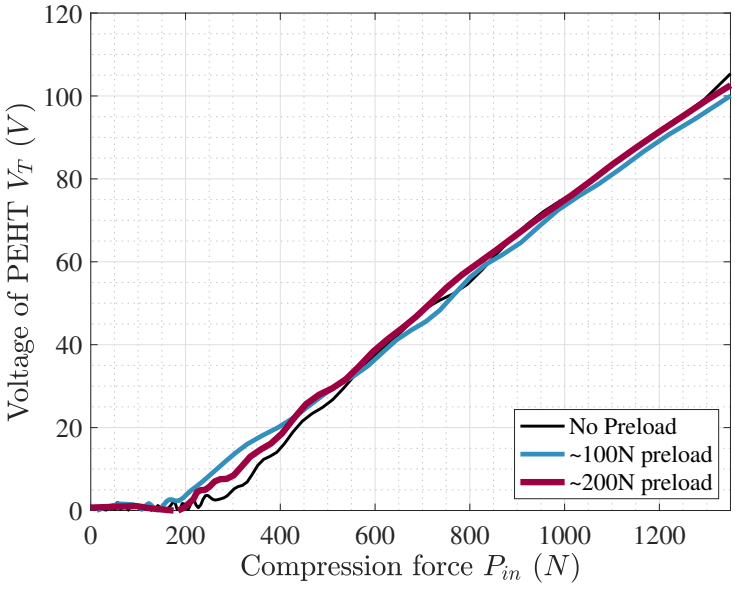

Figure 5.4: The open circuit voltage V_T of a PEHT prototype under quasi-static compression of 1333N with vertical preload up to about 200N.

The performance of a PEHT prototype in a quasi-static compression test is illustrated in Fig. 5.3 and 5.4. As the load increased up to 1333 N, a max open circuit voltage (V_T) of 106 V was generated with the sinking displacement of 18.5 mm. Stiffness hardening was observed as predicted by theoretical analysis. It is worth noting that a large portion of the sinking displacement occurred in the soft region of nonlinear stiffness. However, this initial deformation didn't really contribute to power generation. This observation indicates that d_{sk} can be significantly reduced by applying vertical preload through rotating the top cap downwards. With a preload of ∼100 N, d_{sk} was sharply decreased to 9.4 mm while V_T maintained to be above 100 V. By increasing the preload to ∼200 N, d_{sk} was further reduced to 7.3 mm with negligible electric energy loss.

48 PEHTs were manufactured and tested in laboratory before installation in pavement for drive tests. The mechanical behavior of 48 piezoelectric energy harvesting towers was evaluated in the first 50 quasi-static tests of 1333 N. The nonlinear stiffness of PEHT exhibits the same pattern as PEHU's. Fig. 5.5 illustrates the distribution of a PEHT's sinking displacement (d_{sk}) with increasing compression force up to 1333 N during the first 50 tests without vertical preload. The red curve represents the mean of test results, which can be used for prediction of d_{sk} in massive cycles before fatigue occurs. During the first few tests, internal gaps inside PEHT were eliminated. Then, the mechanical behavior of PEHT became stable gradually, which can also be confirmed from the decreased variance. Under compression of 1333 N, the mean of d_{sk} is 17.96 mm, with 25^{th} and 75^{th} percentile of 17.78 mm and 18.20 mm, respectively.

Fig. 5.6 illustrates the distributions of sinking displacement among 48 PEHTs during the first 50 tests under compression force of 1333 N. Each box represents

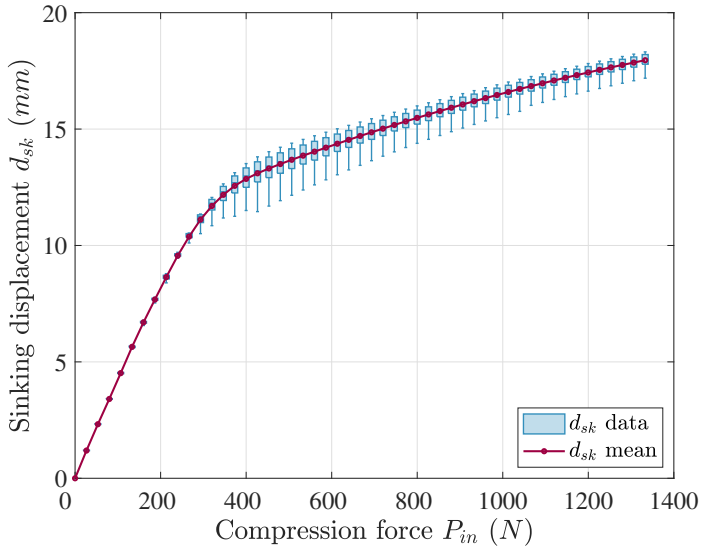

Figure 5.5: The sinking displacement (d_{sk}) of a piezoelectric energy harvesting tower during the first 50 quasi-static tests of 1333 N without vertical preload.

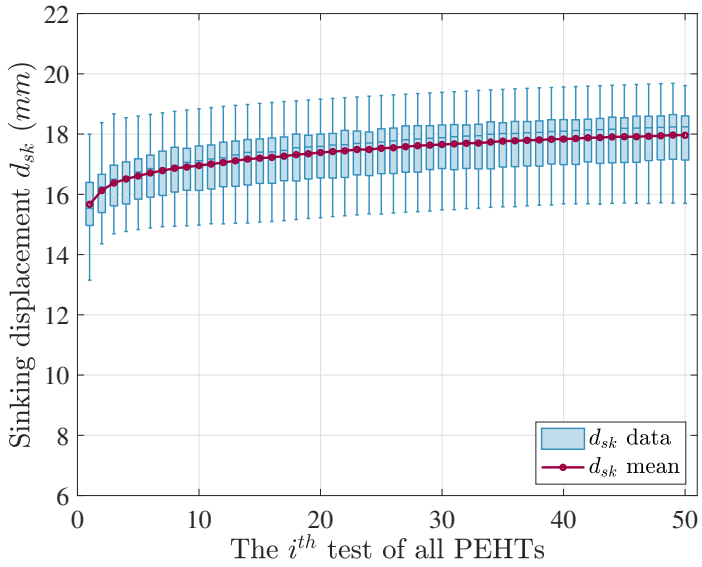

Figure 5.6: The sinking displacement (d_{sk}) of 48 piezoelectric energy harvesting towers under compression force P_{in} of 1333 N without vertical preload during the first 50 tests.

the distribution of d_{sk} of all 48 PEHTs in the i^{th} round of tests under the same compression force. In the first few tests, the mean of d_{sk} distribution raised up quickly as PEHTs were tightened up. It can be found that the distribution of d_{sk} in each round of tests exhibits the similar range and variance, which implies reliable mechanical performance. The distribution of d_{sk} became stable after around 30 tests.

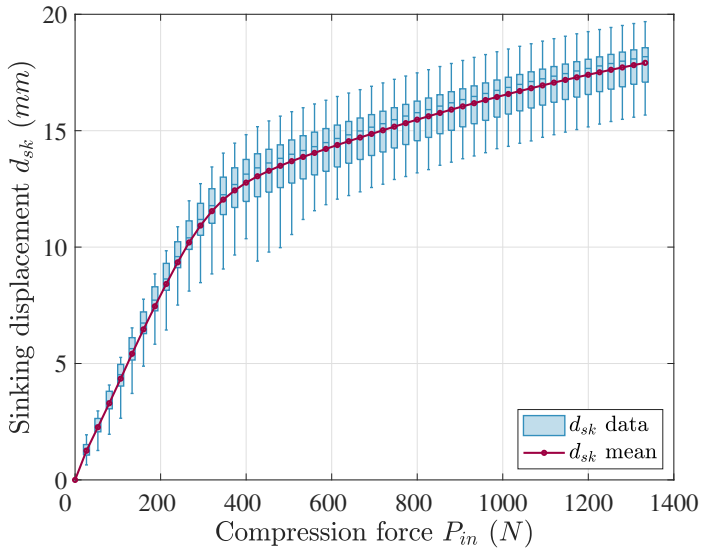

Figure 5.7: The sinking displacement (d_{sk}) of the 48 piezoelectric energy harvesting towers under compression force P_{in} of 1333 N without vertical preload during the first 50 tests.

To investigate the difference in deflection, the distributions of sinking displacement among the 48 PEHTs during last 10 tests were measured, as showed in Fig. 5.7. Each box represents the distribution of d_{sk} in 480 tests under the same compression force. When load was increased to 1333 N, the mean of d_{sk} is 17.91 mm, the 25^{th} and 75^{th} percentile are 17.09 mm and 18.56 mm, respectively. The corresponding minimum and maximum are 15.67 mm and 19.68 mm, respectively.

Compared to Fig. 5.5, a larger variation was observed, which is caused by manufacturing errors. To compensate that, PEHTs with similar stiffness and height were grouped in rows. Overall, the mechanical performance of 48 PEHTs are stable and repeatable.

5.3 Charging Battery with PEHT

To explore rectifying and storing the harvested energy, laboratory experiments were conducted to investigate PEHT's performance in charging a DC battery with a nominal voltage of 12 V. Experimental setup and schematic circuit diagram of battery charging are described in Fig. 5.8 a and b.

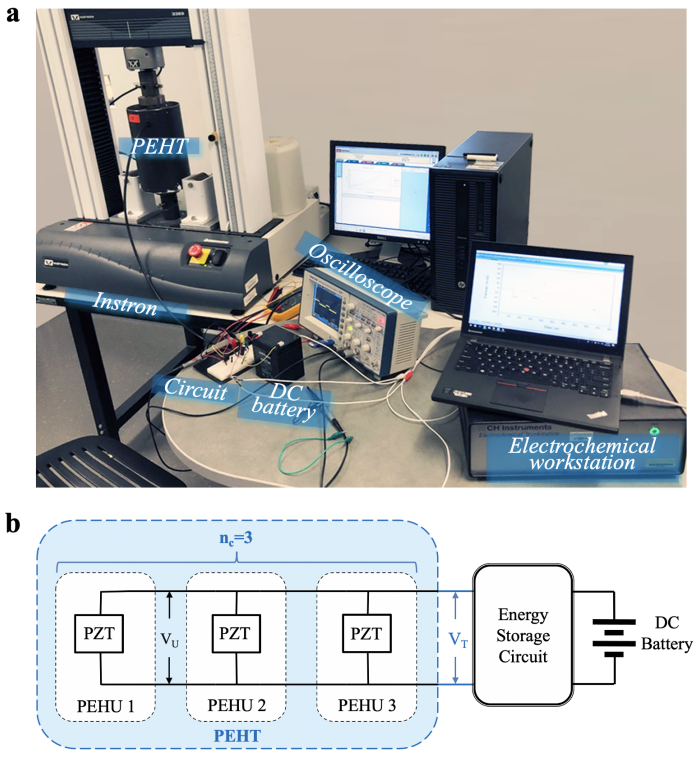

Figure 5.8: Laboratory tests of charging a 12 V DC battery by a PEHT. **a**, Experimental setup. **b**, Schematic circuit diagram.

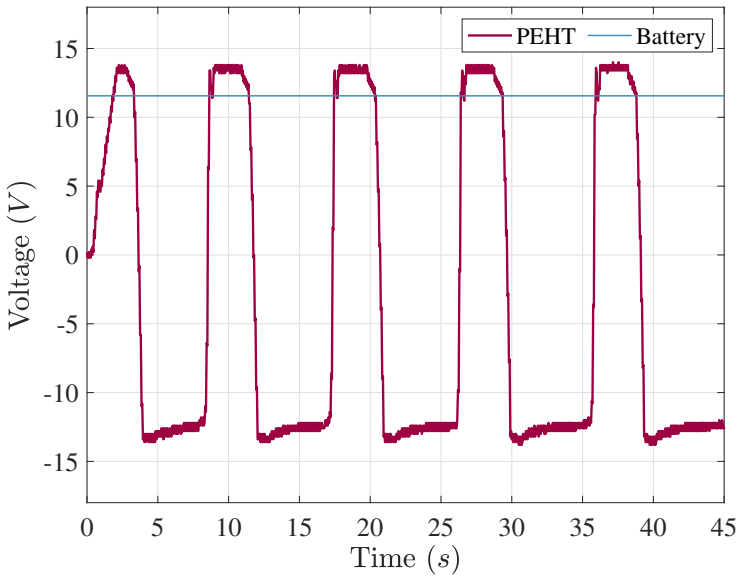

Figure 5.9: Voltage of PEHT and battery in the test of charging a 12 V DC battery in 5 quasi-static load cycles with amplitude of 1333 N.

Voltage and current of PEHT and DC battery were measured during five quasi-static loading cycles with amplitude of 1333 N, as shown in Fig. 5.9 and 5.10, respectively. The output from PEHT was rectified by a full bridge rectifier in circuit to charge the DC battery during both compression and releasing. The voltage of PEHT (V_T) oscillated between $\pm$13.80 V, while the DC battery held a constant voltage of 11.56 V during tests. The difference between them was caused by the diodes in circuit. The maximum current of PEHT and battery during releasing are higher than those during compression due to the faster unloading speed in contrast to loading.

The output power of PEHT and input power of battery are estimated by multiplying voltage and current, as shown in Fig. 5.11. The maximum output power of PEHT was 31.02 mW and 68.93 mW in compression and releasing, respectively.

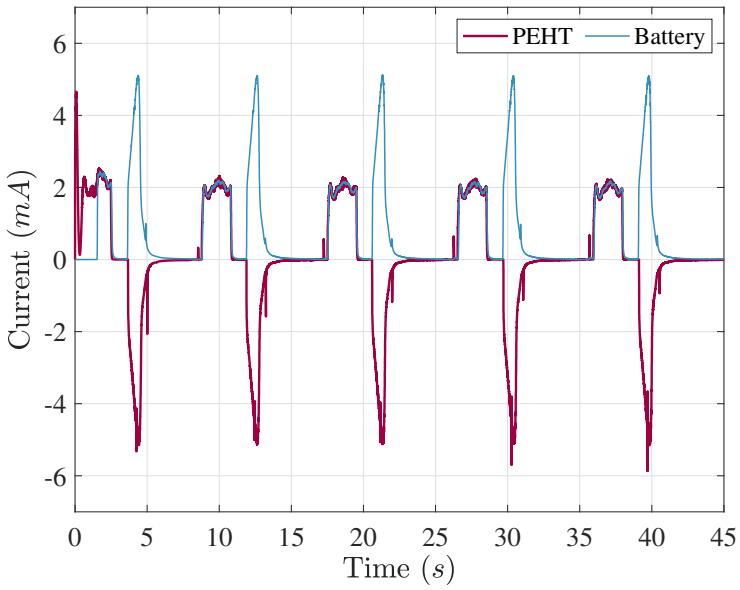

Figure 5.10: Current of PEHT and battery in the test of charging a 12 V DC battery in 5 quasi-static load cycles with amplitude of 1333 N.

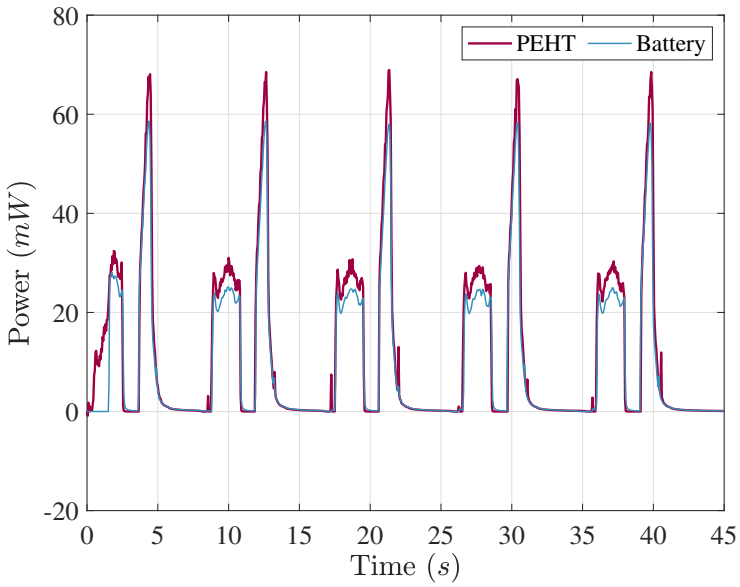

Figure 5.11: Output power of PEHT and charging power of 12 V DC battery in 5 quasi-static load cycles with amplitude of 1333 N.

At the meantime, the maximum power charging the battery was 25.10 mW and 58.27 mW, correspondingly. This difference shows that loading speed has significant influence on maximum power. As loading from roadway traffic is much faster than that of quasi-static tests, the maximum power generated from mid-size vehicle will be much higher.

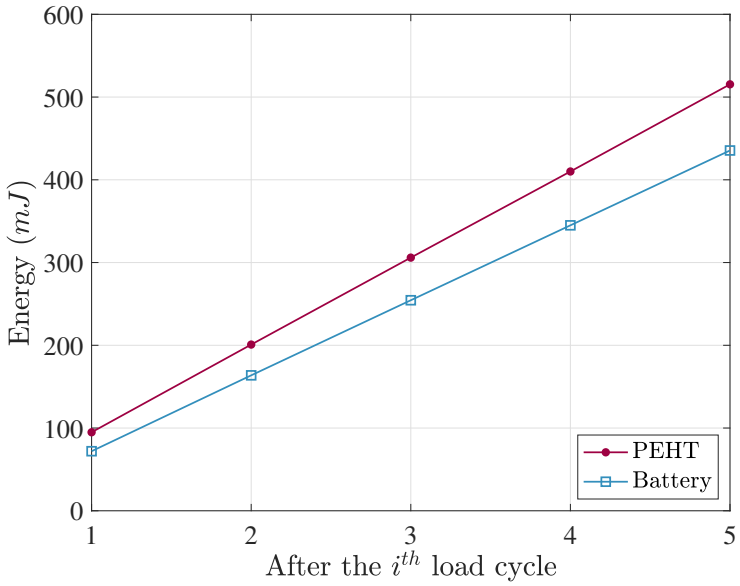

Figure 5.12: Output Energy of PEHT and stored energy in 12 V DC battery in 5 quasi-static load cycles with amplitude of 1333 N.

The accumulated output energy generated by PEHT and energy stored in battery are obtained through integration of power, as shown in Fig. 5.12. The linear relationship shows that the performance of PEHT was stable and repeatable. In each cycle, the output energy from PEHT (E_T) was 105.13 mJ and the stored energy in battery (E_B) was 90.87 mJ on average. According to the open circuit voltage ($V_T = 116$ V) and capacitance ($C_T = 22\ \mu F$) of the PEHT in tests, the open-circuit electric energy ($E_{TO} = C_T V_T^2$) is 296.03 mJ. This indicates that storage rate

($\eta_s = E_B/E_{TO}$) of harvested energy based on proposed circuit is 30.7%. Additional properties of circuit efficiency are discussed in Table 5.1.

Table 5.1: Electric properties of energy storage.

Symbol	Description	Value	Unit
V_T	Open circuit voltage of PEHT	116	V
C_T	Capacitance of a PEHT	22	μF
P_{in}	Amplitude of quasi-static load	1333	N
d_{sk}	Sinking displacement of PEHT	7.27	mm
E_{TO}	Open circuit electric energy	296.03	mJ/cycle
E_T	Output energy from PEHT	105.13	mJ/cycle
E_B	Stored energy in battery	90.87	mJ/cycle
W_{in}	Input mechanical work	4845.46	mJ/cycle
α_s	Efficiency of storage circuit	86.44	%
η_c	Percentage of collectable energy	35.51	%
η_s	Percentage of storable energy	30.7	%
α_p	Energy conversion efficiency	6.11	%
η_{tot}	Percentage of stored energy in work	1.88	%

where $E_{TO} = C_T V_T^2, W_{in} = P_{in} d_{sk}/2, \alpha_s = E_B/E_T, \eta_c = E_T/E_{TO}, \eta_s = E_B/E_{TO}, \alpha_p = E_{TO}/W_{in}, \eta_{tot} = E_B/W_{in}$.

5.4 Methods

Manufacture of PEHTs. PZT package in each PEHU consists of three multi-layer PZT stacks in dimension of $7 \times 7 \times 32.4\ mm^3$ (CeramTec, Germany). The PZT material is from Sonox P505 of d33 mode. High-strength Grade 5 Titanium sheet with thickness of 0.8128 mm was used to make the beams.

Quasi-static compression test. Loading from rest up to 1333 N was applied by an Instron universal testing machine via controlling the displacement ramp rate at 100 mm/min. Meanwhile, open circuit voltage was measured using an oscilloscope.

Battery charging test. Instron universal testing machine was employed to apply quasi-static cyclic load up to 1333 N on a PEHT prototype by controlling the force ramp at rate of 500 $N/\sec$ during compression and free to return. Voltage and current were measured by an oscilloscope and an electrochemical workstation (CH Instruments, CHI750E), respectively.

5.5 Conclusions

Three PEHUs are integrated into a PEHT as a packaged energy harvesting device. Quasi-static compression tests validated the mechanical design of PEHT, and the non-linear stiffness follows the similar pattern of PEHU. A energy storage circuit was developed to collect the harvested energy by PEHT into a DC battery. It was observed that the PEHT was able to harvest energy from mechanical compression and charge a DC battery stably and repeatably. The waterproof has been tested by immersing PEHT into water for 3 days. 48 PEHTs has been manufactured and tested for the implementation of PEHS in roadway.

Chapter 6

PEHS AND ROAD TESTS

In this Chapter, the piezoelectric energy harvesting system (PEHS) will be introduced, including the electric circuit design and mechanical packaging. The construction progress of a prototype system will be briefly reported. The performance of PEHS has been measured in real road tests. Speed effect was evaluated based on measurements.

6.1 Piezoelectric Energy Harvesting System

Systematic design is crucial to the implementation of PEHTs in roadway on a large scale. To enhance the energy density of PEHS, the space in pavement needs to be fully utilized with optimized layout of PEHTs. A key parameter is the number of PEHTs in one row that share the load under one wheel, which is determined to be 3 via multi-objective optimization. When a vehicle drives over PEHS, rows of PEHTs will be activated one by one on both the left and right wheel paths.

In the proposed PEHS, there are n_s piezoelectric energy harvesting boxes (PEHBs) under both left and right wheels pass in parallel electrically, as shown in Fig. 6.1a. In general, each piezoelectric energy harvesting box (PEHB) consisting of n_b rows of PEHTs, which are independent mechanically to make full use of dynamic load from vehicles. Rows are connected in parallel, in which n_r PEHTs are connected

in series electrically, as shown in Fig. 6.1b and c, which present the case when $n_b = 4$, $n_r = 3$. This wire connection strategy aims to lower the risk of PEHS being disconnected or shorted.

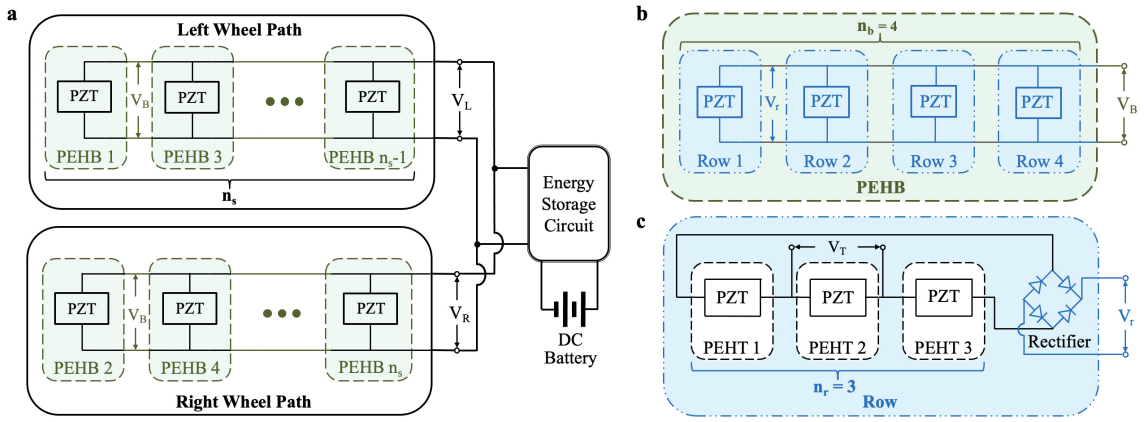

Figure 6.1: Schematic of circuit for charging a DC battery on road. **a**, Piezoelectric energy harvesting system. **b**, Piezoelectric energy harvesting box. **c**, A row of PEHTs with a full bridge rectifier.

The corresponding mechanical design of PEHB is illustrated in Fig. 6.2. Steel plate is placed on the top of PEHTs in each row to share the traffic load. The bridge rectifier in each row is critical to avoid leakage and improve the efficiency of storage circuit especially on a large scale. Rows of PEHTs in proposed PEHS are independent preferably to make full use of vehicles' weight. As a vehicle drives over PEHS in lane, rows in PEHBs will be activated to harvest energy and charge a DC battery.

In PEHB, four steel plates attached to a nylon cover are on the top of rows to distribute the traffic load among PEHTs. A steel plate is placed under PEHTs for uniform reactions between PEHTs and ground under the concrete traffic rated box

(JENSEN PRECAST, HT2436). Electric wires go through underground conduits to the utility box by the side of road.

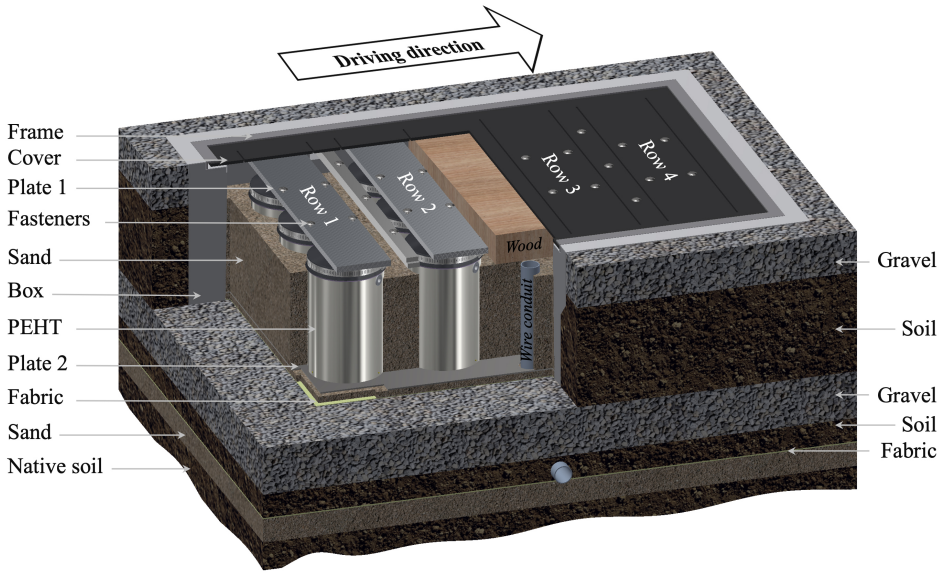

Figure 6.2: 3D model of a piezoelectric energy harvesting box for implementation in pavement.

6.2 Construction of PEHS on Road

To investigate the performance of this technology on road, we constructed a prototype PEHS which has 4 PEHBs in a lane on campus of the University of California Merced. Brief construction progress is shown in Fig. 6.3. First, native soil was excavated and a solid foundation of compacted gravel with wire conduits buried inside was build. Then, four concrete boxes and a wire connection box were placed in position, as shown in Fig. 6.3a. After calibration, compacted soil and gravel were filled around concrete boxes, as shown in Fig. 6.3b. 48 PEHTs were installed in site to assemble 4 PEHBs with sand filled around, as shown in Fig.

6.3c. Fig. 6.3d shows the completed PEHS. Through conduits, electric cables were connected with an utility box where the electric circuit was placed. The center distance between left and right PEHBs is designed to be 1.57 m in consideration of mid-size vehicles. The width and length of completed PEHS is 2.36 m and 2.49 m, respectively.

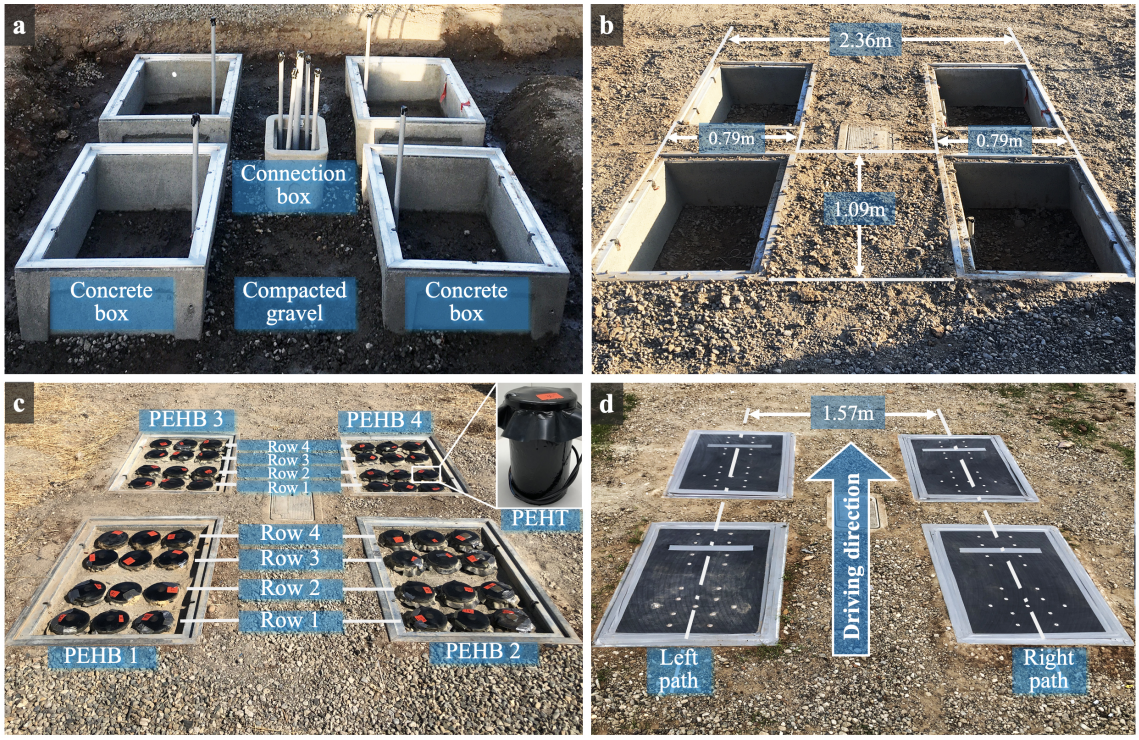

Figure 6.3: Construction progress of the piezoelectric energy harvesting system. **a**, Traffic concrete boxes installation after excavation. **b**, Fixed concrete boxes. **c**, Installation of piezoelectric energy harvesting towers. **d**, Completed piezoelectric energy harvesting system.

6.3 Road Test Results

To evaluate the energy density of PEHS with respect to mid-size vehicles, open circuit voltage in drive tests of a Nissan Altima was measured. PEHBs 1

and 3 in left path are connected in parallel. PEHBs 2 and 4 in the right path are in parallel as well. Open circuit voltage of left and right paths were measured simultaneously. As the vehicle drives over PEHS, rows along the driving direction generate impulsive open circuit voltage sequentially, which can be used to estimate electric energy by

$$E_{oc} = E_L + E_R = \sum_{i=1}^{16} C_r(V_{Li}^2 + V_{Ri}^2) \tag{6.1}$$

where $C_r = C_T/3 = 7.32\ \mu F$ is the capacitance of a row on average, V_{Li} and V_{Ri} are the i^{th} peak voltage in the left and right wheel path, respectively.

Fig. 6.4a illustrates the representative generated open circuit voltage on both sides in road test at speed of ∼40 km/h. The PEHS generated an open circuit electric energy of 20.29 J. The maximum voltage was observed as high as 484 V. The energy density of PEHS was calculated by

$$\rho_E = E_{oc}/l_s \tag{6.2}$$

where l_s is the length of PEHS in lane.

The effective value of our PEHS is 1.32 m determined by 8 times of the outer diameter of PEHT. As a result, an energy density of 15.37 J/(m.pass.lane) was obtained. There is difference in power generation between rows. One reason is the roughness of test road. Another reason is the differences between PEHTs in terms of height, mechanical stiffness, and power generation.

To investigate the effect of driving speed on energy harvesting, drive tests have been conducted from speed of 8 km/h to 40 km/h at step of 8 km/h. Fig.

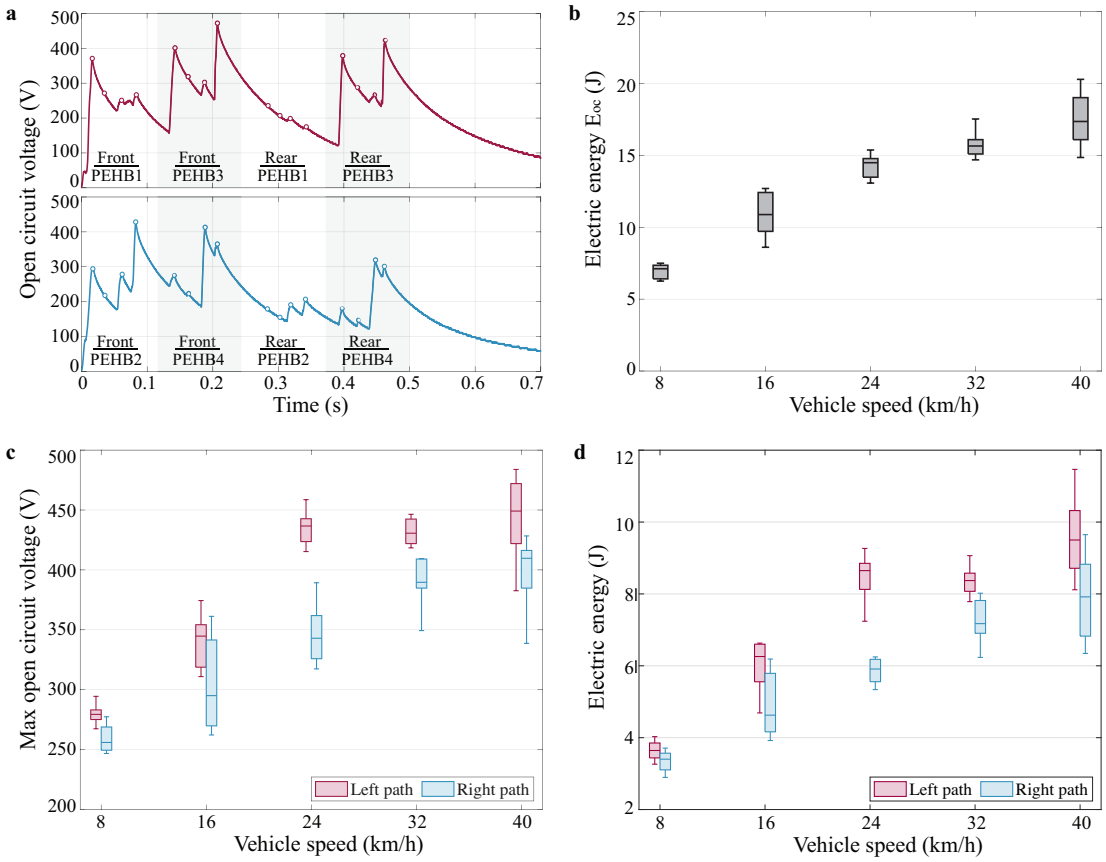

Figure 6.4: Drive test results of piezoelectric energy harvesting system. **a**, Open circuit voltage of PEHS during Altima passage at speed of 40 km/h. Each PEHB was activated twice by the front and rear wheel. Therefore, 16 voltage peaks in each path generated as marked in circles. **b**, Harvested electric energy in tests at different speeds statistically indicates a positive effect of vehicle speed on energy harvesting. **c**, The maximum open circuit voltage in left and right paths at different speeds. **d**, Harvested electric energy in left and right paths at different speeds.

6.4b shows the harvested electric energy E_{oc} per passage with different speeds. 10 measurements was taken for each speed group. Harvested energy in left and right paths are shown in Fig. 6.4d. The median harvested energy increases from 7.11 J at 8 km/h to 17.36 J at 40 km/h gradually, which demonstrates a positive effect of vehicle speed on energy harvesting in tested range.

In the same tests, maximum voltage in left and right path at different speeds are recorded, as shown in Fig. 6.4c. Voltage in the left path is greater than the right side in general because the left side of vehicle is heavier than the right side.

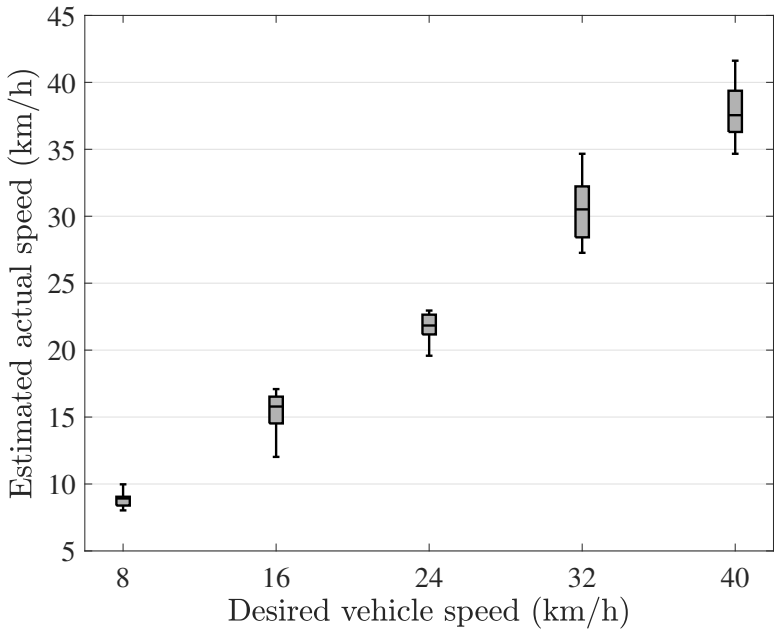

Figure 6.5: Estimated speeds in drive tests based on open circuit voltage measurements.

In drive tests, the vehicle speed was measured and compared with the value shown in car speedometer, as shown in Fig. 6.5. The velocities were determined by calculating the ratio of physical distance of two voltage peaks to the corresponding time interval. To make estimation more reliable, we can take an average of multiple

peaks and both paths. It can be found that the calculated speeds match well with records.

6.4 Discussions

A system solution to harvest energy from roadway traffic has been presented. Due to the COVID-19 pandemic, the drive tests were conducted after the PEHTs have been installed in field for 11 months. Test results not only demonstrate the outstanding capability of energy harvesting, but also validate the reliable mechanical design in terms of strength and waterproof. Because of the optimized sinking displacement and stiffness, driving comfort and safety is confirmed. In addition, due to the sensor nature of piezoelectricity, PEHS is able to detect vehicle speed precisely. The proposed energy harvesting system has great potential to be part of the future smart road as power supply and sensors for vehicle speed and weigh-in-motion.

In addition, the proposed PEHS is promising to be applied on a large scale for power generation. The harvested energy can be estimate by

$$E = \rho_E L_{rd} N_{lane} N_{pass} \tag{6.3}$$

where L_{rd} is the length of implemented roadway, N_{lane} is the number of implemented lanes, N_{pass} is the total passages of traffic in one year.

Based on the drive test results, assuming that heavy traffic following 3 second safety rule all day long, one lane of 1609.34 m (1 mile) can generate at least electric

energy

$$E = 15.37 \times 1609.34 \times 1 \times (365 \times 24 \times 3600)/3J/year = 7.22 \times 10^4 kWh/year \tag{6.4}$$

According to the efficiency of storage 30.7% estimated from laboratory tests, 2.22×10^4 kWh can be stored in 12 V DC battery in a year.

Chapter 7

SCALED-UP DESIGN FOR HEAVY TRUCKS

Energy harvesting with proposed technology from traffic of heavy trucks has the potential of even higher energy density than that from mid-size vehicles. To make full use of trucks, parameters of PEHS needs to be redesigned. In this chapter, the optimal design parameters for traffic of heavy trucks will be discussed and the power generation of PEHS will be estimated based on our validated mathematical model.

7.1 Multi-Objective Optimal Design

As discussed in Chapter 4, there are many design parameters in proposed system influencing energy harvesting, which mainly include geometric parameters of beam (l_b,b_b,h_b) and system layout parameters (n_p,n_r,n_c), as illustrated in Fig. 4.2. The maximum allowed weight of a 5-axis truck is $G_{truck} = 80,000lbs$. The weight at one end of an axis can be $35586N$ on average, which is nearly 9 times as the loading of a mid-size car. The load acting on a PEHU is $P_{in} = G_{truck} \times 9.80665/2.205/10/n_r$. In order to achieve high energy density, a high force amplification factor of 10 times or more is desired based on the previous design experience. Meanwhile, the sinking displacement d_{sk} is aimed to be less than $10mm$, which can be extended to $14mm$ before vertical preload is applied. Due to the huge compression force and limited allowed deflection, the design of PEHU becomes extremely challenging.

Beams of larger size are preferred as the long and wide beams are likely to have smaller maximum stress, which was concluded based on the design for mid-size vehicles. The search range of l_b and b_b are enlarged up to $200mm$. Meanwhile, the sinking displacement of PEHU is likely to increase as well. To achieve small sinking displacement, n_c is preferably selected to be 1, therefore $d_{sk} = d_U$. This could reduce the complexity of system and enable in-plane packaging design, which is beneficial to the even force distribution in a row.

The multi-objective design problem in this case is updated as follows.

$$\min_{\mathbf{k}} (d_{sk}, -E_U) \tag{7.1}$$

where $\mathbf{k} = \{l_b, b_b, h_b, n_p, n_r, n_c\} \in Q$ and Q is the union of the following sets of the design parameters.

$$\begin{aligned}
&\{32.4 \leq l_b \leq 200\}, \quad \{21 \leq b_b \leq 200\} \\
&\{h_b \subset \{0.4064, 0.8128, 1.6002, 3.175\}\} \\
&\{3 \leq n_p \leq 50\}, \quad \{2 \leq n_r \leq 5\}, \quad \{n_c = 1\}, \quad \{d_{sk} \leq 14\} \\
&\{\max\{\sigma_{PZT}(x)\} \leq 110MPa\}, \quad \{\max\{\sigma_b(x,z)\} \leq \sigma_{yield}FoS\}
\end{aligned} \tag{7.2}$$

n_p and n_r can be preliminary estimated based on the allowed stress in PZT stacks. The amplified compression at the end of PZT stacks in a PEHU is $P = P_{in} \times \alpha_f$. The minimum number of PZT stacks needed in a PEHU can be determined by $n_p = P/(\sigma_{PZTallowed}A_p)$, where $\sigma_{PZTallowed}$ is the maximum allowed stress in PZT, A_p is the cross-section area of a single multi-layer PZT stack. Because there are two tires at each end of an axis, so it is reasonable to allow the span of a row to be up

to one meter. Due to the allowed stress in PZT $110MPa$, $n_r = 5$ and $n_p = 36$ can be the start point of search.

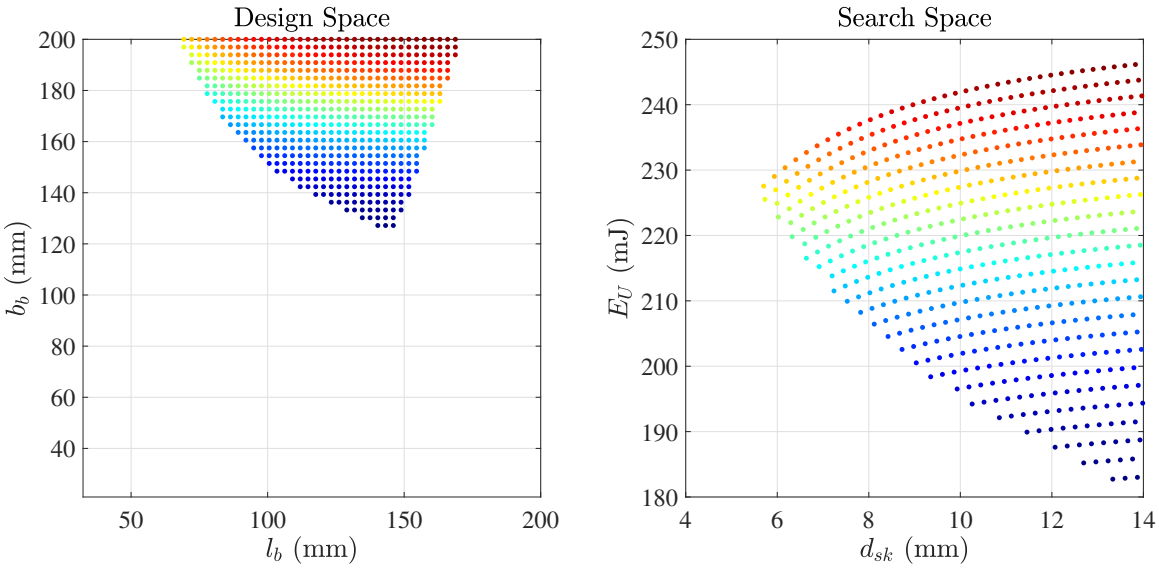

Figure 7.1: The feasible candidates in design space and their performance in search space for heavy trucks when $n_r = 5$, $n_p = 19$, $h_b = 0.4064mm$.

Bulk search in cases of different n_r and n_p were conducted. A pattern was observed that for a given n_r and n_p, the design with highest E_U regardless of thickness has the maximum allowed length and width of $200mm$. In addition to that, the overall highest E_U among design with different thickness has a thickness of $1.6002mm$. Figs. 7.1, 7.2, 7.3 and 7.4 show a design example when $n_r = 5$ and $n_p = 19$. Feasible designs and corresponding performance in the four cases of different thickness are shown in these figures.

Based on the observation, the search in the 5D space includes two steps. First, we assume that the preferred optimal design in our interested range may have beams of dimension of $l_b = 200mm$, $b_b = 200mm$, $h_b = 1.6002mm$. With the

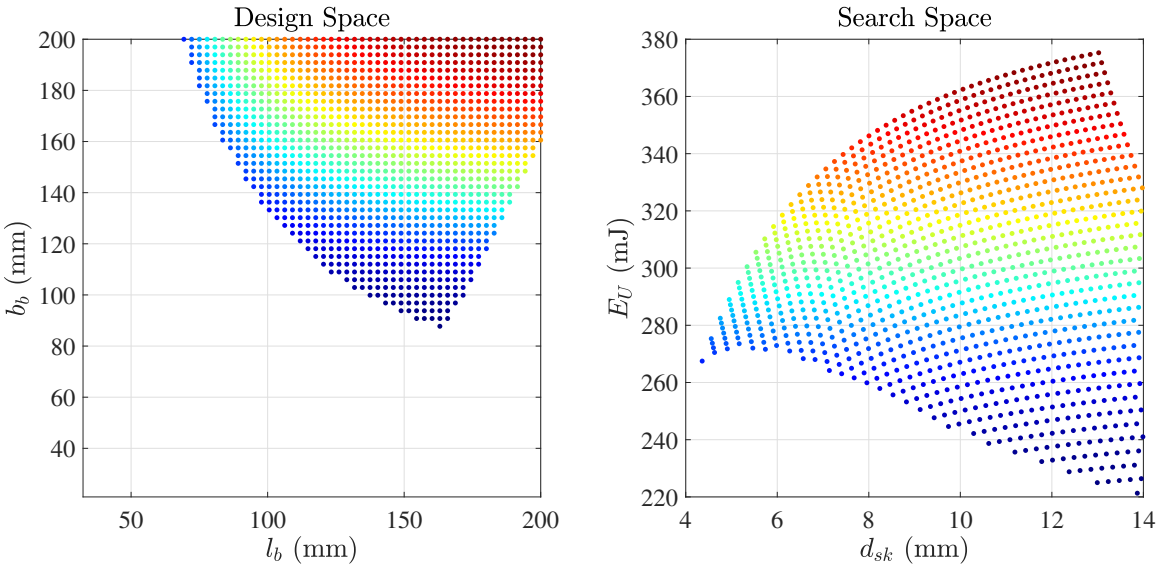

Figure 7.2: The feasible candidates in design space and their performance in search space for heavy trucks when $n_r = 5$, $n_p = 19$, $h_b = 0.8128mm$.

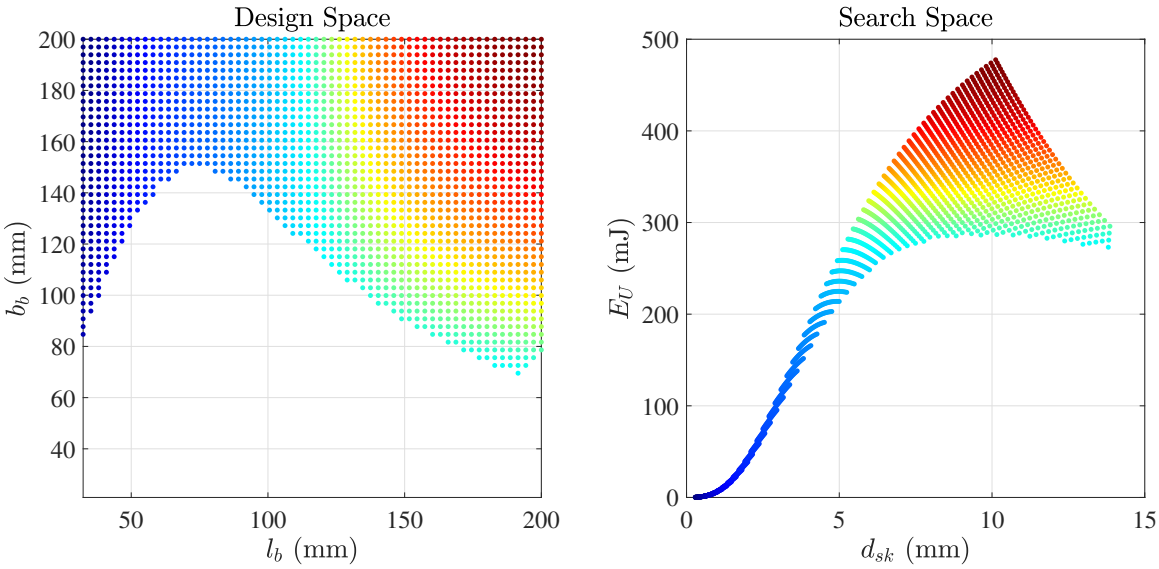

Figure 7.3: The feasible candidates in design space and their performance in search space for heavy trucks when $n_r = 5$, $n_p = 19$, $h_b = 1.6002mm$.

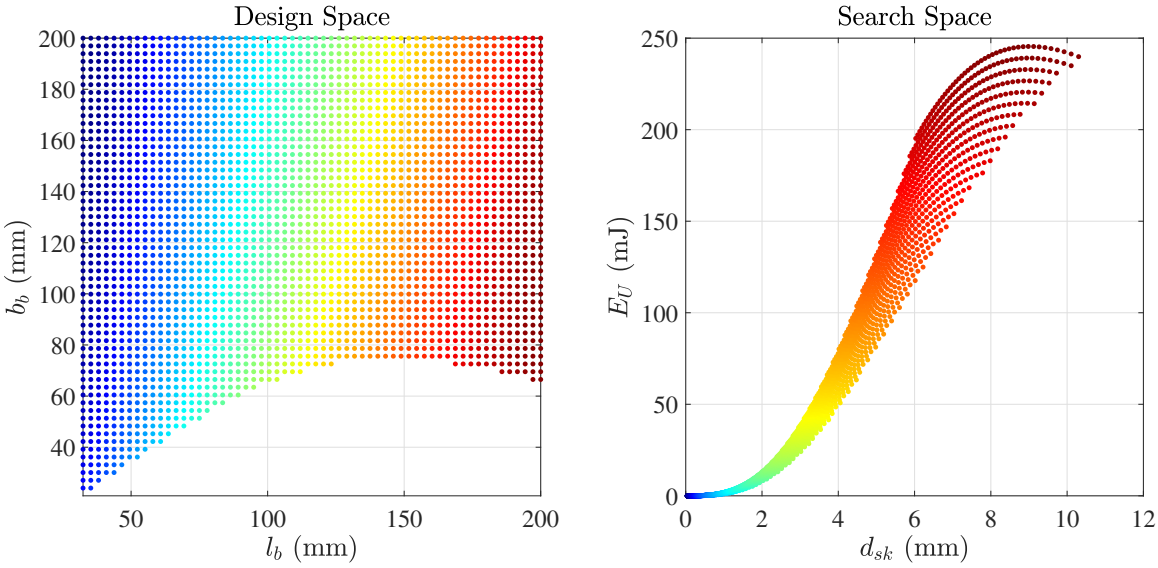

Figure 7.4: The feasible candidates in design space and their performance in search space for heavy trucks when $n_r = 5$, $n_p = 19$, $h_b = 3.175mm$.

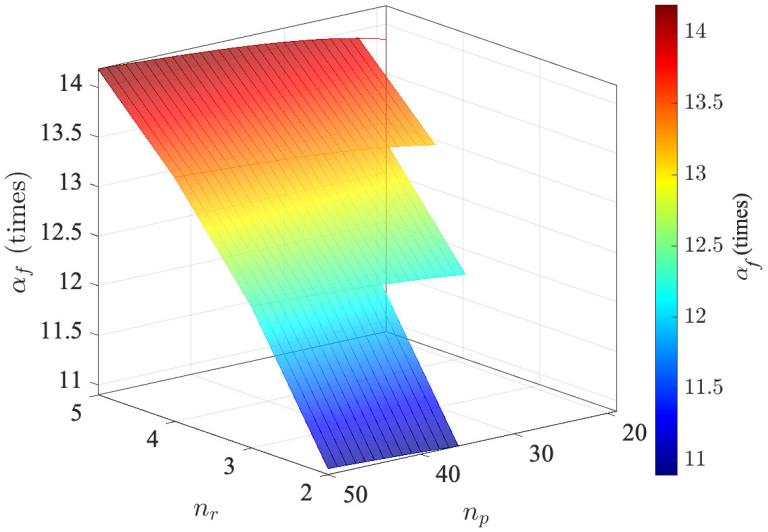

Figure 7.5: The force amplification factor α_f of feasible candidates in design space of n_r and n_p for heavy trucks when $l_b = 200mm$, $b_b = 200mm$, $h_b = 1.6002mm$.

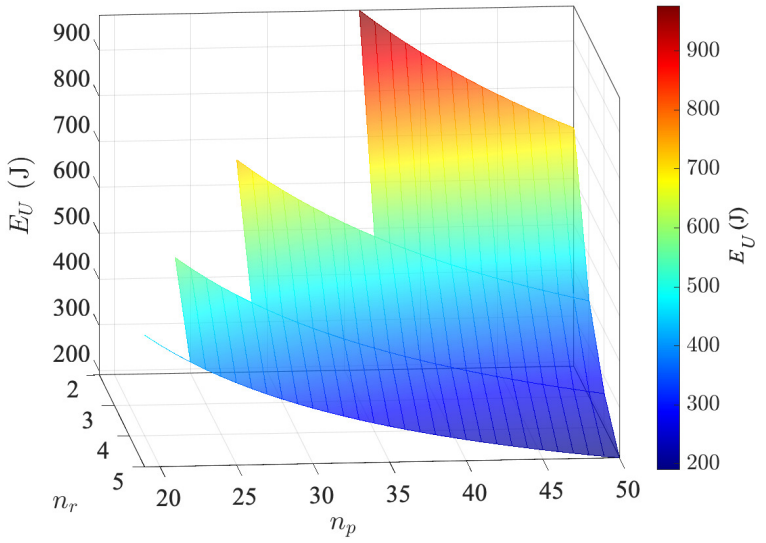

Figure 7.6: The electric energy E_U of feasible candidates in design space of n_r and n_p for heavy trucks when $l_b = 200mm$, $b_b = 200mm$, $h_b = 1.6002mm$.

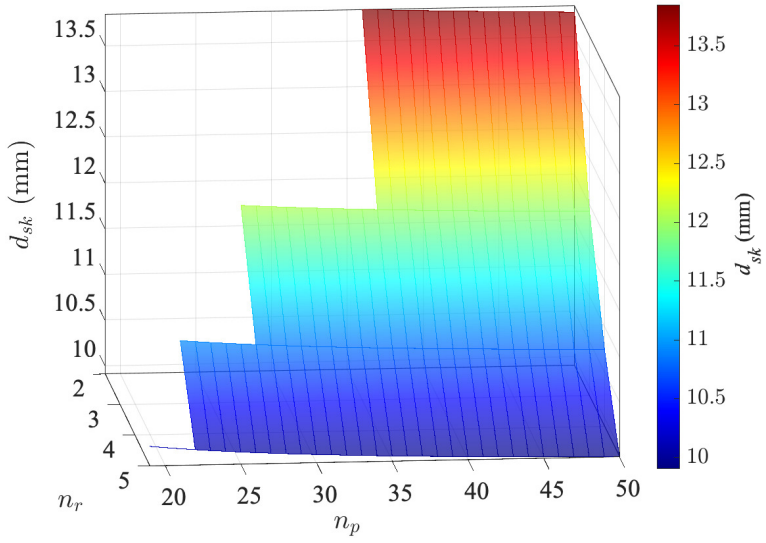

Figure 7.7: The sinking displacement d_{sk} of feasible candidates in design space of n_r and n_p for heavy trucks when $l_b = 200mm$, $b_b = 200mm$, $h_b = 1.6002mm$.

geometry of beams determined, optimal designs with respect to parameters of n_r and n_p were explored. Second, for given n_r and n_p, beams with varying dimensions were compared to validate the assumption. Fig. 7.5 shows PEHU with the largest beam can achieve a force amplification of greater than 11 times,which is even batter than the design for mid-size vehicle. Fig. 7.6 shows that a single PEHU can generate electric energy up to $975.87mJ$ in a quasi-static cycle. The sinking displacement of PEHU is in the range of $(10mm, 14mm)$, as shown in Fig 7.7. Fig. 7.8 illustrates the influence of n_r and n_p on PEHU's performance. As n_r increases, the load on PEHU decreases, power generation decreases for the same n_p. For a given n_r, E_U increases as n_p decreases because of the quadratic relationship between energy and voltage, at the meanwhile, d_{sk} increases slightly.

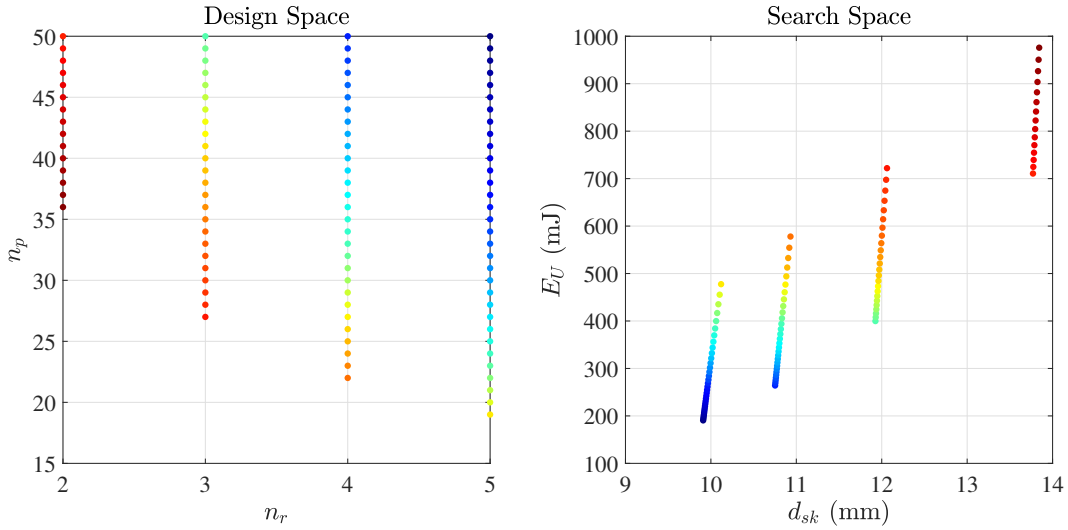

Figure 7.8: The feasible candidates in design space and their performance in search space of n_r and n_p for heavy trucks when $l_b = 200mm$, $b_b = 200mm$, $h_b = 1.6002mm$.

As the difference of sinking displacement between all candidates is relatively

small and in the acceptable range, the preference focuses on the power generation. The suggested optimal designs are $n_r = 2$ and $n_p = 36$, $n_r = 3$ and $n_p = 27$, $n_r = 4$ and $n_p = 22$. and $n_r = 5$ and $n_p = 19$, with beam of dimensions of $l_b = 200mm$, $b_b = 200mm$, $h_b = 1.6002mm$.

Since the size of beam is assumed based on observation, it is necessary to validate that the largest beam contributes to the highest energy. For the four cases with different n_r and n_p, brutal searching in 3D parameter space of l_b, and b_b and h_b were executed. Furthermore, MOPSO was applied to find the Pareto front for each case as the secondary confirmation of the optimal design.

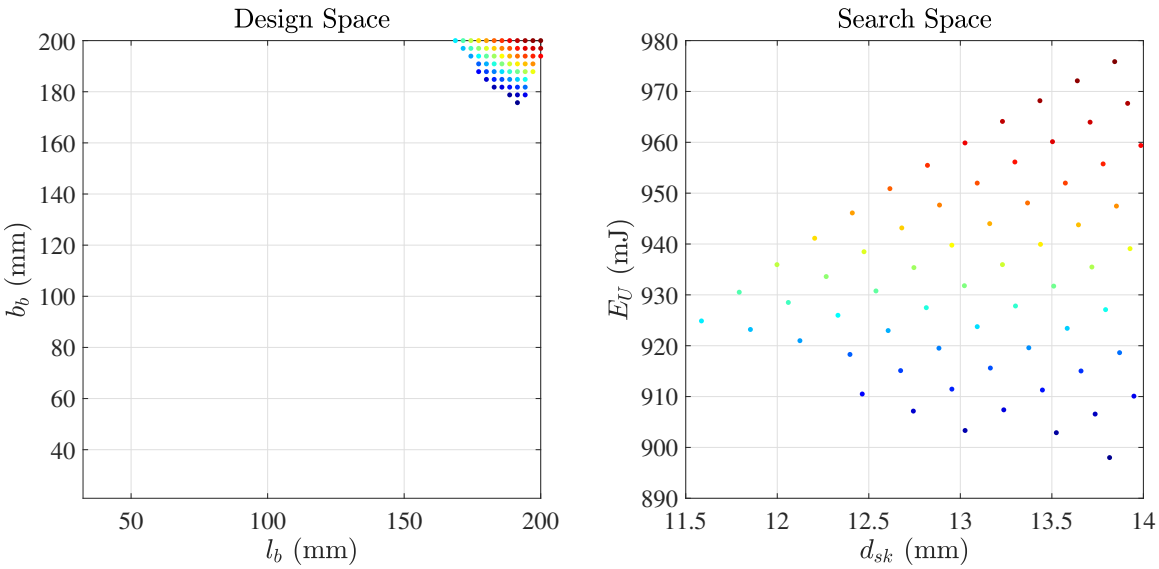

Figure 7.9: The feasible candidates in design space and their performance in search space of l_b and b_b for heavy trucks when $n_r = 2$, $n_p = 36$, $h_b = 1.6002mm$.

Fig. 7.9 shows the feasible sampled design and performance for the case of $n_r = 2$, $n_p = 36$, $h_b = 1.6002mm$. Fig. 7.10 presents the pareto sets and pareto front of the same case by using MOPSO method with the same parameters listed in

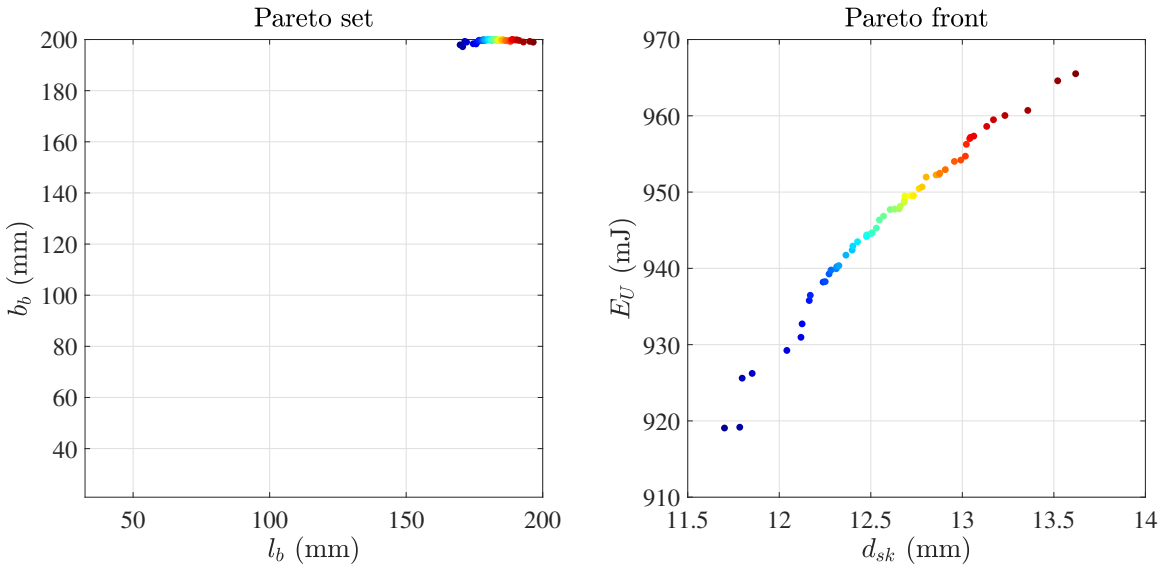

Figure 7.10: The Pareto set and front of PEHU for heavy trucks by multi-objective particle swarm optimization when $n_r = 2$, $n_p = 36$, $h_b = 1.6002mm$.

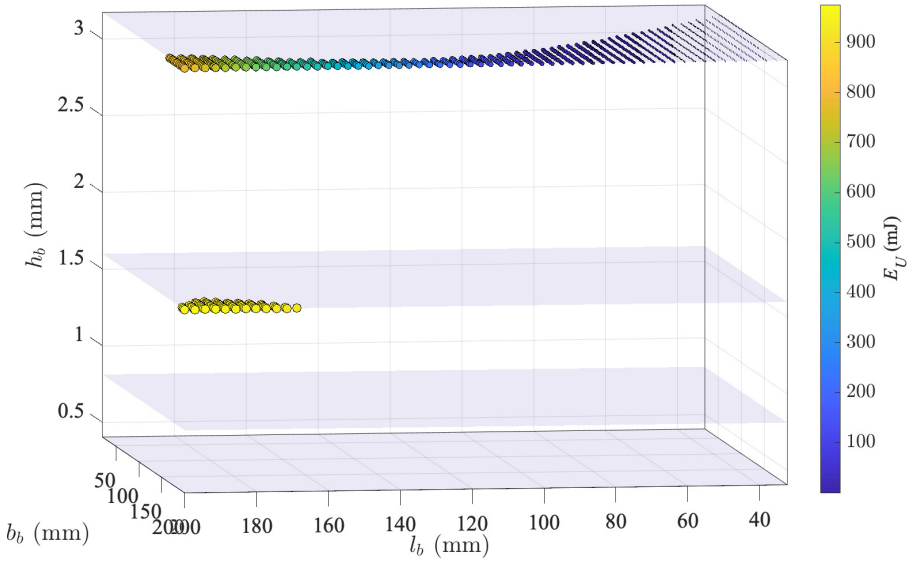

Figure 7.11: The electric energy E_U of sampled feasible candidates in design space when $n_r = 2$, $n_p = 36$.

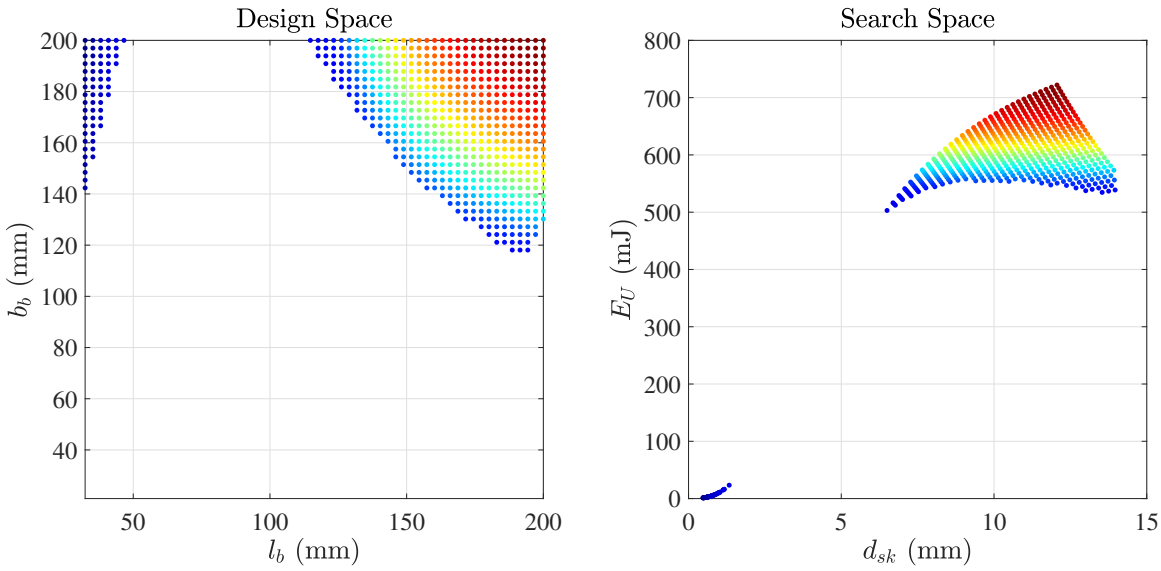

Figure 7.12: The feasible candidates in design space and their performance in search space of l_b and b_b for heavy trucks when $n_r = 3$, $n_p = 27$, $h_b = 1.6002mm$.

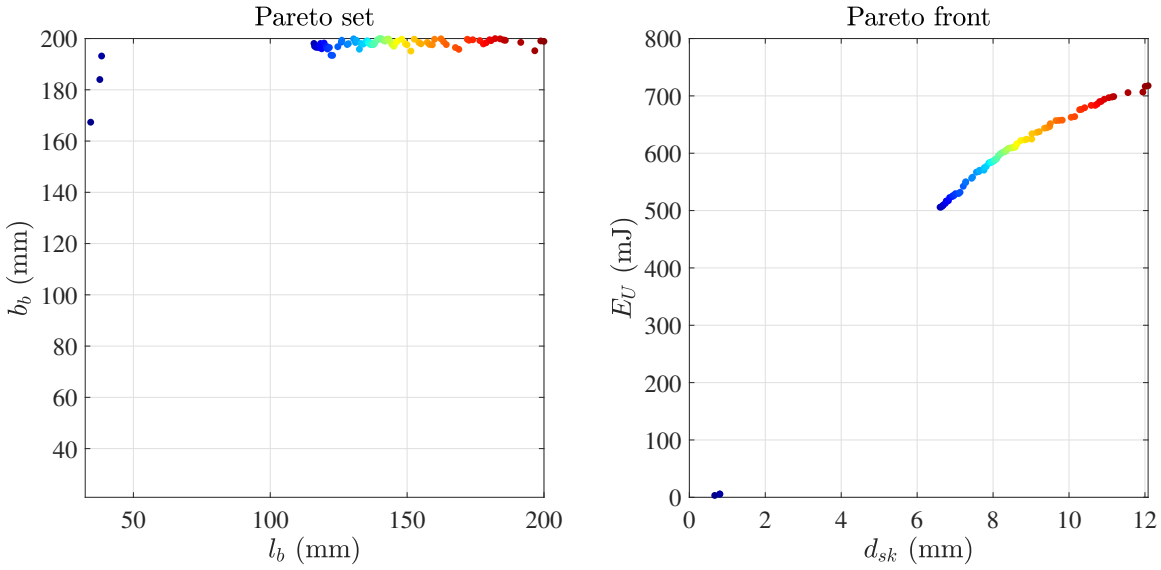

Figure 7.13: The Pareto set and front of PEHU for heavy trucks by multi-objective particle swarm optimization when $n_r = 3$, $n_p = 27$, $h_b = 1.6002mm$.

Table 4.2. It matches well with the results of discretized searching. The results of cases with other thickness are not presented here as they are dominated. Fig. 7.11 shows distribution of E_U in the 3D space of geometry, from which, we can clearly conclude the beam of size $l_b = 200mm$, $b_b = 200mm$ and $h_b = 1.6002mm$ has the highest power generation.

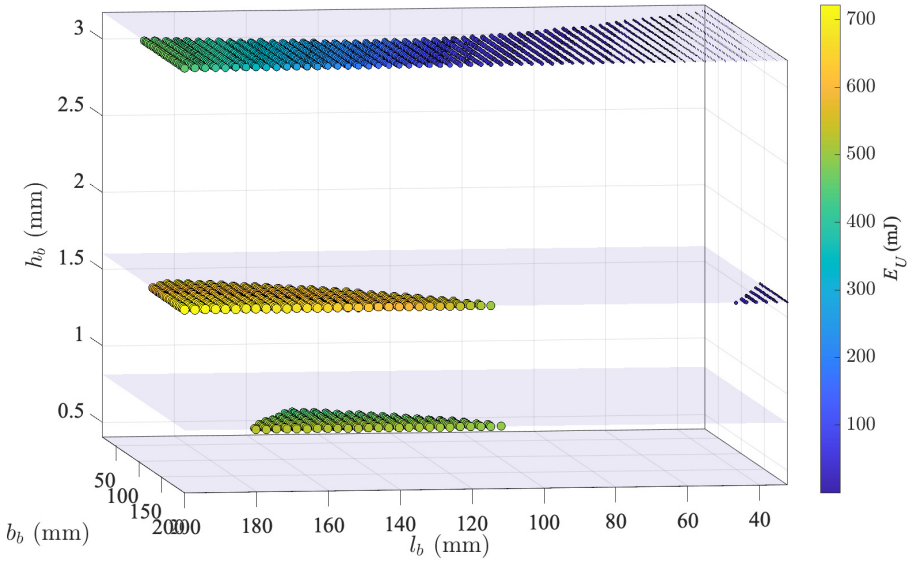

Figure 7.14: The electric energy E_U of sampled feasible candidates in design space when $n_r = 3$, $n_p = 27$.

This pattern is confirmed in other three cases as well. Figs. 7.12, 7.13 and 7.14 present the results of case $n_r = 3$ and $n_p = 27$. Figs. 7.15, 7.16 and 7.17 present the results of case $n_r = 4$ and $n_p = 22$. Fig. 7.3 7.18 7.19 present the results of case $n_r = 5$ and $n_p = 19$.

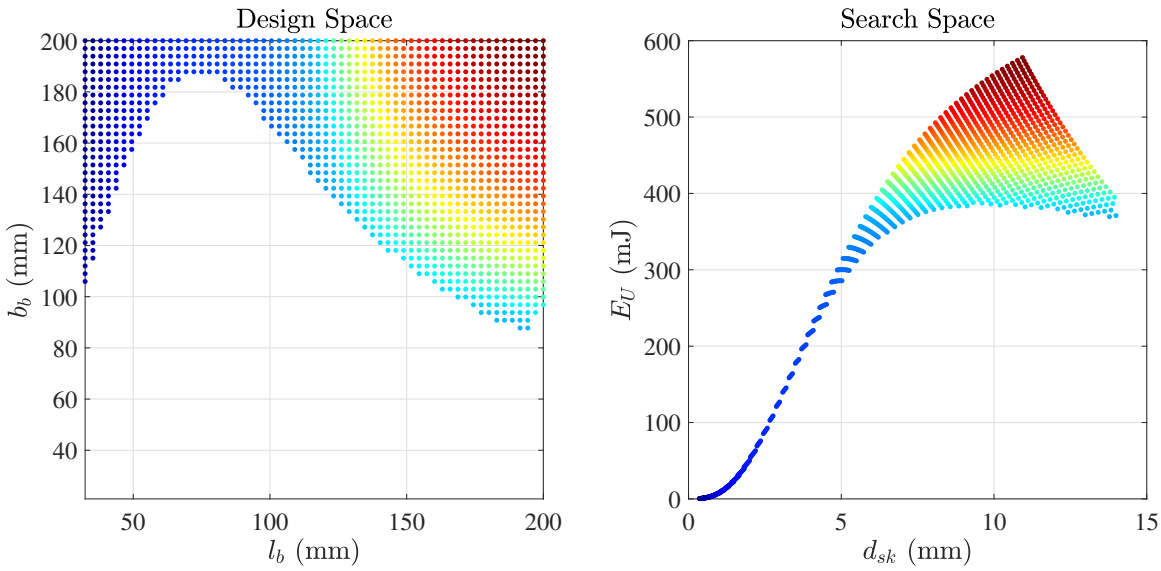

Figure 7.15: The feasible candidates in design space and their performance in search space of l_b and b_b for heavy trucks when $n_r = 4$, $n_p = 22$, $h_b = 1.6002mm$.

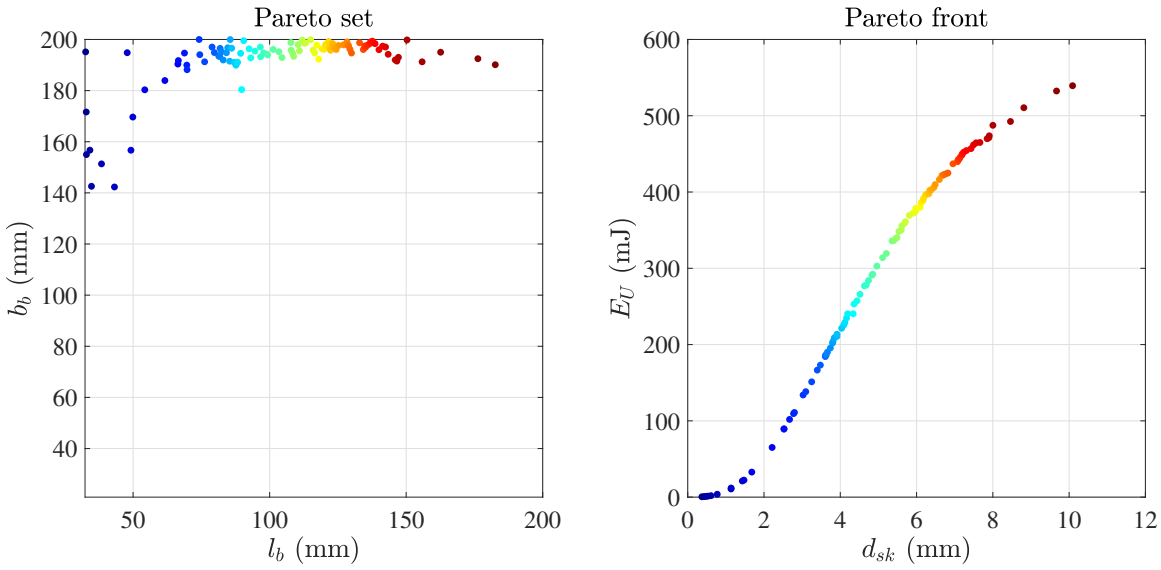

Figure 7.16: The Pareto set and front of PEHU for heavy trucks by multi-objective particle swarm optimization when $n_r = 4$, $n_p = 22$, $h_b = 1.6002mm$.

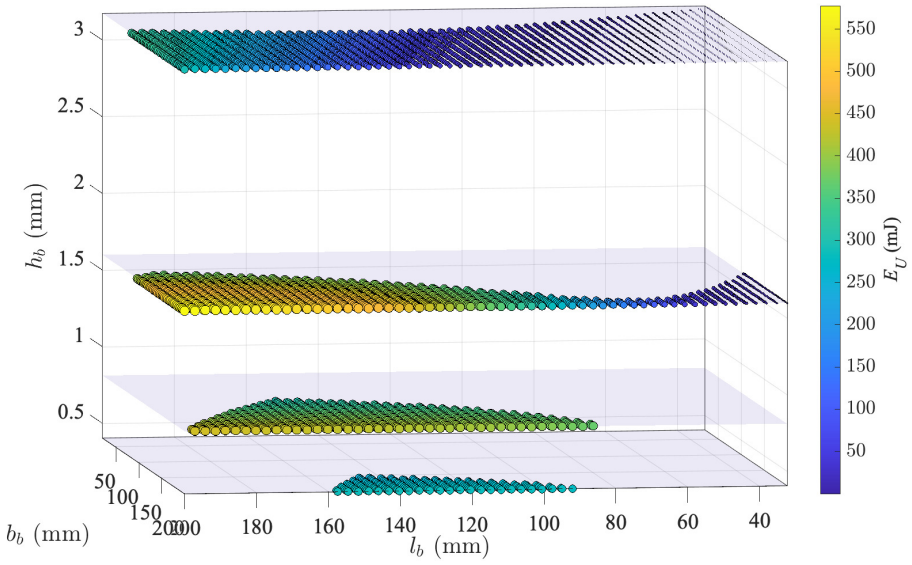

Figure 7.17: The electric energy E_U of sampled feasible candidates in design space when $n_r = 4$, $n_p = 22$.

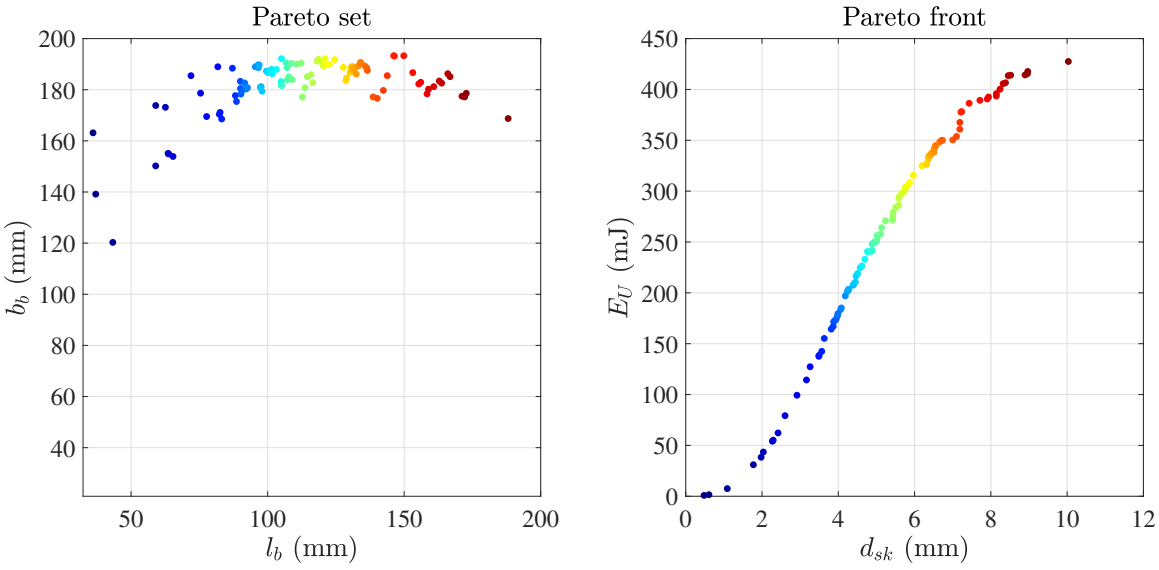

Figure 7.18: The Pareto set and front of PEHU for heavy trucks by multi-objective particle swarm optimization when $n_r = 5$, $n_p = 19$, $h_b = 1.6002mm$.

7.2 Energy Density Estimate

The energy density ρ_E is important to evaluate the performance of PEHS in application for heavy trucks on a large scale, which is the generated open-circuit electric energy by the PEHS with one passage of a 5-axis heavy truck with weight $80,000$ lbs over a 1 meter long lane where the energy harvesting technology is implemented. It can be estimated as

$$\rho_E = 10 \times n_r \times n_c \times n_l \times E_U \ , J/(m.pass.lane) \tag{7.3}$$

where n_l is the number of rows of the PEHUs in one meter long lane, which is assumed to be 4.

Then, the harvested energy E of the PEHS on a large scale can be estimated by

$$E = \rho_E \times L_{rd} \times N_{lane} \times N_{pas} \ , (J/year) \tag{7.4}$$

where L_{rd} is the length of the implemented roadway, N_{lane} is the number of lanes, N_{pas} is the number of passages of traffic in one year. Here, we assume that the traffic follows the 3 second safety rule all day long, $N_{pas} = \frac{365 \times 24 \times 3600}{3}$, and implementation in 1 mile in a lane. E can be expressed in terms of $kWh/year$ by divided by 3.6×10^6.

To compare with the design for mid-size vehicle, α_{Truck} is defined as

$$\alpha_{Truck} = E/(3.6 \times 10^6)/(8.12 \times 10^4), (times) \tag{7.5}$$

$8.12 \times 10^4 kWh/year$ is the harvested energy in the case of mid-size vehicle. α_{Truck} indicates how many times the energy that truck design is capable to generate than mid-size vehicle design on 1-mile scale in a year.

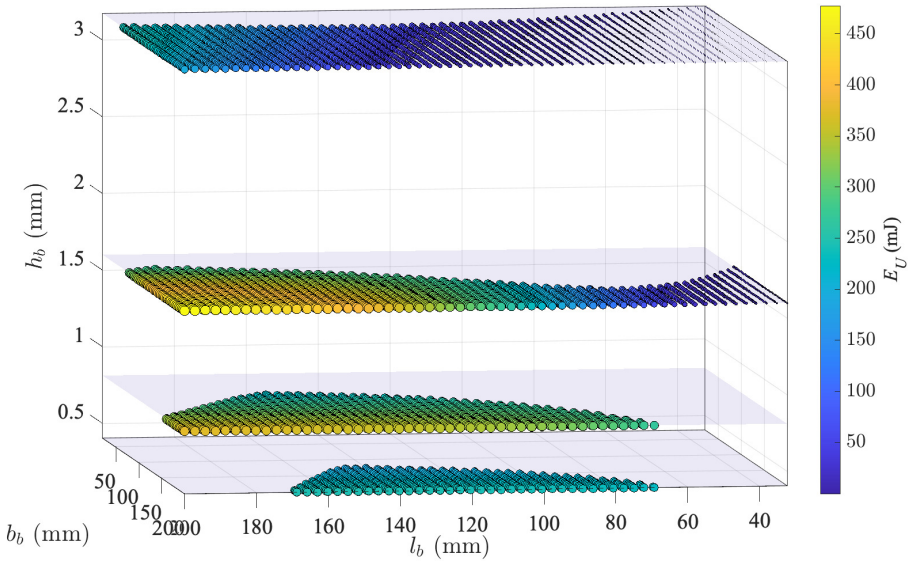

Figure 7.19: The electric energy E_U of sampled feasible candidates in design space when $n_r = 5$, $n_p = 19$.

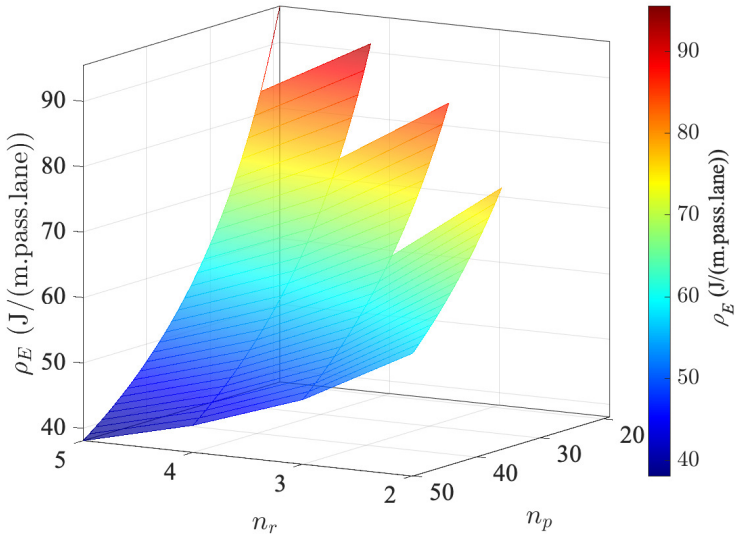

Figure 7.20: The energy density ρ_E of feasible candidates in design space of n_r and n_p for heavy trucks when $l_b = 200mm$, $b_b = 200mm$, $h_b = 1.6002mm$.

The energy density not only depend on the capability of PEHU, but also the systematic layout. It means that the optimal design of PEHU with highest E_U can not guarantee the highest energy density of PEHS. To find the system design with highest energy density, a search in the space of n_r and n_p is necessary. Fig. 7.20 illustrates the distribution of energy density in the design space. The relationship between ρ_E and d_{sk} with respect to n_r and n_p is shown in Fig. 7.21. The relationship between generated energy E and d_{sk} is shown in Fig. 7.22.

It is clear that the highest energy density of $95.51 J/(m.pass.lane)$ belongs to the design of $n_r = 5$ and $n_p = 19$, corresponding PEHS is able to generated $4.49 \times 10^5 kWh$ in a year. In addition, it has the smallest d_{sk} of $10.12mm$. If manufacturing cost and realization of mathematics model are taken into account, optimal designs in other cases with $n_r \in \{1, 2, 3\}$ should be considered for potential advantages. Four selected optimal designs for heavy trucks and their static properties are listed in Table 7.1.

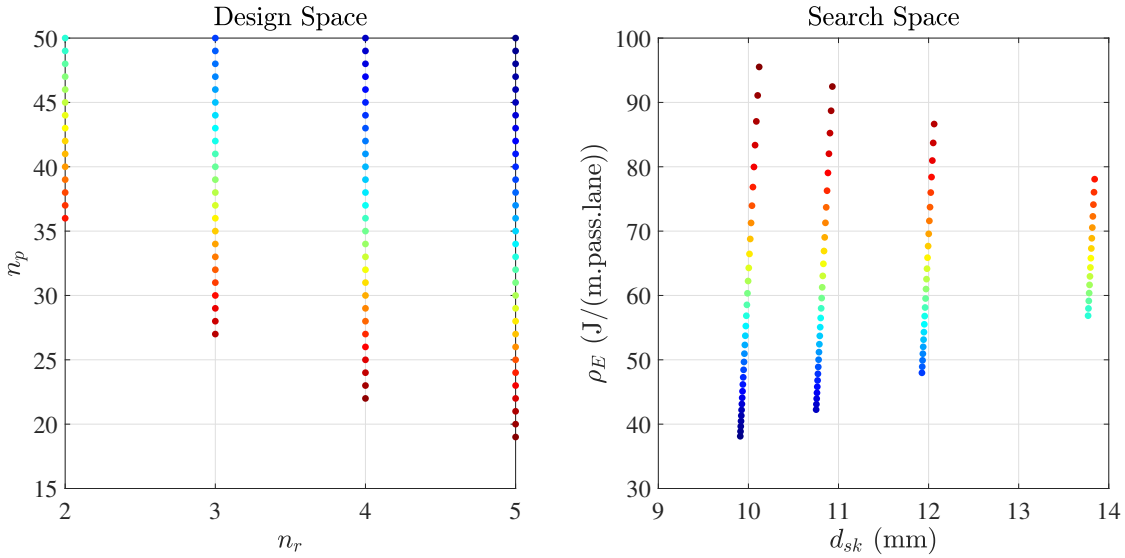

Figure 7.21: The energy density ρ_E and sinking displacement d_{sk} of feasible candidates in design space of n_r and n_p for heavy trucks when $l_b = 200mm$, $b_b = 200mm$, $h_b = 1.6002mm$.

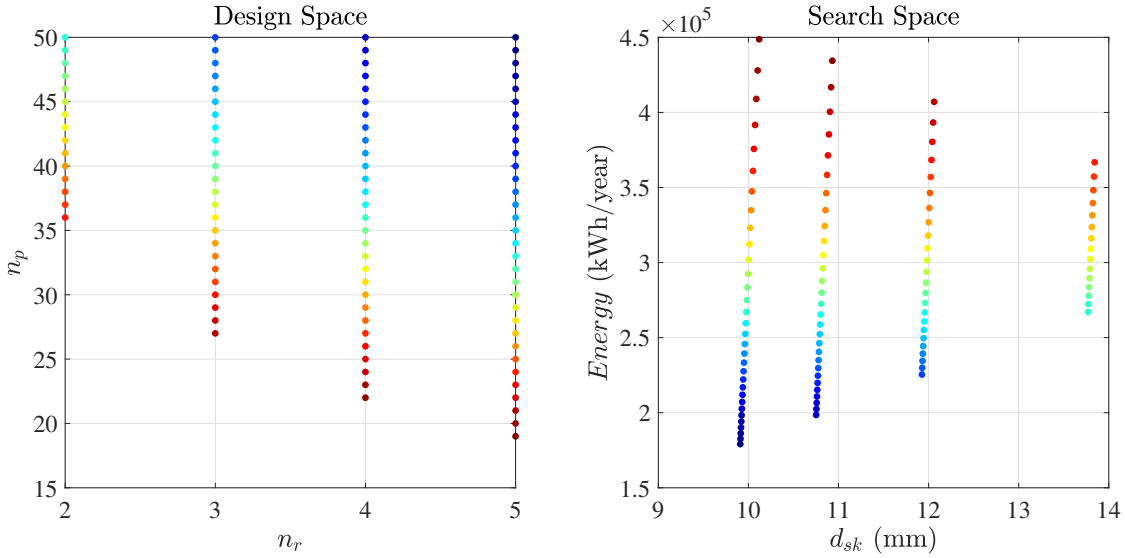

Figure 7.22: The harvested energy E and sinking displacement d_{sk} of feasible candidates in design space of n_r and n_p for heavy trucks when $l_b = 200mm$, $b_b = 200mm$, $h_b = 1.6002mm$.

Table 7.1: Selected optimal designs for heavy trucks and their static properties.

Parameters	Optimal 1	Optimal 2	Optimal 3	Optimal 4	Units
l_b	200	200	200	200	mm
h_b	1.6	1.6	1.6	1.6	mm
b_b	200	200	200	200	mm
n_r	2	3	4	5	N/A
n_p	36	27	22	19	N/A
n_c	1	1	1	1	N/A
E_U	975.87	722	577.92	477.57	mJ
d_{sk}	13.84	12.06	10.93	10.12	mm
V_U	105.25	104.54	103.61	101.35	V
α_f	10.9	12.18	13.11	13.84	$times$
α_e	118.73	148.23	171.88	191.66	$times$
σ_{PZT}	109.89	109.14	108.18	105.82	MPa
$Max(\sigma_b)$	731.94	599.47	521.04	467.58	MPa
ρ_E	78.07	86.64	92.47	95.51	$J/(m.pass.lane)$
α_{Truck}	4.52	5.01	5.35	5.53	$times$
E	3.67	4.07	4.34	4.49	$10^5 kWh/year$

7.3 Conclusions

In this chapter, the optimal designs for traffic of heavy truck have been investigated based on the modeling and analysis tools that we developed for mid-size vehicle. The multi-objective optimal design was developed for heavy trucks. A set of optimal designs and their performance are evaluated for future application. At the unit level, the conflicting factors include the sinking displacement and harvested energy. However, at the system level, the configuration of PEHUs matters as the loading on single PEHU varies under the same traffic load. Additionally, the configuration relates to the complexity of system and manufacturing cost. The optimal design #1 in Table 7.1 is the most economic among the selected designs, whereas, the optimal design #4 is more capable of achieving high energy density than others.

Chapter 8

SUMMARY

This dissertation has presented a systematic solution to high density energy harvesting from roadway traffic. A scalable high energy density PEHS, which is capable to generate electricity from traffic and store it in a DC battery, has been developed. A novel force amplification mechanism (FAM) was proposed and incorporated in PEH units, which amplified the harvested energy by a factor of 100. To quantify the performance of this invention in real road, a prototype system with length of 2.49 m was fabricated and tested. The reported system generated electric energy of 20.29 J and maximum open circuit voltage of 484 V from one passage of a mid-size vehicle at speed of 40 km/h, resulting in a high energy density of 15.37 J/(m.pass.lane).

The methodology that we used to investigate the potential of the conceptual force amplification mechanism is an interesting example of applying structural dynamics in piezoelectric energy harvesting. The mathematical modeling involves nonlinear beam theorem and finite element method. Mode expansion theorem was used to approximate the deformation of elastic beams, which has the advantage of significantly less computational cost in contrast to finite element analysis because

even only a few modes can construct a good estimate of the continuous displacement field. This is important when evolutionary algorithm is employed to explore the search space as it usually involves solving the similar problem for many times.

The numerical analysis of the design model was conducted using self-developed algorithm and code based on MATLAB without commercial finite element software. The development of the analysis tool is challenging, however, it enables the incorporation of mode expansion theorem, simplification of coefficients in equations and automated evolutionary searching for solutions to the multi-objective optimization problems. Afterwards, good knowledge of the design space can be obtained in a much more efficient manner compared to the iterative and tedious procedure using commercial finite element software. The MOPSO has been successfully applied in our practical engineering design based on proposed mathematical modeling. With the analysis tool available, we can efficiently explore the design spaces corresponding to different multi-objective problems as demonstrated in Chapter 7.

In this project, many innovative mechanical designs have been proposed. A cone-flat contact in PEHU was invented to realize the clamp boundary condition of nonlinear beams which is challenging due to the significantly increased load after amplification. This clamp design was found to be extremely effective in lab tests, and it held the clamp boundary condition even when the plastic deformation of Titanium beams occurred in some tests. The side plate design enables the compression loading acting at the middle of PEHU and each PEHU moving independantly from others. PEHUs stacked up vertically are designed to be oriented at 90 degrees for improving stability. Silicon sealant was used to make PEHT waterproof, which was validated in lab tests. Packaging of PEHTs for the implementation in roadway has been designed for real traffic condition.

Results of road tests showed high energy density of proposed PEHS and validated the mechanical design. The road test results also confirmed the driving safety and comfort, and showed that high vehicle speed is beneficial to energy harvesting. To the best of our knowledge, the proposed system has achieved the highest energy density reported in the literature. It holds great potential for power generation on large scale and enabling smart road self-powered.

The prototype PEHS demonstrates the promising future of harvesting energy from traffic by piezoelectric effect. Many interesting topics need to be investigated in the future to further advance this technology. Some are listed as follows.

1. Fatigue study of PEHU

   One of the objectives is that the serve life of PEH devices can last 20 years in the field. Fatigue is one possible type of failure. With traffic density assumption, we can estimate total number of compression load cycles that a PEHU should withstand to survive in 20 years. Following 3-second safety rule, the maximum number of cycles $Nload_{max}$ can be estimated as.

$$Nload_{max} = (20 \times 365 \times 24 \times 60 \times 60)/3 = 2.1 \times 10^8 cycles \tag{8.1}$$

   To make PEHU durable enough, the maximum stress in Titanium alloy should below $\sim$ 500MPa according to the SN curve of Ti6AL4V alloy. A fatigue test is necessary to validate the reliability. If the current design fails in fatigue test, measures to reduce the max stress in beams should be taken into account.

2. New design for PEHU

   The selected design of PEHU was found in the design space of rectangle beam with uniform thickness. There maybe better designs in other similar configurations. It would be interesting to explore the extended design spaces with more complicated geometry, such as beams of varying width along the length, beams of varying thickness along the length, and the combination of both. The methodology demonstrated in this thesis can be an useful reference.

3. New packaging of PEHUs

   The PEHT and PEHB serve as the packaging of PEHUs for up-scaled applications. Exploration of other packaging methods that enable easier manufacturing and assembly efforts and low cost will be beneficial to large-scale application. In addition to that, materials selection for waterproof sealant and seal cover of PEHT is of great importance for long-term service. Since the interaction between wheels and PEH devices is extremely violent, the seal design and material for PEH devices should be extremely durable.

4. High efficient energy storage circuit

   The energy storage circuit is crucial to utilize the harvested electricity for further applications. The circuit design should be optimized for different application. For example, in large scale implementation, the generated electric signal can be continuous if the system is long enough. The rectifier bridge is useful to prevent charges from spreading out to PEH devices which are not in working mode. This can help maintain the generated voltage high and avoid unnecessary electric energy loss. If the system is too long, it may need to be segmented for better efficiency. In small scale implementation, the generated

electricity will be discontinuous and impulsive, which is not good for battery storage. Instead, an appropriate capacitor may be a good choice. To sum up, the circuit design needs to be optimized with consideration of the mechanical system design and the use plan of the harvested energy.

5. Road surface design

   The PEHU acts as a nonlinear spring which causes unwanted sinking displacement during vehicles' passing over. We have achieved drive safety and comfort in current design. However, it is not clear yet whether the performance is satisfying for long term. The nylon cover that we used as the road surface needs to be validated for all weather conditions and durability in 20 years. Noise is another topic that should be studied in road surface design in the future.

6. Effect on gas consumption

   The intention of PEH is to harvest the wasted mechanical energy of vehicles that dissipate in the interaction between wheels and road. The input force of PEH system is the vertical load which includs the friction and dynamic reaction, and gravity. The implementation of PEHS will have effects on the friction and dynamic reaction compared to the normal roadway. In addition, as part of the input energy, the work done by the gravity originally comes from the gas consumption, although this energy is significantly less than the kinetic energy of vehicles. Therefore, people may have concern about the effect on gas consumption. In the future, experiments can be designed and conducted to evaluate this effect.

7. Applications in self-powered electronics

The proposed PEHS from traffic is a power supply of utility value. It is capable to power many kinds of electronics with appropriate implementation scale and energy management. Therefore, it can be part of self-powered electronic equipment for smart road. For example, the feasibility of self-powered weight-in-motion system is worth exploring. The sense nature of PZT supports the estimate of vehicle weight, and the harvested energy can be used to power data collection and wireless transportation. This system can be totally independent from the power grid and applied in rural roadway.

BIBLIOGRAPHY

[1] M. Lee, C.-Y. Chen, S. Wang, S. N. Cha, Y. J. Park, J. M. Kim, L.-J. Chou, Z. L. Wang, A hybrid piezoelectric structure for wearable nanogenerators, Advanced Materials 24 (13) (2012) 1759–1764.

[2] Q.-L. Zhao, G.-P. He, J.-J. Di, W.-L. Song, Z.-L. Hou, P.-P. Tan, D.-W. Wang, M.-S. Cao, Flexible semitransparent energy harvester with high pressure sensitivity and power density based on laterally aligned PZT single-crystal nanowires, ACS Applied Materials & Interfaces 9 (29) (2017) 24696–24703.

[3] J.-H. Lee, J. Y. Park, E. B. Cho, T. Y. Kim, S. A. Han, T.-H. Kim, et al., Reliable piezoelectricity in bilayer WSe_2 for piezoelectric nanogenerators, Advanced Materials 29 (29) (2017) 1606667.

[4] C. K. Jeong, K.-I. Park, J. Ryu, G.-T. Hwang, K. J. Lee, Large-area and flexible lead-free nanocomposite generator using alkaline niobate particles and metal nanorod filler, Advanced Functional Materials 24 (18) (2014) 2620–2629.

[5] K.-I. Park, J. H. Son, G.-T. Hwang, C. K. Jeong, J. Ryu, M. Koo, et al., Highly-efficient, flexible piezoelectric PZT thin film nanogenerator on plastic substrates, Advanced Materials 26 (16) (2014) 2514–2520.

[6] D.-J. Shin, J.-H. Ji, J. Kim, G. H. Jo, S.-J. Jeong, J.-H. Koh, Enhanced flexible piezoelectric energy harvesters based on $BaZrTiO_3 - BaCaTiO_3$ nanoparticles/PVDF composite films with Cu floating electrodes, Journal of Alloys and Compounds 802 (2019) 562–572.

[7] S. Zhou, J. Cao, D. J. Inman, J. Lin, S. Liu, Z. Wang, Broadband tristable energy harvester: Modeling and experiment verification, Applied Energy 133 (2014) 33–39.

[8] C. Wang, Q. Zhang, W. Wang, Low-frequency wideband vibration energy harvesting by using frequency up-conversion and quin-stable nonlinearity, Journal of Sound and Vibration 399 (2017) 169–181.

[9] C. Wang, Q. Zhang, W. Wang, J. Feng, A low-frequency, wideband quad-stable energy harvester using combined nonlinearity and frequency up-conversion by cantilever-surface contact, Mechanical Systems and Signal Processing 112 (2018) 305–318.

[10] S. Sun, P. W. Tse, Modeling of a horizontal asymmetric U-shaped vibration-based piezoelectric energy harvester (U-VPEH), Mechanical Systems and Signal Processing 114 (2019) 467–485.

[11] H. Fu, E. M. Yeatman, Rotational energy harvesting using bi-stability and frequency up-conversion for low-power sensing applications: Theoretical modelling and experimental validation, Mechanical Systems and Signal Processing 125 (2019) 229–244.

[12] S.-K. Lai, C. Wang, L.-H. Zhang, A nonlinear multi-stable piezomagnetoelastic harvester array for low-intensity, low-frequency, and broadband vibrations, Mechanical Systems and Signal Processing 122 (2019) 87–102.

[13] S. Bouhedma, Y. Rao, A. Schütz, C. Yuan, S. Hu, F. Lange, T. Bechtold, D. Hohlfeld, System-level model and simulation of a frequency-tunable vibration energy harvester, Micromachines 11 (1) (2020) 91.

[14] F. Huet, F. Formosa, A. Badel, J.-F. Capsal, M. Lallart, Vibration energy harvesting device using P(VDF-TrFE) hybrid fluid diaphragm, Sensors and Actuators A: Physical 247 (2016) 12–23.

[15] Z. Xiao, T.-Q. Yang, Y. Dong, X.-C. Wang, Energy harvester array using piezoelectric circular diaphragm for broadband vibration, Applied Physics Letters 104 (22) (2014) 223904.

[16] F. Shu, T. Yang, Y. Liu, Enhancement of power output by a new stress-applied mode on circular piezoelectric energy harvester, AIP Advances 8 (4) (2018) 045102.

[17] Y. Han, Y. Li, Y. Yang, M. Li, T. Yang, Improvement of uneven charge distribution on piezoelectric circular diaphragm with notched-substrate, AIP Advances 10 (4) (2020) 045330.

[18] Y. Wu, J. Qiu, S. Zhou, H. Ji, Y. Chen, S. Li, A piezoelectric spring pendulum oscillator used for multi-directional and ultra-low frequency vibration energy harvesting, Applied Energy 231 (2018) 600–614.

[19] R. Hua, H. Liu, H. Yang, Y. Wang, J. Ferrante, A nonlinear interface integrated lever mechanism for piezoelectric footstep energy harvesting, Applied Physics Letters 113 (5) (2018) 053902.

[20] Y.-H. Shin, I. Jung, M.-S. Noh, J. H. Kim, J.-Y. Choi, S. Kim, C.-Y. Kang, Piezoelectric polymer-based roadway energy harvesting via displacement amplification module, Applied Energy 216 (2018) 741–750.

[21] Z. Li, Z. Yang, H. E. Naguib, Introducing revolute joints into piezoelectric energy harvesters, Energy 192 (2020) 116604.

[22] J. Feenstra, J. Granstrom, H. Sodano, Energy harvesting through a backpack employing a mechanically amplified piezoelectric stack, Mechanical Systems and Signal Processing 22 (3) (2008) 721–734.

[23] M. Ling, J. Cao, Z. Jiang, J. Lin, Theoretical modeling of attenuated displacement amplification for multistage compliant mechanism and its application, Sensors and Actuators A: Physical 249 (2016) 15–22.

[24] F. Qian, T.-B. Xu, L. Zuo, Piezoelectric energy harvesting from human walking using a two-stage amplification mechanism, Energy 189 (2019) 116140.

[25] Q. Xu, Y. Li, Analytical modeling, optimization and testing of a compound bridge-type compliant displacement amplifier, Mechanism and Machine Theory 46 (2) (2011) 183–200.

[26] C. Chen, A. Sharafi, J.-Q. Sun, A high density piezoelectric energy harvesting device from highway traffic - design analysis and laboratory validation, Applied Energy 269 (2020) 115073.

[27] W. He, J. Zhang, A. Yang, Energy harvesting from low-frequency vibration using a shear-mode rectangular cymbal transducer with a piezoelectric array, IOP Conference Series: Earth and Environmental Science 227 (2019) 042058.

[28] X. Gao, C. Qiu, G. Li, M. Ma, S. Yang, Z. Xu, F. Li, High output power density of a shear-mode piezoelectric energy harvester based on $Pb(In_{1/2}Nb_{1/2})O_3 - Pb(Mg_{1/3}Nb_{2/3})O_3 - PbTiO_3$ single crystals, Applied Energy 271 (2020) 115193.

[29] S. Lee, S.-H. Bae, L. Lin, Y. Yang, C. Park, S.-W. Kim, et al., Super-flexible nanogenerator for energy harvesting from gentle wind and as an active deformation sensor, Advanced Functional Materials 23 (19) (2013) 2445–2449.

[30] S. Siddiqui, D.-I. Kim, E. Roh, L. T. Duy, T. Q. Trung, M. T. Nguyen, N.-E. Lee, A durable and stable piezoelectric nanogenerator with nanocomposite nanofibers embedded in an elastomer under high loading for a self-powered sensor system, Nano Energy 30 (2016) 434–442.

[31] S. Ye, C. Cheng, X. Chen, X. Chen, J. Shao, J. Zhang, et al., High-performance piezoelectric nanogenerator based on microstructured P(VDF-TrFE)/BNNTs composite for energy harvesting and radiation protection in space, Nano Energy 60 (2019) 701–714.

[32] X. Chou, J. Zhu, S. Qian, X. Niu, J. Qiao, X. Hou, et al., All-in-one filler-elastomer-based high-performance stretchable piezoelectric nanogenerator for kinetic energy harvesting and self-powered motion monitoring, Nano Energy 53 (2018) 550–558.

[33] X. Guan, B. Xu, J. Gong, Hierarchically architected polydopamine modified $BaTiO_3@P(VDF-TrFE)$ nanocomposite fiber mats for flexible piezoelectric nanogenerators and self-powered sensors, Nano Energy 70 (2020) 104516.

[34] Y. Kuang, T. Ruan, Z. J. Chew, M. Zhu, Energy harvesting during human walking to power a wireless sensor node, Sensors and Actuators A: Physical 254 (2017) 69–77.

[35] I. Izadgoshasb, Y. Y. Lim, N. Lake, L. Tang, R. V. Padilla, T. Kashiwao, Optimizing orientation of piezoelectric cantilever beam for harvesting energy from human walking, Energy Conversion and Management 161 (2018) 66–73.

[36] A. Jasim, G. Yesner, H. Wang, A. Safari, A. Maher, B. Basily, Laboratory testing and numerical simulation of piezoelectric energy harvester for roadway applications, Applied Energy 224 (2018) 438–447.

[37] H. Xiong, L. Wang, Piezoelectric energy harvester for public roadway: On-site installation and evaluation, Applied Energy 174 (2016) 101–107.

[38] L. Guo, Q. Lu, Modeling a new energy harvesting pavement system with experimental verification, Applied Energy 208 (2017) 1071–1082.

[39] I. Jung, Y.-H. Shin, S. Kim, J.-Y. Choi, C.-Y. Kang, Flexible piezoelectric polymer-based energy harvesting system for roadway applications, Applied Energy 197 (2017) 222–229.

[40] J. Kim, T. H. Lee, Y. Song, T. H. Sung, Robust design optimization of fixed-fixed beam piezoelectric energy harvester considering manufacturing uncertainties, Sensors and Actuators A: Physical 260 (2017) 236–246.

[41] W. Hwang, K.-B. Kim, J. Y. Cho, C. H. Yang, J. H. Kim, G. J. Song, et al., Watts-level road-compatible piezoelectric energy harvester for a self-powered temperature monitoring system on an actual roadway, Applied Energy 243 (2019) 313–320.

[42] Y. Bai, H. Jantunen, J. Juuti, Energy harvesting research: the road from single source to multisource, Advanced Materials 30 (34) (2018) 1707271.

[43] M. Z. Jacobson, M. A. Delucchi, Z. A. Bauer, S. C. Goodman, W. E. Chapman, M. A. Cameron, et al., 100 % clean and renewable wind, water, and sunlight all-sector energy roadmaps for 139 countries of the world, Joule 1 (1) (2017) 108–121.

[44] M. Safaei, H. A. Sodano, S. R. Anton, A review of energy harvesting using piezoelectric materials: state-of-the-art a decade later (2008-2018), Smart Materials and Structures 28 (11) (2019) 113001.

[45] C. Wei, X. Jing, A comprehensive review on vibration energy harvesting: Modelling and realization, Renewable and Sustainable Energy Reviews 74 (2017) 1–18.

[46] H. Li, C. Tian, Z. D. Deng, Energy harvesting from low frequency applications using piezoelectric materials, Applied Physics Reviews 1 (4) (2014) 041301.

[47] G.-T. Hwang, M. Byun, C. K. Jeong, K. J. Lee, Flexible piezoelectric thin-film energy harvesters and nanosensors for biomedical applications, Advanced Healthcare Materials 4 (5) (2015) 646–658.

[48] J. Briscoe, S. Dunn, Piezoelectric nanogenerators - a review of nanostructured piezoelectric energy harvesters, Nano Energy 14 (2015) 15–29.

[49] R. Caliò, U. B. Rongala, D. Camboni, M. Milazzo, C. Stefanini, G. D. Petris, C. M. Oddo, Piezoelectric energy harvesting solutions, Sensors 14 (3) (2014) 4755–4790.

[50] A. Toprak, O. Tigli, Piezoelectric energy harvesting: State-of-the-art and challenges, Applied Physics Reviews 1 (3) (2014) 031104.

[51] M. Gholikhani, H. Roshani, S. Dessouky, A. T. Papagiannakis, A critical review of roadway energy harvesting technologies, Applied Energy 261 (2020) 114388.

[52] Z. L. Wang, X. Wang, J. Song, J. Liu, Y. Gao, Piezoelectric nanogenerators for self-powered nanodevices, IEEE Pervasive Computing 7 (1) (2008) 49–55.

[53] C. D. et al., Conformal piezoelectric energy harvesting and storage from motions of the heart, lung, and diaphragm, Proceedings of the National Academy of Sciences 111 (5) (2014) 1927.

[54] H. W. Kim, S. Priya, K. Uchino, R. E. Newnham, Piezoelectric energy harvesting under high pre-stressed cyclic vibrations, Journal of Electroceramics 15 (1) (2005) 27–34.

[55] C. R. Bowen, H. A. Kim, P. M. Weaver, S. Dunn, Piezoelectric and ferroelectric materials and structures for energy harvesting applications, Energy & Environmental Science 7 (1) (2014) 25–44.

[56] G.-T. H. et al., Self-powered wireless sensor node enabled by an aerosol-deposited PZT flexible energy harvester, Advanced Energy Materials 6 (13) (2016) 1600237.

[57] X. Gao, J. Wu, Y. Yu, Z. Chu, H. Shi, S. Dong, Giant piezoelectric coefficients in relaxor piezoelectric ceramic PNN-PZT for vibration energy harvesting, Advanced Functional Materials 28 (30) (2018) 1706895.

[58] F. Li, D. Lin, Z. Chen, Z. Cheng, J. Wang, C. Li, et al., Ultrahigh piezoelectricity in ferroelectric ceramics by design, Nature Materials 17 (4) (2018) 349–354.

[59] K. Morimoto, I. Kanno, K. Wasa, H. Kotera, High-efficiency piezoelectric energy harvesters of c-axis-oriented epitaxial PZT films transferred onto stainless steel cantilevers, Sensors and Actuators A: Physical 163 (1) (2010) 428–432.

[60] D. Isarakorn, D. Briand, P. Janphuang, A. Sambri, S. Gariglio, J.-M. Triscone, et al., The realization and performance of vibration energy harvesting MEMS devices based on an epitaxial piezoelectric thin film, Smart Materials and Structures 20 (2) (2011) 025015.

[61] Y. Li, G. Lu, J. J. Chen, J. C. Jing, T. Huo, R. Chen, L. Jiang, Q. Zhou, Z. Chen, PMN-PT/epoxy 1-3 composite based ultrasonic transducer for dual-modality photoacoustic and ultrasound endoscopy, Photoacoustics 15 (2019) 100138.

[62] B. Ren, S. W. Or, X. Zhao, H. Luo, Energy harvesting using a modified rectangular cymbal transducer based on $0.71Pb(Mg_{1/3}Nb_{2/3})O_3-0.29PbTiO_3$ single crystal, Journal of Applied Physics 107 (3) (2010) 034501.

[63] M. A. Karami, O. Bilgen, D. J. Inman, M. I. Friswell, Experimental and analytical parametric study of single-crystal unimorph beams for vibration energy harvesting, IEEE Transactions on Ultrasonics, Ferroelectrics, and Frequency Control 58 (7) (2011) 1508–1520.

[64] S. Xu, G. Poirier, N. Yao, PMN-PT nanowires with a very high piezoelectric constant, Nano Letters 12 (5) (2012) 2238–2242.

[65] S. Xu, N. Yao, M. McAlpine, R. Register, Flexible piezoelectric PMN-PT nanowire-based nanocomposite and device, Nano Letters 13.

[66] Z. Yang, J. Zu, Comparison of PZN-PT, PMN-PT single crystals and PZT ceramic for vibration energy harvesting, Energy Conversion and Management 122 (2016) 321–329.

[67] Y. Chen, Y. Zhang, L. Zhang, F. Ding, O. G. Schmidt, Scalable single crystalline PMN-PT nanobelts sculpted from bulk for energy harvesting, Nano Energy 31 (2017) 239–246.

[68] H.-T. Oh, J.-Y. Lee, H.-Y. Lee, Mn-modified PMN-PZT [$Pb(Mg_{1/3}Nb_{2/3})O_3 - Pb(Zr,Ti)O_3$] single crystals for high power piezoelectric transducers, J. Korean Ceram. Soc 54 (2) (2017) 150–157.

[69] G.-T. Hwang, J. Yang, S. H. Yang, H.-Y. Lee, M. Lee, D. Y. Park, et al., A reconfigurable rectified flexible energy harvester via solid-state single crystal grown PMN-PZT, Advanced Energy Materials 5 (10) (2015) 1500051.

[70] D. H. Kim, H. J. Shin, H. Lee, C. K. Jeong, H. Park, G.-T. Hwang, et al., In vivo self-powered wireless transmission using biocompatible flexible energy harvesters, Advanced Functional Materials 27 (25) (2017) 1700341.

[71] K. Shibata, R. Wang, T. Tou, J. Koruza, Applications of lead-free piezoelectric materials, MRS Bulletin 43 (8) (2018) 612–616.

[72] K.-I. Park, S. Xu, Y. Liu, G.-T. Hwang, S.-J. L. Kang, Z. L. Wang, K. J. Lee, Piezoelectric $BaTiO_3$ thin film nanogenerator on plastic substrates, Nano Letters 10 (12) (2010) 4939–4943.

[73] K.-I. Park, M. Lee, Y. Liu, S. Moon, G.-T. Hwang, G. Zhu, et al., Flexible nanocomposite generator made of $BaTiO_3$ nanoparticles and graphitic carbons, Advanced Materials 24 (22) (2012) 2999–3004.

[74] A. Koka, Z. Zhou, H. A. Sodano, Vertically aligned $BaTiO_3$ nanowire arrays for energy harvesting, Energy & Environmental Science 7 (1) (2014) 288–296.

[75] M. Acosta, N. Novak, V. Rojas, S. Patel, R. Vaish, J. Koruza, G. A. Rossetti, J. Rödel, $BaTiO_3$-based piezoelectrics: Fundamentals, current status, and perspectives, Applied Physics Reviews 4 (4) (2017) 041305.

[76] M. Yuan, L. Cheng, Q. Xu, W. Wu, S. Bai, L. Gu, et al., Biocompatible nanogenerators through high piezoelectric coefficient $0.5Ba(Zr_{0.2}Ti_{0.8})O_3 - 0.5(Ba_{0.7}Ca_{0.3})TiO_3$ nanowires for in-vivo applications, Advanced Materials 26 (44) (2014) 7432–7437.

[77] L. Cheng, M. Yuan, L. Gu, Z. Wang, Y. Qin, T. Jing, Z. L. Wang, Wireless, power-free and implantable nanosystem for resistance-based biodetection, Nano Energy 15 (2015) 598–606.

[78] Y. Sun, Y. Chang, J. Wu, Y. Liu, L. Jin, S. Zhang, B. Yang, W. Cao, Ultrahigh energy harvesting properties in textured lead-free piezoelectric composites, Journal of Materials Chemistry A 7 (8) (2019) 3603–3611.

[79] J. Liu, B. Yang, L. Lu, X. Wang, X. Li, X. Chen, J. Liu, Flexible and lead-free piezoelectric nanogenerator as self-powered sensor based on electrospinning BZT-BCT/P(VDF-TrFE) nanofibers, Sensors and Actuators A: Physical 303 (2020) 111796.

[80] S. Bairagi, S. W. Ali, Influence of high aspect ratio lead-free piezoelectric fillers in designing flexible fibrous nanogenerators: Demonstration of significant high output voltage, Energy Technology 7 (10) (2019) 1900538.

[81] S. Bairagi, S. W. Ali, Effects of surface modification on electrical properties of KNN nanorod-incorporated PVDF composites, Journal of Materials Science 54 (17) (2019) 11462–11484.

[82] S. Bairagi, S. W. Ali, Flexible lead-free PVDF/SM-KNN electrospun nanocomposite based piezoelectric materials: Significant enhancement of energy harvesting efficiency of the nanogenerator, Energy 198 (2020) 117385.

[83] G. Zhu, A. C. Wang, Y. Liu, Y. Zhou, Z. L. Wang, Functional electrical stimulation by nanogenerator with 58 v output voltage, Nano Letters 12 (6) (2012) 3086–3090.

[84] C. Fei, X. Liu, B. Zhu, D. Li, X. Yang, Y. Yang, Q. Zhou, Aln piezoelectric thin films for energy harvesting and acoustic devices, Nano Energy 51 (2018) 146–161.

[85] I. Gablech, J. Klempa, J. Pekárek, P. Vyroubal, J. Hrabina, M. Holá, J. Kunz, J. Brodský, P. Neužil, Simple and efficient AlN-based piezoelectric energy harvesters, Micromachines 11 (2) (2020) 143.

[86] K. S. Ramadan, D. Sameoto, S. Evoy, A review of piezoelectric polymers as functional materials for electromechanical transducers, Smart Materials and Structures 23 (3) (2014) 033001.

[87] V. Strashilov, G. Alexieva, B. Vincent, V. Nguyen, D. Rouxel, Structural impact on piezoelectricity in PVDF and P(VDF-TrFE) thin films, Applied Physics A 118 (4) (2015) 1469–1477.

[88] W.-S. Jung, M.-J. Lee, M.-G. Kang, H. G. Moon, S.-J. Yoon, S.-H. Baek, C.-Y. Kang, Powerful curved piezoelectric generator for wearable applications, Nano Energy 13 (2015) 174–181.

[89] S. Kim, I. Towfeeq, Y. Dong, S. Gorman, A. M. Rao, G. Koley, P(VDF-TrFE) film on PDMS substrate for energy harvesting applications, Applied Sciences 8 (2) (2018) 213.

[90] S. Park, Y. Kim, H. Jung, J.-Y. Park, N. Lee, Y. Seo, Energy harvesting efficiency of piezoelectric polymer film with graphene and metal electrodes, Scientific Reports 7 (1) (2017) 1–8.

[91] W. Wu, L. Wang, Y. Li, F. Zhang, L. Lin, S. Niu, et al., Piezoelectricity of single-atomic-layer MoS_2 for energy conversion and piezotronics, Nature 514 (7523) (2014) 470–474.

[92] G.-J. Lee, M.-K. Lee, J.-J. Park, D. Y. Hyeon, C. K. Jeong, K.-I. Park, Piezoelectric energy harvesting from two-dimensional boron nitride nanoflakes, ACS Applied Materials & Interfaces 11 (41) (2019) 37920–37926.

[93] K.-A. N. Duerloo, M. T. Ong, E. J. Reed, Intrinsic piezoelectricity in two-dimensional materials, The Journal of Physical Chemistry Letters 3 (19) (2012) 2871–2876.

[94] M. N. Blonsky, H. L. Zhuang, A. K. Singh, R. G. Hennig, Ab initio prediction of piezoelectricity in two-dimensional materials, ACS Nano 9 (10) (2015) 9885–9891.

[95] R. Guo, Y. Guo, H. Duan, H. Li, H. Liu, Synthesis of orthorhombic perovskite-type $ZnSnO_3$ single-crystal nanoplates and their application in energy harvesting, ACS Applied Materials & Interfaces 9 (9) (2017) 8271–8279.

[96] Z. L. Wang, J. Song, Piezoelectric nanogenerators based on zinc oxide nanowire arrays, Science 312 (5771) (2006) 242.

[97] Z. L. Wang, Nanogenerators, self-powered systems, blue energy, piezotronics and piezo-phototronics - a recall on the original thoughts for coining these fields, Nano Energy 54 (2018) 477–483.

[98] X. Chen, S. Xu, N. Yao, Y. Shi, 1.6 V nanogenerator for mechanical energy harvesting using PZT nanofibers, Nano Letters 10 (6) (2010) 2133–2137.

[99] Y. Qi, J. Kim, T. D. Nguyen, B. Lisko, P. K. Purohit, M. C. McAlpine, Enhanced piezoelectricity and stretchability in energy harvesting devices fabricated from buckled PZT ribbons, Nano Letters 11 (3) (2011) 1331–1336.

[100] C. Chang, V. H. Tran, J. Wang, Y.-K. Fuh, L. Lin, Direct-write piezoelectric polymeric nanogenerator with high energy conversion efficiency, Nano Letters 10 (2) (2010) 726–731.

[101] N. Soin, T. H. Shah, S. C. Anand, J. Geng, W. Pornwannachai, P. Mandal, et al., Novel "3-d spacer" all fibre piezoelectric textiles for energy harvesting applications, Energy & Environmental Science 7 (5) (2014) 1670–1679.

[102] Y. Yu, H. Sun, H. Orbay, F. Chen, C. G. England, W. Cai, X. Wang, Biocompatibility and in vivo operation of implantable mesoporous pvdf-based nanogenerators, Nano Energy 27 (2016) 275–281.

[103] L. Persano, C. Dagdeviren, Y. Su, Y. Zhang, S. Girardo, D. Pisignano, Y. Huang, J. A. Rogers, High performance piezoelectric devices based on aligned arrays of nanofibers of poly(vinylidenefluoride-co-trifluoroethylene), Nature Communications 4 (1) (2013) 1633.

[104] G.-T. Hwang, H. Park, J.-H. Lee, S. Oh, K.-I. Park, M. Byun, et al., Self-powered cardiac pacemaker enabled by flexible single crystalline PMN-PT piezoelectric energy harvester, Advanced Materials 26 (28) (2014) 4880–4887.

[105] Q. Zheng, B. Shi, Z. Li, Z. L. Wang, Recent progress on piezoelectric and triboelectric energy harvesters in biomedical systems, Advanced Science 4 (7) (2017) 1700029.

[106] C. Jin, N. Hao, Z. Xu, I. Trase, Y. Nie, L. Dong, A. Closson, Z. Chen, J. X. J. Zhang, Flexible piezoelectric nanogenerators using metal-doped ZnO-PVDF films, Sensors and Actuators A: Physical 305 (2020) 111912.

[107] P. Pillatsch, E. M. Yeatman, A. S. Holmes, Magnetic plucking of piezoelectric beams for frequency up-converting energy harvesters, Smart Materials and Structures 23 (2) (2013) 025009.

[108] A. Erturk, D. J. Inman, A distributed parameter electromechanical model for cantilevered piezoelectric energy harvesters, Journal of Vibration and Acoustics 130 (4).

[109] A. Erturk, D. J. Inman, An experimentally validated bimorph cantilever model for piezoelectric energy harvesting from base excitations, Smart Materials and Structures 18 (2) (2009) 025009.

[110] M. Khazaee, L. Rosendahl, A. Rezania, A comprehensive electromechanically coupled model for non-uniform piezoelectric energy harvesting composite laminates, Mechanical Systems and Signal Processing 145 (2020) 106927.

[111] S.-B. Kim, H. Park, S.-H. Kim, H. C. Wikle, J.-H. Park, D.-J. Kim, Comparison of mems pzt cantilevers based on d_{31} and d_{33} modes for vibration energy harvesting, Journal of Microelectromechanical Systems 22 (1) (2012) 26–33.

[112] G. Tang, B. Yang, J. q. Liu, B. Xu, H. y. Zhu, C. s. Yang, Development of high performance piezoelectric d_{33} mode MEMS vibration energy harvester based on PMN-PT single crystal thick film, Sensors and Actuators A: Physical 205 (2014) 150–155.

[113] M. Peddigari, G.-Y. Kim, C. H. Park, Y. Min, J.-W. Kim, C.-W. Ahn, et al., A comparison study of fatigue behavior of hard and soft piezoelectric single crystal macro-fiber composites for vibration energy harvesting, Sensors 19 (9) (2019) 2196.

[114] S. Zhou, J. Cao, A. Erturk, J. Lin, Enhanced broadband piezoelectric energy harvesting using rotatable magnets, Applied Physics Letters 102 (17) (2013) 173901.

[115] Z. Yang, S. Zhou, J. Zu, D. Inman, High-performance piezoelectric energy harvesters and their applications, Joule 2 (4) (2018) 642–697.

[116] H. Liu, J. Zhong, C. Lee, S.-W. Lee, L. Lin, A comprehensive review on piezoelectric energy harvesting technology: Materials, mechanisms, and applications, Applied Physics Reviews 5 (4) (2018) 041306.

[117] M. F. Daqaq, R. Masana, A. Erturk, D. D. Quinn, On the role of nonlinearities in vibratory energy harvesting: A critical review and discussion, Applied Mechanics Reviews 66 (4).

[118] F. Goldschmidtboeing, P. Woias, Characterization of different beam shapes for piezoelectric energy harvesting, Journal of Micromechanics and Microengineering 18 (10) (2008) 104013.

[119] S. B. Ayed, A. Abdelkefi, F. Najar, M. R. Hajj, Design and performance of variable-shaped piezoelectric energy harvesters, Journal of Intelligent Material Systems and Structures 25 (2) (2013) 174–186.

[120] S. Nathan, A. Abdessattar, P. Shashank, Comparative analysis of one-dimensional and two-dimensional cantilever piezoelectric energy harvesters, Energy Harvesting and Systems 1 (3-4) (2014) 209–216.

[121] N. Sharpes, A. Abdelkefi, S. Priya, Two-dimensional concentrated-stress low-frequency piezoelectric vibration energy harvesters, Applied Physics Letters 107 (9) (2015) 093901.

[122] D. Upadrashta, Y. Yang, Trident-shaped multimodal piezoelectric energy harvester, Journal of Aerospace Engineering 31 (5) (2018) 04018070.

[123] J. M. Ramírez, C. D. Gatti, S. P. Machado, M. Febbo, A piezoelectric energy harvester for rotating environment using a linked e-shape multi-beam, Extreme Mechanics Letters 27 (2019) 8–19.

[124] L. Gu, C. Livermore, Impact-driven, frequency up-converting coupled vibration energy harvesting device for low frequency operation, Smart Materials and Structures 20 (4) (2011) 045004.

[125] Y. Zhang, C. S. Cai, A retrofitted energy harvester for low frequency vibrations, Smart Materials and Structures 21 (7) (2012) 075007.

[126] K. Ashraf, M. H. M. Khir, J. O. Dennis, Z. Baharudin, A wideband, frequency up-converting bounded vibration energy harvester for a low-frequency environment, Smart Materials and Structures 22 (2) (2013) 025018.

[127] M. A. Halim, J. Y. Park, Theoretical modeling and analysis of mechanical impact driven and frequency up-converted piezoelectric energy harvester for low-frequency and wide-bandwidth operation, Sensors and Actuators A: Physical 208 (2014) 56–65.

[128] S. C. Stanton, C. C. McGehee, B. P. Mann, Reversible hysteresis for broadband magnetopiezoelastic energy harvesting, Applied Physics Letters 95 (17) (2009) 174103.

[129] R. L. Harne, K. W. Wang, A review of the recent research on vibration energy harvesting via bistable systems, Smart Materials and Structures 22 (2) (2013) 023001.

[130] D. Hoffmann, A. Willmann, T. Hehn, B. Folkmer, Y. Manoli, A self-adaptive energy harvesting system, Smart Materials and Structures 25 (3) (2016) 035013.

[131] D. D. Quinn, A. L. Triplett, L. A. Bergman, A. F. Vakakis, Comparing linear and essentially nonlinear vibration-based energy harvesting, Journal of Vibration and Acoustics 133 (1).

[132] G. Shi, Y. Xia, Y. Yang, J. Chen, Y. Peng, H. Xia, X. Wang, L. Qian, A sensor-less self-tuning resonance system for piezoelectric broadband vibration energy harvesting, IEEE Transactions on Industrial Electronics (2020) 1–1.

[133] S. Bouhedma, Y. Zheng, F. Lange, D. Hohlfeld, Magnetic frequency tuning of a multimodal vibration energy harvester, Sensors 19 (5) (2019) 1149.

[134] C. Mo, L. J. Radziemski, W. W. Clark, Analysis of piezoelectric circular diaphragm energy harvesters for use in a pressure fluctuating system, Smart Materials and Structures 19 (2) (2010) 025016.

[135] C. Mo, L. J. Radziemski, W. W. Clark, Experimental validation of energy harvesting performance for pressure-loaded piezoelectric circular diaphragms, Smart Materials and Structures 19 (7) (2010) 075010.

[136] M. Deterre, E. Lefeuvre, Y. Zhu, M. Woytasik, B. Boutaud, R. D. Molin, Micro blood pressure energy harvester for intracardiac pacemaker, Journal of Microelectromechanical Systems 23 (3) (2014) 651–660.

[137] M. Bakhtiari-Shahri, H. Moeenfard, Energy harvesting from unimorph piezoelectric circular plates under random acoustic and base acceleration excitations, Mechanical Systems and Signal Processing 130 (2019) 502–523.

[138] X.-R. Chen, T.-Q. Yang, W. Wang, X. Yao, Vibration energy harvesting with a clamped piezoelectric circular diaphragm, Ceramics International 38 (2012) S271–S274.

[139] Y. Yang, S. Wang, P. Stein, B.-X. Xu, T. Yang, Vibration-based energy harvesting with a clamped piezoelectric circular diaphragm: analysis and identification of optimal structural parameters, Smart Materials and Structures 26 (4) (2017) 045011.

[140] Y. Yang, Y. Li, Y. Guo, B.-X. Xu, T. Yang, Improved vibration-based energy harvesting by annular mass configuration of piezoelectric circular diaphragms, Smart Materials and Structures 27 (3) (2018) 035004.

[141] T.-C. Yuan, J. Yang, L.-Q. Chen, Nonlinear dynamics of a circular piezoelectric plate for vibratory energy harvesting, Communications in Nonlinear Science and Numerical Simulation 59 (2018) 651–656.

[142] M. H. Ansari, M. A. Karami, Energy harvesting from controlled buckling of piezoelectric beams, Smart Materials and Structures 24 (11) (2015) 115005.

[143] J. H. Ahn, W. S. Hwang, J. Y. Cho, S. Y. Jeong, G. J. Song, S. D. Hong, T. H. Sung, S. Jeong, H. H. Yoo, A bending-type piezoelectric energy harvester with a displacement-amplifying mechanism for smart highways, Journal of the Korean Physical Society 73 (3) (2018) 330–337.

[144] H. Yang, L. Wang, B. Zhou, Y. Wei, Q. Zhao, A preliminary study on the highway piezoelectric power supply system, International Journal of Pavement Research and Technology 11 (2) (2018) 168–175.

[145] F. Qian, T.-B. Xu, L. Zuo, Material equivalence, modeling and experimental validation of a piezoelectric boot energy harvester, Smart Materials and Structures 28 (7) (2019) 075018.

[146] A. T. Papagiannakis, A. Montoya, S. Dessouky, J. Helffrich, Development and evaluation of piezoelectric prototypes for roadway energy harvesting, Journal of Energy Engineering 143 (5) (2017) 04017034.

[147] H. Zhang, K. Huang, Z. Zhang, T. Xiang, L. Quan, Piezoelectric energy harvesting from roadways based on pavement compatible package, Journal of Applied Mechanics 86 (9).

[148] H. Roshani, P. Jagtap, S. Dessouky, A. Montoya, A. T. Papagiannakis, Theoretical and experimental evaluation of two roadway piezoelectric-based energy harvesting prototypes, Journal of Materials in Civil Engineering 30 (2) (2018) 04017264.

[149] H. Xiao, X. Wang, S. John, A multi-degree of freedom piezoelectric vibration energy harvester with piezoelectric elements inserted between two nearby oscillators, Mechanical Systems and Signal Processing 68-69 (2016) 138–154.

[150] T.-B. Xu, E. J. Siochi, J. H. Kang, L. Zuo, W. Zhou, X. Tang, X. Jiang, Energy harvesting using a PZT ceramic multilayer stack, Smart Materials and Structures 22 (6) (2013) 065015.

[151] H. W. Kim, A. Batra, S. Priya, K. Uchino, D. Markley, R. E. Newnham, H. F. Hofmann, Energy harvesting using a piezoelectric "cymbal" transducer in dynamic environment, Japanese Journal of Applied Physics 43 (9A) (2004) 6178–6183.

[152] H. Kim, S. Priya, K. Uchino, Modeling of piezoelectric energy harvesting using cymbal transducers, Japanese Journal of Applied Physics 45 (7) (2006) 5836–5840.

[153] H. Zhao, J. Ling, J. Yu, A comparative analysis of piezoelectric transducers for harvesting energy from asphalt pavement, Journal of the Ceramic Society of Japan 120 (1404) (2012) 317–323.

[154] J. Ueda, T. W. Secord, H. H. Asada, Large effective-strain piezoelectric actuators using nested cellular architecture with exponential strain amplification mechanisms, IEEE/ASME Transactions on Mechatronics 15 (5) (2010) 770–782.

[155] W. Zhou, L. Zuo, A novel piezoelectric multilayer stack energy harvester with force amplification, in: Proceedings of ASME 2013 International Design Engineering Technical Conferences and Computers and Information in Engineering Conference, Vol. Volume 8: 22nd Reliability, Stress Analysis, and Failure Prevention Conference; 25th Conference on Mechanical Vibration and Noise, 2013.

[156] W. Q. Liu, A. Badel, F. Formosa, Y. P. Wu, A. Agbossou, Novel piezoelectric bistable oscillator architecture for wideband vibration energy harvesting, Smart Materials and Structures 22 (3) (2013) 035013.

[157] L. Wang, S. Chen, W. Zhou, T.-B. Xu, L. Zuo, Piezoelectric vibration energy harvester with two-stage force amplification, Journal of Intelligent Material Systems and Structures 28 (9) (2016) 1175–1187.

[158] W. Chen, Y. Wang, W. Deng, Deformable force amplification frame promoting piezoelectric stack energy harvesting: Parametric model, experiments and energy analysis, Journal of Intelligent Material Systems and Structures 28 (7) (2016) 827–836.

[159] Y. Wang, W. Chen, P. Guzman, Piezoelectric stack energy harvesting with a force amplification frame: Modeling and experiment, Journal of Intelligent Material Systems and Structures 27 (17) (2016) 2324–2332.

[160] G. Ye, W. Li, Y. Wang, X. Yang, L. Yu, Kinematics analysis of bridge-type micro-displacement mechanism based on flexure hinge, in: Proceedings of The 2010 IEEE International Conference on Information and Automation, 2010, pp. 66–70.

[161] M. Ling, J. Cao, M. Zeng, J. Lin, D. J. Inman, Enhanced mathematical modeling of the displacement amplification ratio for piezoelectric compliant mechanisms, Smart Materials and Structures 25 (7) (2016) 075022.

[162] P. Liu, P. Yan, A new model analysis approach for bridge-type amplifiers supporting nano-stage design, Mechanism and Machine Theory 99 (2016) 176–188.

[163] K.-B. Choi, J. J. Lee, G. H. Kim, H. J. Lim, S. G. Kwon, Amplification ratio analysis of a bridge-type mechanical amplification mechanism based on a fully compliant model, Mechanism and Machine Theory 121 (2018) 355–372.

[164] X. Wang, Z. Shi, Double piezoelectric energy harvesting cell: modeling and experimental verification, Smart Materials and Structures 26 (6) (2017) 065002.

[165] S. Wen, Q. Xu, B. Zi, Design of a new piezoelectric energy harvester based on compound two-stage force amplification frame, IEEE Sensors Journal 18 (10) (2018) 3989–4000.

[166] B. Ren, S. W. Or, Y. Zhang, Q. Zhang, X. Li, J. Jiao, et al., Piezoelectric energy harvesting using shear mode $0.71Pb(Mg_{1/3}Nb_{2/3})O_3 - 0.29PbTiO_3$ single crystal cantilever, Applied Physics Letters 96 (8) (2010) 083502.

[167] S. Gao, G. Zhang, L. Jin, P. Li, H. Liu, Study on characteristics of the piezoelectric energy-harvesting from the torsional vibration of thin-walled cantilever beams, Microsystem Technologies 23 (12) (2017) 5455–5465.

[168] D.-A. Wang, N.-Z. Liu, A shear mode piezoelectric energy harvester based on a pressurized water flow, Sensors and Actuators A: Physical 167 (2) (2011) 449–458.

[169] J. Zhao, X. Zheng, L. Zhou, Y. Zhang, J. Sun, W. Dong, S. Deng, S. Peng, Investigation of a d_15 mode PZT-51 piezoelectric energy harvester with a series connection structure, Smart Materials and Structures 21 (10) (2012) 105006.

[170] L. Zhou, J. Sun, X. J. Zheng, S. F. Deng, J. H. Zhao, S. T. Peng, Y. Zhang, X. Y. Wang, H. B. Cheng, A model for the energy harvesting performance of shear mode piezoelectric cantilever, Sensors and Actuators A: Physical 179 (2012) 185–192.

[171] Z. Zeng, B. Ren, L. Gai, X. Zhao, H. Luo, D. Wang, Shear-mode-based cantilever driving low-frequency piezoelectric energy harvester using $0.67Pb(Mg_{1/3}Nb_{2/3})O_3 - 0.33PbTiO_3$, IEEE Transactions on Ultrasonics, Ferroelectrics, and Frequency Control 63 (8) (2016) 1192–1197.

[172] X. Yuan, Z. Chen, M. Wu, H. Luo, C. Chen, K. Zhou, D. Zhang, A novel thickness polarized d_15 shear piezoelectric fiber composites, Sensors and Actuators A: Physical 260 (2017) 185–190.

[173] M. H. Malakooti, H. A. Sodano, Piezoelectric energy harvesting through shear mode operation, Smart Materials and Structures 24 (5) (2015) 055005.

[174] S. Banerjee, S. Roy, A timoshenko like model for piezoelectric energy harvester with shear mode, Composite Structures 204 (2018) 677–688.

[175] X. Zheng, Z. Zhang, Y. Zhu, J. Mei, S. Peng, L. Li, Y. Yu, Analysis of energy harvesting performance for d_{15} mode piezoelectric bimorph in series connection based on timoshenko beam model, IEEE/ASME Transactions on Mechatronics 20 (2) (2015) 728–739.

[176] L. Qin, J. Jia, M. Choi, K. Uchino, Improvement of electromechanical coupling coefficient in shear-mode of piezoelectric ceramics, Ceramics International 45 (2, Part A) (2019) 1496–1502.

[177] V. Kulkarni, R. Ben-Mrad, S. E. Prasad, S. Nemana, A shear-mode energy harvesting device based on torsional stresses, IEEE/ASME Transactions on Mechatronics 19 (3) (2014) 801–807.

[178] F. Qian, W. Zhou, S. Kaluvan, H. Zhang, L. Zuo, Theoretical modeling and experimental validation of a torsional piezoelectric vibration energy harvesting system, Smart Materials and Structures 27 (4) (2018) 045018.

[179] H. Li, D. Liu, J. Wang, X. Shang, M. R. Hajj, Broadband bimorph piezoelectric energy harvesting by exploiting bending-torsion of l-shaped structure, Energy Conversion and Management 206 (2020) 112503.

[180] B. Shi, Z. Li, Y. Fan, Implantable energy-harvesting devices, Advanced Materials 30 (44) (2018) 1801511.

[181] X. Cheng, X. Xue, Y. Ma, M. Han, W. Zhang, Z. Xu, H. Zhang, H. Zhang, Implantable and self-powered blood pressure monitoring based on a piezoelectric thinfilm: Simulated, in vitro and in vivo studies, Nano Energy 22 (2016) 453–460.

[182] Y. Kuang, Z. Yang, M. Zhu, Design and characterisation of a piezoelectric knee-joint energy harvester with frequency up-conversion through magnetic plucking, Smart Materials and Structures 25 (8) (2016) 085029.

[183] K. Fan, Z. Liu, H. Liu, L. Wang, Y. Zhu, B. Yu, Scavenging energy from human walking through a shoe-mounted piezoelectric harvester, Applied Physics Letters 110 (14) (2017) 143902.

[184] M. B. Khan, D. H. Kim, J. H. Han, H. Saif, H. Lee, Y. Lee, et al., Performance improvement of flexible piezoelectric energy harvester for irregular human motion with energy extraction enhancement circuit, Nano Energy 58 (2019) 211–219.

[185] G.-T. Hwang, Y. Kim, J.-H. Lee, S. Oh, C. K. Jeong, D. Y. Park, et al., Self-powered deep brain stimulation via a flexible PIMNT energy harvester, Energy & Environmental Science 8 (9) (2015) 2677–2684.

[186] J. Zhao, Z. You, A shoe-embedded piezoelectric energy harvester for wearable sensors, Sensors 14 (7) (2014) 12497–510.

[187] C. Sun, J. Shi, D. J. Bayerl, X. Wang, Pvdf microbelts for harvesting energy from respiration, Energy & Environmental Science 4 (11) (2011) 4508–4512.

[188] G.-T. Hwang, M. Byun, C. K. Jeong, K. J. Lee, Flexible piezoelectric thin-film energy harvesters and nanosensors for biomedical applications, Advanced Healthcare Materials 4 (5) (2015) 646–658.

[189] J. Zhang, Y. Lu, Z. Lu, C. Liu, G. Sun, Z. Li, A new smart traffic monitoring method using embedded cement-based piezoelectric sensors, Smart Materials and Structures 24 (2) (2015) 025023.

[190] C. H. Yang, Y. Song, M. S. Woo, J. H. Eom, G. J. Song, J. H. K. et al., Feasibility study of impact-based piezoelectric road energy harvester for wireless sensor networks in smart highways, Sensors and Actuators A: Physical 261 (2017) 317–324.

[191] P. Laplante, "smarter" roads and highways, IEEE Internet of Things Magazine 1 (2) (2018) 30–35.

[192] S. Pundir, M. Wazid, D. P. Singh, A. K. Das, J. J. P. C. Rodrigues, Y. Park, Intrusion detection protocols in wireless sensor networks integrated to internet of things deployment: Survey and future challenges, IEEE Access 8 (2020) 3343–3363.

[193] J. Pei, B. Zhou, L. Lyu, e-road: The largest energy supply of the future?, Applied Energy 241 (2019) 174–183.

[194] D. Rys, Investigation of weigh-in-motion measurement accuracy on the basis of steering axle load spectra, Sensors 19 (15) (2019) 3272.

[195] H. Xiong, Y. Zhang, Feasibility study for using piezoelectric-based weigh-in-motion (wim) system on public roadway, Applied Sciences 9 (15) (2019) 3098.

[196] J. Gajda, R. Sroka, P. Burnos, Sensor data fusion in multi-sensor weigh-in-motion systems, Sensors 20 (12) (2020) 3357.

[197] A. Dogan, J. F. Fernandez, K. Uchino, R. E. Newnham, The "cymbal" electromechanical actuator, in: Proceedings of ISAF '96. Proceedings of the Tenth IEEE International Symposium on Applications of Ferroelectrics, Vol. 1, 1996, pp. 213–216 vol.1.

[198] A. Moure, M. A. I. Rodríguez, S. H. Rueda, A. Gonzalo, F. Rubio-Marcos, D. U. Cuadros, A. Pérez-Lepe, J. F. Fernández, Feasible integration in asphalt of piezoelectric cymbals for vibration energy harvesting, Energy Conversion and Management 112 (2016) 246–253.

[199] A. Jasim, H. Wang, G. Yesner, A. Safari, A. Maher, Optimized design of layered bridge transducer for piezoelectric energy harvesting from roadway, Energy 141 (2017) 1133–1145.

[200] G. Yesner, A. Jasim, H. Wang, B. Basily, A. Maher, A. Safari, Energy harvesting and evaluation of a novel piezoelectric bridge transducer, Sensors and Actuators A: Physical 285 (2019) 348–354.

[201] A. F. Jasim, H. Wang, G. Yesner, A. Safari, P. Szary, Performance analysis of piezoelectric energy harvesting in pavement: Laboratory testing and field simulation, Transportation Research Record 2673 (3) (2019) 115–124.

[202] C. Chen, T.-B. Xu, A. Yazdani, J.-Q. Sun, A high density piezoelectric energy harvesting device from highway traffic—system design and road test, Applied Energy 299 (2021) 117331.

[203] X. Jiang, Y. Li, J. Li, J. Wang, J. Yao, Piezoelectric energy harvesting from traffic-induced pavement vibrations, Journal of Renewable and Sustainable Energy 6 (4) (2014) 043110.

[204] H. Yang, L. Wang, Y. Hou, M. Guo, Z. Ye, X. Tong, D. Wang, Development in stacked-array-type piezoelectric energy harvester in asphalt pavement, Journal of Materials in Civil Engineering 29 (11) (2017) 04017224.

[205] M. Khalili, A. Biten, G. Vishwakarma, S. Ahmed, A. Papagiannakis, Electromechanical characterization of a piezoelectric energy harvester, Applied Energy 253.

[206] C. Wang, S. Wang, Q. J. Li, X. Wang, Z. Gao, L. Zhang, Fabrication and performance of a power generation device based on stacked piezoelectric energy-harvesting units for pavements, Energy Conversion and Management 163 (2018) 196–207.

[207] C. Wang, J. Zhao, Q. Li, Y. Li, Optimization design and experimental investigation of piezoelectric energy harvesting devices for pavement, Applied Energy 229 (2018) 18–30.

[208] Y. Song, C. H. Yang, S. K. Hong, S. J. Hwang, J. H. Kim, J. Y. Choi, S. K. Ryu, T. H. Sung, Road energy harvester designed as a macro-power source using the piezoelectric effect, International Journal of Hydrogen Energy 41 (29) (2016) 12563–12568.

[209] J. Y. Cho, K.-B. Kim, W. S. Hwang, C. H. Yang, J. H. Ahn, S. Do-Hong, et al., A multifunctional road-compatible piezoelectric energy harvester for

autonomous driver-assist LED indicators with a self-monitoring system, Applied Energy 242 (2019) 294–301.

[210] G. J. Song, K.-B. Kim, J. Y. Cho, M. S. Woo, J. H. Ahn, J. H. Eom, et al., Performance of a speed bump piezoelectric energy harvester for an automatic cellphone charging system, Applied Energy 247 (2019) 221–227.

[211] G. J. Song, J. Y. Cho, K.-B. Kim, J. H. Ahn, Y. Song, W. Hwang, S. D. Hong, T. H. Sung, Development of a pavement block piezoelectric energy harvester for self-powered walkway applications, Applied Energy 256 (2019) 113916.

[212] M. Peigney, D. Siegert, Piezoelectric energy harvesting from traffic-induced bridge vibrations, Smart Materials and Structures 22 (9) (2013) 095019.

[213] D. Zhu, S. P. Beeby, M. J. Tudor, N. R. Harris, A credit card sized self powered smart sensor node, Sensors and Actuators A: Physical 169 (2) (2011) 317–325.

[214] F. R. Fan, W. Tang, Z. L. Wang, Flexible nanogenerators for energy harvesting and self-powered electronics, Advanced Materials 28 (22) (2016) 4283–4305.

[215] H. Wu, Y. Huang, F. Xu, Y. Duan, Z. Yin, Energy harvesters for wearable and stretchable electronics: From flexibility to stretchability, Advanced Materials 28 (45) (2016) 9881–9919.

[216] J. He, T. Wen, S. Qian, Z. Zhang, Z. Tian, J. Zhu, et al., Triboelectric-piezoelectric-electromagnetic hybrid nanogenerator for high-efficient vibration energy harvesting and self-powered wireless monitoring system, Nano Energy 43 (2018) 326–339.

[217] K. Y. Lee, M. K. Gupta, S.-W. Kim, Transparent flexible stretchable piezoelectric and triboelectric nanogenerators for powering portable electronics, Nano Energy 14 (2015) 139–160.

[218] J. M. McCarthy, S. Watkins, A. Deivasigamani, S. J. John, Fluttering energy harvesters in the wind: A review, Journal of Sound and Vibration 361 (2016) 355–377.

[219] N. V. Viet, N. Wu, Q. Wang, A review on energy harvesting from ocean waves by piezoelectric technology, Journal of Modeling in Mechanics and Materials 1 (2) (2017) 20160161.

[220] X. Li, V. Strezov, Modelling piezoelectric energy harvesting potential in an educational building, Energy Conversion and Management 85 (2014) 435–442.

[221] K. B. Singh, V. Bedekar, S. Taheri, S. Priya, Piezoelectric vibration energy harvesting system with an adaptive frequency tuning mechanism for intelligent tires, Mechatronics 22 (7) (2012) 970–988.

[222] J. Lee, B. Choi, Development of a piezoelectric energy harvesting system for implementing wireless sensors on the tires, Energy Conversion and Management 78 (2014) 32–38.

[223] L. Guo, Q. Lu, Potentials of piezoelectric and thermoelectric technologies for harvesting energy from pavements, Renewable and Sustainable Energy Reviews 72 (2017) 761–773.

[224] H.-X. Zou, L.-C. Zhao, Q.-H. Gao, L. Zuo, F.-R. Liu, T. Tan, K.-X. Wei, W.-M. Zhang, Mechanical modulations for enhancing energy harvesting: Principles, methods and applications, Applied Energy 255 (2019) 113871.

[225] M. B. Khan, D. H. Kim, J. H. Han, H. Saif, H. Lee, Y. Lee, et al., Performance improvement of flexible piezoelectric energy harvester for irregular human motion with energy extraction enhancement circuit, Nano Energy 58 (2019) 211–219.

[226] I. Izadgoshasb, Y. Y. Lim, L. Tang, R. V. Padilla, Z. S. Tang, M. Sedighi, Improving efficiency of piezoelectric based energy harvesting from human motions using double pendulum system, Energy Conversion and Management 184 (2019) 559–570.

[227] H. Wang, A. Jasim, X. Chen, Energy harvesting technologies in roadway and bridge for different applications - a comprehensive review, Applied Energy 212 (2018) 1083–1094.

[228] S. Ahmad, M. A. Mujeebu, M. A. Farooqi, Energy harvesting from pavements and roadways: A comprehensive review of technologies, materials, and challenges, International Journal of Energy Research .

[229] S. H. K. et al., Harvesting electrical energy from carbon nanotube yarn twist, Science 357 (6353) (2017) 773.

[230] J. B. et al., Flutter-driven triboelectrification for harvesting wind energy, Nature Communications 5 (2014) 4929.

[231] M. A. Ilyas, J. Swingler, Piezoelectric energy harvesting from raindrop impacts, Energy 90 (2015) 796–806.

[232] C. Wang, S. Wang, Z. Gao, X. Wang, Applicability evaluation of embedded piezoelectric energy harvester applied in pavement structures, Applied Energy 251 (2019) 113383.

[233] L. Guo, Q. Lu, Numerical analysis of a new piezoelectric-based energy harvesting pavement system: Lessons from laboratory-based and field-based simulations, Applied Energy 235 (2019) 963–977.

[234] C. Chen, A. Sharafi, J. Flores, R. L. D. Pena, P. Mendoza, H. Ayala, S. Ortiz-Donato, J.-Q. Sun, Design and laboratory validation of a force-amplified piezoelectric energy harvesting unit, in: Proceedings of ASME 2020 International Design Engineering Technical Conferences and Computers and Information in Engineering Conference, Vol. Volume 7: 32nd Conference on Mechanical Vibration and Noise (VIB), 2020, p. V007T07A006.

[235] H. W. Kim, A. Batra, S. Priya, K. Uchino, D. Markley, R. E. Newnham, H. F. Hofmann, Energy harvesting using a piezoelectric "cymbal" transducer in dynamic environment, Japanese Journal of Applied Physics 43 (9A) (2004) 6178–6183.